JANUARY 1, 1990

Analytical CHEMISTRY

LASERS in MEDICINE

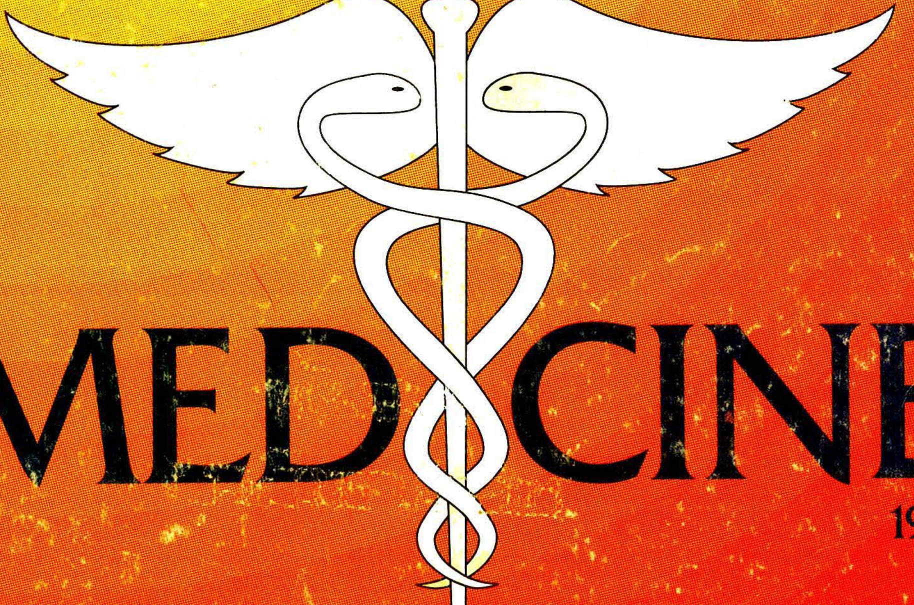

19A

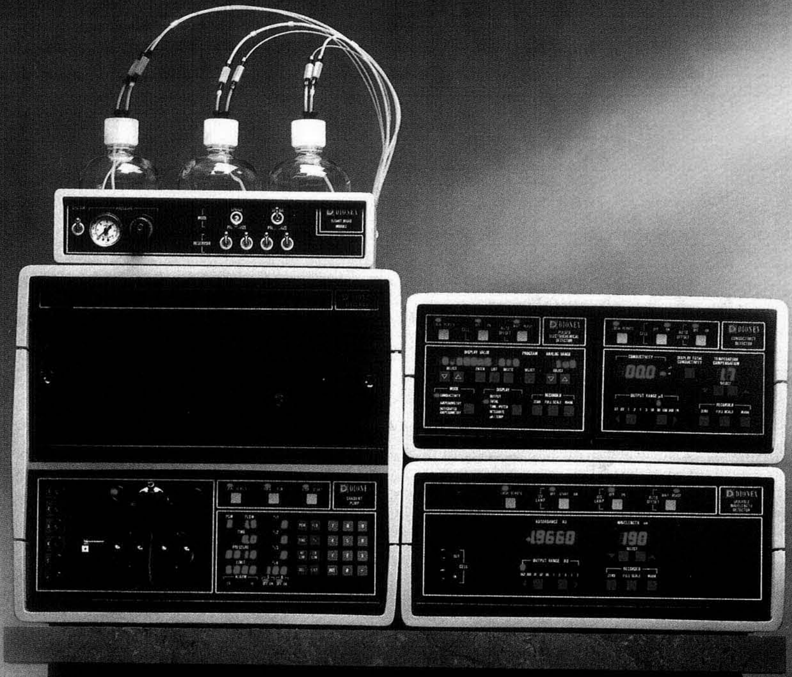

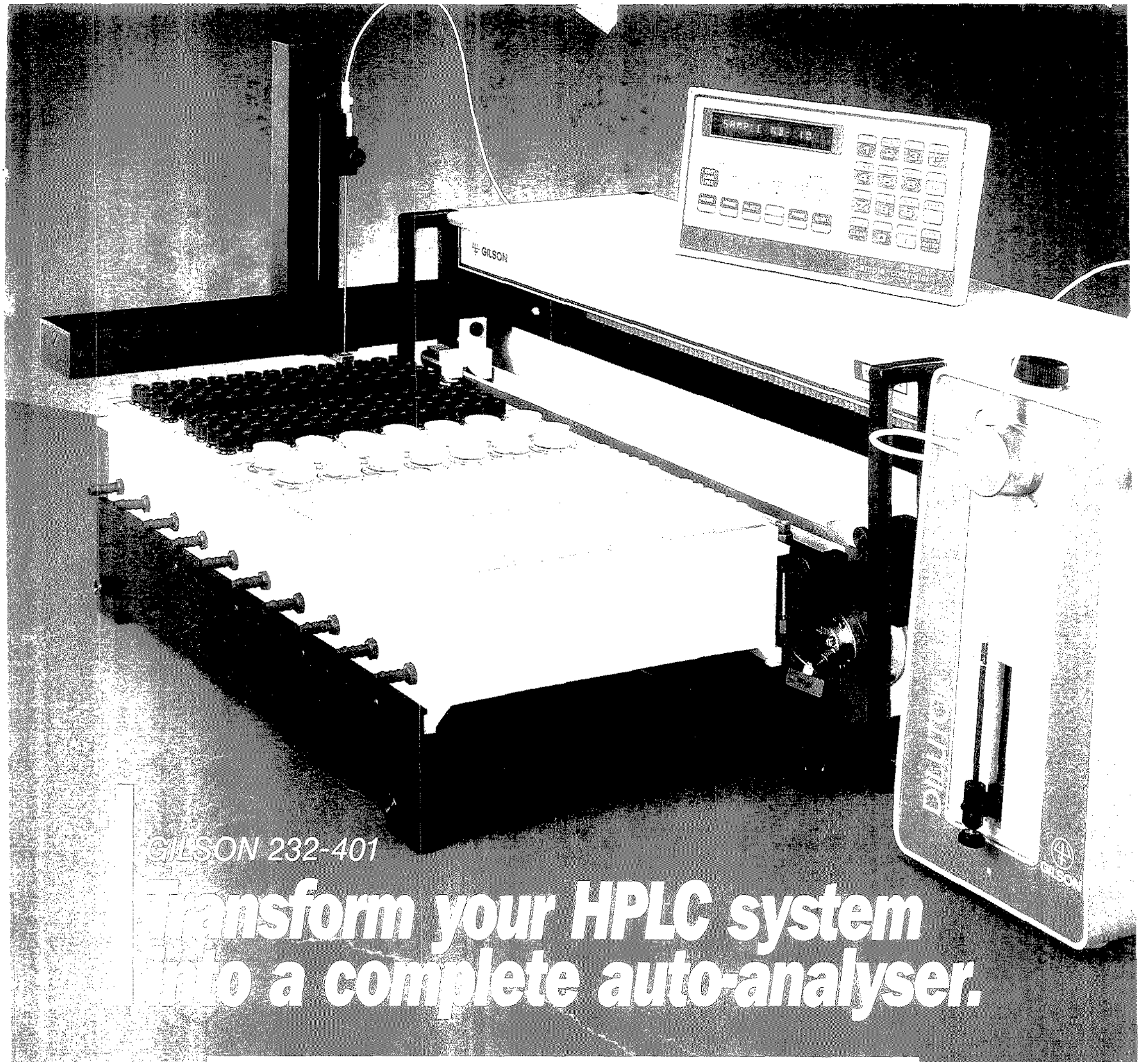
GILSON
GILSON 232-401
Transform your HPLC system into a complete auto-analyser.

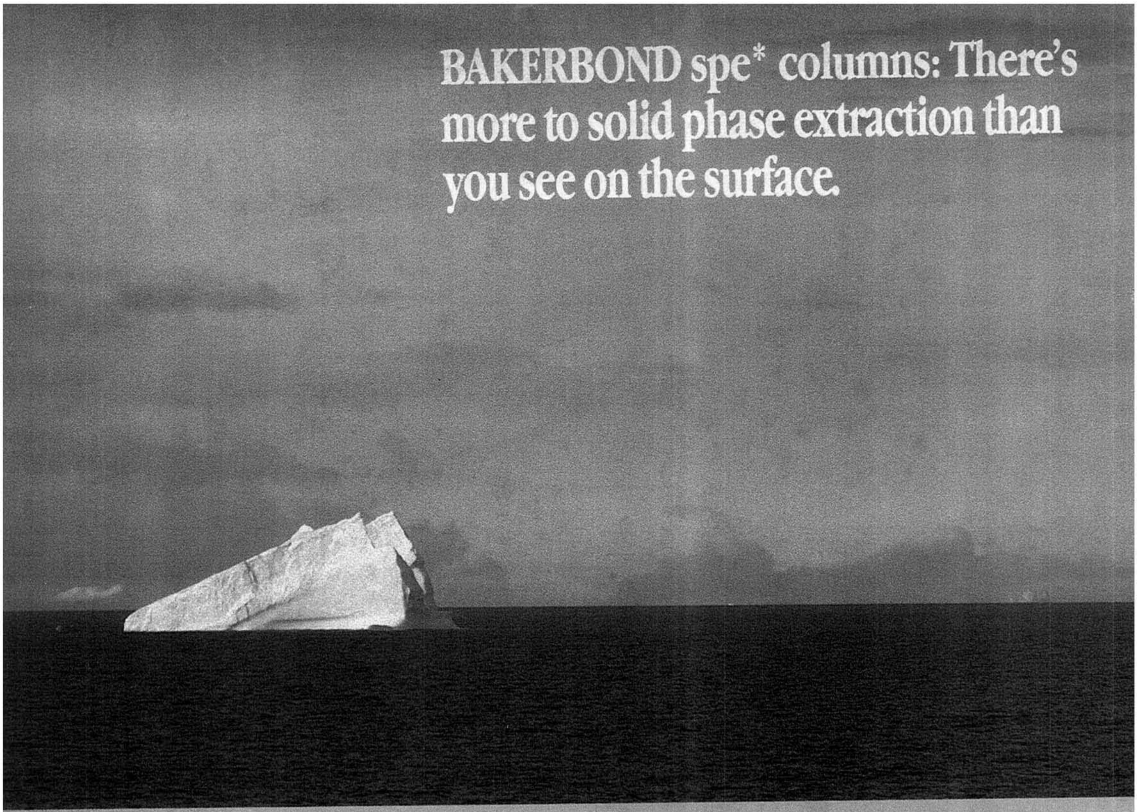
BAKERBOND spe* columns: There's more to solid phase extraction than you see on the surface.

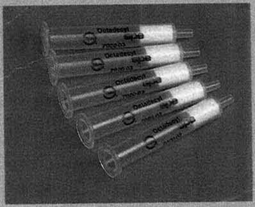

JANUARY 1, 1990
VOLUME 62
NUMBER 1

The Audit Bureau
ANCHAM
62(1) 1A–50A/1–96 (1990)
ISSN 0003-2700

Registered in U.S. Patent and Trademark Office; Copyright 1989 by the American Chemical Society

ANALYTICAL CHEMISTRY (ISSN 0003-2700) is published semimonthly by the American Chemical Society at 1155 16th St., N.W., Washington, DC 20036. Editorial offices are located at the same ACS address (202-872-4570; FAX 202-872-6325; TDD 202-872-8733). Second-class postage paid at Washington, DC, and additional mailing offices. Postmaster: Send address changes to ANALYTICAL CHEMISTRY Member & Subscriber Services, P.O. Box 3337, Columbus, OH 43210.

Claims for missing numbers will not be allowed if loss was due to failure of notice of change of address to be received in the time specified; if claim is dated (a) North America: more than 90 days beyond issue date, (b) all other foreign: more than one year beyond issue date, or if the reason given is "missing from files."

Copyright Permission: An individual may make a single reprographic copy of an article in this publication for personal use. Reprographic copying beyond that permitted by Section 107 or 108 of the U.S. Copyright Law is allowed, provided that the appropriate per-copy fee is paid through the Copyright Clearance Center, Inc., 27 Congress St., Salem, MA 01970. For reprint permission, write Copyright Administrator, Publications Division, ACS, 1155 16th St., N.W., Washington, DC 20036.

Registered names and trademarks, etc., used in this publication, even without specific indication thereof, are not to be considered unprotected by law.

Advertising Management: Centcom, Ltd., 500 Post Rd. East, Westport, CT 06880 (203-226-7131)

1990 subscription rates include air delivery outside the U.S., Canada, and Mexico

	1 yr	2 yr
Members		
Domestic	$ 29	$ 49
Canada and Mexico	64	119
Europe	96	183
All Other Countries	118	227
Nonmembers		
Domestic	59	100
Canada and Mexico	94	170
Europe	186	336
All Other Countries	208	380

Three-year and other rates contact: Member & Subscriber Services, ACS, P.O. Box 3337, Columbus, OH 43210 (614-447-3776 or 800-333-9511).

Subscription orders by phone may be charged to VISA, MasterCard, Barclay card, Access, or American Express. Call toll free 800-ACS-5558 in the continental United States; in the Washington, DC, metropolitan area and outside the continental United States, call 202-872-8065. Mail orders for new and renewal subscriptions should be sent with payment to the Business Management Division, ACS, P.O. Box 28597, Central Station, Washington, DC 20005.

Subscription service inquiries and changes of address (Include both old and new addresses with ZIP code and *recent mailing label*) should be directed to the ACS Columbus address noted above. Please allow six weeks for changes to become effective.

ACS membership information: Lorraine Bowlin (202-872-4567)

Single issues, current year, $8.00 except review issue, $14.00, and LabGuide, $49.00; **back issues and volumes and microform editions** available by single volume or back issue collection. For information or to order, call the number listed for subscription orders by phone; or write the Microform & Back Issues Office at the Washington address.

Nonmembers rates in Japan: Rates above do not apply to nonmember subscribers in Japan, who must enter subscription orders with Maruzen Company Ltd., 3–10 Nihonbashi 2-chome, Chuo-ku, Tokyo 103, Japan. Tel: (03) 272-7211.

Analytical® CHEMISTRY

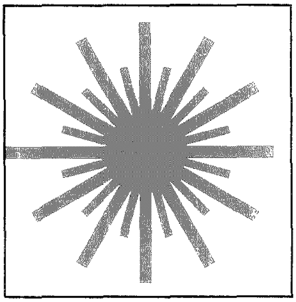

INSTRUMENTATION 19 A

On the cover. **Fluorescence diagnosis and photochemical treatment of diseased tissue using lasers.** In the second of a two-part series, Sune and Katarina Svanberg and co-workers from the Lund Institute of Technology (Sweden) and The Lund University Hospital describe the use of laser-induced fluorescence for tumor and plaque diagnostics as well as imaging systems that use LIF

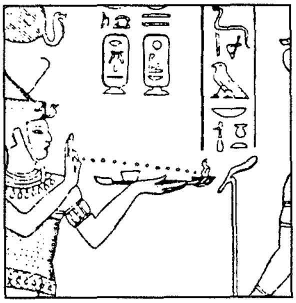

ANALYTICAL APPROACH 41 A

Identification of a Bronze Age resin. In 1982 a shipwrecked vessel dating back to the fourteenth century B.C. was discovered near Turkey. Among the items retrieved from the ship were numerous jars of yellow resin. Hampton H. Hairfield, Jr., and Elizabeth M. Hairfield of Mary Baldwin College discuss the analytical techniques used to identify this unknown resin

BRIEFS 6 A

EDITORIAL 13 A

Analysis in the service of medicine. Laser technology can aid in the diagnosis and treatment of diseased tissue, as highlighted in the two-part INSTRUMENTATION feature by Sune and Katarina Svanberg and co-workers in the December 15 and January 1 issues

NEWS 15 A

William Hancock, Alan Marshall, John Rabolt, Debra Rolison, and Shigeru Terabe join ANALYTICAL CHEMISTRY's **Advisory Board.** ▶ Procter & Gamble's Summer Research Program. ▶ Better scrubbers. ▶ Detecting Lyme disease

FOCUS 29 A

Send in the robots. As the availability of laboratory robots and supporting equipment grows, researchers are finding novel applications for these machines. Three unique and versatile robotic systems are being developed for what were once considered specialized operations

BRIEFS

Perspective: Analytical Biotechnology

Protein Structure Determination in Solution by Two-Dimensional and Three-Dimensional Nuclear Magnetic Resonance Spectroscopy 2

NMR spectroscopy has evolved into a powerful method for determining structures of biological macromolecules. This "Perspective" outlines the methodology used for solving protein structures in solution, describes the basic NMR experiments necessary, and introduces concepts on which the computational algorithms are founded.

Angela M. Gronenborn* and G. Marius Clore*, Laboratory of Chemical Physics, National Institute of Diabetes and Digestive and Kidney Diseases, National Institutes of Health, Bethesda, MD 20892

Articles

Reduction of Reequilibration Time following Gradient Elution Reversed-Phase Liquid Chromatography 16

The addition of 3% 1-propanol to both components of a reversed-phase solvent gradient reduces reequilibration time.

Lynn A. Cole and John G. Dorsey*, Department of Chemistry, University of Florida, Gainesville, FL 32611

Immobilized 8-Oxine Units on Different Solid Sorbents for the Uptake of Metal Traces 21

The sorption of 8-hydroxyquinoline units on XAD-2 ST-DVB resin or on an anion-exchange resin is used for the uptake of a series of trace metal ions. Uptake mechanisms are discussed. Enrichment procedures are derived and applied to the analysis of real samples at the μg/mL level.

O. Abollino, E. Mentasti*, V. Porta, and C. Sarzanini, Department of Analytical Chemistry, University of Torino, Via Giuria 5, 10125 Torino, Italy

Copper Determination in Urine by Flow Injection Analysis with Electrochemical Detection at Platinum Disk Microelectrodes of Various Radii 27

The detection limit for flow injection analysis with amperometric detection at microdisk electrodes is a function of the electrode radius. A 28-μm electrode is optimal for the determination of copper in urine.

Darryl L. Luscombe and Alan M. Bond*, Department of Chemical and Analytical Sciences, Deakin University, Geelong, Victoria 3217, Australia, **David E. Davey,** The South Australian Institute of Technology, The Levels, P.O. Box 1, Ingle Farm, South Australia 5098, Australia, and **John W. Bixler,** Chemistry Department, State University College at Brockport, Brockport, NY 14420

Surface Acoustic Wave Sensor Response and Molecular Modeling: Selective Binding of Nitrobenzene Derivatives to (Aminopropyl)triethoxysilane 32

Nitroaromatics bind selectively to (aminopropyl)triethoxysilane covalently attached to the quartz substrate of a SAW sensor. The selectivity is associated with hydrogen bonding and is studied by the AM1 method.

Wolfgang M. Heckl, Francesca M. Marassi, Krishna M. R. Kallury, David C. Stone, and Michael Thompson*, Department of Chemistry, University of Toronto, 80 St. George Street, Toronto, Ontario M5S 1A1, Canada

How Long Does It Take a Microelectrode To Reach a Voltammetric Steady State? 37

The potentiostatic and galvanostatic approaches of hemispherical and disk microelectrodes to the steady state are investigated.

Cynthia G. Zoski and Alan M. Bond, Department of Chemical and Analytical Sciences, Deakin University, Geelong, Victoria 3217, Australia and **E. Tracey Allinson and Keith B. Oldham*,** Department of Chemistry, Trent University, Peterborough, Ontario K9J 7B8, Canada

Infrared Spectroscopic Determination of pH Changes in Diffusionally Decoupled Thin-Layer Electrochemical Cells 45

Fourier transform reflection absorption infrared spectroscopy is used to monitor changes in the pH of thin-layer cells induced by the passage of current between the working and counter electrodes.

I. T. Bae, Daniel A. Scherson*, and Ernest B. Yeager, Case Center for Electrochemical Sciences and the Department of Chemistry, Case Westen Reserve University, Cleveland, OH 44106

---

* Corresponding author

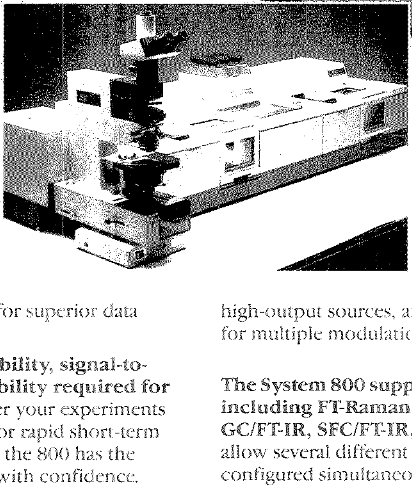

Discover FT-IR 800

The new Nicolet System 800 shapes the future of FT-Spectroscopy

The System 800 represents the new generation in research tools. It is the synthesis of advances in optical, electronic and mechanical design. The System 800 combines an ultra-stable interferometer design with a unique dynamic alignment system, for superior data throughout the spectral range.

The System 800 provides the stability, signal-to-noise performance, and repeatability required for demanding applications. Whether your experiments involve long-term data acquisitions or rapid short-term dynamic spectroscopy applications, the 800 has the capabilities to solve your problems with confidence.

The System 800 incorporates the features demanded by leading research investigators throughout the world. Standard features include optical bench communications, optical bench configuration monitoring and status, rapid spectral range conversion, ultra-quiet electronics train, highest throughput optical design, dynamic alignment, fully expandable optical path, ultra high-output sources, and simplified experimental design for multiple modulation techniques.

The System 800 supports the full range of experiments including FT-Raman, Emission, Microspectroscopy, GC/FT-IR, SFC/FT-IR, and more. Multiple beam paths allow several different experiments or applications to be configured simultaneously.

Nicolet sets the standard for research performance. Let us show you the future of FT-Spectroscopy.

Nicolet
INSTRUMENTS OF DISCOVERY

Belgium: 02-762-2511
Canada: 416-625-8302
France: 1-30-81-3081
Germany: 069-837001
Japan: 06-863-1550
Netherlands: 03403-74754
Switzerland: 056-834545
United Kingdom: 0926-494111

Nicolet Analytical Instruments / 5225-1 Verona Rd. / Madison, WI 53711 / (608) 271-3333 / FAX: (608) 273-5046

To complement these direct Nicolet offices, Nicolet maintains a network of representatives in countries throughout the world.

CIRCLE 95 ON READER SERVICE CARD

BRIEFS

Multivariate Analysis of Carbon-13 Nuclear Magnetic Resonance Spectra. Identification and Quantification of Average Structures in Petroleum Distillates 49

Two series of distillate fractions from North Sea petroleum samples are investigated using DEPT ^{13}C NMR and multivariate analysis. The content of saturated isoprenoid structures is quantitated and is used to discriminate between the two oils in all fractions.

Trond Brekke*, Tanja Barth, Olav M. Kvalheim, and Einar Sletten, Department of Chemistry, University of Bergen, Bergen N-5007, Norway

Simultaneous Monitoring for Parent Ions of Targeted Daughter Ions: A Method for Rapid Screening Using Mass Spectrometry/Mass Spectrometry 56

A screening method used with MS/MS instruments that employ a quadrupole mass filter as the first analyzer is described.

Scott A. McLuckey*, Gary L. Glish, and Barry C. Grant, Analytical Chemistry Division, Oak Ridge National Laboratory, Oak Ridge, TN 37831-6365

Laser Desorption/Fourier Transform Ion Cyclotron Resonance Mass Spectrometry of Polymer Additives 61

The formation of both Na$^+$ and K$^+$ adducts of the additives allows for the recognition of the quasimolecular ions in a mixture spectrum. In one polyethylene extract, the molecular weights of seven compounds are determined, and two of the compounds are identified.

Bruce Asamoto*, Judy R. Young, and Robert J. Citerin, BP Research, Warrensville Research Center, 4440 Warrensville Center Road, Cleveland, OH 44128-2837

Precise Relative Ion Abundances from Fourier Transform Ion Cyclotron Resonance Magnitude-Mode Mass Spectra 70

The best FT/ICR measure of relative ion abundance is based on least-squares fit to an (unphased) magnitude-mode spectrum.

Zhenmin Liang and Alan G. Marshall*, Department of Chemistry, The Ohio State University, 120 West 18th Avenue, Columbus, OH 43210

Determination of Organic Acids in Dilute Hydrocarbon Solution Using Poly(ethylenimine)-Coated Piezoelectric Crystals 76

Piezoelectric crystals coated with a water-soluble basic polymer are used as sensing devices for organic acids dissolved in neutral hydrocarbons. Their application as selective LC detectors is demonstrated.

John M. Charlesworth, DSTO, Materials Research Laboratory, P.O. Box 50, Ascot Vale, Victoria, Australia 3032

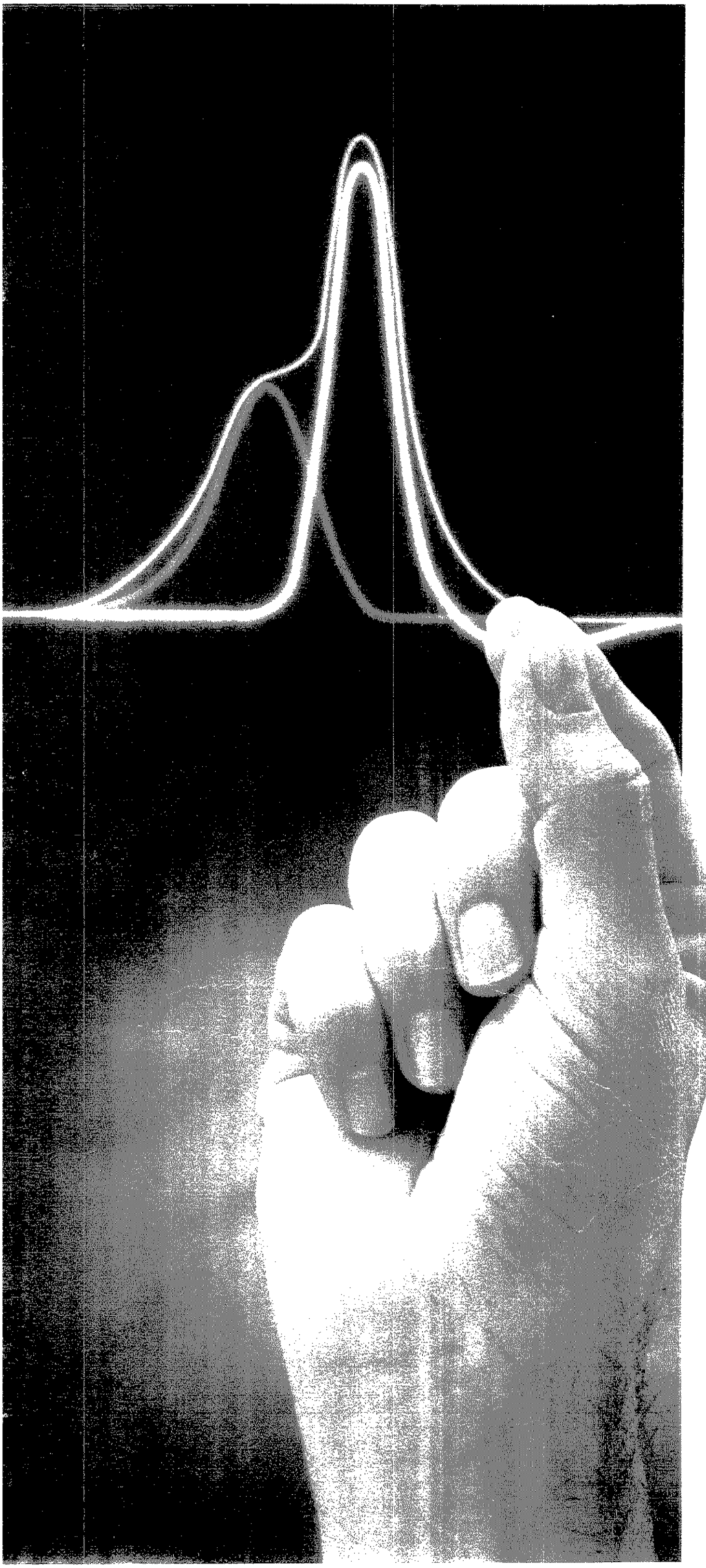

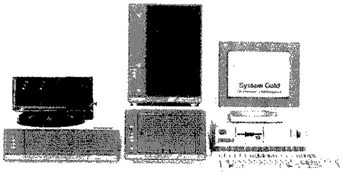

System Gold

BRIEFS

Technical Notes

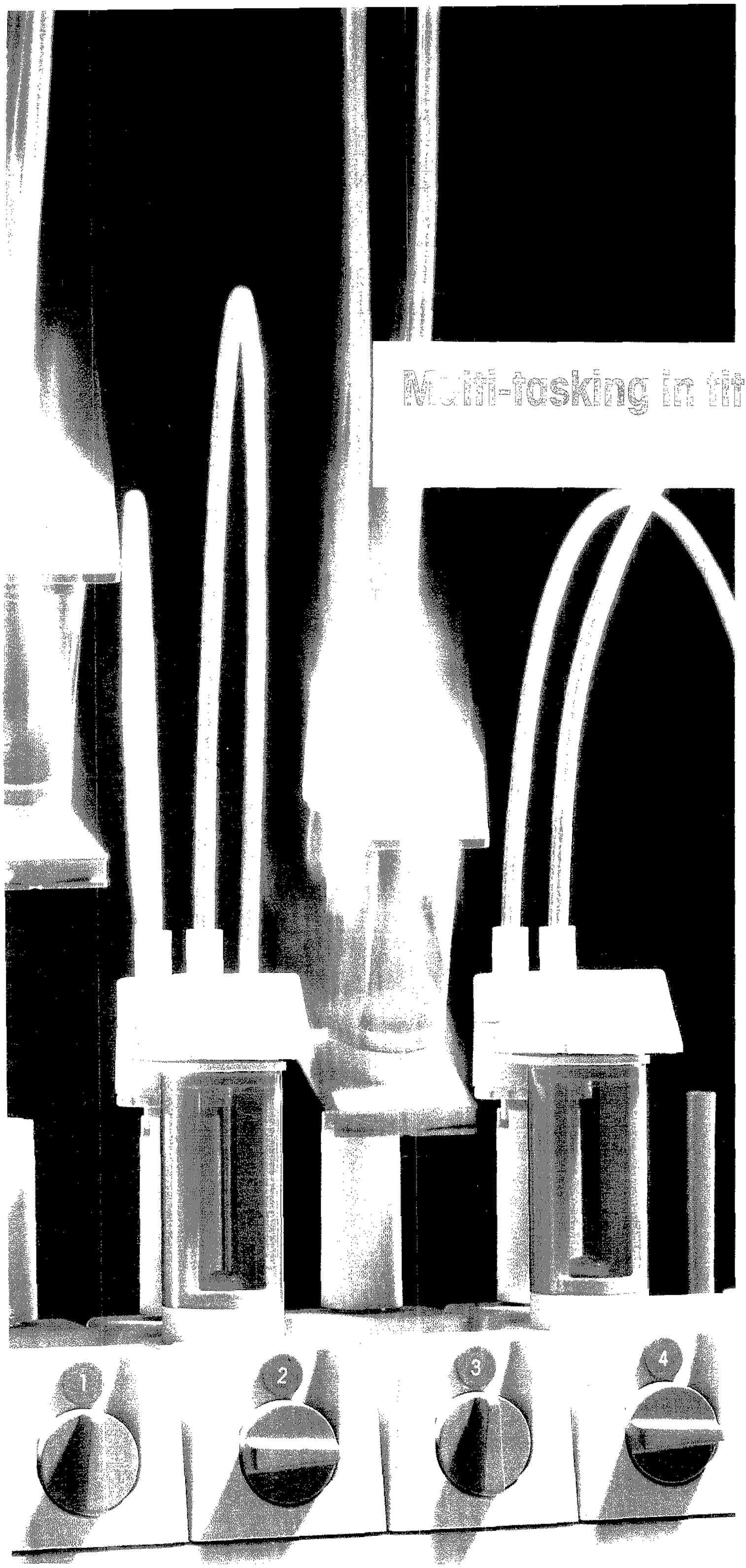

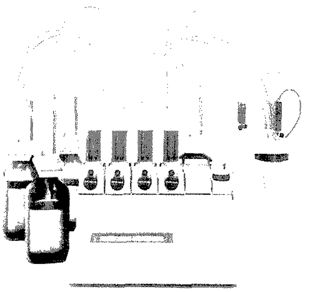

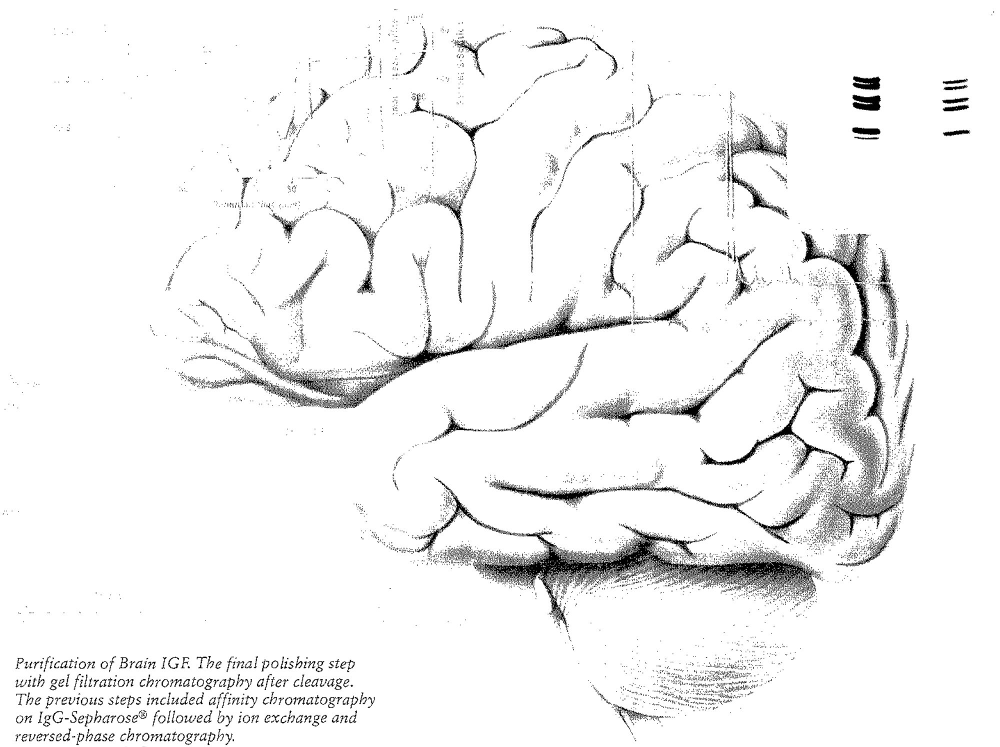PHARMACIA LKB BIOTECHNOLOGY

Purification of ß-casomorphine from defatted human milk. ß-casomorphines are believed to play a role in postpartum depression. The shaded area shows the ß-casomorphine (1-8) immunoreactivity. Column: Analytical Superpac® Pep-S.

Analysis of synthetic Δ-sleep inducing hormones (9 residues) synthesized on the Biolynx® Plus Peptide Synthesizer. Purity check on PhastSystem®.

Purification of Brain IGF. The final polishing step with gel filtration chromatography after cleavage. The previous steps included affinity chromatography on IgG-Sepharose® followed by ion exchange and reversed-phase chromatography. Column: Superdex™ 75 prep grade.

What's so special about peptides?

A lot. Peptides wouldn't be peptides otherwise. The fact is that the vast majority are *biologically active* messengers of very special events.

Pharmacia LKB have been isolating and purifying peptides for more than 30 years. Over the years, we've gained unique insights into how to optimize their separation, analysis and synthesis. We maintain updated information on the latest techniques, applications and instrument systems for peptide work. That's one of our specialties. Why not contact us to make it one of yours too?

We help you manage biomolecules

Pharmacia

Pharmacia LKB Biotechnology

Head office Sweden Tel 46 (018) 163000. **Australia** Tel (02) 8883622. **Austria** Tel (0222) 6866250. **Belgium** Tel (02) 2424660. **Brazil** Tel 55-11 2845815/2898967. **Canada** Tel (514) 4576661. **Denmark** Tel (02) 265200. **East Europe** Tel 43 (0222) 921607. **Federal Republic of Germany** Tel (0761) 49030. **Finland** Tel (90) 5021077. **France** Tel (01) 3064 3400. **Great Britain** Tel (0908) 661101. **Holland** Tel (031) 348077911. **India** Tel (0812) 29634. **Italy** Tel (02) 2532844/26700475. **Japan** Tel (03) 4929181. **Norway** Tel (02) 549095. **Soviet Union** Tel 46 (08) 7998000. **Spain** Tel (34)-36754411. **Sweden** Tel 46 (08) 79980 00. **Switzerland** Tel (01) 8211816. **United States** Tel (201) 4578000. **Far East** Tel 852 (5) 8148421. **Middle East** Tel 30 (1) 8947396. **Other countries** Tel 46 (08) 7998000. *(8904) 1129*

CIRCLE 107 ON READER SERVICE CARD

EDITORIAL

Analysis in the Service of Medicine

This issue of ANALYTICAL CHEMISTRY features Part II of an INSTRUMENTATION article by Svanberg, Svanberg, and co-workers detailing the applications of laser fluorescence in medical diagnostics and therapy. In addition to being an excellent review of an exciting new field, this work serves as an example of the successful melding of analytical science and medicine.

In Part I (December 15, 1989 issue) the standard medical applications of laser technology were introduced in surgical practice and in laboratory atomic and molecular analysis. The role of hematoporphyrin as a fluorescence tag for tumor diagnosis and photodynamic therapy was also outlined. The use of photochemistry to destroy cancerous cells was particularly fascinating. By combining fluorescence analysis with ablation, the laser system becomes a "smart" scalpel. In Part II the broader potential for tumor and atherosclerosis diagnosis is explored, and the unique tool of laser fluorescence imaging is discussed.

This work demonstrates the importance of practical problem solving when biomedical applications are involved. Far too often a technique is heralded as having great utility in biology and medicine before practical applications are explored. In the quest for funding, publicity, and prestige, methods are labeled significant to the life sciences before a single biological analysis is performed, let alone a problem solved. The need for advanced methods of analysis in systems critical to biology and medicine cannot be denied. This need can only be met if the analytical chemistry community maintains strong ties to the biologists and physicians who target the problems. It has always been our role as analytical chemists to provide answers to other scientists' most pressing questions. This can't be done in a vacuum; it requires constant communication and cooperation. The importance of collaborative research efforts in this regard cannot be overemphasized.

The potential significance of modern analytical chemistry to the biomedical community is enormous. We must always, however, provide practical solutions to real-world problems, regardless of the impressive complexity or power of a technique. The current tools of modern analysis and those still to be developed will allow biologists and physicians to confront and solve problems previously considered unattainable.

G. H. Morrison

VARIAN NMR FLEXIBILITY NOW RESOLVES PROBLEM DIVERSITY

MICROIMAGING SOLIDS LIQUIDS

UNITY lets you switch from one to the other with ease

Combine high performance capabilities with unparalleled flexibility using Varian's new UNITY™ NMR spectrometer. This unique spectrometer is a true, multi-capability instrument that performs high resolution microimaging as easily as it analyzes liquid and solid samples.

UNITY's revolutionary system architecture employs a modular design that addresses all NMR applications with a single instrument.

Analyze liquid samples using a variety of techniques over a wide range of nuclei. Perform CP/MAS, wideline and multipulse for solid samples. Examine microimaging samples with ease. Maximum flexibility has been built in to cover future experimental capabilities for every application.

Resolve problem diversity: invest in the most flexible technology of today to better address the research of tomorrow. Invest in a UNITY NMR spectrometer. For additional information, please call **800-231-8134.** In Canada, call **416-457-4130.**

Varian is your full-line company for analytical instrumentation
UV-Visible-NIR
LIMS
Atomic Absorption
NMR
Liquid Chromatography
Gas Chromatography

CIRCLE 142 ON READER SERVICE CARD

NMR WITH A FUTURE

New Advisory Board Members Appointed

Five new members have been selected to serve three-year terms on ANALYTICAL CHEMISTRY's Advisory Board. Each January, membership on the board is rotated as new appointees replace those members whose terms have expired.

New members of the board are William Hancock, Genentech, Inc.; Alan Marshall, The Ohio State University; John Rabolt, IBM Almaden Research Laboratory; Debra Rolison, Naval Research Laboratory; and Shigeru Terabe, Kyoto University (Japan).

Leaving the board are Peter Griffiths, University of Idaho; Nobuhiko Ishibashi, Kyushu University (Japan); Mary Kaiser, E. I. du Pont de Nemours & Co.; David Nelson, Office of Naval Research; and Andrew Zander, Varian Research Center.

Continuing to serve on the board are Bernard Bulkin, BP America; Michael Epstein, National Institute of Standards and Technology; Renaat Gijbels, University of Antwerp (Belgium); Thomas Isenhour, Kansas State University; James Jorgenson, University of North Carolina, Chapel Hill; Peter Jurs, The Pennsylvania State University; Lawrence Pachla, Sterling Drug Co.; Ralph Sturgeon, National Research Council of Canada; George Wilson, University of Kansas; Mary Wirth, University of Delaware; and Richard Zare, Stanford University. In addition, the past chairman of the ACS Division of Analytical Chemistry, Sam Perone of San Jose State University, continues to serve as the 1990 ex officio member.

Established in the 1940s to advise the JOURNAL's editors, the advisory board meets formally once a year at ACS headquarters in Washington, DC. The board members are a vital link between the editors and the analytical community, providing guidance and advice throughout the year with regard to editorial content and policy. Brief biographical sketches of the new members follow.

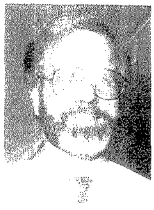

William Hancock received a B.Sc. degree (1967) and a Ph.D. (1970) from Adelaide University (South Australia) and is currently head of the analytical chemistry department at Genentech. His work involves the separation and structural analysis of recombinant DNA-derived proteins and the application of reversed-phase high-performance liquid chromatography for the analysis of polypeptides. Along with J. T. Sparrow, Hancock co-authored *A Laboratory Manual for the Isolation of Biological Materials by HPLC* and edited *HPLC in Biotechnology* as well as two volumes of the *CRC Handbook of HPLC for the Separation of Amino Acids, Peptides, and Proteins.*

Alan Marshall, professor of chemistry and biochemistry and director of the Campus Chemical Instrument Center at The Ohio State University (OSU), received a B.A. degree (1965) from Northwestern University and a Ph.D. (1970) from Stanford University under the direction of John Baldeschwieler. His research centers around method development and the application of Fourier transform ion cyclotron resonance mass spectrometry. A fellow of the American Physical Society and the American Association for the Advancement of Science, Marshall is the 1988 recipient of the OSU Distinguished Scholar Award.

John Rabolt, of the Polymer Science Department at IBM's Almaden Research Laboratory, studies the characterization of solid-state polymer structure, morphology, and orientation using Fourier transform IR and Raman spectroscopies. In addition, his research spans the areas of Langmuir–Blodgett films, polymer complexes, integrated optics, and interfacial interactions. Rabolt received a B.S. degree (1970) from the State University of New York College at Oneonta and a Ph.D. in physics (1974) from Southern Illinois University. He is a fellow and chairman of the American Physical Society Division of High Polymer Physics and recipient of the 1985 Coblentz Award and the 1990 Williams–Wright Award.

Debra Rolison received a B.S. degree (1975) from Florida Atlantic University and a Ph.D. (1980) from the University of North Carolina, Chapel Hill, under the guidance of Royce Murray. As a research chemist at the Surface Chemistry Branch of the Naval Research Laboratory, she is studying the interaction between zeolites and nanometer-size supported metals for use as ultramicroelectrodes. She is also interested in the use of extended X-ray absorption fine structure spectroscopy (EXAFS) to explore small-particle environments in the presence and absence of electric fields.

Shigeru Terabe received B. Eng. (1963), M. Eng. (1965), and D. Eng. (1973) degrees from Kyoto University. From 1965 to 1978, he was employed by the Shionogi Research Laboratory in Japan. Currently Terabe is an associate professor of industrial chemistry at Kyoto University where his research interests include capillary electrophoresis, electrokinetic chromatography, and open-tubular capillary liquid chromatography. On April 1, Terabe will join the faculty at the Himeji Institute of Technology as a professor of chemistry.

Summer Analytical Research Program

Procter & Gamble has announced that it will again sponsor a Summer Analytical Research Program for graduating college seniors majoring in chemistry. Students accepted in the program will work full time for 10–12 weeks in an analytical research laboratory at one of four corporate technical centers in Cincinnati.

Applicants must be U.S. citizens or permanent residents who are in their senior year and plan to enter graduate school as Ph.D. candidates in analytical chemistry. Deadline for applications is March 1. For more information, write to Coordinator, Summer Analytical Research Program, Procter & Gamble, Miami Valley Laboratories, Room 1D42, Cincinnati, OH 45247.

Lyme Disease Test

The polymerase chain reaction (PCR), which has become a powerful tool in genetic testing and basic research, could also aid in the diagnosis of tick-borne Lyme disease. Patricia Rosa and Tom Schwan, researchers at the National Institute of Allergy and Infectious Disease's Rocky Mountains Laboratory in Hamilton, MT, have developed a PCR-based test that can detect as few as five of the spiral-shaped bacterium, *Borrelia burgdorferi*, that causes the disease.

Lyme disease is now the most commonly reported arthropod-transmitted infection in the United States. (In 1988 there were more than 4500 cases.) Prompt treatment with antibiotics usually eliminates the infection. Otherwise, chronic arthritic, neurologic, or cardiac symptoms could develop.

Lyme disease is commonly diagnosed by the appearance of characteristic symptoms and from patient history. However, up to 40% of infected individuals never develop the telltale skin rash, and about half do not recall being bitten by a tick.

Tests for antibodies to *B. burgdorferi* can also identify the disease. Unfortunately, it can take up to six months following infection for these antibodies to reach levels high enough to detect, and antibodies to other bacteria can cross-react, yielding false positive results.

On the other hand, *B. burgdorferi* collected in different geographic areas and from a range of hosts—including ticks, rodents, and humans—has been detected in low concentrations by PCR. The test could become a standard clinical test when researchers identify which human tissue(s) harbor the disease, thereby avoiding false negative results.

PCR targets a DNA sequence distinctive to the bacterium, then copies the sequence. Repeated cycles quickly generate enough material for analysis.

New Process for Smokestack Scrubbers

Lawrence Berkeley Laboratory (LBL) researchers have developed what could be an economical and efficient process for scrubbing SO_2 and NO_x from smokestake emissions. Decreasing the output of these pollutants could ease the problem of acid rain and lung-damaging ozone in the lower atmosphere.

The LBL process, discovered by a research team led by chemist Shih-Ger Chang, removes 90% of SO_2 and up to 100% of NO_x. The best system currently used, in some power plants in Japan and Europe, removes up to 90% of these pollutants. However, that process is expensive and, unlike the LBL method, requires separate systems for SO_2 and NO_x.

The Chang process modifies the standard limestone slurry scrubber by adding yellow phosphorus, seen glowing in the reactor in the accompanying photograph. Limestone removes SO_2, whereas the yellow phosphorus eliminates NO_x. Byproducts of the LBL treatment include commercially valuable products such as phosphoric acid, ammonium phosphate, and gypsum.

On the other hand, the high-efficiency scrubbers in Japan and Europe remove NO_x by selective catalytic reduction, which reduces the oxides to ammonia at high temperatures. Costs for selective catalytic reduction run as low as around $2100 per ton of NO_x eliminated. In comparison, the LBL process is estimated to cost as little as $1300 per ton each of NO_x and SO_2 removed. A typical 500-MW fossil fuel plant discharges 300–400 tons of SO_2 and NO_x daily. Tests of a scaled-up version of the new scrubber process are now under way.

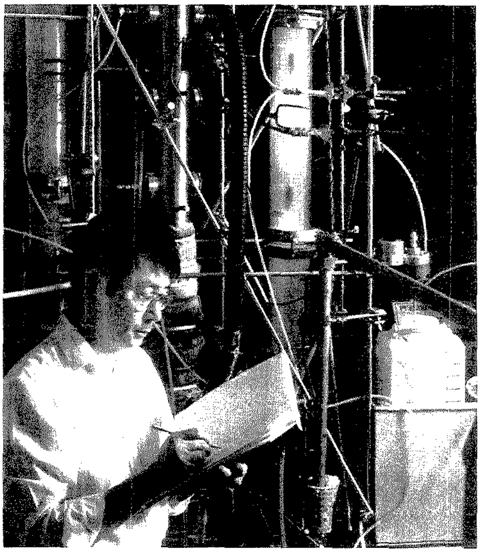

COURTESY OF LAWRENCE BERKELEY LABORATORY

Lawrence Berkeley Laboratory chemist Shih-Ger Chang tabulates results in his laboratory during a run of a new power plant emissions treatment system invented by his research team. The glowing glass cylinder behind Chang is the heart of the system, a scrubber capable of removing both sulfur dioxide and the oxides of nitrogen from emissions. Phosphorus, an agent used in the process, causes the glowing effect.

DIALOG INTRODUCES ANOTHER TABLE OF BASIC ELEMENTS FOR YOUR LAB.

There's no symbol for *information* in the Periodic Table. Yet nothing could be more crucial to your research than complete, accurate technical and business information.

That's why many chemists consider DIALOG an essential element in the modern lab.

As the world's largest online knowledgebank, DIALOG gives you access to a whole world of critical information. Right in your own lab.

For starters, you can tap into the crucial scientific data. DIALOG has detailed information on everything from compound identification to chemical safety data, property data, substance and substructure.

Then you can expand your focus by accessing important, related data that will enable you to look at your work in a broader context.

For example, you can investigate patents, competitive projects, new product markets, and worldwide industry trends. In fact, you can investigate any topic, anytime.

And you won't have to sacrifice depth for the sake of breadth. DIALOG is updated continuously, so the data is always comprehensive and current. And many citations can be conveniently retrieved in full text.

Call today for more information and a free Periodic Table Reference Card. Once you've examined them, you'll see how DIALOG can become a basic element of all your research.

Call us toll free at 800-3-DIALOG, (800-334-2564). Or request information by Fax at 415-858-7069.

DIALOG INFORMATION SERVICES, INC
A Knight-Ridder Company

The world's largest online knowledgebank.

© 1989 Dialog Information Services, Inc., 3460 Hillview Avenue, Palo Alto, California 94304. All rights reserved. DIALOG is a service mark of Dialog Information Services, Inc. Registered U.S. Patent and Trademark Office

CIRCLE 30 ON READER SERVICE CARD

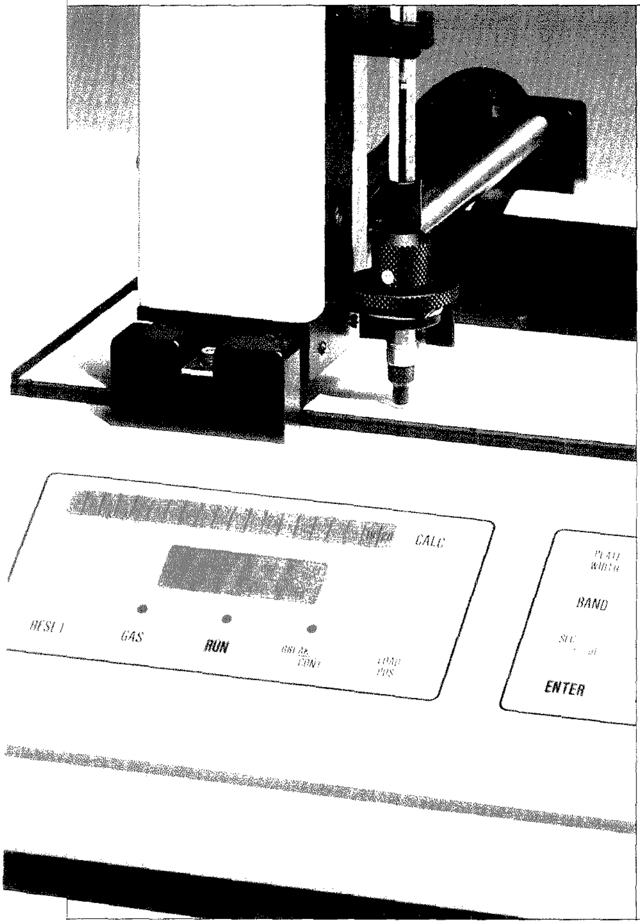
CALC
RESET
GAS
RUN
BAND
ENTER

Stefan Andersson-Engels, Jonas Johansson, and Sune Svanberg
Department of Physics
Lund Institute of Technology
P.O. Box 118
S-221 00 Lund
Sweden

Katarina Svanberg
Department of Oncology
Lund University Hospital
S-221 85 Lund
Sweden

INSTRUMENTATION

In this two-part series, Sune and Katarina Svanberg and co-workers focus on the spectroscopic aspects of laser use in several emerging applications of medical importance. Part I, which appeared in the December 15 issue (1), surveyed laser techniques for atomic and molecular analyses of samples of clinical interest, spectroscopic analysis of the laser-induced plasma obtained when a high-power pulsed laser beam interacts with tissue, and the use of tumor-seeking agents in combination with laser radiation to provide new possibilities for malignant tumor detection and treatment.

In Part II, we describe the use of laser-induced fluorescence (LIF) for tumor and plaque diagnostics. The diagnostic potential is increased by including the temporal characteristics of the fluorescence decay. The extension of point monitoring to imaging measurements also is described, together with implications for practical clinical work.

Tumor diagnostics using LIF

LIF studies are performed in a laser regime where no change in the tissue is induced. The photon energy is chosen sufficiently below the limit for DNA photodissociation to avoid mutagenicity.

LIF has proven to be useful for diagnostic purposes, and early work was reported by American (*2, 3*) and Chinese (*4–6*) groups as well as by our research group (*7, 8*). The ground state and the first excited electronic levels of large molecules such as biological ones are broadened by vibrational motion and interactions with surrounding molecules. Thus, absorption occurs in a broad band, allowing a fixed-frequency laser such as the nitrogen laser (λ = 337 nm) to be used for the excitation. A radiationless relaxation to the bottom of the excited band then occurs on a picosecond time scale. The molecules remain here for a typical lifetime of a few nanoseconds. Fluorescent light is released in a broad band, which does not normally exhibit any sharp features. Intersystem crossing to the triplet state, internal conversion, and the transfer of energy to surrounding molecules are strongly competing radiationless processes. Tissue containing hematoporphyrin derivative (HPD) molecules will exhibit sharp spectral features in the red spectral region.

In exploiting tissue LIF for medical diagnosis, it is useful to start with detailed laboratory studies of tissue samples. In most of our studies, a N_2 laser emitting 5-ns pulses at 337 nm has been employed for excitation; a XeCl excimer laser (λ = 308 nm) and an excimer-pumped dye laser have also been used. The radiation is directed onto the sample by mirrors. Fluorescent light is collected and directed to an optical multichannel analyzer system that

0003-2700/90/0362-019A/$02.50/0

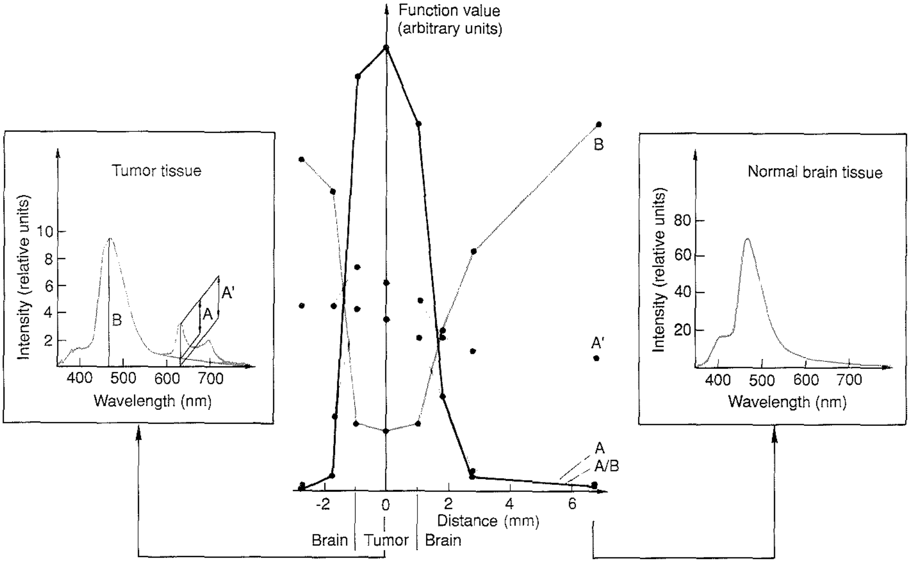

Figure 1. Fluorescence data obtained with 337-nm excitation in a scan over a tumor in the brain of a rat that received 1 mg/kg body weight Photofrin II (dihematoporphyrin ether/ester) prior to the investigation.

Left: Fluorescence spectrum of the central tumor is shown with fluorescence intensities A, A′, and B. Right: Fluorescence spectrum of the nonaffected normal surrounding brain tissue. Note the different intensity scales. Functions of the fluorescence intensities along the scan are presented in the center. (Adapted with permission from Reference 10.)

captures the entire fluorescent light distribution for every laser pulse. The system incorporates a gated image-intensified diode array detector that is placed in the focal plane of the small spectrometer. The detector gating, normally set to 500 ns, makes it possible to suppress continuous background light while collecting all fluorescent light. Spectra can be stored on floppy disks and printed out on paper. Fluorescence intensities are measured according to a standard.

For clinical fluorescence studies we have used a similar system that is equipped with a fiber-optic probe. Light from a N_2 laser or a dye laser pumped by the fixed-frequency laser is focused into 600-μm-diameter quartz fibers via a dichromic beam splitter that reflects the UV light but transmits all visible radiation. Fluorescent light from the sample is collected by the same fiber and is directed to the entrance slit of the optical multichannel analyzer system. The fiber can be inserted through the biopsy channel of an endoscope for investigations of corpular lumina (*9*).

As a first illustration of tissue diagnostics, data from a fluorescence scan through an experimental malignant brain tumor in a rat are shown in Figure 1 (*10*). The animal received an injection of dihematoporphyrin ether/ester (DHE) corresponding to 1 mg/kg body weight before the investigation. The recorded spectrum on the left shows a clear signature of DHE in the 600–700-nm wavelength region that was obtained using 337-nm excitation. In the right-hand part of the figure, the HPD signal is absent in normal brain tissue. In addition, the bluish autofluorescence is strongly reduced in the malignant tumor tissue.

To display these observations more quantitatively, the intensity at 630 nm was evaluated as the signal A′. By subtracting the background, we obtain the intensity A; the blue fluorescence intensity at 470 nm is denoted by B. In the plot the strong contrast enhancement obtained by using the background-free intensity A is demonstrated, and the decrease in the autofluorescence intensity is clearly displayed. By forming the ratio A/B, contrast can be further improved, as illustrated in Figure 1. Such a ratio forms a dimensionless quantity, which has the attractive feature of being independent of surface topography and variations in distance, excitation, and detection efficiency.

We have performed extensive studies in tissue fluorescence diagnostics in rats (*7, 8, 10–13*) to explore the effect of drug uptake and retention, tissue autofluorescence, and optimization of excitation wavelength. We have also compared the tumor-marking capability of different sensitizers. As an example, fluorescence spectra from tumors in rats injected with 15 mg/kg body weight are shown in Figure 2 for 337-nm excitation (*13*). An interesting feature of polyhematoporphyrin ester (PHE) is that the fluorescence peak is found further to the red compared with the other porphyrins. PHE is a highly aggregated and stable substance, whereas DHE still contains a substantial fraction of monomers. This might indicate that PHE is not converted to monomers in tissue, which is probably the case for DHE. This theory is supported in the study of HPD using the

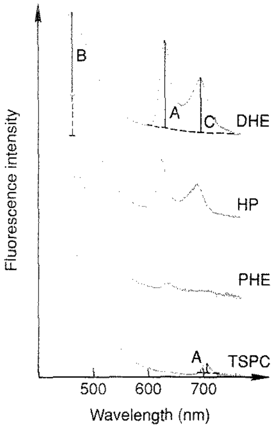

Figure 2. Typical LIF spectra (relative units) from rat tumors.

The rats were injected with 15 mg/kg body weight of hematoporphyrin (HP), dihematoporphyrin ether/ester (DHE), polyhematoporphyrin ester (PHE), and tetrasulfonated phthalocyanine (TSPC). The excitation wavelength was 337 nm. (Adapted with permission from Reference 13.)

HPLC method (illustrated in Part I of this series), where a fluorescence red shift was found for the more aggregated components.

Human tumor demarcation is illustrated by data from a fluorescence study of a metastasis of recurrent breast cancer (Figure 3). The patient received 2.5 mg/kg body weight of DHE one day before the study (*14*, *15*). Again, the tumor exhibited an increased red fluorescence and a decreased blue autofluorescence, which in combination yield a distinct tumor demarcation.

Plaque diagnostics using LIF

Atherosclerosis is another disease for which the use of laser light in diagnosis and therapy can have a great impact. Atherosclerosis can affect all kinds of arteries and most likely results from risk factors such as hyperlipidemia, hypertension, and smoking. The condition affects the endothelium cells at the surface as well as the underlying layer, the intima. A diseased region—a plaque—starts to develop with inclusions of different anomalies such as lipid droplets, cholesterol crystals, and

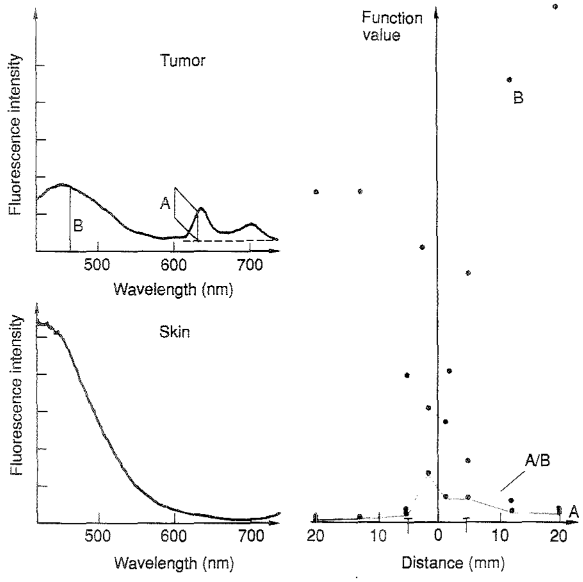

Figure 3. Fluorescence data from a scan across a breast carcinoma metastasis one day after DHE injection.

Sample spectra for tumor and surrounding tissue are shown with evaluated fluorescence intensities. The drug dose was 2.5 mg/kg body weight. (Adapted with permission from Reference 15.)

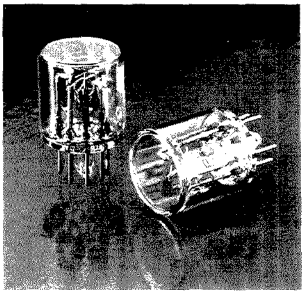

calcifications (Figure 4). The surface of the lesion consists of fibrotic constituents such as collagen and elastin. The pigment β-carotene is also present in plaques. When the damage has reached a serious level, calcification also occurs at the surface and the endothelium is severely disrupted, with the potential for thrombosis formation.

The removal of plaque in diseased or obstructed vessels by laser radiation administered through a fiber-optic light guide (laser angioplasty) is an extremely attractive possibility (*16*, *17*). However, the risk of vessel perforation presents a serious problem, and improved diagnostics are needed to ensure that the fiber tip is placed at the correct location within the vessel. An interesting task is to try to spectroscopically distinguish atherosclerotic plaque from normal vessel tissue.

The first fluorescence experiments aimed at spectroscopic guidance in laser angioplasty were reported by Kittrell et al. (*18*), who used excitation at 480 nm. We find that by using N_2 laser excitation at 337 nm, prominent differences between atherosclerotic plaque and normal artery wall can be found in fluorescence spectra—for both large vessels, such as the aorta and pulmonary arteries, and small ones, such as coronary vessels (*19*, *20*). Examples of spectra can be found in Figure 5 (*19*). The intensities at 390, 415, 480, 580, and 600 nm are evaluated as signals a, b, c, d, and e, respectively. We have experimented with different dimensionless contrast functions to obtain good discrimination between plaque and normal tissue. As can be seen from the fluorescence scan shown in the figure, ratios such as a/c and b/c discriminate well between plaque and normal artery wall, whereas d/e does not.

Fluorescence studies of arteries have been performed by several groups using different excitation wavelengths (*21–24*). Most of the studies have been performed in vitro. The data shown in Figure 5 are obtained from a resectioned and rinsed segment of a human artery. Although superficial blood is removed, the spectra show clear signs of hemoglobin reabsorption at 415, 540, and 580 nm. Clearly, varying amounts of blood between the tissue and the

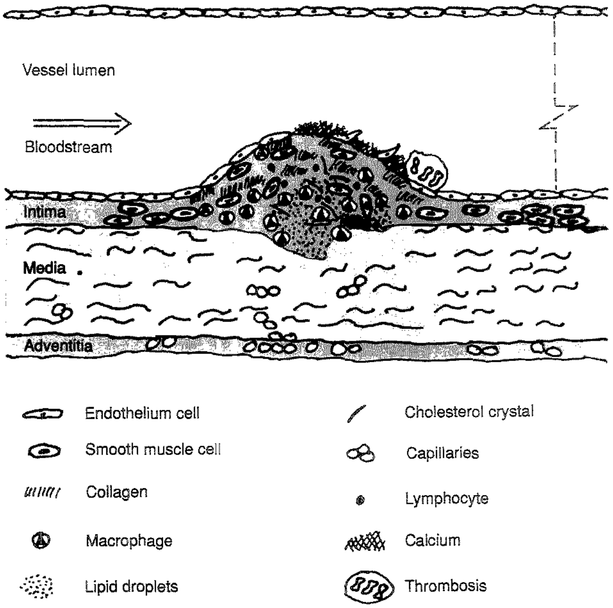

Figure 4. Illustration of a cross section through a blood vessel with an atherosclerotic plaque.
A thrombosis is under development on the downstream side of the plaque.

measurement fiber could strongly affect the spectral characteristics of the fluorescence spectrum. Thus, for reliable clinical applications, the plaque identification criteria must be largely independent of blood.

One way to achieve this is to evaluate the fluorescence intensities at two wavelengths where the blood absorption is the same, so that the blood interference is eliminated when a ratio of the absorptions is formed (*19*, *25*). Such a wavelength pair is 380 and 437 nm. Another possibility is to use the temporal characteristics of the fluorescence decay. We have recently shown that the signal attributable to plaque has a longer decay time than normal nondiseased vessel wall, as illustrated in Figure 6a (*26*). A synchronously pumped dye laser was cavity dumped, and the 6-ps pulses were frequency doubled to 325 nm in these studies. The lifetimes are actually long enough to allow the use of a N_2 laser with 3-ns pulses in conjunction with a dual-channel boxcar integrator, as illustrated in Figure 7 (*25*). The gate of one channel is set for "late" fluorescence (5–15 ns) and the other is set for "early" fluores-

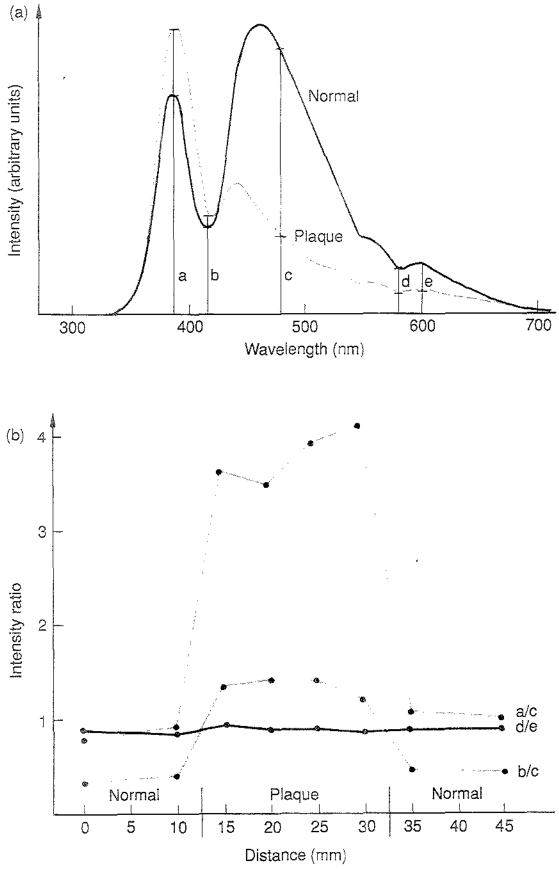

Figure 5. Fluorescence spectra of normal and atherosclerotic aorta.
(a) The fluorescence intensities at five different wavelengths—390, 415, 480, 580, and 600 nm (a–e)—are indicated. (b) Scan through an atherosclerotic plaque region with data from three dimensionless contrast functions displayed. The excitation wavelength was 337 nm. (Adapted with permission from Reference 19.)

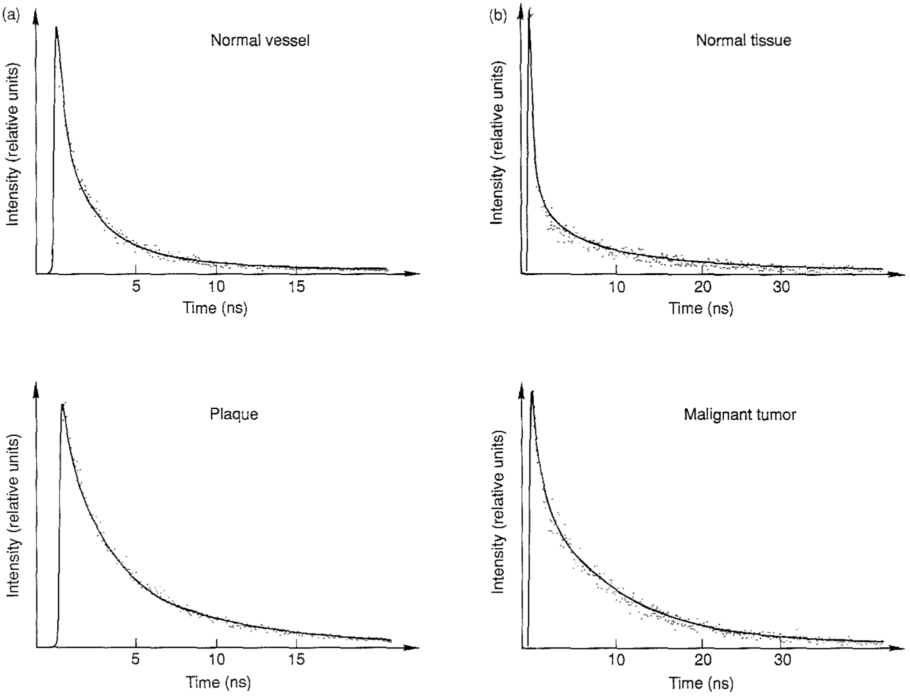

Figure 6. Fluorescence decay curves of (a) a normal blood vessel and an atherosclerotic plaque as well as (b) normal muscle tissue and a malignant tumor.

The excitation wavelength was 325 nm. Emission wavelengths were (a) 400 nm and (b) 630 nm. The colon adenocarcinoma tumor was subcutaneously grown on the hind leg muscle of a rat injected with 15 mg/kg body weight of DHE.

cence (0–5 ns). By dividing the signals, a higher value is obtained for the slowly decaying plaque fluorescence than for the normal wall.

In Figure 7, the different tissue types can be readily identified when the fiber-optic probe is moved from spot to spot. Because the detection is performed at a single wavelength (400 nm) for which light absorption has a higher cross section than scattering in blood, and because the blood is nonfluorescing, the blood acts only as a passive light attenuator and does not influence the fluorescence decay.

Time-resolved fluorescence monitoring using porphyrin localizers is another way to achieve enhanced tumor detection. The HPD fluorescence at 630 nm has a longer decay time than the autofluorescence background at the same wavelength, as illustrated in Figure 6b for the case of the rat tumor (*27*). Thus, by gating the detection system for late fluorescence, the HPD signal can be recorded background free.

Point monitoring for clinical work, aimed particularly at HPD-assisted tumor detection, has been constructed. Filter spectrometers (*28–30*) and optical multichannel detection (*31–32*) have been employed.

Fluorescence imaging

Medical imaging based on computerized X-ray and NMR tomography has recently reached an advanced state of development. Clearly, fluorescence imaging systems with contrast enhancement as discussed above would be of considerable interest. However, normally one must make a choice between monitoring the whole LIF spectrum at one point and monitoring a spatial region in one fluorescence band. Using special optical arrangements and employing contrast functions of the type discussed above, an interesting combination of these two possibilities can be achieved (*33*). We will describe the development of a multicolor imaging system now under way in our laboratory (*34, 35*).

To obtain spatial and spectral resolution simultaneously, we divide the fluorescence light with a multimirror arrangement, as shown in Figure 8 (*25*). The object is illuminated with a UV light source, which may be a laser or a flashlamp. Using a spherical mirror divided into four individually adjustable parts, it is possible to arrange four identical images as quadrants in an intensified matrix detector (charge-coupled device, or CCD detector). An interference filter arrangement in front

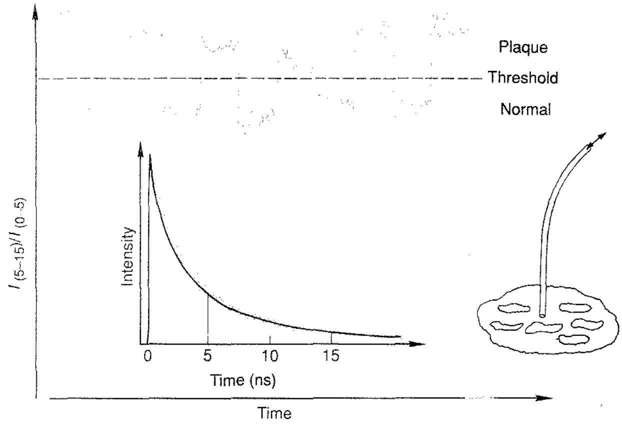

Figure 7. Time-resolved fluorescence measurement on the ratio of "late" to "early" fluorescence in a scan through a plaque region.
The excitation and emission wavelengths were 337 and 380 nm, respectively. The fluorescence light was guided through an optical fiber to a photomultiplier tube. The time gating and signal division were obtained in a boxcar integrator. (Adapted with permission from Reference 25, © 1990 IEEE.)

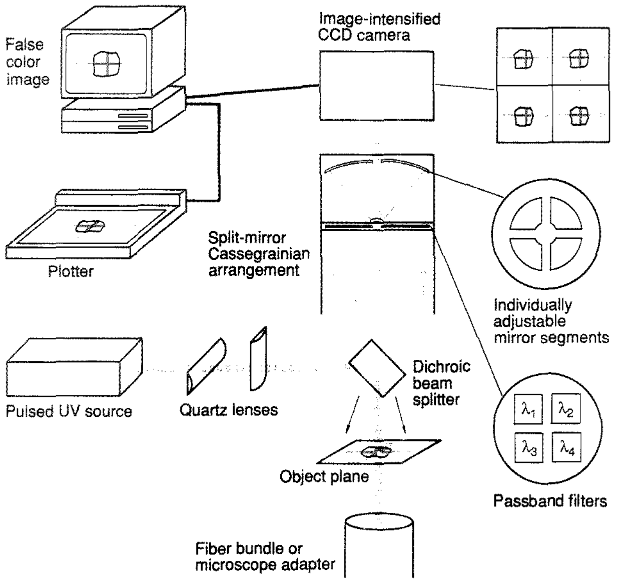

Figure 8. Arrangement for multicolor fluorescence imaging.
(Adapted with permission from Reference 25, © 1990 IEEE.)

of the split mirror is used to filter out individual transmission bands for the four images. From the four images a dimensionless contrast function is calculated for each spatial location using the corresponding pixel values in the fluorescence images. Finally, a generalized image that spatially displays the contrast function is formed. By choosing suitable passband filters based on

point measurements of the full spectral distribution, as discussed above, and by forming the relevant function to optimize contrast, tissues can be imaged with a contrast far exceeding that obtained by individual spectral bands or visual inspection.

Our system incorporates a Delli-Delta image-intensified CCD camera and an IBM 386-compatible computer with a Data Translation Model DT 7020 vector processor (*35*). An example of the simultaneously recorded images is shown in Figure 9. When linear mathematical operations such as image subtraction are performed, a system calibration accounting for different detector efficiencies in two channels must be applied. For precision processing, imaging vignetting and geometrical distortions must be eliminated. The imaging correction information is provided by a well-defined fluorescent test image.

Modern microchannel plate image intensifiers are gateable down to at least 5 ns. Thus contrast can be further enhanced by combining images of early fluorescence with images of late fluorescence. As discussed above, this time response is sufficient to allow time-resolved imaging of plaque in a blood-free inspection field and for enhanced tumor demarcation.

Image equipment monitoring the fluorescence from a certain area in a given fluorescence band has been constructed by Profio and co-workers (*36, 37*). Such instrumentation has also been used successfully for the detection of human bronchogenic tumors. In one construction, Profio and co-workers have demonstrated that background can be intermittently subtracted by switching to a blue-transmitting filter (38).

Future trends

Lasers in conjunction with fiber optics provide new and fascinating possibilities for the detection and treatment of human malignancies as well as heart and circulatory system diseases. Furthermore, discomfort that results from gallstones and kidney stones can be alleviated. Substituting simple fiber-optic procedures for traumatic major surgery is a challenge for doctors in collaboration with physicists.

Optical spectroscopy of laser-induced phenomena in tissue is rapidly increasing in importance. Fluorescence diagnostics of tissue has potential as a clinical aid both for localizing small occult malignant tumors and for ensuring proper surgical removal. It is important to use all information available in the spectral and temporal domains, particularly in the effort to keep the concentration of tumor-seeking agents at the lowest possible level to reduce light hypersensitization of the skin. New photosensitizers with attractive properties are being developed. Tissue autofluorescence also provides interesting possibilities for enhanced tumor localization and for plaque demarcation. In using autofluorescence, one must pay attention to eliminating the influences of strong and nonspecific chromophores, such as those in hemoglobin.

Point monitoring or imaging systems employing LIF also have important applications outside the field of medicine, where they were first used. Other applications include industrial (*39–41*) and environmental monitoring (*42, 43*), combustion (*44–46*), semiconductor processing diagnostics (*47, 48*), and forensic science investigations (*49*).

This work was supported by the Swedish Cancer Society (RmC), the Swedish Board for Technical Development (STU), and the Knut and Alice Wallenberg Foundation.

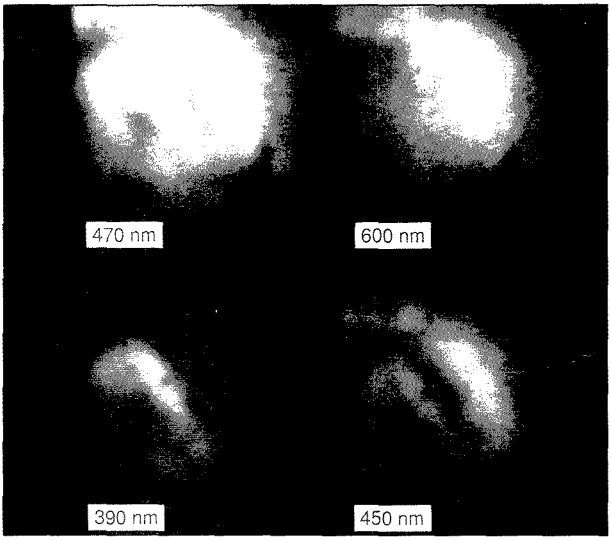

Figure 9. Two-dimensional fluorescence image of an aortic sample with an atherosclerotic plaque in the lower left corner.

The image was obtained using the experimental arrangement in Figure 8. The four detection wavelengths are indicated in the photograph. The darker line in the right lower corner is a thin metal wire. (Adapted with permission from Reference 25, © 1990 IEEE.)

References

(1) Andersson-Engels, S.; Johansson, J.; Svanberg, K.; Svanberg, S. *Anal. Chem.* **1989,** *61*, 1367 A.
(2) Alfano, R. R.; Darayash, B. T.; Cordero, J.; Tomashefsky, P.; Longo, F. W.; Alfano, M. A. *IEEE J. Quantum Electron.* 1984, *20*, 1507.
(3) Alfano, R. R.; Tang, G. C.; Pradhan, A.; Lam, W.; Choy, D.S.J.; Opher, E. *IEEE J. Quantum Electron.* **1987,** *23*, 1806.
(4) Ye, Y.; Yang, Y.; Li, Y.; Li, F. *CLEO '85 Technical Digest;* Optical Society of America: Baltimore, MD, 1985; p. 84.
(5) Ye, Y.; Yang, Y.; Xia, J.; Li, F.; Li, Y. *Chinese Physics—Lasers* 1987, 284.
(6) Yang, Y.; Ye, Y.; Li, F.; Li, Y.; Ma, P. *Lasers Surg. Med.* 1987, *7*, 528.
(7) Ankerst, J.; Montán, S.; Svanberg, K.; Svanberg, S. *Appl. Spectrosc.* 1984, *38*, 890.
(8) Svanberg, K.; Kjellén, E.; Ankerst, J.; Montán, S.; Sjöblom, E.; Svanberg, S. *Cancer Res.* **1986,** *46*, 3803.
(9) Andersson-Engels, S.; Elner, Å.; Johansson, J.; Karlsson, S.-E.; Salford, L. G.; Strömblad, L.-G.; Svanberg, K.; Svanberg, S. *Lasers Med Sci.*, in press.
(10) Andersson, P. S.; Kjellén, E.; Salford, L. G.; Strömblad, L.-G.; Svanberg, K.; Svanberg, S. *Lasers Med. Sci.*, in press.
(11) Andersson, P. S.; Kjellén, E.; Montán, S.; Svanberg, K.; Svanberg, S. *Lasers Med. Sci.* **1987,** *2*, 41.
(12) Andersson, P. S.; Ankerst, J.; Montán, S.; Svanberg, K.; Svanberg, S. *Lasers Med. Sci.* **1988,** *3*, 239.
(13) Andersson-Engels, S.; Ankerst, J.; Jo-

hansson, J.; Svanberg, K.; Svanberg, S. *Lasers Med. Sci.* **1989,** *4,* 119.
(14) Andersson-Engels, S.; Johansson, J.; Kjellén, E.; Killander, D.; Svaasand, L. O.; Svanberg, K.; Svanberg, S. *LIA ICALEO* 1987, *60,* 67.
(15) Andersson-Engels, S.; Johansson, J.; Kjellén, E.; Killander, D.; Olivo, M.; Svaasand, L. O.; Svanberg, K.; Svanberg, S. *SPIE* **1988,** *908,* 197.
(16) Grundfest, W. S.; Litvack, F.; Forrester, J. S.; Goldenberg, T.; Swan, H.J.C.; Morgenstern, L.; Fishbein, M.; McDermid, S.; Rider, D. M.; Pacala, T. J.; Laudenslager, J. B. *J. Am. Coll. Cardiol.* **1985,** *5,* 929.
(17) Isner, J. M.; Steg, P. G.; Clarke, R. H. *IEEE J. Quantum Electron.* **1987,** *23,* 1756.
(18) Kittrell, C.; Willett, R. L.; de los Santos-Pacheo, C.; Ratliff, N. B.; Kramer, J. R.; Malk, E. G.; Feld, M. S. *Appl. Opt.* **1985,** *24,* 2280.
(19) Andersson-Engels, S.; Gustafson, A.; Johansson, J.; Stenram, U.; Svanberg, K.; Svanberg, S. *Lasers Med Sci.* **1989,** *4,* 171.
(20) Andersson, P. S.; Gustafson, A.; Stenram, U.; Svanberg, K.; Svanberg, S. *Lasers Med. Sci.* **1987,** 2, 261.
(21) Cothren, R. N.; Hayes, G. B.; Kramer, J. R.; Sacks, B.; Kittrell, C.; Feld, M. S. *Lasers Life Sci.* **1986,** *1,* 1.
(22) Orayevski, A. A.; Letokhov, V. S.; Omelyanenko, V. G.; Ragimov, S. E.; Belyaev, A. A.; Akchurin, R. S. In *Laser Spectroscopy VII*; Persson, W.; Svanberg, S., Eds.; Springer: Heidelberg, 1987; p. 370.
(23) Sartori, M.; Sauerbrey, R.; Kubodera, S.; Tittel, F. K.; Romperts, R.; Henry, P. H. *IEEE J. Quantum Electron.* **1987,** *23,* 1794.
(24) Deckelbaum, L. I.; Sarembock, I. J.; Stetz, M. L.; O'Brien, K. M.; Cutrozzola, F. W.; Gmitro, A. F.; Ezekowitz, M. D. *Proc. SPIE* **1988,** *906,* Contribution 316.
(25) Andersson-Engels, S.; Johansson, J.; Stenram, U.; Svanberg, K.; Svanberg, S. *IEEE J. Quantum Electron.*, in press.
(26) Andersson-Engels, S.; Johansson, J.; Stenram, U.; Svanberg, K.; Svanberg, S. *J. Photochem. Photobiol.*, in press.
(27) Andersson-Engels, S.; Johansson, J.; Svanberg, S., unpublished work.
(28) Kinsey, J. H.; Cortese, D. A. *Rev. Sci. Instrum.* **1980,** *51,* 1403.
(29) Profio, A. E.; Doiron, D. R.; Sarnaik, J. *Med. Phys.* **1984,** *11,* 516.
(30) Andersson, P. S.; Karlsson, S.-E.; Montán, S.; Persson, T.; Svanberg, S.; Tapper, S. *Med. Phys.* **1987,** *14,* 633.
(31) Aizawa, K. et al. In *Porphyrin Localization and Treatment of Tumours*; Liss, A. R., Ed.; 1984, p. 227.
(32) Kato, H.; Cortese, D. A. *Clinics in Chest Medicine* **1985,** *6,* 237.
(33) Montán, S.; Svanberg, K.; Svanberg, S. *Opt. Lett.* **1985,** *10,* 56.
(34) Andersson, P. S.; Montán, S.; Svanberg, S. *IEEE J. Quantum Electron.* **1987,** 23, 1978.
(35) Andersson-Engels, S. A.; Johansson, J.; Svanberg, S. *Proc. SPIE* **1990,** 1205, Contribution 19.
(36) Profio, A. E.; Doiron, D. R.; Balchum, O. J.; Huth, G. C. *Med. Phys.* **1983,** *10,* 35.
(37) Profio, A. E. *Proc. SPIE* **1988,** *907,* 150.
(38) Profio, A. E.; Carvelin, M. J.; Sarnaik, J.; Wudl, L. R. In *Porphyrin in Tumor Phototherapy*; Andreoni, A.; Cubeddu, R., Eds.; Plenum: New York, 1984; p. 321.
(39) Montán, S.; Svanberg, S. *Appl. Phys.* **1985,** *B38,* 241.
(40) Montán, S.; Svanberg, S. *LIA. ICALEO* **1985,** *47,* 153.
(41) Andersson, P. S.; Montán, S.; Svanberg, S. *Appl. Phys.* **1987,** *B44,* 19.
(42) Measures, R. M. In *Analytical Laser Spectroscopy*; Omenetto, N., Ed.; Wiley: New York, 1984.
(43) Measures, R. M. *Laser Remote Sensing: Fundamentals and Applications*; Wiley: New York, 1984.
(44) Crosley, D. R.; Smith, G. P. *Opt. Eng.* **1983,** *22,* 545.
(45) Kychakoff, G.; Howe, R. D.; Hanson, R. K. *Appl. Opt.* **1984,** *23,* 704.
(46) Alden, M.; Edner, H.; Grafström, P.; Hertz, H. M.; Holmstedt, G.; Högberg, T.; Lundberg, H.; Svanberg, S.; Wallin, S.; Wendt, W.; Westblom, U. *Lasers 86*; STS Press: McLean, VA, 1985; p. 219.
(47) *Laser Diagnostics and Photochemical Processing for Semiconductor Devices*; Osgood, R. M.; Brueck, S.R.J.; Schlossberg, H. R., Eds.; North Holland: Amsterdam, 1983.
(48) Bauerle, D. *Chemical Processing with Lasers*; Springer: Berlin, 1986; Vol. I.
(49) Everse, K. E.; Menzel, E. R. *J. Forensic Sci.* **1986,** *31,* 466.

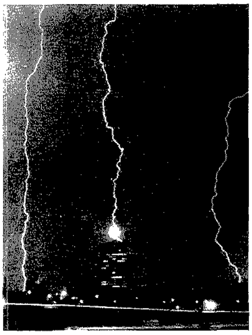

Wiley Books...

Now on 15-Day Free Exam

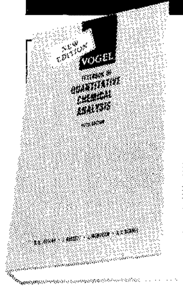

Vogel's Textbook of Quantitative Chemical Analysis, 5th Ed.

A.I. Vogel, G.H. Jeffrey, J. Bassett,
J. Mendham and R.C. Denney

"...the continued success of the book points to a large number of satisfied customers." - NATURE, ON THE 4TH ED.

Presenting recent changes in chemical analysis, this classic text explores a range of organic analyses, especially those related to environmental topics, such as heavy metals, dissolved oxygen and chemical oxygen demand. Includes traditional methods and up-to-date instrumental techniques. Discusses theory underlying chemical processes and practical aspects, such as sampling, statistical treatment of data and equipment requirements.

784 pp. 0-470-21517-8 1989 $87.95

Secondary Ion Mass Spectrometry: A Practical Handbook For Depth Profiling and Bulk Impurity Analysis

R. Wilson, F. Stevie & C. Magee

Provides the SIMS analyst with information on acquiring and interpreting data. Examples illustrate the effects of various analytical parameter choices. Appendices include data on the unique relative sensitivity factors.

384 pp. 0-471-51945-6 1989 $79.95

Interpretations of Carbon 13 NMR Spectra, 2nd Ed.

F. Wehrli, A. Marchand & S. Wehrli

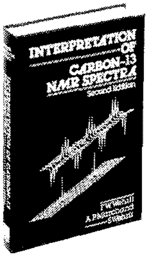

"...the authors have done a fine job of updating and expanding the material to reflect the significant advances made in instrumentation and NMR techniques. The applications section is the meat of the book. People truly learn by doing. ...well rounded, giving problems in almost every aspect of NMR..."
- APPLIED SPECTROSCOPY

484 pp. 0-471-91742-7 1988 $94.95

New!

Planar Chromatography in the Life Sciences

Editors: J.C. Touchstone & S.S. Levin

Presents recent developments in thin layer chromatography with biochemical applications. Describes scanners for evaluating separations, including those for spectrocharacterization as well as quantitation of isotope levels. Considers applications of TLC in pharmaceutical research, *in situ* reactions and spectrodensitometry, bioanalytical aspects of TLC-Fourier transform infrared spectrometry, and new techniques in two-dimensional data processing.

208 pp. 0-471-50109-3 1990 $59.95

Order through your bookseller
or write to:
J. Fernandez, Dept 092, 0-0225
To Order call Toll Free 1-800-526-5368
For all other inquiries call (212)850-6418

WILEY
John Wiley & Sons, Inc.
605 Third Avenue
New York, NY 10158

Prices subject to change & higher outside the U.S.

CIRCLE 150 ON READER SERVICE CARD

Chemical Analysis of Polycyclic Aromatic Compounds

T. Vo-Dinh

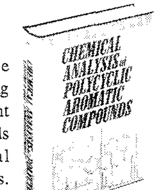

A comprehensive monograph focusing on the development of effective methods for the chemical analysis of PACs. Discusses early detection, safety technologies and the prevention of PAC-related carcinogenesis. Includes PACs in the atmosphere, gas and liquid chromatography, and phase-resolved fluorescence spectroscopy.

494 pp. 0-471-62889-1 1989 $90.00

Practical High Performance Liquid Chromatography Method Development

L.R. Snyder,
J.L. Glajch &
J.J. Kirkland

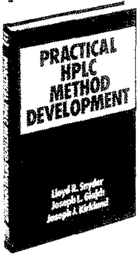

"...highly recommended to chromatographers..."
J. AM. CHEM. SOC.

Examines the basics of HPLC method development designed at Du Pont. Introduces practical, time saving computer tools and discusses reversed phase separations of small molecules and the development of normal phase and ion pair separations.

260 pp. 0-471-62782-8 1988 $48.00

High Performance Liquid Chromatography

Editors: P.R. Brown & R.A. Hartwick

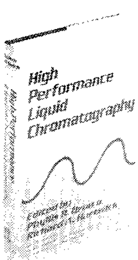

Provides chemists with comprehensive coverage of HPLC. Includes theory, terminology, thermodynamics, kinetics, detectors, derivatization, stationary phases, separations, equipment, error analysis, and advanced techniques such as supercritical fluid chromatography.

688 pp. 0-471-84506-X 1989 $79.00

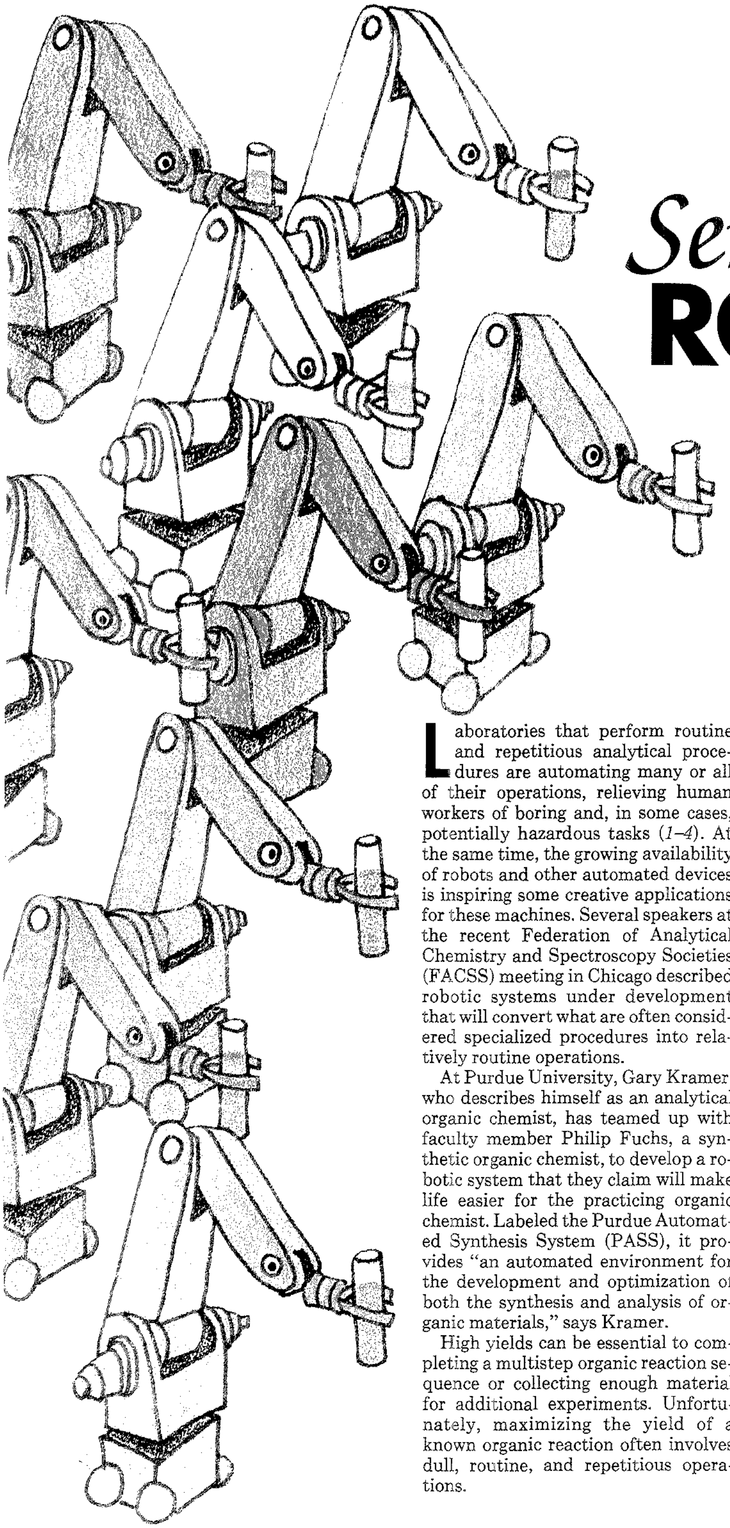

Send in the ROBOTS

Laboratories that perform routine and repetitious analytical procedures are automating many or all of their operations, relieving human workers of boring and, in some cases, potentially hazardous tasks (*1–4*). At the same time, the growing availability of robots and other automated devices is inspiring some creative applications for these machines. Several speakers at the recent Federation of Analytical Chemistry and Spectroscopy Societies (FACSS) meeting in Chicago described robotic systems under development that will convert what are often considered specialized procedures into relatively routine operations.

At Purdue University, Gary Kramer, who describes himself as an analytical organic chemist, has teamed up with faculty member Philip Fuchs, a synthetic organic chemist, to develop a robotic system that they claim will make life easier for the practicing organic chemist. Labeled the Purdue Automated Synthesis System (PASS), it provides "an automated environment for the development and optimization of both the synthesis and analysis of organic materials," says Kramer.

High yields can be essential to completing a multistep organic reaction sequence or collecting enough material for additional experiments. Unfortunately, maximizing the yield of a known organic reaction often involves dull, routine, and repetitious operations.

Kramer and Fuchs recognized that automation could free researchers from these chores. They launched PASS with four criteria in mind: The system would rely on known analytical procedures, all products and reactants would be in solution, it would have inert atmosphere capabilities, and it would handle research-size quantities—typically as little as 100 μmol of starting material dissolved in 3 mL of solvent.

As it now exists, PASS consists of two work areas, each centered around a Zymark robotic arm (Figure 1). The synthesis table contains four independent, self-cleaning reactors capable of running reactions under inert atmosphere and at temperatures ranging from −80 °C to 150 °C. Chemical supplies are taken from a "stockroom" composed of up to 20 septum capped serum bottles containing reagents already in solution. The appropriate reagents are introduced into a reactor by a robot-operated syringe or computer-controlled pump. Wherever possible, internal standards are also added to the stockroom reagents, providing a check on the automated delivery system.

Following the setup, reactions are run to completion and quenched, or sampled periodically by removing aliquots. The product can be isolated by a technique such as liquid–liquid extraction, then derivatized for gas chromatography studies or, via the evaporation station, redissolved in an appropriate solvent for liquid chromatography. Because PASS does not handle solids, the final sample must be in solution.

FOCUS

The prepared analyte is then eluted through a silica gel plug into a sample vial marked with a bar code. The vial is transported to the analysis workstation on top of a modified model train engine

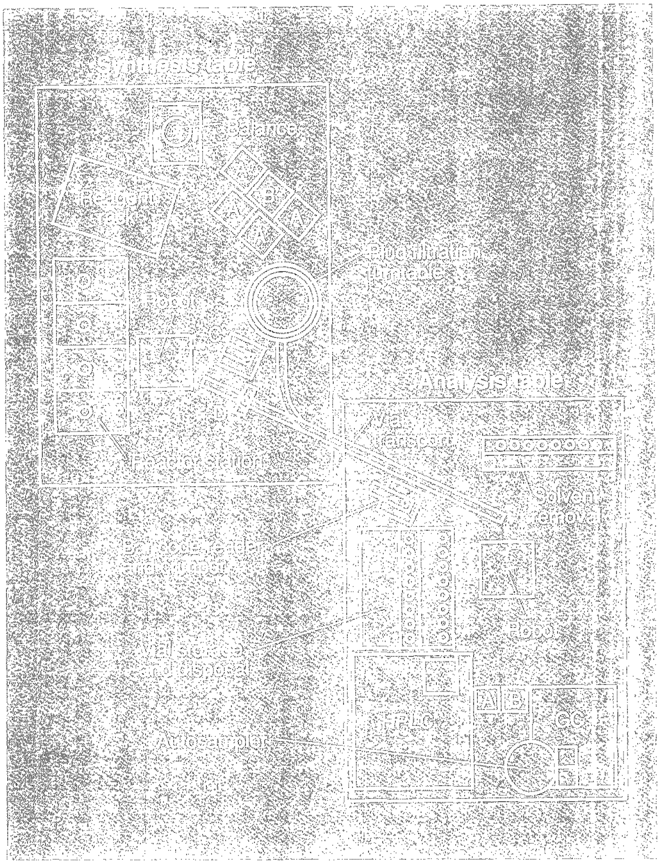

Figure 1. Schematic of the Purdue Automated Synthesis Station.
A = syringe hand, B = general-purpose hand, C = liquid–liquid extractor, and D = arc of the syringe. (Courtesy Gary Kramer.)

running on a computer-controlled track (Figure 2).

At the analysis table, samples are picked up and moved to either a high-performance liquid chromatograph or a gas chromatograph. To expedite sample handling, there are two injection ports and columns on the gas chromatograph for simultaneous runs. The samples are automatically injected into the appropriate instrument, and the data—stored on computer disk—are either used to begin another experiment or saved for later analysis. After every five runs, a standard mixture is injected to ensure the accuracy of the chromatography data. The sample vials are then automatically saved for future reference.

The entire system is controlled by a central executive computer that transmits directions to a network of satellite computers, called managers. In turn, the managing computers delegate tasks to the working devices.

When fully operational, PASS will be controlled by three main programs: a user interface program that works like a laboratory notebook to establish reaction conditions, a system-checking program that makes sure that the reaction conditions are reasonable and that the various valves and components are properly set to begin a robot-controlled reaction, and a program that runs the entire system.

PASS operates in two different modes. In the system's open-loop operation it stores data and waits for further instructions. In the closed-loop mode the computer turns the data into an "analytical goodness factor" and then designs new experiments to optimize the reaction. This goodness factor, which ranges from 0 to 1, is derived from a mathematical relationship defined by the operator. It can be as simple as relating the factor to percent yield, or it can take into account several variables such as remaining starting material and reaction conditions.

A SIMPLEX method, using data from at least three experimental runs, designs the additional experiments. In the future, the Purdue scientists hope to introduce a more sophisticated artificial intelligence program for designing new experiments.

Another analytical procedure, seldom thought of as routine, is undergoing automation because of its importance to the growing biotechnology industry. These companies are investing in X-ray crystal structure determinations of key proteins to aid in the development of new drugs and the elucidation of their pharmacological roles.

Before crystallographers can begin collecting data they must grow a suitable crystal for X-ray analysis. Unfortunately, that is often a tedious process. The crystal structure of human growth hormone, for instance, required approximately 3000 crystallizations performed manually.

Because it is such a tedious process, most crystallographers use the first decent crystal they find and seldom bother to optimize conditions for better crystals. "Automation is faster in the long run," says crystallographer Noel Jones, "and conserves protein."

Jones and his co-workers at Eli Lilly's Research Laboratories in Indianapolis are developing what they believe is the first fully automated robotic system for growing protein crystals. Labeled APOCALYPSE—"from the Greek to uncover, literally meaning revelation," explains Jones—the name also works as an acronym for Automated Protein Crystallization System.

APOCALYPSE, with some help from its human creators, has already performed more than 10^4 crystallizations since September 1988, providing X-ray-quality crystals for six proteins whose structures are unknown. The present system can prepare, although not regularly check or evaluate, crystallizations. Eventually the entire process will be fully automated.

To set up a crystallization, an operator selects conditions from a computer menu. Up to 450 crystallizations can be programmed at one time. "We define an *n*-dimensional array of conditions," says Jones, "protein concentration, pH, how much precipitating agent or other ingredients such as nonionic detergent, and volume drop." These pa-

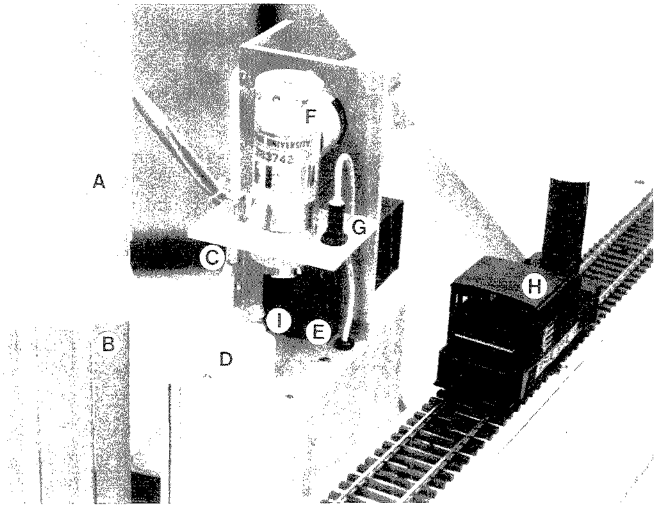

Figure 2. Vial handler station.
The robot removes empty, capped vials from the storage rack (A), the vacuum pick-off removes the cap (C), the vial is rotated (D), and the bar code is read (E). After the vial is filled elsewhere, it is returned, capped, crimped (F), checked for a cap (G), and loaded onto the train (H). Analyzed samples return and are stored under the table (B). A vial sits in the station (I). (Courtesy Gary Kramer.)

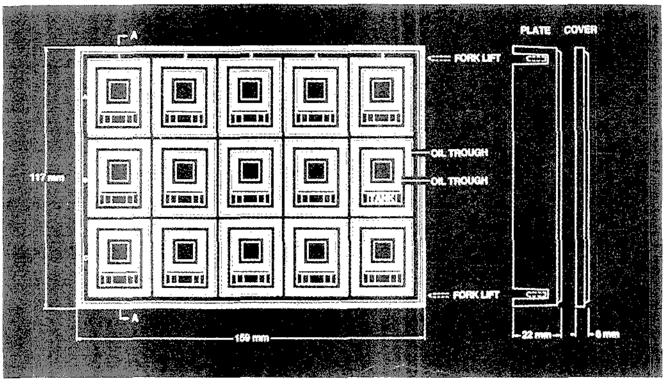

Figure 3. Crystal-growing plate.
Fifteen cells surrounded by troughs for oil. (Courtesy Noel Jones.)

rameters must be tightly defined. For example, most proteins crystallize within tolerances of ±0.1 pH unit.

To maintain these limits, the buffer, detergent, and other ingredients are pumped by individual syringes. Any drops clinging to syringe needle tips are blown off. The chemicals are taken from a bank of 16 commonly used crystallization reagents, which are injected into a mixer bowl and vortexed. This is the reservoir solution to which protein dissolved in a buffer solution is added.

The crystallizations are carried out on a unique plastic plate designed at the Lilly Research Laboratories in collaboration with Keith Ward and Mary Ann Perozzo at the Naval Research Laboratory in Washington, DC. The plate is equipped with 15 cells for experiments (see Figure 3). Each cell is filled with as little as 2 μL of solution, the transfer syringe touching the plate to deliver the droplet of liquid. Because the crystals grow by vapor diffusion, some of the reservoir solution is added to a well next to the droplet.

A glass cover is then placed over each cell. If 5 μL or more of the protein solution have been placed in the cell, the cover will touch the droplet, creating a tiny column suspended between the

Probing Bioactive Mechanisms

*N*ew! Reveals innovative techniques in statistics and computer modeling that are being used to study common mechanistic themes in bioactive substances. Synthesizes the latest work of scientists in industrial, academic, and government laboratories. Probes the common molecular mechanisms in three diverse fields—medicinal chemistry, agrochemicals, and chemical toxicology. Details experimental, statistical, and computational approaches coupled with SAR and QSAR studies for developing and detecting drugs, pesticides, and toxic substances.

Describes a variety of statistical and modeling approaches to designing biologically active molecules, elucidating structure-activity relationships, and defining the characteristics of the receptor and receptor-ligand interaction. Blends theory and applications in twenty-four chapters covering the following topics:
- an overview of the design of bioactive molecules; prediction of mechanism and activity, and the interface of statistics, quantum chemistry, and molecular modeling
- new tools for the study of bioactive mechanisms, including SAR in three dimensions and micellar liquid chromatography with QSAR studies
- sixteen uses of computational analysis techniques to study bioactive mechanisms in agrochemicals, drugs, and toxic substances

Medicinal, environmental, toxicological, and agrochemical scientists with a basic interest in QSAR and modes of action will welcome this most current approach to the study of bioactive compounds.

John H. Block, *Editor,* Oregon State University
Douglas R. Henry, *Editor,* Molecular Design Limited
Philip S. Magee, *Editor,* Biosar Research Project

Developed from a symposium sponsored by the Division of Agrochemicals of the American Chemical Society

ACS Symposium Series No. 413
400 pages (1989) Clothbound
ISBN 0-8412-1702-5 LC 89-17988
$59.95

O·R·D·E·R F·R·O·M

American Chemical Society
Distribution Office, Dept. 52
1155 Sixteenth St., N.W.
Washington, DC 20036
or CALL TOLL FREE

800-227-5558
(in Washington, D.C. 872-4363) and use your credit card!

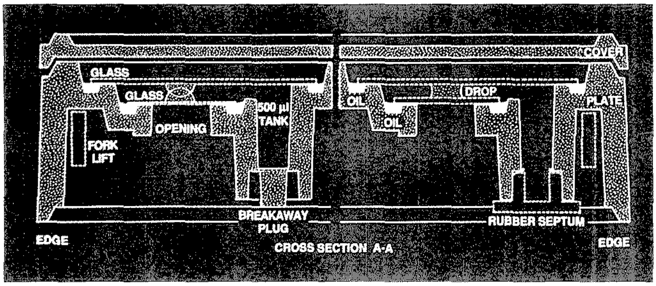

Figure 4. Cell schematic with cross section showing protein droplet and reservoir solution tank.
(Courtesy Noel Jones.)

top and bottom layers (Figure 4). The cover also contacts vacuum pump oil in troughs that surround the cell, effectively sealing the protein droplet from the outside environment. Inside the cell, water slowly diffuses out of the protein solution and into the more concentrated reservoir solution.

It takes a mere seven seconds for the robot to deliver a protein droplet to the crystallization plate and cover it. Setting up each crystallization requires about 5 min.

The completed plates are bar coded and carefully stacked. From this point on, humans take over. The plates are stored and checked three days later under a microscope equipped with a movable *x-y* stage and a video camera. Each droplet is examined, and "interesting" images are recorded on a laser disk. Currently a human operator determines whether an image is interesting. Eventually the computer will examine the image and generate a score for each cell based on changes in birefringence from growing crystals, edge analysis (looking for straight lines), and particle size analysis. High-scoring images will automatically be recorded on the laser disk along with a bar code number, date, and experimental conditions. These plates will then be flagged for more frequent monitoring. The system will monitor experiments for months, if necessary.

APOCALYPSE's hardware is controlled by PC-based software written in C language. To fully automate the entire crystal-growing process, seven software packages will be developed. Already in operation are programs to set initial crystallization conditions and maintain bookkeeping on bar codes. Future software will prompt the system to check a plate, perform image analysis, interpret the image analysis and decide what to do next, and generate optimized conditions for the next experiments. According to Jones, APOCALYPSE will also become more flexible in the future. The system's software and hardware could easily be modified to grow crystals by another common technique, microdialysis.

Flexibility is the key consideration in another robotic system. At the Upjohn Company's laboratories in Kalamazoo, MI, an ambitious system called Generic Analytical Sample Preparation (GASP) (*8*) is being developed to handle everything from solids to ointments to liquids.

Most robotic systems rely on uniformity, analyzing large numbers of similar samples by one or two well-established techniques. In addition, a robot system may run with a customized operating language that cannot communicate with another company's device.

"We tried to develop our applications with [the automation vendors'] materials," says Robert Sharp. However, because of the diversity of Upjohn's products, Sharp and his colleagues switched to what they describe as a flexible, factory-line approach to robotics. Analytical procedures are broken down in different classes of procedures. "You can imagine a car assembly line with the welder, painter, and riveter," says Sharp.

In the same spirit, GASP is being designed around seven unique workstations. Bar-coded sample vials will be shuttled back and forth by elevators and conveyors to each area performing specialized tasks. In the various workstations, pneumatically controlled arms and devices working simultaneously will carry out their designated functions. Each arm or device will perform just one specific task, thereby increasing the precision of that operation, according to Sharp.

The system will adapt to samples with varying needs. "It can handle one or 100 samples," says Sharp. The bar code on the vial defines the operations and the workstations that must be involved in the sample preparation. At the end, the prepared samples are collected and physically carried to an autosampler for chromatographic or spectroscopic analysis.

What makes GASP generic is that pieces snap in and out (Figure 5). A lab can modify and use only those workstations that fit its sample preparation needs. Furthermore, the entire system is being constructed with "off-the-shelf" equipment and materials. The central minicomputer uses the UNIX operating system, which Sharp says is ideal for multitasking and data security. The robotics are industrial-style pneumatics, which Sharp predicts will

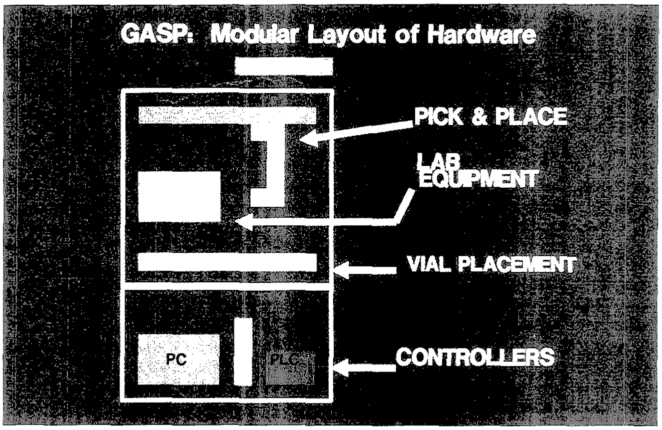

Figure 5. Schematic of a typical workstation showing vertical arrangement of Generic Analytical Sample Preparation.
(Courtesy Robert Sharp.)

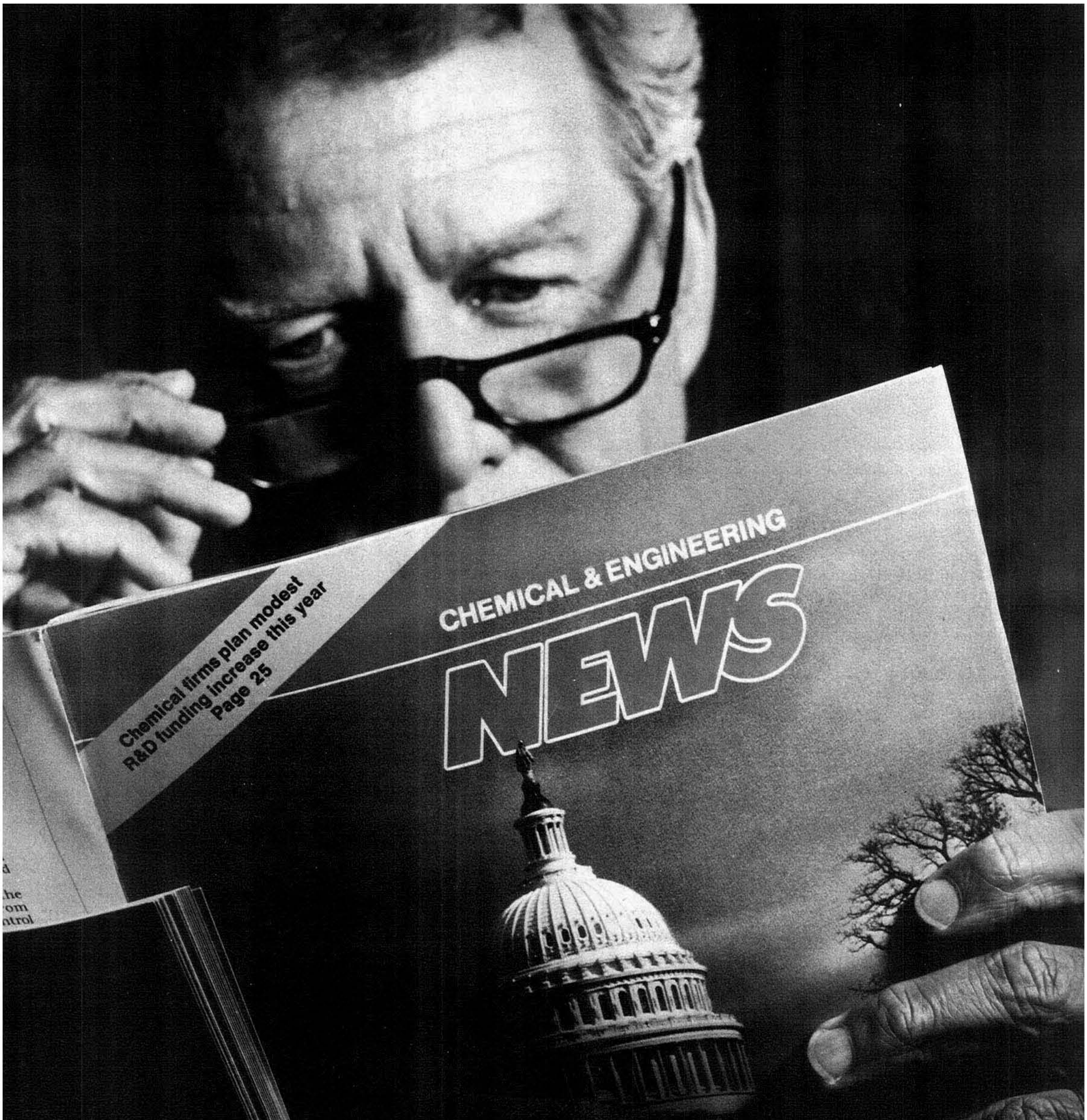

People who make the news, read the News.

When you're sitting at the top, you need to get to the bottom of news that affects your business. That's why senior executives throughout industry read Chemical & Engineering News each week.

It's the only weekly chemical magazine that covers the news from three angles. Not just science. Not just technology. Not just business. But all three. So you not only know what's happening in chemistry, you know how it's going to affect your business.

Read the weekly the newsmakers read. Read Chemical & Engineering News.

Call 800-227-5558

American Chemical Society, 1155 Sixteenth Street, N.W., Washington, D.C. 20036.

CHEMICAL&ENGINEERING
NEWS

BUSINESS
SCIENCE
TECHNOLOGY

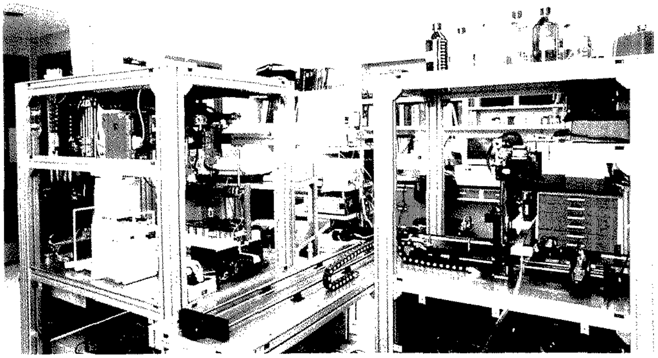

Figure 6. Liquid-handling workstation (left) adjacent to the automatic dilution workstation.
(Courtesy Robert Sharp.)

have a long operating life.

At present, three of the workstations are in operation: the central computer, called the network manager; a liquid-handling station; and an automatic dilution station. Still in the planning stages are workstations for solids, ointments, mixing, and separations.

The liquid-handling station has the role of obtaining an aliquot of sample, placing it into a tared vial, either pipetting or weighing the sample, capping the vial, and sending it to the next workstation. The dilution station reads the bar code and meters liquids into the sample. To conserve laboratory space, consumables are dispensed vertically (Figure 6).

GASP's central computer is hardwired to the PCs running each workstation. Programs for workstation operation are written in C language which, in turn, talks to a database where preparation information is collected.

Like the other two systems, GASP still requires lots of work before it can reach its stated goals. However, as these developing systems demonstrate, robotics are becoming more responsive to chemists' needs and finding niches in specialized activities.

Alan R. Newman

References

(1) Borman, S. *Anal. Chem.* 1985, *57*, 651 A–652 A.
(2) Dessy, R. *Anal. Chem.* 1983, *55*, 1100 A–1114 A.
(3) Dessy, R. *Anal. Chem.* 1983, *55*, 1232 A–1242 A.
(4) Isenhour, T.; Eckert, S. E.; Marshall, J. C. *Anal. Chem.* 1989, *61*, 805 A–814 A.
(5) Frisbee, A. R.; Nantz, M. H.; Kramer, G. W.; Fuchs, P. L. *J. Am. Chem. Soc.* 1984, *106*, 7143.
(6) Kramer, G. W.; Fuchs, P. L. *Advances in Laboratory Automation Robotics* 1986, 361.
(7) Kramer, G. W.; Fuchs, P. L. *Advances in Laboratory Automation Robotics* 1987, 339.
(8) Sharp, R. L.; Whitfield, R. G.; Fox, L. E. *Anal. Chem.* 1988, *60*, 1056 A–1062 A.

LAB DATA SERVICE

If you have an immediate need for information on the products, components, accessories or services associated with the following categories, simply circle on our reply card the numbers preceding these categories and you will receive data directly from our advertisers.

327 AA SPECTROSCOPY
328 ANALYTICAL SERVICES
329 BATHS/CIRCULATORS
330 BIOTECHNOLOGY
331 BOOKS/PERIODICALS
332 CENTRIFUGATION
333 CHEMICALS/GASES/SOLVENTS
334 COMPUTERS/SOFTWARE
335 COOLING/FREEZING/REFRIG
336 DATABASES, ONLINE
337 DENSITOMETRY
338 DETECTORS
339 DRYERS/EVAPORATORS
340 ELECTROCHEMISTRY
341 ELEMENTAL ANALYSIS
342 FILTRATION
343 FLOW METERS/REGULATORS
344 FT-IR SPECTROSCOPY
345 FURNACES/OVENS
346 GAS CHROMATOGRAPHY
347 GENERAL LAB EQUIPMENT
348 HEATING/TEMPERATURE
349 ION CHROMATOGRAPHY
350 LAB FURNITURE/HOODS
351 LABWARE/APPARATUS
352 LASERS/FIBER OPTICS
353 LIQUID CHROMATOGRAPHY
354 MASS SPECTROSCOPY
355 MICROSCOPY, ELECTRON
356 MICROSCOPY, OPTICAL
357 MIX/STIR/BLEND/GRIND
358 NMR SPECTROSCOPY
359 PARTICLE SIZE ANALYSIS
360 PLASMA SPECTROSCOPY
361 pH/ION METERS/TITRATORS
362 PUMPING/MONITORING
363 RECORDING/INTEGRATING
364 ROBOTICS/AUTOMATION
365 SAMPLING/DISPENSING
366 SCINTILLATION
367 SPECTROFLUOROMETRY
368 STILLS/PURIFICATION
369 SURFACE ANALYSIS
370 THERMAL ANALYSIS
371 THIN LAYER CHROM
372 UV-VIS SPECTROSCOPY
373 VALVES/TUBES/FITTINGS
374 VISCOMETRY
375 WATER/MOISTURE ANALYSIS
376 WEIGHING/BALANCES
377 X RAY DIFFRACTION
378 X-RAY SPECTROSCOPY

AC JANUARY 1, 1990 MAY 1990

ADVERTISED PRODUCTS:					1	2	3	4	5	6	7	8	9	10	11
12	13	14	15	16	17	18	19	20	21	22	23	24	25	26	27
28	29	30	31	32	33	34	35	36	37	38	39	40	41	42	43
44	45	46	47	48	49	50	51	52	53	54	55	56	57	58	59
60	61	62	63	64	65	66	67	68	69	70	71	72	73	74	75
76	77	78	79	80	81	82	83	84	85	86	87	88	89	90	91
92	93	94	95	96	97	98	99	100	101	102	103	104	105	106	107
108	109	110	111	112	113	114	115	116	117	118	119	120	121	122	123
124	125	126	127	128	129	130	131	132	133	134	135	136	137	138	139
140	141	142	143	144	145	146	147	148	149	150	151	152	153	154	155
156	157	158	159	160	161	162	163	164	165	166	167	168	169	170	171
172	173	174	175	176	177	178	179	180	181	182	183	184	185	186	187
188	189	190	191	192	193	194	195	196	197	198	199	200	201	202	203
204	205	206	207	208	209	210	211	212	213	214	215	216	217	218	219
220	221	222	223	224	225	226	227	228	229	230	231	232	233	234	235
236	237	238	239	240	241	242	243	244	245	246	247	248	249	250	251
252	253	254	255	256	257	258	259	260	261	262	263	264	265	266	267
268	269	270	271	272	273	274	275	276	277	278	279	280	281	282	283
284	285	286	287	288	289	290	291	292	293	294	295	296	297	298	299
300	301	302	303	304	305	306	307	308	309	310	311	312	313	314	315
316	317	318	319	320	321	322	323	324	325	326	327	328	329	330	331
332	333	334	335	336	337	338	339	340	341	342	343	344	345	346	347
348	349	350	351	352	353	354	355	356	357	358	359	360	361	362	363
364	365	366	367	368	369	370	371	372	373	374	375	376	377	378	379

NEW PRODUCTS				401	402	403	404	405	406	407	408	409	410	411	412
413	414	415	416	417	418	419	420	421	422	423	424	425	426	427	428
429	430	431	432	433	434	435	436	437	438	439	440	441	442	443	444
445	446	447	448	449	450	451	452	453	454	455	456	457	458	459	460
461	462	463	464	465	466	467	468	469	470	471	472	473	474	475	476

Intensity of product need:
☐ 1. Have salesman call
☐ 2. Need within 6 mos.
☐ 3. Future project

CIRCLE 314 FOR
SUBSCRIPTION
FORM TO
ANALYTICAL
CHEMISTRY

Primary field of work:
☐ A. Energy
☐ B. Environmental
☐ C. Medical/Clinical
☐ D. Drug/Toiletries
☐ E. Forensic/Narcotic
☐ F. Biotechnology
☐ G. Metals
☐ H. Pulp/Paper/Wood
☐ I. Soaps/Cleaners
☐ J. Paint/Coating/Ink
☐ K. Electrical/Electronic
☐ L. Instrument Dev./Des
☐ M. Plastic/Polymer/Rub
☐ N. Agricultural/Food
☐ O. Inorganic Chemicals
☐ P. Organic Chemicals

Primary area of employment.
INDUSTRIAL
☐ A. Research Development
☐ B. Quality/Process Control
MEDICAL/HOSPITAL
☐ C. Research Development
☐ D. Clinical/Diagnostic
GOVERNMENT
☐ E. Research Development
☐ F. Regulate/Investigate
COLLEGE/UNIVERSITY
☐ G. Research Development
☐ H. Teaching
INDEPENDENT/CONSULTING
☐ I. Research Development
☐ J. Analysis/Testing

NAME: ____________________

TITLE: ____________________

COMPANY: ____________________

STREET: ____________________

CITY: ____________________

STATE: ____________________ ZIP: __________

TELEPHONE: (______) ____________________

NO POSTAGE
NECESSARY
IF MAILED
IN THE
UNITED STATES

BUSINESS REPLY MAIL
FIRST CLASS PERMIT NO. 410 RIVERTON, NJ

POSTAGE WILL BE PAID BY ADDRESSEE

Analytical
CHEMISTRY

P.O. BOX 1662
RIVERTON, NJ 08077-9662

LAB DATA SERVICE

If you have an immediate need for information on the products, components, accessories or services associated with the following categories, simply circle on our reply card the numbers preceding these categories and you will receive data directly from our advertisers:

327 AA SPECTROSCOPY
328 ANALYTICAL SERVICES
329 BATHS/CIRCULATORS
330 BIOTECHNOLOGY
331 BOOKS/PERIODICALS
332 CENTRIFUGATION
333 CHEMICALS/GASES/SOLVENTS
334 COMPUTERS/SOFTWARE
335 COOLING/FREEZING/REFRIG.
336 DATABASES, ONLINE
337 DENSITOMETRY
338 DETECTORS
339 DRYERS/EVAPORATORS
340 ELECTROCHEMISTRY
341 ELEMENTAL ANALYSIS
342 FILTRATION
343 FLOW METERS/REGULATORS
344 FT-IR SPECTROSCOPY
345 FURNACES/OVENS
346 GAS CHROMATOGRAPHY
347 GENERAL LAB EQUIPMENT
348 HEATING/TEMPERATURE
349 ION CHROMATOGRAPHY
350 LAB FURNITURE/HOODS
351 LABWARE/APPARATUS
352 LASERS/FIBER OPTICS
353 LIQUID CHROM/HPLC
354 MASS SPECTROSCOPY
355 MICROSCOPY
356 CAPILLARY ELECTROPHORESIS
357 MIX/STIR/BLEND/GRIND
358 NMR SPECTROSCOPY
359 PARTICLE SIZE ANALYSIS
360 PLASMA SPECTROSCOPY
361 pH/ION METERS/TITRATORS
362 PUMPING/MONITORING
363 RECORDING/INTEGRATING
364 ROBOTICS/AUTOMATION
365 SAMPLING/DISPENSING
366 SUPERCRITICAL FLUID CHROM
367 SPECTROFLUOROMETRY
368 STILLS/PURIFICATION
369 SURFACE ANALYSIS
370 THERMAL ANALYSIS
371 THIN LAYER CHROM.
372 UV-VIS SPECTROSCOPY
373 VALVES/TUBES/FITTINGS
374 VISCOMETRY
375 WATER/MOISTURE ANALYSIS
376 WEIGHING/BALANCES
377 X-RAY DIFFRACTION
378 X-RAY SPECTROSCOPY

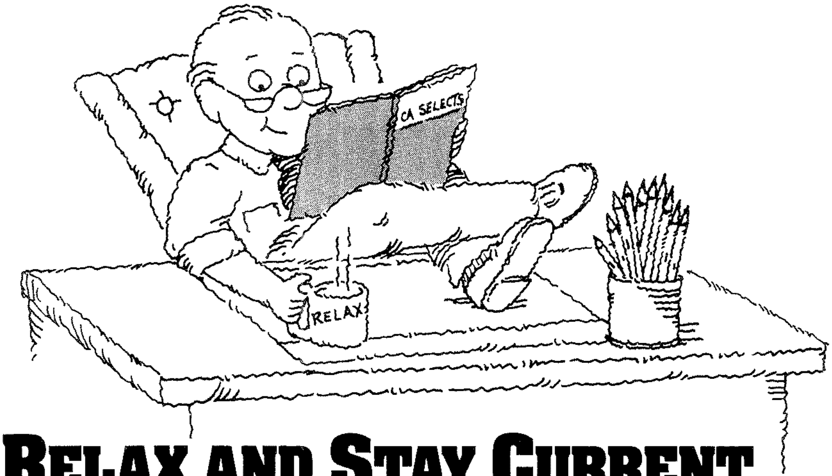
CA SELECTS
RELAX

NEW PRODUCTS

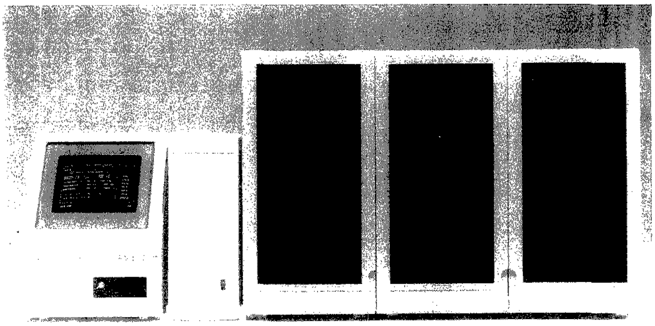

Model 300 pilot-scale liquid chromatograph is designed for large-scale protein purification in industrial applications. The software controls the design, operation, and documentation of chromatographic methods. Oros Instruments 401

Clinical analysis. Synchron EL-ISE electrolyte system can be used as a stand-alone primary routine electrolyte analyzer or as a complement to a random access profiler. The system completes more than 100 total electrolyte panels per hour and features a 40-sample turntable for high-volume testing. Beckman Instruments 404

Viscometer. Rotovisco RV20 rotational viscometer measures elasticities and viscosities from 0.02 to 10^9 mPa·s. Features include built-in electronic speed control and safety circuits that check for system overload and incorrect speed settings. Haake/Fisons Instruments 405

X-ray diffraction. X-2000 area detector system consists of an X-ray area detector for direct electronic imaging of diffracted X-rays, frame buffer processor, DEC VAX station host computer, real-time display, and peripherals. Siemens Analytical X-Ray Instruments 406

NMR. ANMR9200 series NMR spectrometers feature RF electronics for acquisition and decoupling; a 16-bit, 100-kHz A/D converter system; an 18-channel, 16-bit shim system; and a PC/AT-compatible computer system. The series is available in 300-, 360-, 400-, and 500-mHz system configurations. Analogic 407

Detector. Model 994 programmable photodiode array detector features postrun analyses that include spectrum index plot, integration, and calibration. Peak purity can be checked with automatic spectral overlay, purity number, or library correlation. Waters Chromatography Division of Millipore 408

Autosampler. GINA Gynkotek Injection Automatic system is a nonpneumatic module for automating liquid chromatography. Sample injection volumes range from 1 to 250 μL, and repeatability of injection is better than 0.3% RSD. Analytical Sales and Services 409

Spectroscopy. FF250 spectrograph/monochromator features resolution of 0.06 nm, a 25 mm × 50 mm flat focal field for full compatibility with the largest CCD and diode array detectors, immediate keypad conversion from spectrograph to monochromator, and digitally controlled bilateral slits designed to accept fiber-optic accessories. Aries 410

Proteins. Protein sequencer includes reagents and start-up kits for 1000 cycles and software for control, sequence program transfer, and storage. Sequencing is based on Edman degradation followed by HPLC. Jaytee Biosciences 413

Sampling. Automatic process sampler is designed for analysis of volatile organic compounds in water samples. The unit samples up to six aqueous streams that can be monitored either sequentially or on a timed basis using an internal real-time clock. Tekmar 411

IR. MONITIR 400 is a high-speed analysis system for quality control of chemical and biological processes in pharmaceutical production. The system accommodates a variety of materials, including aqueous and nonaqueous solutions, solids, and semisolids. Spectra-Tech 412

Software

Molecular drawing. WIMP 2001 is a molecule-drawing program that features built-in templates and special characters, including 12 bond types, 26 rings, orbitals, reaction arrows, shaded options, and brackets. The software is designed for IBM PC, PS/2, and compatible computers. Aldrich Chemical 415

Data analysis. MINSQ 3.0 allows users to develop mathematical models by performing simulations with known parameter values or to fit parameter values in model equations to actual experimental data. Models can be expressed as simple equations or multiline routines. MicroMath Scientific Software 416

Manufacturers' Literature

Sensors. Data sheet describes sensors and detectors for gas and liquid analyses. Included are oxygen and polarographic gas sensors and photometric, flame ionization, and thermal conductivity detectors. Teledyne Analytical Instruments 418

For more information on listed items, circle the appropriate numbers on one of our Readers' Service Cards

Chromatography. *Mac-Mod Forum* features articles on column voiding and optimization of column conditions. Information on local chromatography discussion groups is also provided. Mac-Mod Analytical 419

ICP. Brochure highlights the JY 50 PolyScan simultaneous inductively coupled plasma spectrometer. System components, signal and data processing, and specifications are discussed. Instruments SA 420

IR. Guide provides information on the principles and applications of internal reflection spectroscopy. Accessories for dispersive and FT-IR spectrometers are discussed. 12 pp. Foxboro 421

Surface analysis. *Reflections* contains information on applications of static SIMS and lubricant thickness measurements. 8 pp. Surface Science Laboratories 423

Extraction. Brochure describes the Spe-ed Wiz automated solid-phase extraction system, which can dispense up to 12 different solutions to any combination of up to 30 disposable 1-, 3-, or 6-mL SPE cartridges. Applied Separations 422

Catalogs

LC. Catalog contains instrumentation and supplies for HPLC, including columns, valves, fittings, tubing, filtration and sample preparation products, column heaters, pumps, detectors, and autosamplers. 350 pp. Rainin Instrument Co. 426

Chromatography. Catalog lists columns and accessories for HPLC. Microbore, minibore, analytical, semipreparative, and preparative columns are described for a variety of applications. 100 pp. Phenomenex 428

Circulators. Catalog includes immersion, heating, and refrigerated circulators. Heating/cooling and refrigerated recirculators are also described. 16 pp. PolyScience 429

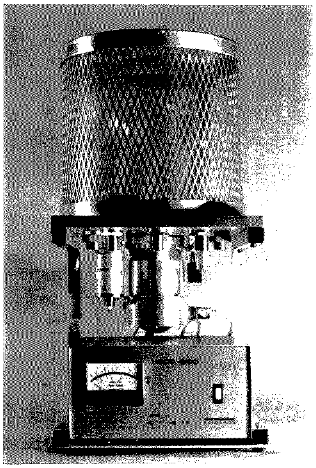

Tandem-80 bell jar system provides automatic pumpdown from atmosphere to ultra high vacuum with full interlock protection. The system achieves pressures down to 10^{-8} torr. Danielson Associates 402

Bio-Rad's refrigerated HPLC automatic sampler–beats all the others cold!

Amino acid analysis and other pre-column derivatization chemistries using the sampler's unique Multi-Mix® feature.

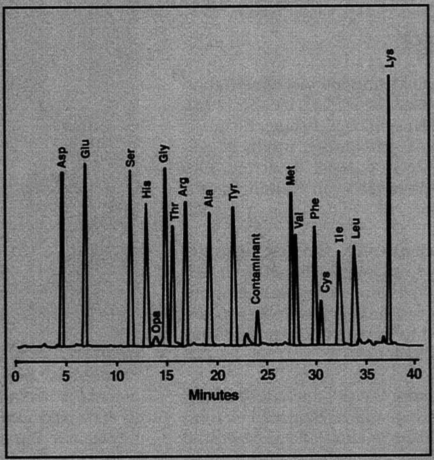

Bio-Rad's automatic sampler not only out performs all the others, but it costs a cool 25% less than anyone else's. And that's with built-in solid state refrigeration!

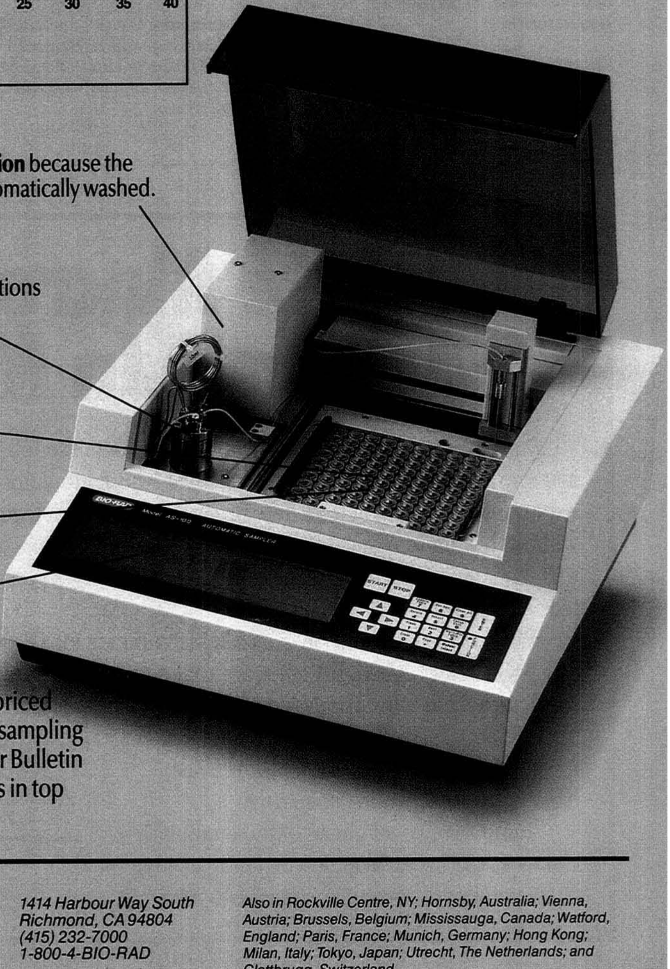

No cross-contamination because the sample needle is automatically washed.

Fixed loop or variable volume injections guarantee reliable and repeatable injections.

Three interchangeable sample trays accommodate standard vials, microtubes, and microtitration trays.

Solid state refrigeration. No gas needed!

Fully programmable

Get the facts on the modestly priced Bio-Rad HRLC® refrigerated sampling system. Call, or contact us for Bulletin 1415. Then you'll know why more is less in top of the line automatic samplers.

BIO-RAD

Chemical Division

1414 Harbour Way South
Richmond, CA 94804
(415) 232-7000
1-800-4-BIO-RAD

Also in Rockville Centre, NY; Hornsby, Australia; Vienna, Austria; Brussels, Belgium; Mississauga, Canada; Watford, England; Paris, France; Munich, Germany; Hong Kong; Milan, Italy; Tokyo, Japan; Utrecht, The Netherlands; and Glattbrugg, Switzerland.

CIRCLE 18 ON READER SERVICE CARD

ANALYTICAL APPROACH

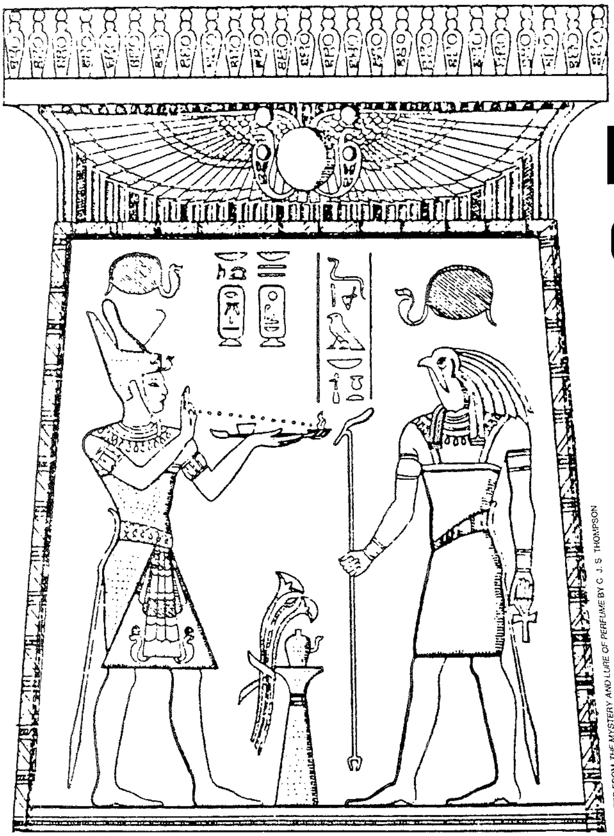

ADAPTED FROM *THE MYSTERY AND LURE OF PERFUME* BY C. J. S. THOMPSON

Identification of a Late Bronze Age Resin

Hampton H. Hairfield, Jr., and Elizabeth M. Hairfield
John Baker Daffin Laboratory of Chemistry
Mary Baldwin College
Staunton, VA 24401

A late Bronze Age vessel, shipwrecked at Ulu Burun near southern Turkey, has been called the archaeological find of the century. Found in 1982, it is the oldest ship discovered (dating back to the fourteenth century B.C.) and its diverse cargo spans seven civilizations (*1*, *2*). Among the numerous items found were approximately 100 amphorae, or jars filled with a yellow resin. This resin was one of the most abundant commodities in the cargo.

The precise identification of the Bronze Age resin is important for two reasons. It is the first archaeological discovery in which resin has been found in abundance, and identifying the resin can provide information about the ship's point of departure and its destination.

Resins, the solid or sticky semisolid secretions from various plants and trees, have been used since ancient times to prepare incense, medicine, cosmetics, and perfumes. Today they are also used to prepare varnish and cement. Of the many resins that have been important since antiquity, terebinth, mastic, and frankincense (olibanum) are likely candidates for the Bronze Age resin because of their yellow color.

The source of the terebinth resin is *Pistacia terebinthus*, a tree that grew abundantly in ancient times in the Mediterranean region. This resin was called "sntr" by the Egyptians, who burned it as incense to worship their gods as far back as the 18th dynasty (1500 B.C.) (*3*). In fact, because the Egyptians burned such large quantities of this resin, it seems likely that a large cargo of terebinth would be destined for Egypt.

Mastic, a resin secreted from *Pistacia lentiscus*, is a close relative of terebinth and native to the Mediterranean region. During the lifetime of Christ, mastic was more valuable than frankincense (*4*). It was used to prepare medicine and embalming mixtures in ancient Egypt (*5*). Because terebinth and mastic resins are similar in geographical origin (*6*) and odor, it would be possible to confuse one resin for the other.

Frankincense, one of the gifts of the Magi, came from Arabia and the Horn of Africa. It is secreted by trees of the genus *Boswellia* and could have made its way to Egypt via trade routes that date back to the fifth dynasty (2800 B.C.). However, there is no official record of the resin in Egypt until the 18th dynasty (*4*).

Identification of resins

For complex mixtures such as resins, IR spectroscopy has limited usefulness; the spectra only provide information about which functional groups are present in the substances. Because these resins contain both acids and esters, their spectra are virtually identical in the 4000–1250-cm^{-1} region. However, resins often afford a characteris-

0003-2700/90/0362-041A/$02.50/0

tic band in the 1200–700-cm^{-1} region. For example, amber can be identified by succinate absorption (a sharp peak preceded by a broad shoulder in the 1200–1150-cm^{-1} region) (7). Unfortunately, no characteristic IR bands were found in the Bronze Age resin.

Gas chromatography/mass spectrometry (GC/MS) has been used successfully to identify triterpenoids in resins. Sample preparation involves either steam distillation of the essential oil fraction (which is volatile and can be analyzed by GC or GC/MS) or extraction of the acidic fraction followed by esterification with diazomethane.

John Mills and Raymond White of the National Gallery in London studied the Bronze Age resin using GC/MS. In the methanol:ether (1:9) extract of the resin, they identified four acids as their methyl esters: oleanoic acid, moronic acid, masticadienonic acid, and *iso*-masticadienonic acid (Figure 1). Because these acids are characteristic of resins from the genus *Pistacia*, Mills and White concluded that the Bronze Age resin is from this genus (*8*).

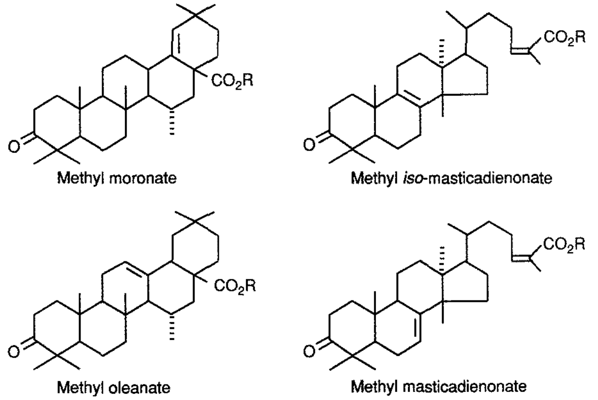

Figure 1. Major acid constituents of the genus *Pistacia* resins (R = CH_3).

Although they did not carry out further analyses, they used an historical argument to speculate that the unknown resin is terebinth. This theory was based solely on their belief that mastic resin was in short supply during the Bronze Age. A large terebinth tree could easily yield up to 2 kg of resin, whereas the more viscous mastic resin could only be collected one drop at a time. Thus Mills and White believed it was unlikely that the 100 jars discovered on the shipwrecked vessel could be filled with mastic resin.

We felt that it was essential to pro-

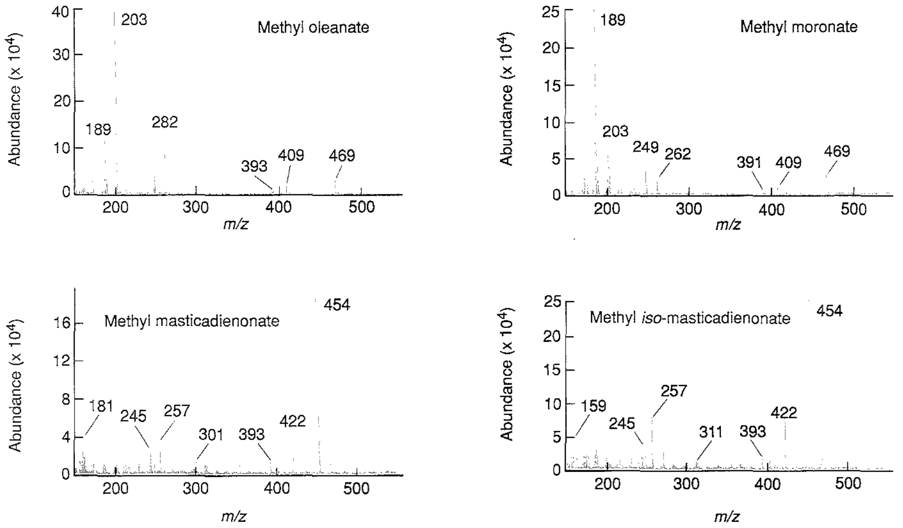

Figure 2. Mass spectra of major acid constituents (as their methyl esters) in the Bronze Age resin.

GC/MS analyses were performed on a 15 m X 0.25 mm bonded capillary column inserted into a gas chromatograph equipped with a mass selective detector. Helium gas flow rate of ~1 mL/min was used. The injector and the transfer line were heated to 280 °C; the column was temperature programmed from 260 °C to 264 °C at 0.1 °C/min, then raised to 280 °C and held for 7 min.

duce chemical evidence to either corroborate or refute their theory. A chemical distinction between the resins was needed to confirm from which species the resins originated.

Both terebinth and mastic contain the four acids that are found in the Bronze Age resin. The mass spectra of the four predominant acid constituents (as their methyl esters) of the Bronze Age resin are shown in Figure 2. Unfortunately, the relative intensity patterns of the esters from the acids do not match one resin more than another. Thus GC/MS did not provide sufficient information for determining the precise source of the Bronze Age resin.

In addition, the total ion chromatograms of the four major esters showed that the percent of each ester in the unknown resin does not match the percent of each ester in either mastic or terebinth resin (Table I).

Thin-layer chromatography

A method that could differentiate these resins was needed to confirm from which species of *Pistacia* the unknown resin originated. Because we had distinguished commercial varieties of frankincense using thin-layer chromatography (TLC) (*9*), we also used this method on the unknown resin.

TLC can be highly selective for separating compounds with small differences in polarity or potential for hydrogen bonding. It is sometimes possible to distinguish compounds by color, even when they have identical mobilities. TLC can be used to analyze solids and liquids; for a complex mixture such as resin, TLC of fractions containing both solid and liquid components can provide more definitive identification. Once the resin has been identified, the chromatogram can serve as a fingerprint for future analysis.

Table I. Percent of the four major esters in each resin determined by ion chromatography

Resin	Methyl oleanate	Methyl moronate	Methyl masticadienonate	Methyl *iso*-masticadienonate
Bronze Age	10.7	34.4	33.4	21.4
Terebinth	17.5	23.6	34.4	24.5
Mastic	20.7	42.1	15.5	21.7

Determination of the species

Three known resins from the genus *Pistacia:* mastic (*P. lentiscus*), terebinth from Chios (*P. terebinthus*), and terebinth from Cyprus (*P. terebinthus, var. atlantica*) and olibanum, from the genus *Boswellia* (*B. papyrifera*) were used for this study.

A 20-mg chip of each resin was extracted with ethanol; a second 20-mg sample was extracted with ether, then separated into neutral and acidic fractions; and an aliquot of the acidic fraction was esterified with diazomethane. The chromatograms of the methyl esters of the Bronze Age resin and of the *Pistacia* resins confirm their close relationship. In both daylight and under UV light, the unknown resin can be distinguished from olibanum. However, the Bronze Age and the two terebinth resins produced a series of spots with R_f (retardation factor) values greater than that of the strong spots at 0.57. The absence of these spots from the mastic extracts suggests that the Bronze Age resin is structurally similar to the terebinth resin.

TLC of the acidic fractions provides evidence that the Bronze Age resin (KW179) favors the Cyprus terebinth resin (Figure 3). The small, faint spots above $R_f = 0.60$ (which are dark in daylight and pink under UV) are more pronounced in the Chios terebinth chromatogram than in the Bronze Age or Cyprus terebinth chromatograms. The acidic fraction of the Bronze Age resin also produces spots at $R_f = 0.54$ and $R_f = 0.42$. The intensity and color of these spots resemble the stronger spots in olibanum; consequently, we have wondered whether the resin from Ulu Burun could be contaminated with traces of olibanum.

The TLC data from the neutral fractions also support the hypothesis that the Bronze Age resin is a terebinth resin. In addition, the chromatogram from the Bronze Age resin favors the Cyprus terebinth resin—the spot at $R_f = 0.43$ in the Chios terebinth chromatogram is absent. Finally, TLC of the ethanol extract shows that the Bronze Age resin is neither olibanum nor mastic resins (Figure 4). Moreover, the Chios chromatogram has a spot at $R_f = 0.46$ that is not seen in the Bronze Age or Cyprus terebinth chromatograms.

Future directions

From the TLC data, it is clear that the Bronze Age resin originates from *P. terebinthus*. However, several questions still remain unanswered. For example, is *atlantica* a distinct variety? Botanists disagree about whether there are different varieties of terebinth, yet our TLC data support the theory that at least two different varieties do exist. Furthermore, do the differences between the Bronze Age resin and the terebrinth resins result from evolutionary changes or chemical decomposition? We are continuing to study terebinth resin samples from different

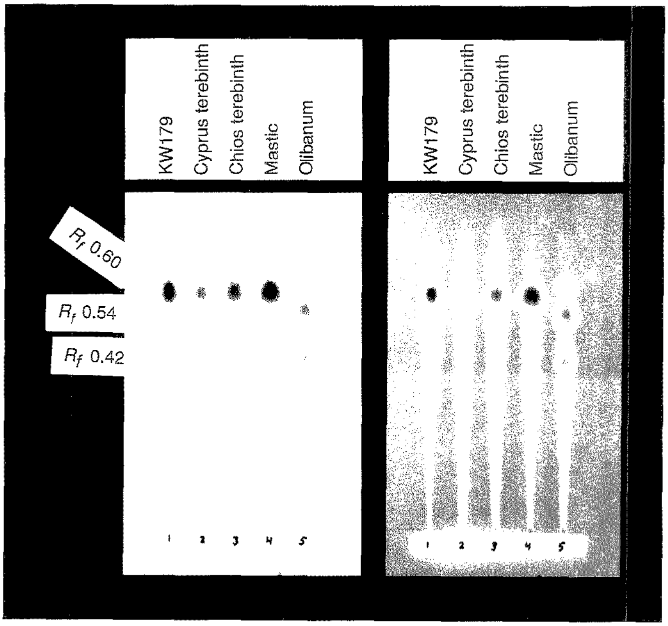

Figure 3. Thin-layer chromatography of the acid fraction.

TLC was carried out on glass plates coated with a 250-μm layer of silica gel developed to a height of 15 cm with methylene chloride containing 2% acetone and visualized with chlorosulfonic acid (30% in acetic acid). Left: in daylight; right: under 354-nm UV light.

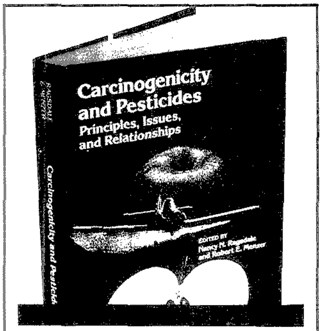

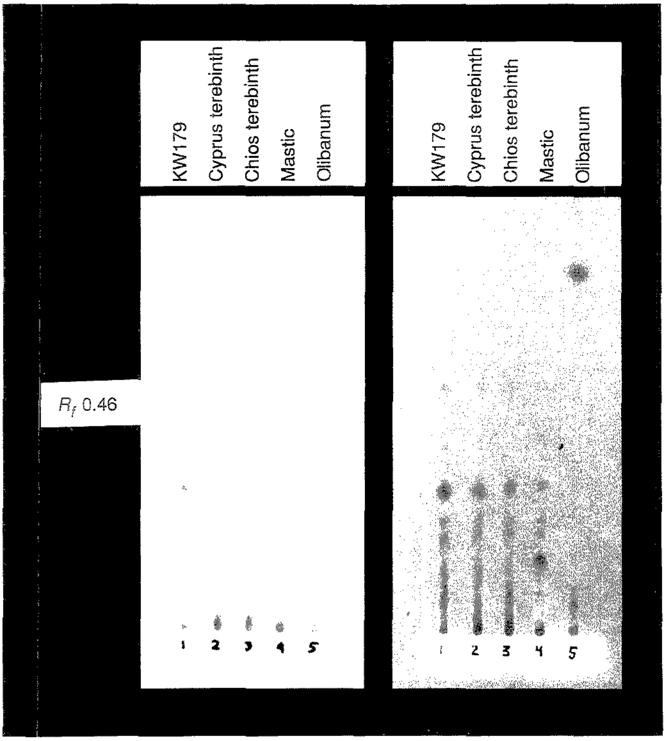

Figure 4. TLC of the ethanol extract.
The ethanol extract was developed in methylene chloride and visualized with antimony pentachloride (1 M in chloroform). Left: in daylight; right: under 354-nm UV light.

trees in various locations in an effort to resolve these questions.

Is the unknown resin contaminated with olibanum? This question is not easily answered. We attempted to identify the compounds whose R_f values suggest olibanum by scraping these spots from the TLC plates followed by extraction with methylene chloride, esterification with diazomethane, and GC analysis. However, these results were not conclusive. The peaks obtained had retention times that were substantially shorter than the retention times in the original sample. It is possible that acidity caused the sample to deteriorate, so we also extracted some methyl ester spots from pure β-boswellic acid and β-acetyl boswellic acid (the compounds that would be present if the sample were contaminated with olibanum) and performed GC analysis. This procedure was also unsuccessful. We concluded that deterioration occurs whenever these materials are run on a TLC plate. Repetition of this procedure in an inert atmosphere has not yet been tried.

Determining the precise origin of the unknown resin can help archaeologists to better understand the Bronze Age civilization. The fact that the ship was probably traveling to Egypt sheds light on ancient trade routes. The quantity of terebinth found supports Egyptian records regarding the vast quantities of incense that were burned. However, a more extensive comparative study of the terebinth resins is needed to elucidate mechanisms of decomposition and to help botanists better understand the history and structure of the terebinth species. We hope that this aspect of the mystery can be solved in the near future through the application of known analytical techniques.

The authors thank Curt Beck of Vassar College for providing the Bronze Age resin samples; John S. Mills of the National Gallery, London, and Rupert Hastings of the Royal Botanical Gardens for providing the known botanicals; Harold McNair and Larry Taylor of Virginia Polytechnic Institute and State University for use of their GC/MS instrument; C. William Saunders for assistance in operating the GC/MS instrument; Martha N. Evans for assistance with French translations; and James B. Patrick, Lundy H. Pentz, Eric N. Jones, Joseph M. Garrison, Jr., and Ramona J. Bosserman for helpful comments. The authors also thank the Virginia Foundation for Independent Colleges for partial support of this work.

References

(1) Bass, G. F. *Am. J. Archaeol.* 1986, *90*, 269–96.
(2) Pulak, C. *Am. J. Archaeol.* 1988, *92*, 1–37.
(3) Loret, V. *Recherches d'Archéologie de Philologie et d'Histoire, Tome 19: La Résine de Térébinthe (Sonter) Chez les Anciens Egyptiens*; Imprimerie de l'Institut Français d'Archéologie Orientale: Cairo, Egypt, 1949.
(4) Groom, M. *Frankincense and Myrrh;* Longman: New York, 1981.
(5) Reutter, L. *De l'Embaumement Avant et Après Jésus Christ;* Vigot Frères: Paris, 1912.
(6) Fluckinger, F. A.; Hanbury, D. *Pharmacographia: A History of the Principal Drugs of Vegetable Origin Met with in Great Britain and British India;* Macmillan: London, 1879.
(7) Beck, C. W. *Appl. Spectrosc. Rev.* 1986, *22*, 57–110.
(8) Mills, J. S.; White, R. *Archaeometry* **1989**, *31*, 37–44.
(9) Hairfield, E. M.; Hairfield, H. H.; Pentz, L. H. *Perfum. Flavor.* 1984, *9*, 33–36.

Hampton H. Hairfield, Jr., received a B.S. degree in education from the University of Virginia in 1963 and, until his retirement in 1988, was a member of the faculty of Wilson Memorial High School (Fishersville, VA). His interest in resins stems from childhood, when he was intrigued by the ceremonial use of incense in the Catholic Church.

Elizabeth M. Hairfield received a B.S. degree from Wheaton College (IL) in 1961 and a Ph.D. in chemistry from Bryn Mawr College in 1970. She then joined the faculty of Mary Baldwin College, where she is a professor of analytical and physical chemistry.

JANAF THERMOCHEMICAL TABLES

Third Edition

A Major Supplement from JOURNAL OF PHYSICAL AND CHEMICAL REFERENCE DATA

Presenting Reliable Data Utilized by Chemists, Chemical Engineers, and Materials Scientists from Around the World for Over 25 Years

JOURNAL OF PHYSICAL AND CHEMICAL REFERENCE DATA is very pleased to publish the Third Edition of the JANAF THERMOCHEMICAL TABLES.

Since the first version appeared 25 years ago, the JANAF THERMOCHEMICAL TABLES have been among the most widely used data tables in science and engineering.

You'll find:

- Reliable tables of thermodynamic properties of substances of wide interest
- A highly professional approach with critical evaluations of the world's thermochemical and spectroscopic literature
- A concise and easy-to-use format

This Third Edition presents an extensive set of tables including thermodynamic properties of more than 1800 substances, expressed in SI units. The notation has been made consistent with current international recommendations.

There is no other reference source of thermodynamic data that satisfies the needs of such a broad base of users.

Order your 2-volume set of the JANAF THERMOCHEMICAL TABLES today! You'll get over 1890 pages of valuable information that is crucial to your research—in two hardback volumes.

Editors:

M.W. Chase, Jr.
National Institute of Standards and Technology
C.A. Davies
Dow Chemical U.S.A.
J.R. Downey, Jr.
Dow Chemical U.S.A.
D.J. Frurip
Dow Chemical U.S.A.
R.A. McDonald
Dow Chemical U.S.A.
A.N. Syverud
Dow Chemical U.S.A.

SUBSCRIPTION INFORMATION

The JANAF THERMOCHEMICAL TABLES, THIRD EDITION is a two-volume supplement of *Journal of Physical and Chemical Reference Data.*

1896 pages, 2 volumes, hardcover
ISBN 0-88318-473-7
Supplement Number 1 to Volume 14, 1985

U.S. & Canada	**$130.00**
All Other Countries	**$156.00**
(Postage included.)	

All orders for supplements must be prepaid.

Foreign payment must be made in U.S. currency by international money order, UNESCO coupons, U.S. bank draft, or order through your subscription agency. For rates in Japan, contact Maruzen Co., Ltd. Please allow four to six weeks for your copy to be mailed.

For more information, write **American Chemical Society**, Marketing Communications Department, 1155 Sixteenth Street, NW, Washington, DC 20036.

In a hurry? Call TOLL FREE 800-227-5558 and charge your order!

Published by the **American Chemical Society** and the **American Institute of Physics** for the **National Institute of Standards and Technology**

Here are 25 of the World's Most Prestigious Journals and Magazines in Chemical Science!

American Chemical Society publications offer:

• Reliable and Accurate Research • Techniques • Trends • Discoveries • Reviews • Developments • And much more!

Take advantage of the most current chemical research and general scientific reporting available — from the many respected researchers worldwide.

Use the postage-paid order card below to order your 1990 subscriptions.

ACCOUNTS OF CHEMICAL RESEARCH*

F.W. McLafferty, Editor; Cornell Univ.

Monthly offering short, critical reviews written by scientists active in the research described.

	U.S.	Canada & Mexico	Europe	All Other Countries
Members				
One Year	$ 24	$ 31	$ 33	$ 36
Two Years	$ 43	$ 57	$ 61	$ 67
Nonmembers	$127	$134	$136	$139

ANALYTICAL CHEMISTRY

George H. Morrison, Editor; Cornell Univ.

The world's foremost publication in the vital field of measurement science. Semi-monthly.

	U.S.	Canada & Mexico	Europe	All Other Countries
Members				
One Year	$ 29	$ 64	$ 96	$118
Two Years	$ 49	$ 119	$ 183	$227
Nonmembers	$ 59	$ 94	$ 186	$208

BIOCHEMISTRY*

NOW WEEKLY!

Hans Neurath, Editor; Univ. of Washington.

Results of original research in all recognized or developing areas of biochemistry. Weekly.

	U.S.	Canada & Mexico	Europe	All Other Countries
Members				
One Year	$ 85	$174	$278	$345
Two Years	$153	$331	$539	$673
Nonmembers	$690	$779	$883	$950

BIOCONJUGATE CHEMISTRY*

NEW JOURNAL!

Claude F. Meares, Editor; Univ. of California, Davis

Six times a year, chemists, biochemists, and molecular biologists will find the most important research in conjugate chemistry in one publication— Bioconjugate Chemistry.

	U.S.	**Canada & Mexico**	**Europe**	**All Other Countries**
Members				
One Year	$ 29	$ 35	$ 39	$ 43
Two Years	$ 52	$ 64	$ 72	$ 80
Nonmembers	$249	$255	$259	$ 263

BIOTECHNOLOGY PROGRESS*

NEW JOURNAL!

Jerome S. Schultz, Editor; Univ. of Pittsburgh

Bimonthly, this publication will focus on the application of fundamental chemical and engineering principles to biological phenomena and to processor product design.

	U.S.	**Canada & Mexico**	**Europe**	**All Other Countries**
ACS/AIChE				
Members	$ 25	$ 31	$ 34	$ 39
Nonmembers	$250	$256	$259	$ 264

CHEMICAL & ENGINEERING NEWS*

Michael Heylin, Editor

Chemical newsweekly and the official publication of the ACS that all members receive as part of their dues.

	U.S.	Canada & Mexico	Europe*	All Other Countries*
Nonmembers				
One Year	$ 60	$ 93	$127	$169
Two Years	$108	$174	$242	$326

Surface Delivery All Countries: 1 Year, $93; 2 Years, $174

** Air service delivery*

CHEMICAL RESEARCH IN TOXICOLOGY*

Lawrence J. Marnett, Editor; Vanderbilt Univ.

Bimonthly international journal for scientists needing the most current research in the highly active field of toxicology.

	U.S.	Canada & Mexico	Europe	All Other Countries
Members				
One Year	$ 46	$ 52	$ 57	$ 60
Two Years	$ 82	$ 94	$104	$110
Nonmembers	$269	$275	$280	$283

CHEMICAL REVIEWS*

Josef Michl, Editor; Univ. of Texas, Austin

Reviews of research in various areas of chemistry that eliminate the need to scan scores of articles concerning particular fields. 8 issues per year.

	U.S.	Canada & Mexico	Europe	All Other Countries
Members				
One Year	$ 26	$ 42	$ 59	$ 70
Two Years	$ 46	$ 78	$112	$134
Nonmembers	$225	$ 241	$258	$269

CHEMISTRY OF MATERIALS*

Leonard V. Interrante, Editor; Rensselaer Polytechnic Institute

This bimonthly journal gives direction in the fundamentals of materials preparation, characterization, and processing science and technology.

	U.S.	Canada & Mexico	Europe	All Other Countries
Members				
One Year	$ 49	$ 57	$ 65	$ 69
Two Years	$ 88	$104	$120	$128
Nonmembers	$299	$307	$315	$319

CHEMTECH

Benjamin J. Luberoff, Editor

Stimulating, personal monthly helping chemists and engineers arrive at innovative solutions to real problems.

	U.S.	Canada & Mexico	Europe	All Other Countries
Members				
One Year	$ 39	$ 48	$ 52	$ 55
Two Years	$ 66	$ 84	$ 92	$ 98
Nonmembers				
Personal	$ 69	$ 78	$ 82	$ 85
Institutional	$299	$308	$312	$315

ENERGY & FUELS*

John W. Larson, Editor; Lehigh Univ.

A bimonthly journal covering all aspects of the transformation, utilization, formation, and production of fuels and non-nuclear energy in addition to studies of fuel structure and properties.

	U.S.	Canada & Mexico	Europe	All Other Countries
Members				
One Year	$ 48	$ 55	$ 59	$ 62
Two Years	$ 86	$ 100	$108	$114
Nonmembers	$294	$301	$305	$308

MAIL THIS ORDER FORM TODAY! **1990**

Please enter my subscription(s) for the following:

Title ____________ 1 yr. $ ____________ 2 yrs. $ ____________

Title ____________ 1 yr. $ ____________ 2 yrs. $ ____________

(If you wish to enter more than two subscriptions, please use a separate piece of paper and mail with this coupon in an envelope.)

Name ________________________________

Company ____________________ Title ____________

Address ☐ Home ☐ Business ________________________

City ____________________ State ______ ZIP ____________

☐ Payment enclosed. (Payable to American Chemical Society)

☐ Bill Me ☐ Bill Company

☐ Charge my ☐ VISA/MasterCard ☐ Diners Club/Carte Blanche

Card No. ________________________________

Expires ____________ Signature ________________________

☐ I am an ACS Member ☐ I am not an ACS Member

☐ Please send me information on how to become an ACS member

Member rates are for personal use only. All journal subscriptions are based on a calendar year. Subscriptions to ANALYTICAL CHEMISTRY, CHEMICAL & ENGINEERING NEWS (nonmembers only), CHEMTECH, and ENVIRONMENTAL SCIENCE & TECHNOLOGY will start the month the order is placed and expire one year later unless subscriber specifies otherwise.

Foreign payment must be made in U.S. dollars by international money order, UNESCO coupons, or U.S. bank draft. Orders accepted through your subscription agency. For nonmember rates in Japan contact Maruzen Co., Ltd.

Air Service Delivery included in all rates listed for countries outside the U.S., Canada, and Mexico.

In a Hurry?
Call TOLL FREE (800)227-5558 (U.S. only) and charge your order!
In D.C. and outside the U.S. call (202)872-4363.
Telex: 440159 ACSPUI OR 89 2582 ACSPUBS
FAX: (202) 872-4615

5471L

ENVIRONMENTAL SCIENCE & TECHNOLOGY*

William H. Glaze, Editor; Univ. of North Carolina, Chapel Hill

Published monthly for those engaged in environmental study and maintenance through the application of chemical principles.

	U.S.	Canada & Mexico	Europe	All Other Countries
Members				
One Year	$ 36	$ 50	$ 65	$ 72
Two Years	$ 61	$ 89	$119	$133
Nonmembers				
Personal	$ 67	$ 81	$ 96	$103
Institutional	$276	$290	$305	$312

INDUSTRIAL & ENGINEERING CHEMISTRY RESEARCH*

Donald R. Paul, Editor; Univ. of Texas, Austin

This monthly provides timely reports on original work in the broad field of chemical engineering and industrial chemical research.

	U.S.	Canada & Mexico	Europe	All Other Countries
Members				
One Year	$ 55	$ 73	$ 84	$ 94
Two Years	$ 99	$135	$157	$177
Nonmembers	$372	$390	$401	$411

INORGANIC CHEMISTRY*

M. Frederick Hawthorne, Editor; Univ. of California, L.A.

Biweekly journal publishes fundamental studies, experimental and theoretical, in all phases of inorganic chemistry.

	U.S.	Canada & Mexico	Europe	All Other Countries
Members				
One Year	$ 82	$120	$146	$170
Two Years	$147	$223	$275	$323
Nonmembers	$612	$650	$676	$700

JOURNAL OF AGRICULTURAL AND FOOD CHEMISTRY*

NOW MONTHLY!

Irvin E. Liener, Editor; Univ. of Minnesota

Monthly reporting on original research into the chemical aspects of agriculture and food.

	U.S.	Canada & Mexico	Europe	All Other Countries
Members				
One Year	$ 25	$ 41	$ 52	$ 61
Two Years	$ 45	$ 77	$ 99	$117
Nonmembers	$204	$220	$231	$240

JOURNAL OF THE AMERICAN CHEMICAL SOCIETY*

Allen J. Bard, Editor; Univ. of Texas, Austin

Most quoted biweekly journal of the widest possible interest to research workers and students in all areas of chemistry.

	U.S.	Canada & Mexico	Europe	All Other Countries
Members				
One Year	$ 75	$131	$191	$236
Two Years	$135	$247	$367	$457
Nonmembers	$630	$686	$746	$791

BUSINESS REPLY MAIL

FIRST CLASS PERMIT NO. 10094 WASHINGTON, D.C.

POSTAGE WILL BE PAID BY ADDRESSEE

AMERICAN CHEMICAL SOCIETY
Attn: Marketing Communications Department
1155 Sixteenth Street, N.W.
Washington, D.C. 20077-5768

NO POSTAGE
NECESSARY
IF MAILED
IN THE
UNITED STATES

JOURNAL OF CHEMICAL AND ENGINEERING DATA*

Bruno J. Zwolinski, Editor; Texas A&M Univ.

This quarterly journal is primarily concerned with the presentation of data of lasting value.

	U.S.	Canada & Mexico	Europe	All Other Countries
Members				
One Year	$ 30	$ 35	$ 37	$ 40
Two Years	$ 54	$ 64	$ 68	$ 74
Nonmembers	$207	$212	$214	$217

JOURNAL OF CHEMICAL INFORMATION AND COMPUTER SCIENCES*

George W.A. Milne, Editor; National Institutes of Health

Quarterly reporting on new R&D, concepts, systems and programs in all areas of information and computers relative to chemistry.

	U.S.	Canada & Mexico	Europe	All Other Countries
Members				
One Year	$ 18	$ 22	$ 24	$ 26
Two Years	$ 32	$ 40	$ 44	$ 48
Nonmembers	$108	$112	$114	$116

JOURNAL OF MEDICINAL CHEMISTRY*

Philip S. Portoghese, Editor; Univ. of Minnesota

Monthly publishing on the relationship of chemistry to biological activity including rapid communication of major advances in drug design and development.

	U.S.	Canada & Mexico	Europe	All Other Countries
Members				
One Year	$ 42	$ 63	$ 81	$ 93
Two Years	$ 75	$117	$153	$177
Nonmembers	$329	$350	$368	$380

THE JOURNAL OF ORGANIC CHEMISTRY*

Clayton H. Heathcock, Editor; Univ. of California, Berkeley

Biweekly offering critical accounts of original work and interpretive reviews of existing data that presents new viewpoints.

	U.S.	Canada & Mexico	Europe	All Other Countries
Members				
One Year	$ 56	$ 98	$134	$162
Two Years	$100	$184	$256	$312
Nonmembers	$428	$470	$506	$534

JOURNAL OF PHYSICAL AND CHEMICAL REFERENCE DATA*

NOW BIMONTHLY!

David R. Lide, Jr., Editor; National Institutes of Standards & Technology

Published bimonthly with Am. Inst. of Physics and NIST presenting critically evaluated data on physical and chemical properties.

	U.S.	Canada & Mexico	Europe	All Other Countries
Members (ACS, AIP affiliated societies)	$ 70	$ 85	$105	$105
Nonmembers	$325	$340	$360	$360

THE JOURNAL OF PHYSICAL CHEMISTRY*

Mostafa A. El-Sayed, Editor; Univ. of California, L.A.

Biweekly. Experimental and theoretical research on fundamental aspects of physical chemistry and chemical physics.

	U.S.	Canada & Mexico	Europe	All Other Countries
Members				
One Year	$ 70	$126	$178	$217
Two Years	$126	$238	$342	$420
Nonmembers	$670	$726	$778	$817

LANGMUIR*

NOW MONTHLY!

Arthur W. Adamson, Editor; Univ. of Southern California

Broad coverage of all areas of fundamental surface and colloid science, wet surface chemistry, UHV surface chemistry, disperse systems, electrochemistry. Monthly.

	U.S.	Canada & Mexico	Europe	All Other Countries
Members				
One Year	$ 58	$ 70	$ 78	$ 85
Two Years	$104	$128	$144	$158
Nonmembers	$429	$441	$449	$456

MACROMOLECULES*

NOW BIWEEKLY!

Field H. Winslow, Editor; AT&T Bell Laboratories

Biweekly publication of original material on all fundamental aspects of polymer chemistry.

	U.S.	Canada & Mexico	Europe	All Other Countries
Members				
One Year	$ 57	$ 95	$121	$144
Two Years	$102	$178	$230	$276
Nonmembers	$553	$591	$617	$640

ORGANOMETALLICS*

Dietmar Seyferth, Editor; M.I.T.

Interdisciplinary approach to organometallic chemistry; synthesis; structure and bonding; reactivity and mechanism; applications in organic, inorganic, polymer, solid state chemistry and materials science. Monthly.

	U.S.	Canada & Mexico	Europe	All Other Countries
Members				
One Year	$ 59	$ 80	$ 98	$110
Two Years	$106	$148	$184	$208
Nonmembers	$521	$542	$560	$572

*Indicates periodicals printed on acid-free paper.

Analytical CHEMISTRY

EDITOR: **GEORGE H. MORRISON**

ASSOCIATE EDITORS: **Catherine C. Fenselau, Georges Guiochon, Walter C. Herlihy, Robert A. Osteryoung, Edward S. Yeung**

Editorial Headquarters
1155 Sixteenth St., N.W.
Washington, DC 20036
Phone: 202-872-4570
Telefax: 202-872-6325

Managing Editor: Sharon G. Boots

Associate Editors: Louise Voress, Mary Warner

Assistant Editors: Grace K. Lee, Alan R. Newman

Editorial Assistant: Felicia Wach

Contributing Editor: Marcia Vogel

Director, Operational Support: C. Michael Phillippe

Head, Production Department: Leroy L. Corcoran

Art Director: Alan Kahan

Designers: Amy Meyer Phifer, Robert Sargent

Production Editor: Elizabeth E. Wood

Circulation: Claud Robinson

Editorial Assistant, LabGuide: Joanne Mullican

Journals Dept., Columbus, Ohio

Associate Head: Marianne Brogan

Journals Editing Manager: Joseph E. Yurvati

Associate Editor: Rodney L. Temos

Advisory Board: Bernard J. Bulkin, Michael S. Epstein, Renaat Gijbels, William S. Hancock, Thomas L. Isenhour, James W. Jorgenson, Peter C. Jurs, Alan G. Marshall, Lawrence A. Pachla, John F. Rabolt, Debra R. Rolison, Ralph E. Sturgeon, Shigeru Terabe, George S. Wilson, Mary J. Wirth, Richard N. Zare
Ex Officio: Sam P. Perone

Instrumentation Advisory Panel: Daniel W. Armstrong, Bruce Chase, Thomas L. Chester, R. Graham Cooks, L. J. Cline Love, Sanford P. Markey, Brenda R. Shaw, Gary W. Small, R. Mark Wightman

Published by the
AMERICAN CHEMICAL SOCIETY
1155 16th Street, N.W.
Washington, DC 20036

Publications Division

Director: Robert H. Marks

Journals: Charles R. Bertsch

Special Publications: Randall E. Wedin

Manuscript requirements are published in the January 1, 1990 issue, page 89. Manuscripts for publication (4 copies) should be submitted to ANALYTICAL CHEMISTRY at the ACS Washington address.

The American Chemical Society and its editors assume no responsibility for the statements and opinions advanced by contributors. Views expressed in the editorials are those of the editors and do not necessarily represent the official position of the American Chemical Society.

AUTHOR INDEX

PERSPECTIVE: ANALYTICAL BIOTECHNOLOGY

Protein Structure Determination in Solution by Two-Dimensional and Three-Dimensional Nuclear Magnetic Resonance Spectroscopy

Angela M. Gronenborn* and G. Marius Clore*

Laboratory of Chemical Physics, National Institute of Diabetes and Digestive and Kidney Diseases, National Institutes of Health, Bethesda, Maryland 20892

Over the last decade, nuclear magnetic resonance (NMR) spectroscopy has evolved into a powerful method for determining structures of biological macromolecules. This has opened a unique opportunity for obtaining high-resolution three-dimensional structures in *solution*, in contrast to the well-established methods of X-ray diffraction, which are applicable only to solids and in particular single crystals. This rapid development has been spurred by several key advances in the field, especially the introduction of two- and three-dimensional NMR experiments, high field spectrometers (500 and 600 MHz), and computational algorithms for converting NMR derived restraints into three-dimensional structures. This review outlines the methodology employed for solving protein structures in solution, describing the basic NMR experiments necessary as well as introducing the concepts upon which the computational algorithms are founded. A variety of examples is discussed, illustrating the present state of the art, and future possibilities are indicated.

INTRODUCTION

Over the last few years there has been a burst of renewed interest in protein studies, especially aimed at understanding their structures, functions, and physiological roles. Some of this increased enthusiasm can be attributed to a variety of technological advances in the area of modern molecular biology. The advent of molecular cloning, particularily of protein encoding genes, and rapid DNA sequencing methods have led to an explosion in the number of available protein sequences, reaching over 15 000 at the latest count. Whereas this wealth of data is clearly impressive, amino acid sequences per se are of limited value in understanding protein function. We need to know the three-dimensional structure before we can begin to make progress in analyzing the intricate reactions carried out by proteins such as catalysis, ligand binding, gene regulation, and assembly. The design of modified proteins and rational design of ligands (drugs), as well as attempts at de novo design of protein molecules, all have to be based on concepts at the atomic level in three-dimensional space, thereby creating an increasing need for detailed structural analysis.

Until recently, the only experimental technique available for determining three-dimensional structures had been single-crystal X-ray diffraction, and most of our structural knowledge about proteins is based on those crystal structures. There are approximately 400 coordinate sets available to date, comprising about 120 different protein folds. Analyzing protein structures by crystallography can be a slow and difficult undertaking since the first, and possibly hardest task, involves growing X-ray quality grade crystals, which have to be well ordered to give rise to good diffraction spots. Even if this task is accomplished, a second hurdle still needs to be overcome, as the phases have to be solved, commonly achieved by collecting data on heavy atom derivatives. Thus, despite spectacular advances in protein crystallography, we are faced with an enormous gap between the available primary sequence data and the tertiary structure data on proteins.

Over the last ten years, a second method for determining protein structures has been developed and is by now well established. This method makes use of nuclear magnetic resonance (NMR) spectroscopy. Unlike crystallography, NMR measurements are carried out in solution under potentially physiological conditions and are therefore not hampered by the ability or inability of a protein to crystallize.

The principal source of information used to solve three-dimensional protein structures by NMR spectroscopy resides in short interproton distances supplemented by torsion angles. The distances are derived from nuclear Overhauser effect (NOE) measurements. The size of the NOE between two protons is proportional to r^{-6}, where r is the distance between them. Torsion angles are obtained from an analysis of three-bond coupling constants, which are related to dihedral angles. An essential prerequisite for obtaining interproton distance restraints and torsion angle restraints is the assignment of the NMR spectrum; that is to say the identity of every proton resonance has to be determined. This is not a trivial task considering that the proton spectrum of even a small protein comprising only 80 amino acids contains approximately 650 resonances. All of these exhibit several cross-peaks in the two-dimensional (2D) spectrum such that the number of cross-peaks can easily reach several thousand whose identity has to be ascertained. Complete spectral assignment is therefore an integral part of the structure determination.

Although it was appreciated relatively early on that NMR could in principle provide the necessary information to obtain three-dimensional structures, it is only fairly recently that this goal has been realized. The reasons for this are 3-fold: (i) The development of 2D NMR experiments (*1–3*) alleviated problems associated with resonance overlap, which for macromolecules prevents any analysis of the traditional one-dimensional spectrum. This is achieved by spreading all the information out in a plane, thereby permitting a detailed interpretation of the pertinent spectral features. This conceptual idea has been extended more recently to three-dimensional (3D) NMR (*4–7*) again relieving problems arising

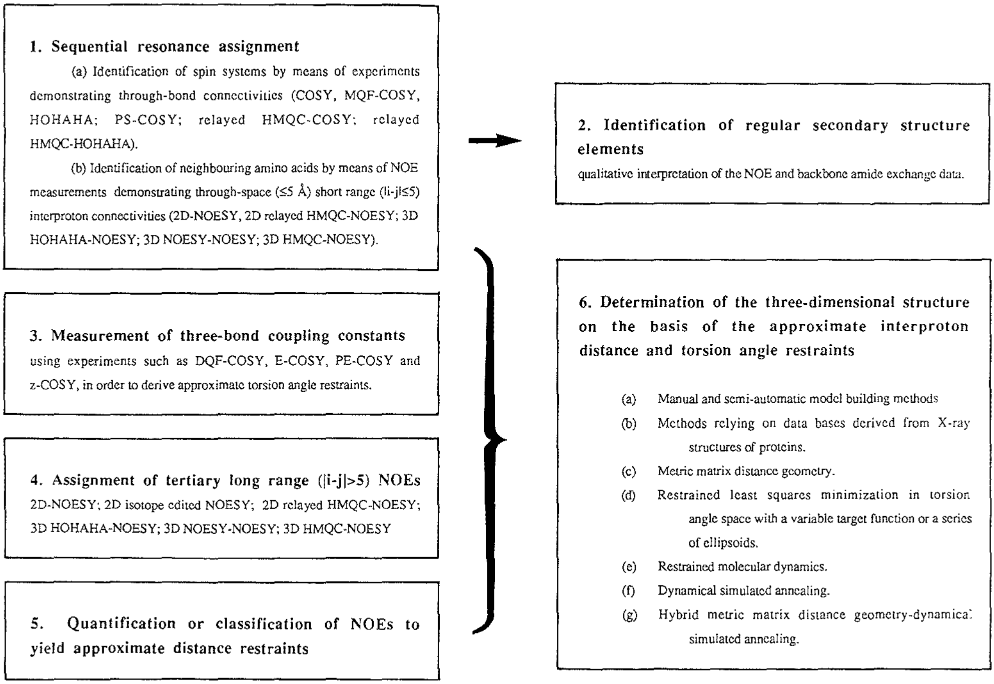

1. Sequential resonance assignment

(a) Identification of spin systems by means of experiments demonstrating through-bond connectivities (COSY, MQF-COSY, HOHAHA; PS-COSY; relayed HMQC-COSY; relayed HMQC-HOHAHA).

(b) Identification of neighbouring amino acids by means of NOE measurements demonstrating through-space (≤5 Å) short range (|i-j|≤5) interproton connectivities (2D-NOESY, 2D relayed HMQC-NOESY; 3D HOHAHA-NOESY; 3D NOESY-NOESY; 3D HMQC-NOESY).

2. Identification of regular secondary structure elements

qualitative interpretation of the NOE and backbone amide exchange data.

3. Measurement of three-bond coupling constants

using experiments such as DQF-COSY, E-COSY, PE-COSY and z-COSY, in order to derive approximate torsion angle restraints.

4. Assignment of tertiary long range (|i-j|>5) NOEs

2D-NOESY; 2D isotope edited NOESY; 2D relayed HMQC-NOESY; 3D HOHAHA-NOESY; 3D NOESY-NOESY; 3D HMQC-NOESY

5. Quantification or classification of NOEs to yield approximate distance restraints

6. Determination of the three-dimensional structure on the basis of the approximate interproton distance and torsion angle restraints

(a) Manual and semi-automatic model building methods

(b) Methods relying on data bases derived from X-ray structures of proteins.

(c) Metric matrix distance geometry.

(d) Restrained least squares minimization in torsion angle space with a variable target function or a series of ellipsoids.

(e) Restrained molecular dynamics.

(f) Dynamical simulated annealing.

(g) Hybrid metric matrix distance geometry-dynamical simulated annealing.

Figure 1. Flow chart of the various steps involved in determining the three-dimensional structure of a protein in solution by NMR.

from spectral crowding, and it is the 3D approach in particular that will extend the present limits with respect to the size of the proteins that can be studied. (ii) The availability of high field magnets (500 and 600 MHz) has resulted in spectrometers with both a significant increase in signal-to-noise ratio and greater spectral resolution, and continuing development in this area again will extend the limits even further. (iii) Suitable mathematical algorithms and computational approaches that convert the NMR derived restraints into three-dimensional structures have been developed (*8–14*) and several robust and efficient methods are now available.

This article reviews the various stages involved in the determination of a three-dimensional protein structure by NMR, and the flow chart in Figure 1 illustrates the individual steps. The general methodology is outlined; however, no attempt is made to provide an in-depth description of either the general NMR theory or the details of the mathematical algorithms. Emphasis is placed on the application of NMR to structural studies and several examples illustrating various points are presented.

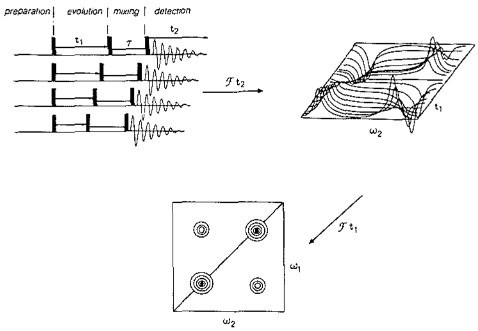

Figure 2. Generalized representation of the 2D NMR experiment.

BASIS OF TWO- AND THREE-DIMENSIONAL NMR

The principles of 2D NMR have been discussed in depth (see ref 15 for a comprehensive review) and only a very basic and brief description will be given here. Each proton (spin) possesses a property known as magnetization. When a molecule is placed in a magnetic field, the magnetization lies parallel to it. Rotation of this magnetization away from its parallel orientation, either by a radio frequency pulse or a combination of pulses allows one to follow the return of the magnetization to its equilibrium state. In any 2D NMR experiment this is called the preparation period. This is followed by an evolution period in which this transient state of the spins is allowed to evolve for varying time periods t_1, a mixing period during which the spins are correlated with each other, and finally the detection period t_2. A number of experiments are recorded with increasing values for t_1 to generate a data matrix $s(t_1,t_2)$. Two-dimensional Fourier transformation of $s(t_1,t_2)$ yields the 2D spectrum $S(\omega_1,\omega_2)$. The second frequency dimension in the 2D spectrum originates from the Fourier transformation of the t_1 modulation pappterns in the 1D spectra. The two frequency coordinates ω_1 and ω_2 of a particular resonance thus correspond to the t_1 and t_2 frequencies associated with the observed magnetization. This is illustrated schematically in Figure 2. Most homonuclear 2D experiments contain the 1D spectrum on the diagonal with symmetrically placed cross-peaks on either side of the diagonal representing different kinds of interactions between the spins. The nature of the interaction depends on the type of experiment, with cross peaks arising from through-bond scalar interactions in a COSY (*co*rrelated *s*pectroscop*y*) (*2*) or HOHAHA (*ho*mo-

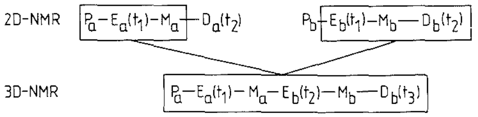

Figure 3. Scheme for combining two 2D NMR experiments into a 3D NMR experiment.

nuclear *H*artmann–*Ha*hn) (*16*) experiment and from through-space correlations in a NOESY (*n*uclear *O*verhauser and *e*xchange *s*pectroscop*y*) (*17*) experiment.

Since every 2D NMR experiment consists of the basic scheme

preparation–evolution (t_1)–mixing–detection (t_2)

it is conceptually very simple to construct a 3D experiment out of two 2D experiments by omitting the detection period of the first 2D experiment and the preparation period of the second one, combining both into a single pulse train as illustrated in Figure 3. The new detection period is now called t_3 and for every time variable t_2, a complete (t_1,t_3) 2D data set is acquired. Fourier transformation of t_2 sections taken through these 2D data sets converts the set of 2D spectra into the 3D spectrum. Since any two 2D experiments can be combined into a 3D experiment, one can envisage an enormous number of such experiments, starting from homonuclear versions and progressing to various heteronuclear 3D experiments. A recent overview over a large number of combinations of 2D experiments for 3D versions can be consulted for further reading (*18*). The power of the 3D NMR experiments lies in overcoming resonance overlap which for larger proteins becomes again a major obstacle in the traditional 2D ones. The first 3D experiments on proteins were of the homonuclear type (*4*, *5*). While elegant and no doubt useful in certain cases, the applicability of these homonuclear 3D experiments to larger proteins is limited, as the efficiency of magnetization transfer is severely reduced with increasing line widths. This is not a problem for 3D heteronuclear experiments (*6*, *7*) which contain a heteronuclear shift correlation (HMQC, *h*eteronuclear *m*ultiple *q*uantum *c*oherence) experiment such as 3D NOESY-HMQC or 3D HOHAHA-HMQC. For those the heteronuclear magnetization transfer occurs via relatively large one-bond couplings and is therefore very effective. Such heteronuclear 3D experiments represent in essence a series of 2D NOESY or HOHAHA spectra edited with respect to the chemical shift of the directly bonded heteronucleus, such as ^{15}N or ^{13}C. Because these spectra can be regarded as stretched out heteronuclear edited 2D spectra, their basic appearance and features resemble 2D spectra, which allows for easy interpretation and data analysis. A schematic drawing of such a 3D spectrum is presented in Figure 4. Major advantages of these heteronuclear 3D experiments are their high sensitivity (provided the protein is isotopically enriched) and ease of analysis.

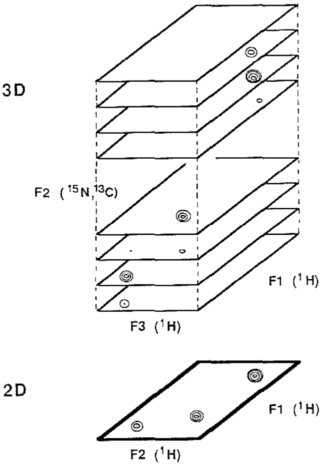

Figure 4. Schematic illustration of a heteronuclear 3D NMR experiment.

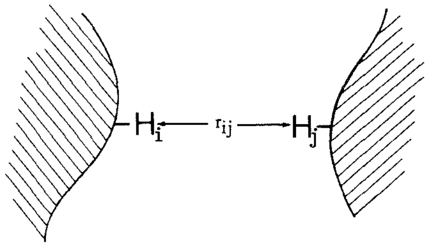

$$N_{ij}(t) \sim \sigma_{ij}\, t$$

$$\sigma_{ij} = \frac{\gamma^4 \hbar^2}{10\, r_{ij}^6} \left(\tau_{app} - \frac{6\tau_{app}}{1 + 4\omega^2 \tau_{app}^2} \right)$$

Figure 5. Basis of the NOE: r_{ij}, distance between the protons i and j; σ, cross-relaxation rate; N, NOE; τ_{app}, correlation time.

NUCLEAR OVERHAUSER EFFECT

NMR-derived protein structures are mainly based on NOE measurements that can demonstrate the proximity of protons in space and allow determination of their approximate separation (*19–21*). The principle of the NOE is relatively straightforward and is summarized in Figure 5. Considering the simplest system with only two protons, each of which possesses a property known as magnetization, exchange of magnetization between the protons occurs by a process known as cross-relaxation. Because the cross-relaxation rates in both directions are equal, the magnetization of the two protons at equilibrium is equal. The approximate chemical analogy of such a system would be one with two interconverting species with an equilibrium constant of 1. The cross-relaxation rate is proportional to two variables: r^{-6}, where r is the distance between the two protons, and τ_{app} the effective correlation time of the interproton vector. It follows that if the magnetization of one of the spins is perturbed, the magnetization of the second spin will change. In the case of macromolecules the cross-relaxation rates are positive and the leakage rate from the system is very small, so that, in the limit, the magnetization of the two protons would be equalized. The change in magnetization of proton i upon perturbation of the magnetization of proton j is known as the nuclear Overhauser effect (NOE). The initial build-up rate of the NOE is equal to the cross-relaxation rate and, hence, proportional to r^{-6}.

In one-dimensional NMR, the NOE can be observed in a number of ways, all of which involve the application of a selective radio frequency pulse at the position of one of the resonances. The simplest experiment involves the irradiation of resonance i for a time t, followed by acquisition of the spctrum. If proton j is close in space to proton i, its magnetization will be reduced and this is best observed in a difference spectrum subtracting a spectrum without irradiation from one with selective irradiation. An alternative approach involves the selective inversion of resonance *i* followed by acquisition after a time *t*. This particular experiment is the one-dimensional analogue of the two-dimensional experiment. In the two-dimensional experiment cross-peaks between proton resonances *i* and *j* are observed when the two protons are close in space and thus exchange magnetization via cross-relaxation.

SEQUENTIAL RESONANCE ASSIGNMENT

Sequential resonance assignment of the ^{1}H NMR spectra of proteins relies on two sorts of experiments: (i) those demonstrating through-bond scalar connectivities, and (ii) those demonstrating through-space (<5 Å) connectivities (*22*). The former, which are generally referred to as correlation experiments, serve to group together protons belonging to the same residue. The latter involve the detection of NOEs and serve to connect one residue with its immediate neighbors in the linear sequence of amino acids.

The first step in the assignment procedure lies in identifying spin systems, that is to say protons belonging to one residue unit in the polypeptide chain. Such experiments have to be carried out both in H_2O and D_2O, the former to establish connectivities involving the exchangeable NH protons and the latter to identify connectivities between nonexchangeable protons. Some spin systems are characteristic of single amino acids. This is the case for Gly, Ala, Thr, Leu, Ile, and Lys. Others are characteristic of several different amino acids. For example, Asp, Asn, Cys, Ser, and the aliphatic protons of all aromatic amino acids belong to the AMX spin system (i.e. they all have one C$^\alpha$H and two C$^\beta$H protons).

The simplest experiment used to delineate spin systems via scalar correlations is the COSY experiment, which was first described in 1976 by Aue et al. (*2*) and demonstrates direct through-bond connectivities. Thus, for a residue which has NH, C$^\alpha$H, C$^\beta$H, and C$^\gamma$H protons, connectivities will only be manifested between the NH and C$^\alpha$H, C$^\alpha$H and C$^\beta$H, and C$^\beta$H and C$^\gamma$H protons. This basic COSY experiment has now been superseeded by slightly more sophisticated experiments such as DQF-COSY (*23*) and P.COSY (*24*), which have the advantage of exhibiting pure phase absorption diagonals when the spectra are recorded in the pure phase absorption mode. This enables one to detect cross-peaks close to the diagonal.

Experiments that demonstrate only direct through-bond connectivities are of limited value if taken alone, due to problems of spectral overlap. In a protein spectrum, the degree of spectral overlap tends to increase as one progresses from the NH and C$^\alpha$H protons to the side chain protons. For this reason, experiments that also demonstrate indirect or relayed through-bond connectivities, for example between the NH and C$^\beta$H protons, are invaluable. In this respect, the most useful experiment is the HOHAHA experiment (*16*) (also referred to as TOCSY for *to*tal *c*orrelated *s*pectroscop*y* (*25*)). By adjusting the experimental mixing time, one can obtain successively direct, single, double, and multiple relayed connectivities. Further, the multiplet components of the cross-peaks are all in-phase in HOHAHA spectra, in contrast to COSY type spectra where they are in antiphase. As a result, the HOHAHA experiment is in general more sensitive and affords better resolution than the COSY type experiment. A schematic representation of cross-peak patterns observed in HOHAHA spectra for the various spin systems is illustrated in Figure 6. Examples of protein HOHAHA spectra in H_2O and D_2O are shown in Figure 7.

Once a few spin systems have been identified, one can then proceed to identify sequential through-space connectivities involving the NH, C$^\alpha$H, and C$^\beta$H protons by means of two-dimensional NOE spectroscopy (NOESY). For the purpose of sequential assignment the most important connectivities are the C$^\alpha$H(*i*)-NH (*i* + 1, 2, 3, 4), C$^\beta$H(*i*)-NH(*i* + 1), NH(*i*)-NH(*i* + 1), and C$^\alpha$H(i)-C$^\beta$H(*i* + 3) NOEs. This is illustrated schematically in Figure 8 and an example of a NOESY spectrum is shown in Figure 9.

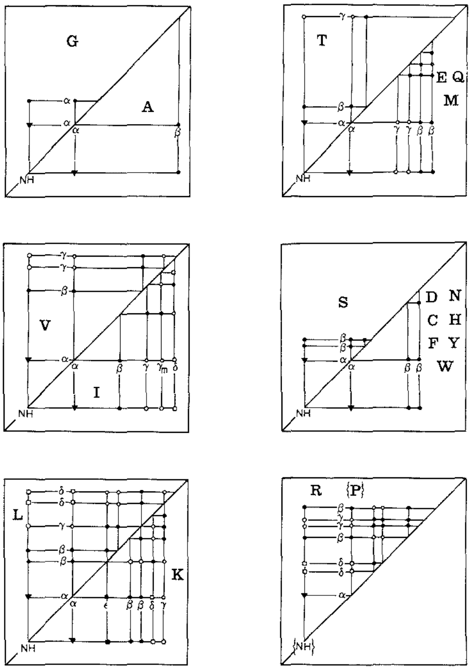

Figure 6. Schematic representation of cross-peak patterns observed in HOHAHA spectra for various amino acid spin systems. In a COSY spectrum, only direct connectivities are observed.

In the case of large molecules where the NH proton resonances are broad, the sensitivity of the conventional COSY spectrum can be improved by a factor of ~2 by recording a ^{15}N-filtered COSY spectrum (*26*) (also known as PS-COSY for *p*seudo *s*ingle quantum COSY). Labeling the protein uniformly with ^{15}N allows for efficient generation of heteronuclear zero and double quantum coherences whose relaxation rates, to a first-order approximation, are not affected by heteronuclear dipolar coupling. This permits one to eliminate one of the major line broadening mechanisms for amide protons in proteins, namely heteronuclear dipolar coupling to the nitrogen nucleus. As a result the multiple quantum resonances are significantly narrower than the corresponding NH resonances. The ^{15}N chemical shift contribution is easily removed from the multiple quantum frequency, yielding spectra that are similar in appearance to a regular COSY spectrum apart from the line narrowing of the NH resonances.

As proteins get larger, problems associated with chemical shift dispersion become increasingly severe. One approach for alleviating such problems in the sequential assignment of proteins involves correlating proton–proton through-space and through-bond connectivities with the chemical shift of a directly bonded NMR active nucleus such as ^{15}N or ^{13}C. In the case of completely ^{15}N labeled protein, two sorts of experiments are particularily useful. The first are relayed experiments combining the heteronuclear multiple quantum coherence scheme (*27–31*) with experiments such as NOESY,

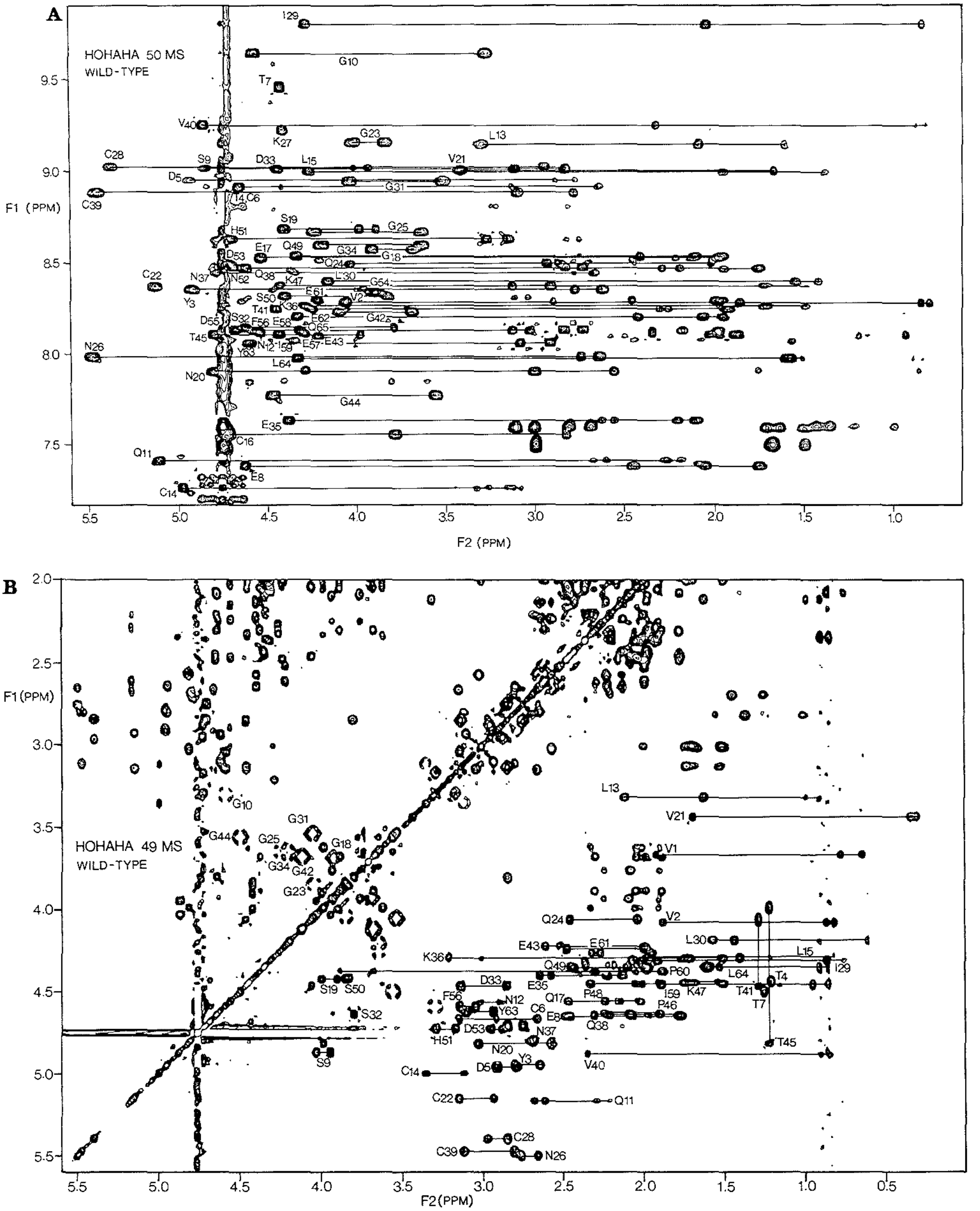

Figure 7. 600-MHz HOHAHA spectrum of hirudin in H_2O showing the NH(F2)–aliphatic(F1) region of the spectrum. Peaks are labeled at the positions of the direct NH–C^{α}H connectivities (A). 600-MHz HOHAHA spectrum of hirudin in D_2O showing the C^{α}H(F1)–aliphatic(F2) region of the spectrum. A number of spin systems are indicated (B) (ref 50).

COSY, or HOHAHA (Figure 10) (*32*). These experiments yield the same information as the homonuclear NOESY, COSY, and HOHAHA experiments but the NH proton chemical shift axis is replaced by that of the ^{15}N chemical shift. Because it is rare to find that both the ^{1}H and ^{15}N chemical shifts of two NH groups are degenerate, NOEs and through-bond correlations involving NH protons with the same chemical shift can readily be resolved in this manner. The second type of experiment involves the detection of long range correlations between ^{15}N and C^{α}H atoms using ^{1}H-detected *h*eteronuclear *m*ultiple-*b*ond *c*orrelation (HMBC) spectroscopy (*33*). In particular, the observation of two-bond $^{15}N(i)$-$C^{\alpha}H(i)$ and three-bond $^{15}N(i)$-$C^{\alpha}H(i-1)$ correlations enables one to connect one residue with the next (*34*). Additionally, because

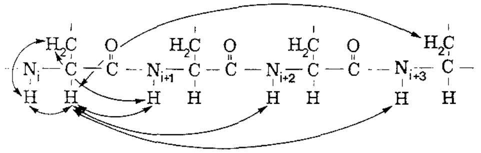

Figure 8. Schematic illustration of the connectivities used for sequential resonance assignment of protein spectra.

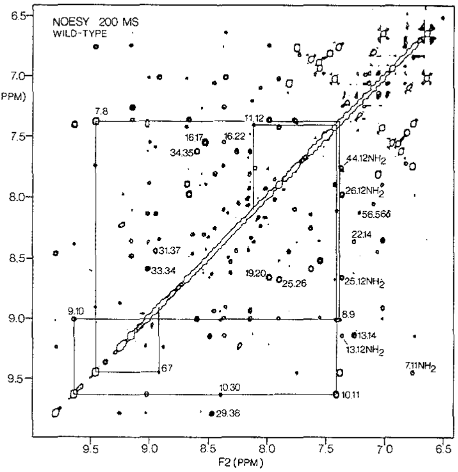

Figure 9. 600-MHz NOESY spectrum of hirudin in H_2O showing the NH(F1)-NH(F2) region of the spectrum. A stretch of NH(i)-NH(i + 1) connectivities extending from residues 6 to 12 is indicated. In addition several long-range NOEs are marked (ref 50).

the size of the ^{15}N(i)-C$^\alpha$H(i − 1) coupling is very sensitive to the Ψ backbone torsion angle, qualitative structural information can readily be derived.

A further avenue for large proteins involves the application of three-dimensional NMR. For ^{15}N 3D spectra, the normal rules for making sequence specific assignments can be readily applied. The only difference to the normal 2D case is that connections between one residue and the next must be made not only between different sets of peaks but also between different planes of the spectrum. The major advantage going from 2D to 3D is that the distribution of overlapping or closely spaced cross-peaks throughout the entire cube removes most of the ambiguities present in the 2D spectrum. A comparison of the ^{15}N edited 2D spectra with slices from the corresponding 3D spectra is presented in Figure 11, demonstrating the dramatic reduction in the number of cross-peaks. Combining such slices from a 3D ^{15}N NOESY-HMQC spectrum with those of a ^{15}N HOHAHA-HMQC spectrum allows the straightforward sequential assignment by hopping from one pair of HOHAHA/NOESY planes to another pair, connecting them either via C$^\alpha$H(i)-NH(i + 1) or NH(i)-NH(i + 1) NOEs in the same manner as for the 2D case. This is illustrated for a stretch of residues for the protein interleukin-1β in Figure 12.

IDENTIFICATION OF REGULAR SECONDARY STRUCTURE ELEMENTS

Because each type of secondary structure element is characterized by a particular pattern of short range ($|i - j| \leq 5$) NOEs (*22, 35*), qualitative interpretation of the sequential NOEs allows the identification of regular secondary structure elements. This is illustrated in Figure 13. Thus, for example, helices are characterized by a stretch of strong or medium NH(i)-NH(i + 1) NOEs and medium or weak C$^\alpha$H(i)-NH(i + 3) and C$^\alpha$H(i) - C$^\beta$H(i + 3) NOEs and C$^\alpha$H(i) - NH(i + 1) NOEs, sometimes supplemented by NH(i) - NH(i + 2) and C$^\alpha$H(i) - NH(i + 4) NOEs. Strands, on the other hand, are characterized by very strong C$^\alpha$H(i) - NH(i + 1) NOEs and by the absence of other short-range NOEs involving the NH and C$^\alpha$H protons. β sheets can be identified and aligned from interstrand NOEs involving the NH, C$^\alpha$H, and C$^\beta$H protons. It should also be pointed out that the identification of secondary structure elements is aided by NH exchange data, in so far that slowly exchanging NH protons are usually involved in hydrogen bonding, and by $^3J_{\mathrm{HN}\alpha}$ coupling constant data. Figure 14 illustrates the application of this method to the protein interleukin-8 (*36*). Inspection of the short range NOE data immediately enables one to identify three β strands, several turns, and a long helix at the carboxy terminus.

Several factors should be borne in mind in assessing the accuracy of secondary structure elements deduced by using this approach. Essentially it is a data based approach in so far that the expected patterns of short range NOE connectivities for different secondary structure elements have been derived by examining the values of all the short range distances involving the NH, C$^\alpha$H, and C$^\beta$H protons in regular secondary structure elements present in protein X-ray structures. Thus, it tends to perform relatively poorly in regions of irregular structure such as loops. In addition, the exact start and end of helices tend to be rather ill-defined, particularly as the pattern of NOEs for turns is not all too dissimilar from that present in helices. Thus, a turn at the end of a helix could be misinterpreted as still being part of the helix. In the case of β sheets, the definition of the start and end is more accurate as the alignment is accomplished from the interstrand NOEs involving the NH and C$^\alpha$H protons. Therefore, although this secondary structure delineation is a very easy and straightforward procedure, it can only be used in a qualitative fashion and accurate positioning of the identified secondary structure elements can be only accomplished after the complete 3D protein structure has been determined.

INTERPROTON DISTANCES RESTRAINTS

The initial slope of the time-dependent NOE, $N_{ij}(t)$, between two protons i and j is equal to the cross-relaxation rate σ_{ij} between the two protons (*37*)

$$\left.\frac{\mathrm{d}N_{ij}}{\mathrm{d}t}\right|_{t=0} = \sigma_{ij} \qquad (1)$$

σ_{ij} is simply the rate constant for exchange of magnetization between the two protons. σ_{ij}, in turn, is proportional to $\langle r_{ij}^{-6} \rangle$ and $\tau_{\mathrm{eff}}(ij)$, where r_{ij} is the distance between the two protons and $\tau_{\mathrm{eff}}(ij)$ the effective correlation time of the i-j vector:

$$\sigma_{ij} = \frac{\gamma^4 \hbar^2}{10 r_{ij}^6} \left(\tau_{\mathrm{eff}}(ij) - \frac{6\tau_{\mathrm{eff}}(ij)}{1 + 4\omega^2 \tau_{\mathrm{eff}}(ij)^2} \right) \qquad (2)$$

(γ is the gyromagnetic ratio of the proton, $\hbar$ is Planck's constant divided by 2π, and ω is the spectrometer frequency). It therefore follows that at short mixing times, τ_{m}, ratios of NOEs can yield either ratios of distances or actual distances, if one distance is already known, through the relationship

$$r_{ij}/r_{kl} = (\sigma_{kl}/\sigma_{ij})^{1/6} \qquad (3)$$

providing the effective correlation times for the two interproton vectors are approximately the same.

In practice, initial slope measurements are not entirely trivial. First the magnitude of the NOEs at very short mixing times are small, inevitably posing a single-to-noise problem. Second, the measured NOE at short mixing times may not

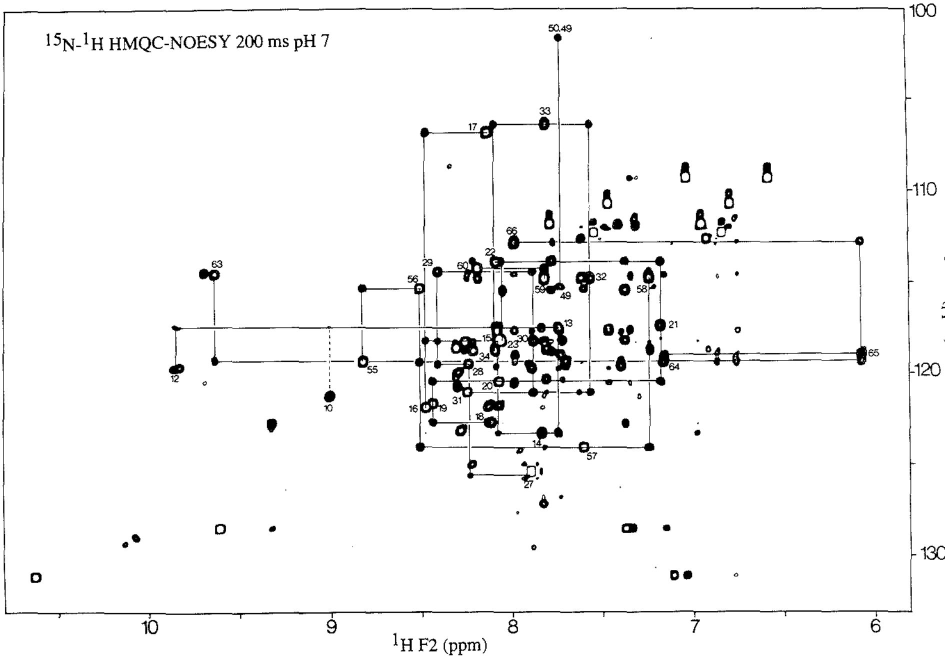

Figure 10. 600-MHz ^{15}N–^{1}H HMQC-NOESY spectrum of uniformly labeled ^{15}N Ner protein in H_2O. The ^{15}N(F1)–NH(F2) region of the spectrum with selected NH(*i*)–NH(*i* + 1) NOE connectivities is shown (ref 32).

reflect the true magnitude of the NOE due to the particularities of the experimental setup. In addition, problems arising from spin diffusion in large multispin systems introduce errors into the initial rate approximation. These can to some degree be minimized by carrying out a full relaxation matrix analysis (*38*), although certain problems still exist (*39*). For proteins, however, variations in effective correlation time will always present a problem if one wants to extract accurate interproton distances and it is therefore advisable to settle for only approximate interproton distance restraints. Because of the $\langle r^{-6}\rangle$ dependence of the NOE, such approximate interproton distance restraints can clearly be derived even in the presence of large variations in effective correlation times. Empirically, the type of classification generally used is one in which strong, medium, and weak NOEs correspond to distance ranges of approximately 1.8–2.7, 1.8–3.3, and 1.8–5.0 Å, where the lower limit of 1.8 Å corresponds to the sum of the van der Waals radii of two protons. By use of such a scheme, variations in effective correlations times do not introduce errors into the distance restraints. Rather, they only result in an increase in the estimated range for a particular interproton distance.

TORSION ANGLE RESTRAINTS

Vicinal spin–spin coupling constants can provide useful information supplementing the interproton distance restraints derived from NOE data. In particular, ranges of torsion angles can be estimated from the size of the coupling constants. The latter may be obtained by analyzing the multiplet patterns in COSY and COSY-like (e.g. DQF-COSY, E-COSY, PE-COSY, z-COSY) spectra.

The easiest coupling constants to determine in proteins are the $^{3}J_{\mathrm{HN}\alpha}$ coupling constants that can be obtained by simply measuring the peak-to-peak separation of the antiphase components of the C$^{\alpha}$H–NH COSY cross-peaks. The size of the $^{3}J_{\mathrm{HN}\alpha}$ coupling constant is related to the ϕ backbone torsion angle through a Karplus-type relationship (*40*). Consequently, values of $^{3}J_{\mathrm{HN}\alpha}$ <6 and >8 Hz correspond to ranges of −10° to −90° and −80° to −180°, respectively, for the ϕ backbone torsion angles. Considerable care, however, has to be taken in deriving ϕ backbone torsion angle ranges from apparent values of $^{3}J_{\mathrm{HN}\alpha}$ coupling constants measured in this way, as the minimum separation between the antiphase components of a COSY cross-peak is equal to approximately half of the NH line width (*41*). That is to say that small coupling constants can only be determined for relatively sharp resonances. This limitation can be overcome by measuring $^{3}J_{\mathrm{HN}\alpha}$ from ^{15}N HMQC-COSY/HMQC-J spectra (*42*) because of the significantly narrower multiple quantum line widths in these experiments.

χ_1 side chain torsion angle restraints and stereospecific assignments can be obtained by analyzing the pattern of $^{3}J_{\alpha\beta}$ coupling constants and the relative intensities of the intraresidue NOEs from the NH and C$^{\alpha}$H protons on the one hand to the two C$^{\beta}$H protons on the other, and in the case of valine to the C$^{\gamma}$H$_3$ protons. The $^{3}J_{\alpha\beta}$ coupling constants are related to the χ_1 torsion angle and are best measured from correlation spectra which yield reduced multiplets such as β-COSY, E-COSY, P.E.COSY, or z-COSY (*43*, *44*). In addition, under suitable conditions, they can be qualitatively assessed from the C$^{\alpha}$H–C$^{\beta}$H cross-peak shapes in HOHAHA spectra (*45*).

If both $^{3}J_{\alpha\beta}$ couplings are small (~3 Hz) then χ_1 must lie in the range 60 ± 60°. If, on the other hand, one of the $^{3}J_{\alpha\beta}$ couplings is large and the other small, χ_1 can lie either in the range 180 ± 60° or −60 ± 60°. These two possibilities are easily distinguished on the basis of short mixing time NOESY experiments which yield simultaneously stereospecific assignments of the β-methylene protons. Clearly, this approach may fail if a side chain has a mixture of conformations or the χ_1 angle deviates by more than ~40° from the staggered rotamer

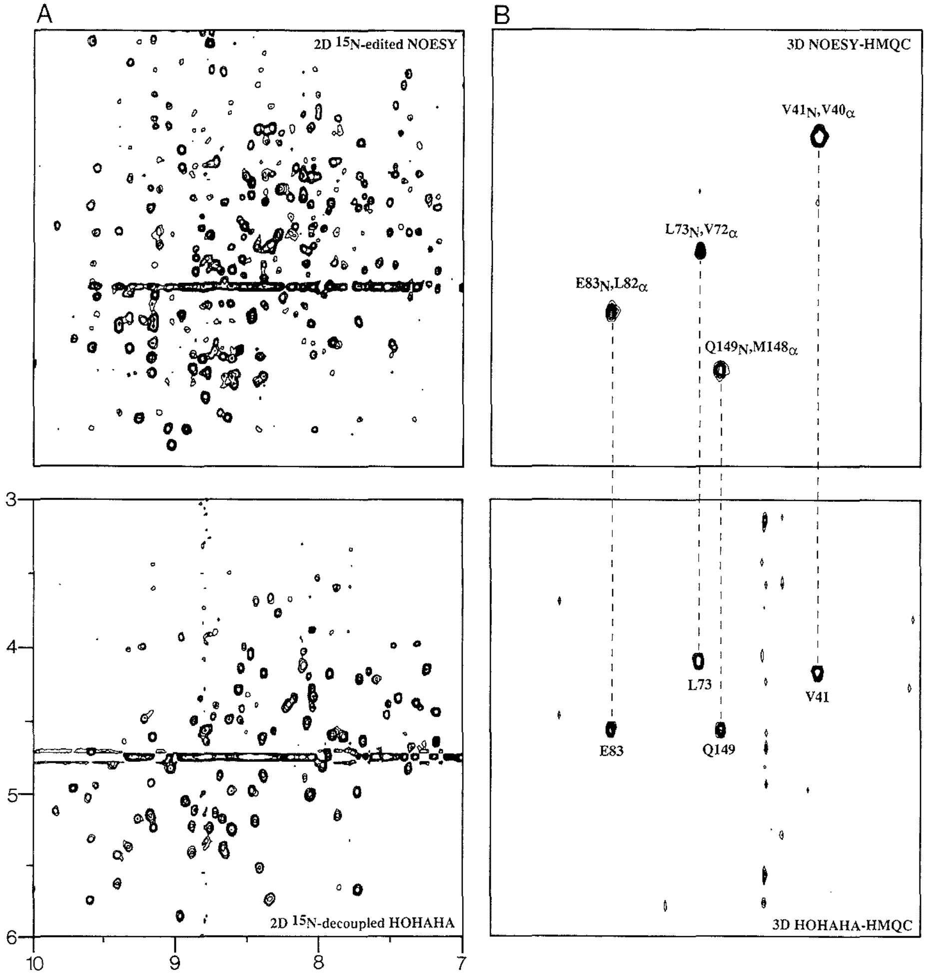

Figure 11. (A) Fingerprint regions of the ^{15}N-edited NOESY (upper) and ^{15}N decoupled HOHAHA (lower) spectra of uniformly ^{15}N labeled interleukin-1β. (B) Corresponding regions of a slice from the 3D heteronuclear NOESY-HMQC (upper) and HOHAHA-HMQC (lower) spectra of the protein under identical conditions (ref 7b).

conformations (60°, 180°, and −60°). In the former case, the coupling and NOE data will be mutually inconsistent, while in the latter, it may not be possible to make an unambiguous distinction between two rotamer conformations. Fortunately, analysis of high-resolution X-ray structures in the protein data bank has shown that 95% of all χ_1 angles lie within ±15° of the staggered rotamer conformations and that there is a very clear correlation between the values of χ_1 and the degree of refinement: the better refined the structures, the closer the χ_1 angles to the ideal staggered rotamer conformations. These results suggest that stereospecific assignments can be obtained for up to 80% of β-methylene protons using this simple approach. In practice, of course, the percentage of stereospecific assignments will be lower due to either spectral overlap or large line widths, preventing the determination of $^3J_{\alpha\beta}$ coupling constants.

A more rigorous approach for stereospecific assignment involves matching the observed $^3J_{HN\alpha}$ and $^3J_{\alpha\beta}$ coupling constants, together with approximate distances from the intraresidue $C^{\alpha}H$–$C^{\beta}H$ and NH–$C^{\beta}H$ NOEs and the interresidue $C^{\alpha}H(i-1)$–NH(i), $C^{\alpha}H(i)$–NH($i+1$), $C^{\beta}H(i-1)$–NH(i), and $C^{\beta}H(i)$–NH($i+1$) NOEs to theoretical values held in a data base which are derived either for all combinations of ϕ, Ψ, and χ_1 torsion angles (varied by 10°) in a model tripeptide segment or for tripeptide segments taken from high-resolution X-ray structures (*46, 53*). The data base search is carried out for both possible stereospecific assignments, and in those cases where only one of the two assignments satisfies the information in the data base, the correct stereospecific assignment, together with ranges for the ϕ, ψ, and χ_1 torsion angles, are obtained. A key advantage of this method is that it allows one to obtain much narrower limits for the ϕ, Ψ, and χ_1 torsion angle restraints than would otherwise be possible.

ASSIGNMENT OF LONG RANGE ($|i - j| > 5$) NOEs IN PROTEINS

In globular proteins the linear amino acid chain is folded into a tertiary structure such that protons far apart in the

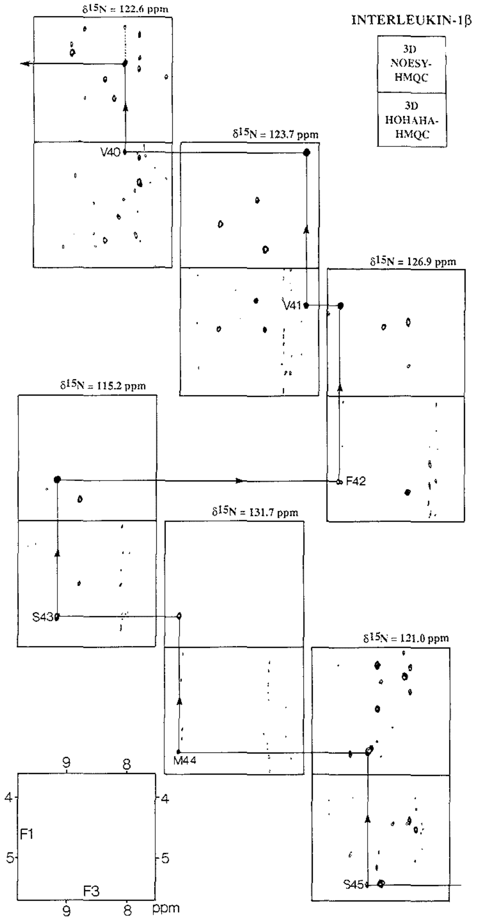

Figure 12. Demonstration of the sequential assignment procedure for the 3D spectra of interleukin-1β. Connectivities between neighboring amino acid spin systems are achieved by "plane hopping" through the 3D cube (ref 7b).

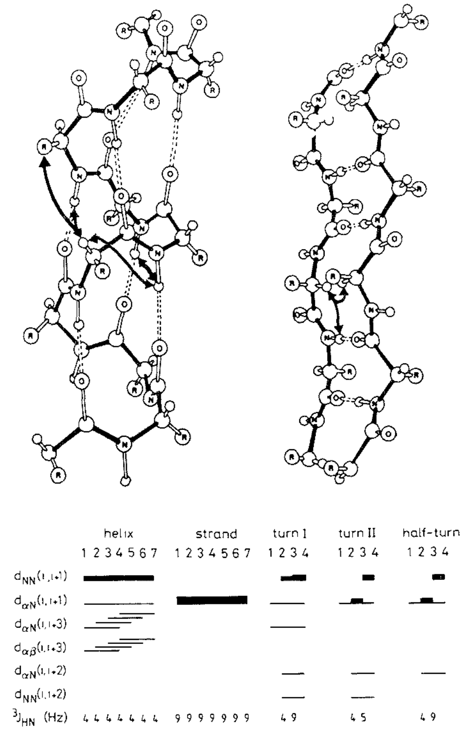

Figure 13. Characteristic patterns of short-range NOEs involving the NH, C$^{\alpha}$H, and C$^{\beta}$H protons seen in various regular secondary structure elements. The NOEs are classified as strong, medium, and weak, reflected in the thickness of the lines.

sequence may be close together in space. These protons give rise to tertiary NOEs whose identification is essential for determining the polypeptide fold. Once complete assignments have been made, many such long-range NOEs can be identified in a straightforward manner. It is usually the case, however, that the assignment of a number of long range NOE cross-peaks remains ambiguous due to resonance overlap. In some cases, this ambiguity can be removed by recording additional spectra. Where ambiguities still remain, it is often possible to resolve them by deriving a low-resolution structure on the basis of the available data (i.e. the secondary structure and the assignment of a subset of all the long-range NOEs) either by model building or by distance geometry calculations. This low-resolution structure can then be used to test possible assignments of certain long-range NOEs. For larger proteins it becomes increasingly difficult to assign tertiary NOEs because of the associated overlap problems. In these cases the 3D approach will become a necessity, in particular ^{13}C 3D experiments since they allow editing with respect to particular side chain positions for which the individual NOEs can then be extracted. In Figure 15 all experimental short- and intermediate-range NOE restraints (A) as well as all long-range NOE restraints (B) that were measured from the NOESY spectra are shown as dotted lines superimposed on the framework of the finally determined structure of hirudin, illustrating the dense network of distances throughout the protein core.

TERTIARY STRUCTURE DETERMINATION

Several different approaches can be used to determine the three-dimensional structure of a protein from experimental NMR data. The simplest approach, at least conceptually, is model building. This can be carried out either with real models or by means of interactive molecular graphics. It suffers, however, from the disadvantage that no unbiased measure of the size of the conformational space consistent with the NMR data can be obtained. Consequently, there is no guarantee that the modeled structure is the only one consistent with the experimental data. Further, in this way nothing more than a very low resolution structure can be obtained. Nevertheless, model building can play an important role in the early stages of a structure determination, particularly with respect to resolving ambiguities in the assignments of some of the long-range NOEs.

The main computational methods for generating structures from NMR data comprise as common feature a conformational search to locate the global minimum of a target function that is made up of stereochemical and experimental NMR restraints. The descent to the global minimum region is not a simple straightforward path as the target function is

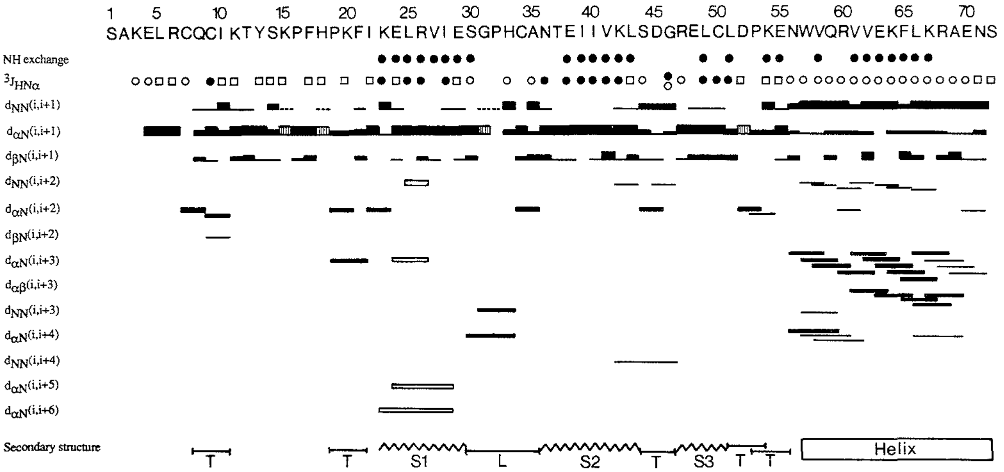

Figure 14. Pattern of short-range NOEs involving the NH, $C^{\alpha}H$, and $C^{\beta}H$ protons, as well as the $C^{\delta}H$ protons, for interleukin-8. The intensities of the NOEs are indicated by the thickness of the lines. In addition, slowly exchanging backbone amide protons and values of $^3J_{HN\alpha}$ are indicated: $J \leq 7$ Hz (O); 7 Hz $< J <$ 9 Hz (□); $J \geq 9$ Hz (●). The secondary structure deduced from these data is shown at the bottom of the figure (ref 36).

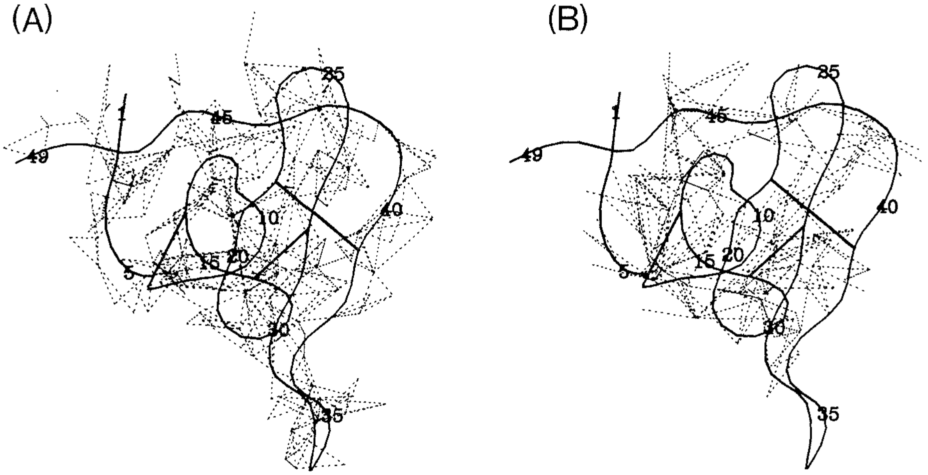

Figure 15. Short-range interresidue ($|i - j| \leq 5$) and intraresidue (A) and long-range interresidue ($|i - j| > 5$) NOE distance restraints (B) shown as dashed lines superimposed on a framework of the final hirudin structure in a smoothed backbone representation.

characterized by many false local minima that have to be avoided or surmounted by all the methods. There are essentially two general classes of methods. The first can be termed real space methods. These include restrained least-squares minimization in torsion angle space with either a variable target function (*9*) or a sequence of ellipsoids of constantly decreasing volume, each of which contains the minimum of the target function (*11*), and restrained molecular dynamics (*10*) and dynamical simulated annealing (*12, 13*) in Cartesian coordinate space. All real space methods require initial structures. These can be (i) random structures with correct covalent geometry; (ii) structures that are very far from the final structure (e.g. a completely extended strand); (iii) structures made up of a completely random array of atoms; and (iv) structures generated by distance space methods. They should not, however, comprise structures derived by model building as this inevitably biases the final outcome. Because these methods operate in real space, great care generally has to be taken to ensure that incorrect folding of the polypeptide chain does not occur. A new real space approach involving the use of dynamical simulated annealing, however, has succeeded in circumventing this problem (*13*). In contrast to the real space methods, the folding problem does not exist in the second class of methods which operates in distance space and is generally referred to as metric matrix distance geometry (*47*). Here the coordinates of the calculated structure are generated by a projection from $N(N - 1)/2$ dimensional distance space (where N is the number of atoms) into three-dimensional Cartesian coordinate space by a procedure known as embedding (see ref 48 for a comprehensive review).

A flow chart of the calculational strategy that is generally used to solve protein structures is shown in Figure 16. Since a detailed description of all the various methods would go far

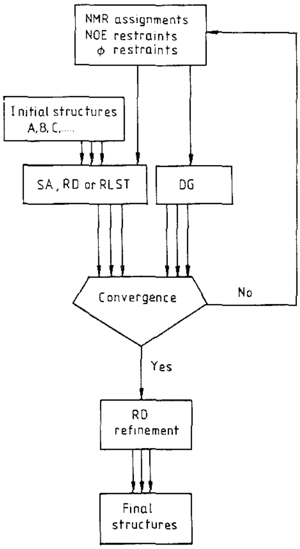

Figure 16. Calculational strategy used to solve three-dimensional structures of macromolecules on the basis of NMR data.

beyond the scope of this review, the interested reader is referred to the references cited above. (A comparison between the different methods is given in ref 49.) All the methods are comparable in convergence power. In general, however, the structures generated by dynamical simulated annealing or refined by restrained molecular dynamics tend to be better in energetic terms than the structures generated by the other methods, particularly with respect to nonbonded contacts and agreement with the experimental NMR data.

In order to assess the uniqueness and the precision of the structures determined by any of the above methods, it is essential to calculate a reasonable number of structures with the same experimental data set, but different starting structures or conditions, and examine their atomic root mean square distribution. If these calculations result in several different folds of the protein while satisfying the experimental restraints, then the data are not sufficient to determine a unique structure and either more data have to be gathered or the structure determination abandoned. If, however, convergence to a single fold is achieved with only small deviations from idealized covalent geometry, exhibiting good nonbonded contacts in addition to satisfying the experimental restraints, then one can be confident that a realistic and accurate picture of the solution structure of the protein has been obtained. The spread observed in the superposition within the family of structures or a plot of the root mean square distribution with respect to the mean allows one to assess the precision associated with different regions of the protein.

EXAMPLES

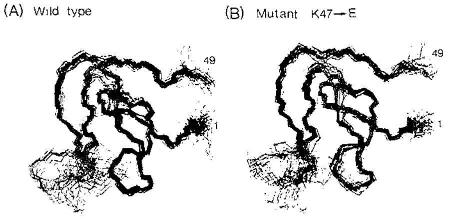

Figure 17. Superposition of the backbone (N, C^{α}, C) atoms of 32 dynamical simulated annealing structures of wild-type hirudin (A) and the Lys-47→Glu mutant (B) for the first 49 amino acids. The wild-type and mutant structures were calculated on the basis of 701 and 677 interproton distance restraints, respectively, 26 ϕ, and 18 χ_1 torsion angle restraints (ref 50).

1. Hirudin. Hirudin is a small 65-residue protein from the leech and is the most potent natural inhibitor of coagulation known. It acts by interacting specifically with α-thrombin, thereby preventing the cleavage of fibrinogen. Two recombinant hirudin variants have been examined by NMR: namely wild-type hirudin and the Lys-47 → Glu mutant (*50*). Analysis of the NMR data indicated that hirudin consists of a N-terminal compact domain (residues 1–49) held together by three disulfide bonds and a disordered C-terminal tail (residues 50–65). Evidence for the presence of a flexible C-terminal tail was provided by the absence of any intermediate-range or long-range NOEs beyond amino acid 49. Therefore structure calculations were restricted to the N-terminal domain using the hybrid distance geometry–dynamical simulated annealing method. Experimental input data consisted of 701 and 677 approximate interproton distance restraints derived from NOE data for the wild-type and mutant hirudin, respectively, 26 ϕ backbone and 18 χ_1 torsion angle restraints derived from NOE and three-bond coupling constant data, and 8 backbone hydrogen bonds identified on the basis of NOE and amide exchange data. A total of 32 structures were computed for both the wild-type and mutant hirudins (Figure 17). The structure of residues 2–30 and 37–48 constitute the core of the N-terminal domain formed by a triple stranded antiparallel β sheet, and the atomic root mean square difference between the individual structures and the mean structure is ~0.7 Å for the backbone atoms and ~1 Å for all atoms. The orientation of the exposed finger of antiparallel β sheet (residues 31–36) with respect to the core could not be determined as no long range NOEs were observed between the exposed finger and the core. This is easily appreciated from Figure 17 since the structures in that region exhibit a very large spread. Locally, however, the polypeptide fold of residues 31–36 is reasonably well-defined.

The first five residues form an irregular strand which leads into a loop closed off at its base by the disulfide bridge between Cys-6 and Cys-14. This is followed by a mini-antiparallel β sheet formed by residues 14–16 (strand I) and 21 and 22 (strand I′) connected by a type II turn. This β sheet is distorted by a β bulge at Cys-16. Strand I′ leads into a second antiparallel β sheet formed by residues 27–31 (strand II) and 36–40 (strand II′) connected by a β turn (residues 32–35). Additionally, residues 10 and 11 exhibit features of a β bulge with the amide of Gly-10 and the carbonyl oxygen atom of Glu-11 hydrogen bonded to the carbonyl and amide groups, respectively, of Cys-28. Finally, strand II′ leads into an irregular strand which folds back onto the protein such that residue 47 (Lys in the wild type, Glu in the mutant) is in close proximity to residues in the loop closed off by the disulfide bridge between Cys-6 and Cys-14. Not only the backbone but also many of the side chain conformations are well-defined, especially those in the interior of the protein.

A superposition of the core (residues 1–30 and 37–49) of the restrained minimized mean structures of the wild-type and mutant hirudin provides a good representation of the differences between the two structures (Figure 18A). Regions of noticeable difference can be identified where the atomic root mean square difference between the two mean structures is larger than the atomic root mean square distribution of the individual structures about their respective means. This analysis indicates the presence of clear differences for the

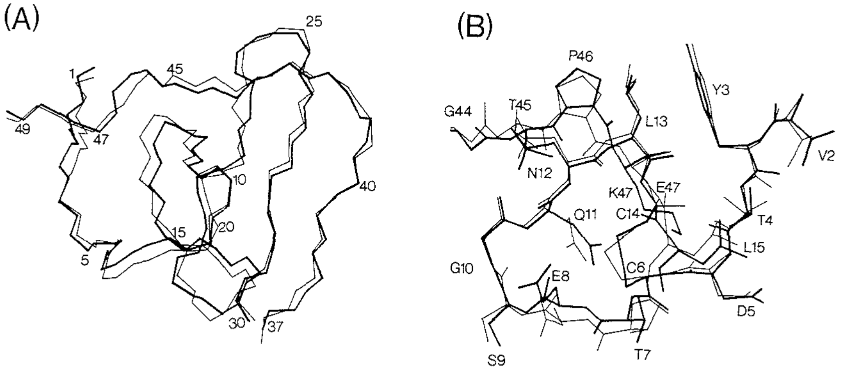

Figure 18. (A) Superposition of the core (residues 1–30 and 37–49) of the restrained minimized mean structure of wild-type (thick lines) and Lys-47→Glu mutant (thin lines) hirudin. (B) View of all atoms around the site of mutation (ref 50).

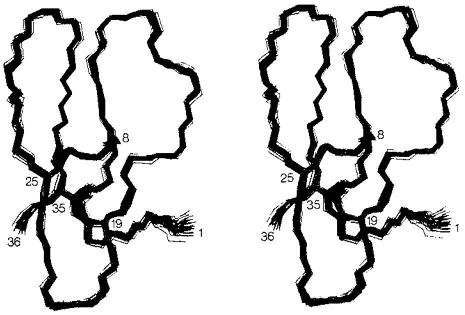

Figure 19. Superposition of the backbone (N, C^α, C) atoms of 41 dynamical simulated annealing structures of the C-terminal domain of CBH I (ref 53).

backbone atoms of residues 3, 5, 8, 11–15, 22, 26, and 27. In the mutant, the backbone atoms of residues 3, 4, and 11–15 are slightly closer to that of residues 45–47 than in the wild-type, a change which can be rationalized in terms of the shorter length of the Glu side chain relative to that of Lys. Concomitantly, the backbone of residue 8 appears to be pushed away in the wild type structure. Residues 22, 26, and 27 also move in the same direction as residues 11–15. This is secondary to the perturbation of residues 11–15 and can be attributed to the presence of numerous contacts between residues 8–11 on the one hand and 28–30 on the other, including hydrogen bonds between Cys-28 and Gly-10 and between Cys-28 and Glu-11. There seems to be no significant differences, however, with respect to the side chain positions within the errors of the coordinates, even within the immediate vicinity of residue 47 (Figure 18B).

At this point it may be worth mentioning that NMR can have two important applications with respect to genetically engineered proteins. The structural studies on hirudin were first initiated by using natural protein extracted from the whole body of leeches (*51*). All further work was subsequently carried out on recombinant products, either comprising the wild-type sequence or mutants thereof (*50*). It was a fast and easy task to assess the structural identity of the recombinant product, since only a comparison of the appropriate 2D spectra had to be carried out. These spectra can be regarded as a fingerprint of a particular protein and, hence, a reflection of the 3D structure in solution. Simple overlay often allows one to ascertain whether the recombinant product is folded indistinguishably from the natural counterpart. In the same way, NMR can establish whether the structure of a mutant is essentially unchanged from the wild type one, since very similar spectra will arise from closely related structures. Analyses of this kind can be carried out without a full assignment of the spectra or a complete structure calculation, thus providing a useful tool for guiding genetic engineering projects.

2. Cellulose Binding Domain of Cellobiohydrolase. Cellulases are enzymes involved in plant cell wall degradation that exhibit a common domain structure consisting of a catalytic domain (~400–500 amino acids), a highly conserved (~70% sequence identity) terminal domain (~40 amino acids) that is located either at the C terminus or N terminus, and a heavily glycosylated linker region (~30 amino acids), which connects the two domains. The domain architecture of the cellulases as well as the observation that the domains of CBH I retain their respective activities after cleavage suggested a dual approach to the problem of obtaining a three-dimensional structure of this cellulase, involving the application of both NMR and X-ray crystallography. To date there has been no success in the crystallization of an intact cellulase, whereas crystals of the catalytic domain of CBH II have been obtained (*52*), opening the possibility for determining its X-ray structure. The cellulose binding domain being a very small polypeptide, on the other hand, seemed ideally suited for a structure determination by NMR. Because of its small size it was possible to chemically synthesize the 36 amino acid domain and it was established that the biological properties were identical to those of the cleavage product. The subsequent NMR structure determination (*53*) was therefore carried out on the synthetic product and a large number of stereospecific assignments obtained by using the data base approach resulted in numerous interproton distance and torsion angle restraints. Thus an exceptionally large experimental data set consisting of 554 interproton distance restraints, 33ϕ, 24Ψ, and $25\chi_1$ torsion angle restraints, and 42 hydrogen bonding restraints was used in the structure determination. The converged set of 41 structures represents the best quality NMR structure to date, exhibiting a root mean square difference between the individual structures and the mean coordinate positions of 0.33 Å for the backbone atoms and 0.52Å for all atoms. It was possible to determine the pairing of the two disulfide bridges, which previously was unknown. A backbone trace of the CBH I structure is shown in Figure 19 and several regions including the amino acid side chains are displayed in Figure 20. The protein has a wedgelike shape with an amphiphilic character, one face being predominantly hydrophobic and the other mainly hydrophilic. As can be readily appreciated from Figures 19 and 20, the quality

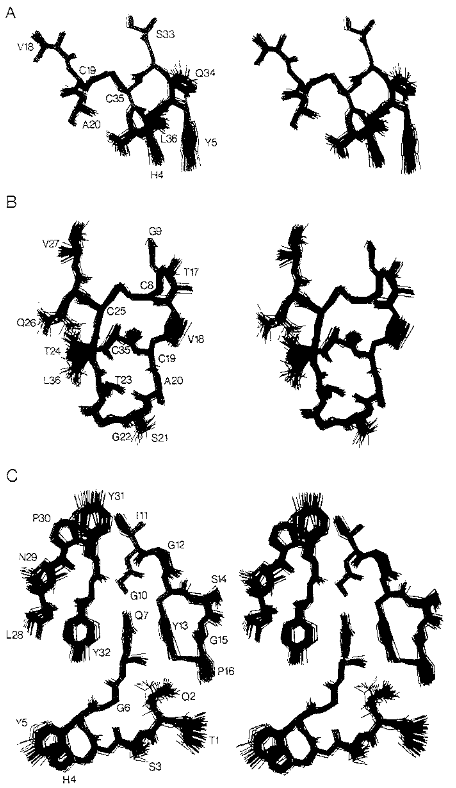

Figure 20. Best fit superpositions (41 structures) of all atoms for three selected regions of the C-terminal domain of CBH I illustrating the excellent definition of side chain positions (ref 53).

of this structure is comparable to a crystal structure at approximately 2–2.5 Å resolution, and such structures permit the detailed analysis of side chain–side chain interactions and other possibly interesting structural features.

PERSPECTIVE AND CONCLUDING REMARKS

It should be clear from the above discussion that NMR now stands side by side with X-ray crystallography as a powerful method for three-dimensional structure determination. What are the limitations of this approach? At present it is limited to proteins of molecular weight ≤20 000. Indeed the largest proteins whose three-dimensional structures have been determined to date are plastocyanin (99 residues (*54*)), the globular domain of histone H5 (79 residues (*55*), α-amylase inhibitor (74 residues (*56*)), and interleukin-8 (a dimer of 72 residues per monomer (*57*)). Virtually complete assignments, however, have been made for a variety of larger systems, in particular hen egg white lysozyme (129 residues (*58*)) and the lac repressor headpiece–operator complex (molecular weight ~15 000 (*59*)), *Staphylococcal* nuclease (148 residues (*60*)), and interleukin-1β (153 residues (*61*)). Further development of novel techniques based on multidimensional NMR in combination with isotopic labeling and the introduction of yet more powerful magnets may make it possible to extend the molecular weight range up to proteins of molecular weight ~40 000 in the future. This, however, will probably present a fundamental limit as the large line widths of such proteins significantly reduce even the sensitivity of ^{1}H-detected heteronuclear correlation experiments.

At this point it is appropriate to add a word of caution concerning the practical limits of structure determination by NMR. It is not always the size or the number of residues in a particular protein that determines the feasibility of an NMR structure determination. Other factors play equally important roles. For example, the protein should be soluble up to millimolar concentrations, nonaggregating, and preferably stable up to at least 40 °C, particularly for large proteins. A further consideration is the chemical shift dispersion of the ^{1}H NMR spectrum. This depends to a large extent on the structure of the protein under investigation. Proteins that are made up only of α-helices, loops and turns, invariably exhibit fairly poor proton chemical shift dispersion, while the chemical shift dispersion in β-sheet proteins is usually very good. To a certain degree such problems associated with chemical shift degeneracy can be overcome by heteronuclear 3D experiments.

Another potential problem may arise from the fact that different regions or domains of a protein may be well-defined and therefore amenable to a NMR structure determination, while other parts of the same protein may not. This will be reflected in the absence of long-range tertiary NOEs for the ill-defined regions and leads to the inability to position these regions with respect to the rest of the protein satisfactorily (e.g. the case of hirudin discussed above). We therefore believe that it is necessary to calculate a reasonable number of structures (ca. 20) with the same experimental data set in order to obtain a good representation of the NMR structure. Only by analyzing such a family of structures can the local and global definition of a structure be assessed.

X-ray crystallography, of course, also has its limitations, the most obvious being the requirement for a protein to crystallize. Thus suitable crystals that diffract to high resolution have to be grown and a successful search for heavy atom derivatives to solve the phase problem is necessary. Therefore not every protein will be amenable to both NMR and X-ray crystallography. In those cases where this is feasable, the information afforded by NMR and crystallography is clearly complementary and may lead to a deeper understanding of the differences between the solution and crystalline state of the protein.

Finally it should be stressed that, in addition to being able to determine three-dimensional structures of proteins, NMR has the potential to address other questions, in particular those concerning the dynamics of the system. This opens the possibility that a whole variety of different NMR studies can be initiated on the basis of an NMR structure, such as the investigation of the dynamics of conformational changes upon ligand binding, unfolding kinetics, conformational equilibria between different conformational states, fast internal dynamics on the nanosecond time scale and below, and slow internal motions on the second and millisecond time scales. The results obtained from these kinetic studies can then be interpreted in the light of the previously determined structure, thus bringing together structure and dynamics of proteins in a unified picture.

ACKNOWLEDGMENT

The work in the authors' laboratory was supported in part by the AIDS targeted Anti-Viral Program of the Office of the Director of the National Institutes of Health.

LITERATURE CITED

(1) Jeener, J., Ampere International Summer School, Basko Polje, Yugoslavia, 1971, unpublished lecture.
(2) Aue, W. P.; Bartholdi, E.; Ernst, R. R. *J. Chem. Phys.* **1976**, *64*, 2229.
(3) Jeener, J.; Meier, B. H.; Bachmann, P.; Ernst, R. R. *J. Chem. Phys.* **1979**, *71*, 4546.
(4) Oschkinat, H.; Griesinger, C.; Kraulis, P. J.; Sørensen, O. W.; Ernst, R. R.; Gronenborn, A. M.; Clore, G. M. *Nature (London)* **1988**, *332*,

374–377. Oschkinat, H.; Cieslar, C.; Holak, T. A.; Clore, G. M.; Gronenborn, A. M. *J. Magn. Reson.* **1989**, *83*, 450.

(5) Vuister, G. W.; Boelens, R.; Kaptein, R. *J. Magn. Reson.* **1988**, *80*, 176–185.

(6) Fesik, S. W.; Zuiderweg, E. R. P. *J. Magn. Reson.* **1988**, *78*, 588–593. Zuiderweg, E. R. P.; Fesik, S. W. *Biochemistry* **1989**, *28*, 2387.

(7) Marion, D.; Kay, L. E.; Sparks, S. W.; Torchia, D. A.; Bax, A. *J. Am. Chem. Soc.* **1989**, *111*, 1515. Marion, D.; Driscoll, P. C.; Kay, L. E.; Wingfield, P. T.; Bax, A.; Gronenborn, A. M.; Clore, G. M. *Biochemistry* **1989**, *28*, 6150.

(8) Havel, T. F.; Kuntz, I. D.; Crippen, G. M. *Math. Biol.* **1983**, *45*, 665. Havel, T. F.; Wüthrich, K. *Bull. Math. Biol.* **1984**, *46*, 673.

(9) Braun, W.; Go, N. *J. Mol. Biol.* **1985**, *186*, 611.

(10) Clore, G. M.; Gronenborn, A. M.; Brünger, A. T.; Karplus, M. *J. Mol. Biol.* **1985**, *186*, 435. Kaptein, R.; Zuiderweg, E. R. P.; Scheek, R. M.; Boelens, R.; van Gunsteren, W. F. *J. Mol. Biol.* **1985**, *182*, 179. Clore, G. M.; Brünger, A. T.; Karplus, M.; Gronenborn, A. M. *J. Mol. Biol.* **1986**, *191*, 523.

(11) Billeter, M.; Havel, T. F.; Wüthrich, K. *J. Comput. Chem.* **1987**, *8*, 132.

(12) Nilges, M.; Gronenborn, A. M.; Clore, G. M. *FEBS Lett.* **1988**, *229*, 317. Nilges, M.; Gronenborn, A. M.; Brünger, A. T.; Clore, G. M. *Protein Eng.* **1988**, *2*, 27.

(13) Nilges, M.; Clore, G. M.; Gronenborn, A. M. *FEBS Lett.* **1988**, *239*, 129.

(14) Litharge, O.; Cornelius, C. W.; Buchanan, B. G.; Jardetzky, O. *Proteins: Struct., Funct. Genet.* **1987**, *2*, 340.

(15) Ernst, R. R.; Bodenhausen, G.; Wokaun, A. *Principles of Nuclear Magnetic Resonance in One and Two Dimensions*: Clarendon Press: Oxford, 1986.

(16) Davis, D. G.; Bax, A. *J. Am. Chem. Soc.* **1985**, *107*, 2821. Bax, A.; Davis, D. G. *J. Magn. Reson.* **1985**, *65*, 355. Bax, A. In *Methods in Enzymology*; James, T. L., Oppenheimer, N., Eds.; Academic Press: New York, 1988; Vol. 176, p 151.

(17) Macura, S.; Ernst, R. R. *Mol. Phys.* **1980**, *41*, 95. Macura, S.; Huang, Y.; Suter, D.; Ernst, R. R. *J. Magn. Reson.* **1981**, *43*, 259.

(18) Griesinger, C.; Sørensen, O. W.; Ernst, R. R. *J. Magn. Reson.* **1989**, *84*, 14.

(19) Overhauser, A. *Phys. Rev.* **1953**, *89*, 689. Overhauser, A. *Phys. Rev.* **1953**, *92*, 411.

(20) Solomon, I. *Phys. Rev.* **1955**, *99*, 559.

(21) Noggle, J. H.; Schirmer, R. E. *The Nuclear Overhauser Effect—Chemical Applications*; Academic Press: New York, 1971.

(22) Wüthrich, K. *NMR of Proteins and Nucleic Acids*; J. Wiley: New York, 1986.

(23) Rance, M.; Sørenson, O. W.; Bodenhausen, G.; Wagner, G.; Ernst, R. R.; Wüthrich, K. *Biochem. Biophys. Res. Commun.* **1983**, *117*, 479.

(24) Marion, D.; Bax, A. *J. Magn. Reson.* **1988**, *79*, 352.

(25) Braunschweiler, L.; Ernst, R. R. *J. Magn. Reson.* **1983**, *53*, 521.

(26) Bax, A.; Kay, L. E.; Sparks, S. W.; Torchia, D. L. *J. Am. Chem. Soc.* **1989**, *111*, 408.

(27) Mueller, L. *J. Am. Chem. Soc.* **1979**, *101*, 4481.

(28) Redfield, A. G. *Chem. Phys. Lett.* **1983**, *96*, 537. Griffey, R. H.; Redfield, A. G. *Q. Rev. Biophys.* **1987**, *19*, 51.

(29) Bax, A.; Griffey, R. H.; Hawkins, B. L. *J. Am. Chem. Soc.* **1983**, *105*, 7188.

(30) Bolton, P. H.; Bodenhausen, G. *Chem. Phys. Lett.* **1982**, *89*, 139.

(31) Sklenar, V.; Bax, A. *J. Magn. reson.* **1987**, *71*, 379.

(32) Gronenborn, A. M.; Bax, A.; Wingfield, P. T.; Clore, G. M. *FEBS Lett.* **1989**, *243*, 93. Gronenborn, A. M.; Wingfield, P. T.; Clore, G. M. *Biochemistry* **1989**, *28*, 5081.

(33) Bax, A.; Summers, M. F. *J. Am. Chem. Soc.* **1986**, *108*, 2093. Bax, A.; Marion, D. *J. Magn. reson.* **1988**, *78*, 186.

(34) Clore, G. M.; Bax, A.; Wingfield, P. T.; Gronenborn, A. M. *FEBS Lett.* **1988**, *238*, 17.

(35) Wüthrich, K., Wider, G., Wagner, G. and Braun, W. *J. Mol. Biol.* **1982**, *155*, 311. Billeter, M.; Braun, W.; Wüthrich, K. *J. Mol. Biol.* **1982**, *155*, 321. Wagner, G.; Wüthrich, K. *J. Mol. Biol.* **1982**, *155*, 347. Wüthrich, K.; Billeter, M.; Braun, W. *J. Mol. Biol.* **1984**, *180*, 715.

(36) Clore, G. M.; Appella, E.; Yamada, M.; Matsushima, K.; Gronenborn, A. M. *J. Biol. Chem.*, in press.

(37) Wagner, G.; Wüthrich, K. *J. Magn. Reson.* **1979**, *33*, 675. Dobson, C. M.; Olejniczak, E. T.; Poulsen, F. M.; Ratcliffe, R. G. *J. Magn. Reson.* **1982**, *48*, 97. Keepers, J. W.; James, T. L. *J. Magn. Reson.* **1984**, *57*, 404. Clore, G. M.; Gronenborn, A. M. *J. Magn. Reson.* **1985**, *61*, 158.

(38) Borgias, B. A.; James, T. L. *J. Magn. Reson.* **1988**, *79*, 493.

(39) Clore, G. M.; Gronenborn, A. M. *J. Magn. Reson.* **1989**, *84*, 398.

(40) Karplus, M. *J. Am. Chem. Soc.* **1963**, *85*, 2870. Pardi, A.; Billeter, M.; Wüthrich, K. *J. Mol. Biol.* **1984**, *180*, 741.

(41) Neuhaus, D.; Wagner, G.; Vasák, M.; Kägi, J. H. R.; Wüthrich, K. *Eur. J. Biochem.* **1985**, *151*, 257.

(42) Kay, L. E.; Bax, A. *J. Magn. Reson.*, in press. Forman-Kay, J. D.; Gronenborn, A. M.; Kay, L. E.; Wingfield, P. T.; Clore, G. M. *Biochemistry*, in press.

(43) Mueller, L. *J. Magn. Reson.* **1987**, *203*, 251.

(44) Oschkinat, H.; Pastore, A.; Pfändler, P.; Bodenhausen, G. *J. Magn. Reson.* **1986**, *69*, 559. Oschkinat, H.; Clore, G. M.; Nilges, M.; Gronenborn, A. M. *J. Magn. Reson.* **1987**, *75*, 534.

(45) Driscoll, P. C.; Clore, G. M.; Beress, L.; Gronenborn, A. M. *Biochemistry* **1989**, *28*, 2178.

(46) Nilges, M.; Clore, G. M.; Gronenborn, A. M. *Biopolymers*, in press.

(47) Crippen, G. M. *J. Comp. Phys.* **1977**, *24*, 96.

(48) Crippen, G. M.; Havel, T. F. *Distance Geometry and Molecular Conformation*; John Wiley: New York, 1988.

(49) Clore, G. M.; Gronenborn, A. M. *CRC Crit. Rev. Biochem.* **1989**, *24*, 479.

(50) Folkers, P. J. M.; Clore, G. M.; Driscoll, P. C.; Dodt, J.; Köhler, S.; Gronenborn, A. M. *Biochemistry* **1988**, *28*, 2601.

(51) Clore, G. M.; Sukumaran, D. K.; Nilges, M.; Zarbock, J.; Gronenborn, A. M. *EMBO J.* **1987**, *6*, 529.

(52) Bergfors, T.; Rouvinen, J.; Lehtovaara, P.; Caldentey, X.; Tomme, P.; Claeyssens, M.; Pettersson, G.; Teeri, T.; Knowles, J.; Jones, T. A. *J. Mol. Biol.* **1989**, *209*, 167.

(53) Kraulis, P. J.; Clore, G. M.; Nilges, M.; Jones, T. A.; Pettersson, G.; Knowles, J.; Gronenborn, A. M. *Biochemistry* **1989**, *28*, 7241.

(54) Moore, J. M.; Case, D. A.; Chazin, W. J.; Gippert, G. P.; Havel, T. F.; Powls, R.; Wright, P. E. *Science* **1988**, *240*, 314.

(55) Clore, G. M.; Gronenborn, A. M.; Nilges, M.; Sukumaran, D. K.; Zarbock, J. *EMBO J.* **1987**, *6*, 1833.

(56) Kline, A. D.; Braun, W.; Wüthrich, K. *J. Mol. Biol.* **1986**, *189*, 377. Kline, A. D.; Braun, W.; Wüthrich, K. *J. Mol. Biol.* **1988**, *204*, 675.

(57) Clore, G. M.; Appella, E.; Yamada, M.; Matsushima, K.; Gronenborn, A. M., submitted for publication.

(58) Redfield, C.; Dobson, C. M. *Biochemistry* **1988**, *27*, 122.

(59) Boelens, R.; Scheek, R. M.; Lamerichs, R. M. J. N.; de Vlieg, J.; van Boom, J. H.; Kaptein, R. *J. Mol. Biol.* **1987**, *193*, 213.

(60) Torchia, D. A.; Sparks, S. W.; Bax, A. *Biochemistry* **1988**, *27*, 5135.

(61) Driscoll, P. C.; Clore, G. M.; Marion, D.; Wingfield, P. T.; Gronenborn, A. M. *Biochemistry*, in press.

ARTICLES

Reduction of Reequilibration Time following Gradient Elution Reversed-Phase Liquid Chromatography

Lynn A. Cole[1] **and John G. Dorsey***[,1]

Department of Chemistry, University of Florida, Gainesville, Florida 32611

A simple and convenient method for the reduction of column reequilibration time following gradient elution reversed-phase liquid chromatography is described. This method utilizes the addition of a constant volume of 3% 1-propanol to the mobile phase throughout the solvent gradient to provide consistent solvation of the reversed-phase stationary phase. Reductions in reequilibration time of up to 78% have been observed. The effect of alkyl chain bonding density on reequilibration volume is also examined. A maximum in the mobile phase volume necessary to reequilibrate the column is found at a bonding density of about 2.9 μmol/m^2. The relationship of reequilibration volume to bonding density supports the partitioning model of retention for reversed-phase liquid chromatography.

INTRODUCTION

Gradient elution is the most common solution to the general elution problem in liquid chromatography (*1–4*). In reversed-phase liquid chromatography (RPLC) this technique involves increasing the percentage of an organic modifier with respect to an aqueous phase as the chromatographic run progresses. This time-dependent increase in mobile phase strength provides greater retention of early eluting compounds and decreases retention of late eluting compounds with respect to isocratic conditions, thus improving the limits of detection and peak shapes for later eluting compounds and providing more evenly spaced bands in the chromatogram. Practical and theoretical aspects of gradient elution have been thoroughly reviewed (*1, 2, 4–7*).

One problem commonly associated with gradient elution is the time required for reequilibration of the column to the starting gradient conditions following elution of the last compound in the chromatogram (*1, 2, 5*). As the mobile phase is varied during the course of the gradient, the stationary phase composition changes due to varying solvation of the bonded alkyl chains, thus making it necessary to flush the column with many volumes of the initial mobile phase to return the stationary phase to its original conditions. Generally it is believed that 15–20 column volumes of the starting mobile phase must be passed through the column to achieve column reequilibration (*2, 5*). Often this reequilibration time is as long as the sample elution time, thus doubling the time of analysis and the volume of solvent used and making gradient elution impractical for routine analysis (*2*). Several attempts have been made to understand and reduce column reequilibration time. Frenz and Horvath (*8*) found that column regeneration time may be reduced by passing a carefully chosen series of regenerating solvents through the column in order of decreasing affinity for the stationary phase. In a recent study of column reequilibration, Payne et al. (*9*) suggest that the rate-limiting steps in column regeneration are mass transfer into and diffusion of mobile phase components within the pores of the column and that column reequilibration time may be reduced by promoting these processes. Finally, a reverse-gradient may be employed to achieve column regeneration, although there does not appear to be a significant advantage to running a reverse-gradient over stepping from the final to the initial solvent conditions to achieve column reequilibration in reversed-phase systems (*5*).

The solvation structure of the stationary phase is an important factor in gradient elution, since changes in stationary phase composition make necessary excessive column reequilibration times. The solvation of RP stationary phases has been studied extensively. McCormick and Karger evaluated the extraction of the most hydrophobic component of the mobile phase into the stationary phase by using distribution isotherms (*10, 11*). Although this work predicts preferential expulsion of the least polar mobile phase constituent into the stationary phase, the stationary phase is considered to be inert with respect to the overall retention process. Yonker et al. showed the importance of various characteristics of the stationary phase to its solvation and developed models for the configuration of the stationary phase at different concentrations of organic modifier (*12, 13*). Gilpin and Gangoda (*14, 15*) and Marshall and McKenna (*16*) used solution NMR experiments to investigate solvent effects on the configuration of the bonded alkyl chains of the stationary phase and found that the configuration of the stationary phase is a function of the mobile phase composition. All of these studies (*10–16*) as well as others (*17–19*) demonstrate that the stationary phase is preferentially solvated by the organic component of the mobile phase. The changing solvation of the stationary phase during a gradient not only makes long

---

[1] Present address: Department of Chemistry, University of Cincinnati, Cincinnati, OH 45221-0172.

0003-2700/90/0362-0016$02.50/0

reequilibration times necessary but also introduces two nonideal processes for theoretical considerations. These nonideal processes are solvent demixing due to the preferential uptake of the organic modifier by the stationary phase and changes in column dead time due to changes in the stationary-phase composition (*20*).

It is apparent from these studies of stationary-phase solvation that in order to reduce column reequilibration time following gradient elution it is necessary to control the solvation of the bonded alkyl chains. The addition of a good wetting agent to the mobile phase has been shown to be valuable for altering the chromatographic properties of the stationary phase. Scott and Simpson (*21*) have shown that the addition of a small percentage of a short-chain alkanol (such as 1-propanol) to the mobile phase provides near monolayer coverage of the RP stationary phase. Their work showed that over 90% of the surface of the stationary phase is solvated by the alcohol when the mobile phase contains 3% (w/v) 1-propanol, but only about 50% of the surface is solvated with the same concentration of methanol. The addition of small percentages of short-chain alkanols to hydroorganic mobile phases has been used previously to improve the selectivity of separations. MacCrehan and Schönberger showed that the addition of 10% 1-butanol to a methanol/water mobile phase significantly improved the selectivity in separations of retinol isomers (*22*), and retinol, α-tocopherol, and β-carotene isomers in serum (*23*). MacCrehan and Brown-Thomas added 3% 1-propanol to an acetonitrile/water mobile phase to improve selectivity in the determination of phenols and naphthols in shale oil (*24*). The addition of small percentages of short-chain alkanols has also been shown to improve the efficiency in separations involving micellar mobile phases. Dorsey et al. (*25*) demonstrated that the addition of 3% 1-propanol to micellar mobile phases dramatically improves the efficiency of the separation without adversely affecting the viscosity or retention characteristics of the mobile phase. The improved efficiency was attributed to better wetting of the stationary phase surface by the 1-propanol, providing better mass transfer of the solutes. In a thorough study of optimization of secondary chemical equilibria in RPLC, Foley and May also found that 4% 1-propanol greatly improved the efficiency of columns used with highly aqueous mobile phases (*26, 27*).

In addition to mobile phase and solvation structure considerations, the nature of the bonded phase, particularly the bonding density of the alkyl chains, must be considered in order to completely understand column reequilibration following gradient elution. Dill has developed a retention model (*28–30*) that predicts a critical alkyl chain bonding density of 2.7 μmol of bonded alkyl chains per square meter of silica surface. At surface densities below this critical bonding density, Dill's theory predicts a linear increase in solute partitioning with increasing surface density. Above the critical bonding density alkyl chain configurational constraints increase the amount of free energy necessary to create a solute-sized cavity in the stationary phase, and partitioning of solutes should decrease. Sentell and Dorsey (*31*) have recently investigated the relationship between partitioning and stationary phase bonding density by determining partition coefficients for several compounds on well-characterized stationary phases of known high and low bonding densities, and their findings closely correlate with Dill's predictions. From this work it is clear that bonding density plays a significant role in the partitioning process. It follows that stationary phase bonding density should play a role in column regeneration following gradient elution, since the solvation of the alkyl chains at any mobile phase composition (i.e., starting and final gradient conditions) is directly influenced by the partitioning of solvent molecules into the stationary phase. Thus columns of different bonding densities should require different volumes of starting mobile phase to achieve column reequilibration.

On the basis of the work with micellar mobile phases in our laboratory (*25*) and the work of Scott and Simpson (*21*), we predicted that the addition of 3% 1-propanol to the mobile phase would significantly reduce column reequilibration time following gradient elution. In this paper we present evidence which shows that the addition of a constant volume of 3% 1-propanol to the mobile phase provides consistent solvation of the stationary phase throughout the mobile phase solvent gradient due to preferential wetting of the stationary phase by the 1-propanol. This consistent solvation provides a robust stationary phase structure, which in turn leads to a dramatic decrease in the volume of mobile phase which must be passed through the column following a solvent gradient to achieve stationary phase reequilibration. We also show the relationship of the bonding density of the stationary phase to the volume of starting mobile phase required to achieve column reequilibration when 1-propanol is not added and to the reduction in reequilibration time achieved by adding 3% 1-propanol to the mobile phase.

EXPERIMENTAL SECTION

Apparatus. All retention measurements were made with a Spectra-Physics SP8700 ternary pump (Spectra-Physics, San Jose, CA) and UV detection at 254 nm with a Beckman Model 153 fixed-wavelength detector (Beckman Instruments, San Ramon, CA). Sample injection was performed with a Rheodyne Model 7125 manual injector (Rheodyne, Inc., Cotati, CA) fitted with a 20-μL sample loop, and detector output was recorded on a Scientific Products Quantigraph chart recorder (Houston Instruments, Austin, TX). Each column was thermostated at 30 °C with a water jacket and a Fisher Scientific Model 73 immersion circulator (Fisher Scientific, Fair Lawn, NJ). The mobile phase flow rate for all experiments was 1.0 mL/min.

Solvents and Columns. HPLC grade acetonitrile and methanol (Fisher Scientific, Fair Lawn, NJ) were used without further purification. Water was obtained from a Barnstead Nanopure II water purification system (Barnstead Co., Boston, MA) fitted with a 0.45-μm filter. Reagent grade 1-propanol (Fisher Scientific, Fair Lawn, NJ) was filtered through a 0.45-μm Nylon-66 membrane filter (Rainin Instruments, Woburn, MA) before being used. Mobile phases containing 3% (v/v) 1-propanol were degassed by sonicating for 30 min prior to use; unmixed mobile phases were degassed by sparging with helium. The acetone sample was prepared by diluting spectral grade acetone (Mallinckrodt, Paris, KY) 1 part to 1000 in water.

Three commercial C_{18} chromatographic columns were used for the gradient elution reequilibration studies: Phenomenex Nucleosil, 5 μm, 25 cm × 4.6 mm i.d. (Phenomenex, Rancho Palos Verdes, CA); Burdick and Jackson OD5, 5 μm, 25 cm × 4.6 mm i.d. (Baxter Healthcare Corp., Muskegon, MI); and Zorbax ODS, 5 μm, 15 cm × 4.6 mm i.d. (Du Pont Instruments, Wilmington, DE). In addition, five columns containing well-characterized stationary phases prepared, packed, and previously used (*31*) in our laboratory were used for the gradient elution studies. The C_{18} bonding densities of these columns were calculated as previously described (*32*) and ranged from 1.60 to 4.07 μmol/m^2. Detailed synthesis procedures for the preparation of these stationary phases may be found elsewhere (*33*). All "homemade" columns were 15 cm × 4.6 mm i.d.

Reequilibration Studies. Column reequilibration following gradient elution was evaluated by measuring the variation in the retention time of acetone after a change in mobile phase conditions. Acetone was chosen as the solute for these studies since it is an early eluting compound and thus will show the greatest variation in retention time with a change in stationary phase solvation (*2, 5*). For each column a gradient was run from 0% to 100% organic modifier (acetonitrile or methanol) and then held at the 100% organic composition for 15 min to ensure complete equilibration of the stationary phase with the organic modifier, as indicated by a steady base line. Following the 15-min equil-

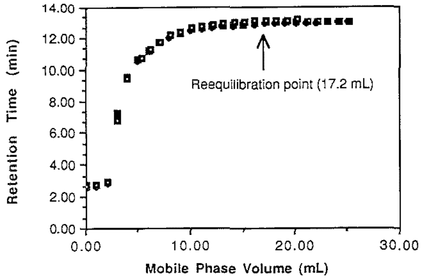

Figure 1. Acetone retention time as a function of the volume of starting mobile phase (100% water) for the Burdick and Jackson column with acetonitrile as the organic modifier.

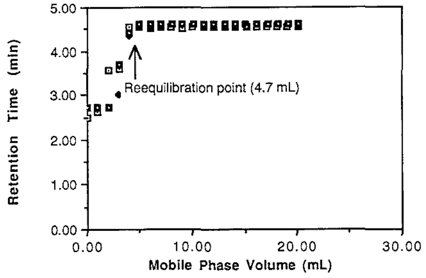

Figure 2. Acetone retention time as a function of the volume of starting mobile phase (97/3 water/1-propanol) for the Burdick and Jackson column with acetonitrile as the organic modifier and a constant volume of 3% 1-propanol added to the mobile phase.

ibration period, the mobile phase was returned to its original conditions (100% water) and injections of acetone were immediately begun at a rate of one injection per minute for 20–30 min. The retention time of acetone was measured and plotted versus the volume of starting mobile phase (100% water) that had passed from the ternary proportioning valve (TPV) of the pump at the time of injection. The time at which the mobile phase was returned to starting conditions and acetone was first injected was considered to be the starting time for the reequilibration experiments. Thus, the retention time of the first acetone injection was plotted versus 0.00 mL of mobile phase, as no volume of starting mobile phase had passed from the TPV at the time of this injection. The column was determined to be completely reequilibrated when the retention time of acetone reached a constant value. This experiment was repeated with mobile phases containing 3% 1-propanol, and the volume of mobile phase necessary to reequilibrate the column without 3% 1-propanol present was compared to the volume of mobile phase necessary to reequilibrate the column with 3% 1-propanol added. Each experiment was run in triplicate.

RESULTS AND DISCUSSION

A plot of the retention time of acetone as a function of the volume of starting mobile phase (100% water) that had passed from the TPV of the pump for the Burdick and Jackson commercial column is shown in Figure 1. A gradient was run from 0% to 100% acetonitrile, held at 100% acetonitrile for 15 min, and then returned to the starting mobile phase conditions, at which time acetone injections were begun. All three reequilibration trials are plotted on the same axes, and the average reequilibration volume, as determined from a constant retention time of acetone, was 17.2 mL of the starting mobile phase. This same experiment was repeated with a constant volume of 3% 1-propanol added to the mobile phase, and the results are shown in Figure 2. Again, all three trials are plotted, but for this experiment the average volume of starting mobile phase (97/3, water/1-propanol) needed to achieve column reequilibration was only 4.7 mL. At a flow rate of 1.0 mL/min these reequilibration volumes correspond to reequilibration times of 17.2 and 4.7 min. The reduction in reequilibration time achieved by adding 3% 1-propanol to the mobile phase was calculated as

$$\mathrm{RT(red)}\ (\%) = \frac{\mathrm{RT(w/o)} - \mathrm{RT(w)}}{\mathrm{RT(w/o)}} \times 100$$

where RT(red) is the reduction in reequilibration time (or improvement in column regeneration) expressed as a percentage, RT(w/o) is the reequilibration time of the system without 3% 1-propanol added to the mobile phase, and RT(w) is the reequilibration time of the system with 3% 1-propanol added to the mobile phase. Thus, for the Burdick and Jackson column with acetonitrile as the organic modifier the time necessary for column reequilibration is reduced by 73% when 3% 1-propanol is added to the mobile phase. This represents a significant savings in time and solvents necessary for a complete gradient run.

Although chromatographic data are most frequently expressed in terms of capacity factors, the data here are expressed in terms of retention times. In order to express these data in terms of capacity factors, it would be necessary to know the dead time (t_0) of the column at the time of each acetone injection. Since t_0 may change as the solvation of the stationary phase changes (*20*), and, in the process of reequilibration, the column solvation is changing, it is impossible to know accurately the value of t_0 at each injection time. Additionally, the value of most interest in these studies is the mobile phase volume at which the retention time becomes constant and not the actual value of the capacity factor. Therefore, retention time is the most convenient and useful way of expressing these data.

Obviously, the process of column reequilibration cannot begin until the starting mobile phase reaches the column. The dead volume of the chromatographic system from the TPV of the pump to the head of the column was determined to be 1.22 mL. Therefore, the starting mobile phase does not reach the column until after the second injection of acetone. Subtraction of this dead volume from the reequilibration volume would give a true measure of the volume of mobile phase needed to reequilibrate the column. However, in practice, the volume (or time) necessary to reequilibrate the column includes the dead volume of the system, so this value was included in all of our data. Taking this dead volume into account for the Burdick and Jackson column, the actual volume of mobile phase needed to reequilibrate the column when 1-propanol is added is 3.5 mL, which is approximately one and one-half column volumes, and considerably less than the 15–20 column volumes generally thought necessary for column regeneration (*2, 5*). This provides evidence that 1-propanol creates consistent stationary phase solvation, leading to a more robust stationary phase structure.

In order to demonstrate that it is the presence of 1-propanol in the mobile phase that provides consistent solvation of the alkyl chains, and not just the presence of any organic modifier, an experiment was performed in which the starting mobile phase contained 10% acetonitrile and the final mobile phase contained 90% acetonitrile. This experiment was performed on one of the stationary phases prepared in our laboratory with a bonding density of 3.06 μmol/m^2. Three trials were performed in which no 1-propanol was added to the mobile phase, and the average reequilibration time was 7.1 min. The experiment was repeated with 3% 1-propanol added to the mobile phase, and the average reequilibration time was 3.7 min. This represented a 48% reduction in reequilibration time, and shows that 1-propanol is preferentially solvating the bonded alkyl chains, creating a consistent solvation structure

Table I. Reequilibration Data for Commercial Columns

column	organic modifier	reequilibration volume, mL: without 1-propanol	reequilibration volume, mL: with 1-propanol	reduction in reequilibration time, %
Phenomenex	acetonitrile	14.0	6.0	57
	methanol	9.0	5.0	44
Zorbax	acetonitrile	15.9	4.4	72
	methanol	11.5	4.1	64
Burdick and Jackson	acetonitrile	17.2	4.7	73
	methanol	11.5	4.0	65

of the stationary phase. This experiment also demonstrates that the addition of 3% 1-propanol to the mobile phase improves column reequilibration in gradient separations where the starting mobile phase is a hydroorganic mixture rather than 100% water. Another experiment was performed in which 3% 1-butanol was added to the mobile phase, but this study proved to be experimentally difficult due to bubble formation within the pump when the mobile phase was switched from the final mobile phase (97/3 acetonitrile/1-butanol) to the starting mobile phase (97/3 water/1-butanol). The choice of 1-propanol as the most useful and practical solvating agent and the volume of 1-propanol needed to achieve consistent solvation (3%) were previously optimized in our laboratory (*25*) and are in agreement with the results of Foley and May (*26*, *27*).

Careful attention to Figures 1 and 2 reveals that the addition of 3% 1-propanol to the mobile phase reduces the retention time of the test solute acetone. In Figure 1, the average retention time of acetone when the Burdick and Jackson column is equilibrated with 100% water is 13.0 min, whereas in Figure 2, the average retention time of acetone when the column is equilibrated with 97/3 water/1-propanol is only 4.6 min. In this particular experiment the reduction in retention time of acetone by the addition of 3% 1-propanol is substantial, primarily because the retention time of any solute in 100% water is extraordinarily long compared with the retention time of that solute in a hydroorganic mobile phase. In the experiment on the 3.06 μmol/m^2 bonding density column in which the starting mobile phase contained 10% acetonitrile and the final mobile phase contained 90% acetonitrile, the reduction in retention time of acetone with the addition of 3% 1-propanol to the mobile phase was less severe. In this experiment the average retention time of acetone when the column was equilibrated with 10/90 acetonitrile/water was 3.2 min, whereas the average retention time of acetone when the column was equilibrated with 87.3/9.7/3 acetonitrile/water/1-propanol was 2.7 min, which is only a 16% decrease in retention time. The effect of adding 3% 1-propanol to the mobile phase on the retention of solutes will vary according to the gradient conditions of the experiment, and in practice, this effect may be diminished by appropriate adjustment of the gradient parameters.

Two other commercial columns were studied in addition to the Burdick and Jackson column. A summary of results for all the commercial columns studied is given in Table I. In every case, the addition of 3% 1-propanol to the mobile phase decreased the column reequilibration time significantly. The results for the Zorbax column were very similar to those for the Burdick and Jackson column, but the results for the Phenomenex column were somewhat different. Since the experimental conditions were identical for each of the columns, the differences in the column reequilibration times were attributed to differences in the stationary phases. Based on knowledge of the effect of alkyl chain bonding density on partitioning, and therefore on column regeneration, the variation in the results is most likely due both to differences in the alkyl chain bonding density and to the surface area of the silica of the three commercial columns.

Table II. Relevant Characteristics of Columns Used for Bonding Density Study

C_{18} bonding density, μmol/m^2	particle size, μm	endcapped?
1.60	20	yes
2.84	20	no
3.06	20	no
3.56	20	no
4.07	10	no

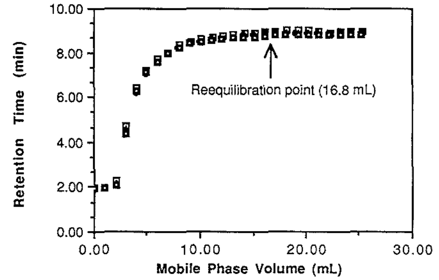

Figure 3. Acetone retention time as a function of the volume of starting mobile phase (100% water) for the column with a C_{18} bonding density of 3.06 μmol/m^2 with acetonitrile as the organic modifier.

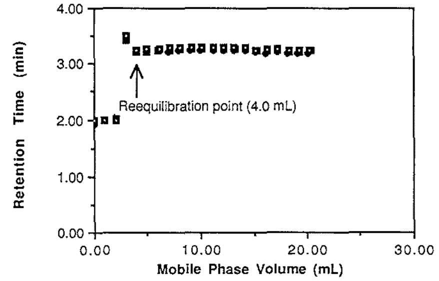

Figure 4. Acetone retention time as a function of the volume of starting mobile phase (97/3 water/1-propanol) for the column with a C_{18} bonding density of 3.06 μmol/m^2 with acetonitrile as the organic modifier and a constant volume of 3% 1-propanol added to the mobile phase.

Relationship to Bonding Density. Five columns of known C_{18} bonding density prepared and packed in our laboratory were used to evaluate the effect of alkyl chain bonding density on column regeneration time. Relevant characteristics of these columns, ranging in bonding density from 1.60 to 4.07 μmol/m^2, are given in Table II. Reequilibration studies were performed in triplicate for each of the columns using methanol and acetonitrile as the organic modifier. Figure 3 shows a plot of the retention time of acetone as a function of the volume of starting mobile phase (100% water) for the column with a C_{18} bonding density of 3.06 μmol/m^2 with acetonitrile as the organic modifier. The average reequilibration time for this column without 1-propanol added to the mobile phase is 16.8 mL. A plot of acetone retention time versus the volume of starting mobile phase with 3% 1-propanol added for this column is shown in Figure 4. With 3% 1-propanol added to the mobile phase the reequilibration volume is only 4.0 mL, which represents a 76% reduction in reequilibration time.

A summary of reequilibration results for all of the columns of known bonding density is given in Table III. Again, in all

Table III. Reequilibration Data for Columns of Known Bonding Density

bonding density, μmol/m^2	organic modifier	reequilibration volume, mL: without 1-propanol	reequilibration volume, mL: with 1-propanol	reduction in reequilibration time, %
1.60	acetonitrile	12.1	6.0	50
	methanol	9.1	5.3	42
2.84	acetonitrile	16.9	3.7	78
	methanol	13.8	3.7	73
3.06	acetonitrile	16.8	4.0	76
	methanol	13.6	4.0	71
3.56	acetonitrile	15.2	4.0	74
	methanol	9.8	5.7	42
4.07	acetonitrile	8.5	5.0	41
	methanol	5.0	3.7	26

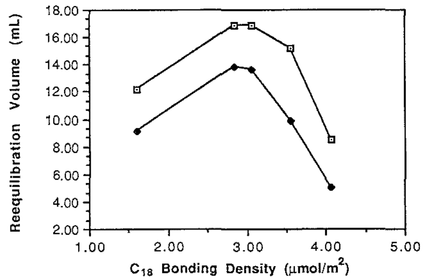

Figure 5. Reequilibration volume as a function of C_{18} bonding density with no 1-propanol added to the mobile phase. Open boxes represent experiments with acetonitrile as the organic modifier, and closed boxes represent experiments with methanol as the organic modifier.

cases, the addition of 3% 1-propanol to the mobile phase produces a marked reduction in reequilibration time. Examination of these data reveals that for every bonding density with either acetonitrile or methanol as the organic modifier, the average reequilibration volume when 3% 1-propanol is added to the mobile phase is roughly the same, but without 1-propanol added the reequilibration volumes are quite different. The fact that the reequilibration volumes for all columns are similar when 3% 1-propanol is added to the mobile phase demonstrates that 1-propanol provides consistent wetting of the stationary phase. A plot of the reequilibration volume as a function of C_{18} bonding density when no 1-propanol is added to the mobile phase is shown in Figure 5. This plot shows that a maximum in the amount of mobile phase required for reequilibration occurs at bonding densities of about 2.9 μmol/m^2. This matches closely the critical alkyl chain bonding density of 2.7 μmol/m^2 predicted by Dill (*29*) and of 3.1 μmol/m^2 observed by Sentell and Dorsey (*31*) and indicates that alkyl chain bonding density plays a prominent role in the partitioning process and therefore in the reequilibration process. At bonding densities greater than the critical bonding density, the mobile phase volume necessary to achieve column reequilibration decreases. At these higher bonding densities chain ordering increases due to configurational constraints imposed by the increased chain density, which in turn decreases partitioning (*28–30*). Since chain ordering increases and partitioning decreases at higher bonding densities, the stationary phase will undergo fewer changes with a change in mobile phase composition. Therefore, as our experimental evidence indicates, the reequilibration volume for columns of high bonding densities should decrease due to the additional rigidity of the stationary phase structure imposed by the higher density of the alkyl chains.

It is interesting to note that for every column examined, both commercial and "homemade", the volume of mobile phase necessary for stationary phase reequilibration when no 1-propanol is added to the mobile phase is greater when acetonitrile is used as the organic modifier than when methanol is used as the organic modifier. Since acetonitrile is less polar than methanol, it will have more affinity for the stationary phase with respect to water than will methanol. Therefore, when the column is equilibrated with acetonitrile (as at the end of a gradient), it is more difficult for water (the starting mobile phase) to replace the acetonitrile in the stationary phase than it is for water to replace methanol. This is in agreement with the results of McCormick and Karger (*10, 11*), who found that acetonitrile is extracted into the stationary phase to a greater extent than methanol, and with Yonker et al. (*13*), who found that acetonitrile is a better C_{18} solvating agent than methanol. This trend is also observed when the mobile phase contains some acetonitrile or methanol at the beginning of the gradient. However, when 1-propanol is added to the mobile phase, this trend is not observed, since the 1-propanol is present at a constant volume percentage throughout the gradient and preferentially wets the alkyl chains.

By maintaining consistent solvation of the stationary phase through the addition of a constant volume of 3% 1-propanol to the mobile phase, it is possible to markedly reduce the column reequilibration time needed following gradient elution. The use of this simple method to reduce column reequilibration time should lead to a significant savings in time, solvents, and money when used for routine gradient separations. Additionally, identification of a critical alkyl chain bonding density of about 2.9 μmol/m^2 provides support for the partitioning mechanism of retention as proposed by Dill (*28–30*) and demonstrates the significance of examining and controlling stationary phase characteristics when performing chromatographic studies.

ACKNOWLEDGMENT

The authors are grateful to Carol Fung-Kee-Fung for preliminary data and to Joe P. Foley for helpful discussions.

Registry No. 1-Propanol, 71-23-8.

LITERATURE CITED

(1) Snyder, L. R. In *High-Performance Liquid Chromatography. Advances and Perspectives*; Horvath, Cs., Ed.; Academic Press: New York, 1980; Vol. 1.
(2) Snyder, L. R.; Glajch, J. L.; Kirkland, J. J. *Practical HPLC Method Development*; Wiley: New York, 1988; Chapter 6.
(3) Quarry, M. A.; Grob, R. L.; Snyder, L. R. *J. Chromatogr.* **1984**, *285*, 1–18.
(4) Dolan, J. W. *LC-GC* **1987**, *5* (5), 384–390.
(5) Dolan, J. W. *LC-GC* **1987**, *5* (6), 466–470.
(6) Snyder, L. R.; Dolan, J. W.; Gant, J. R. *J. Chromatogr.* **1979**, *165*, 3–30.
(7) Dolan, J. W.; Gant, J. R.; Snyder, L. R. *J. Chromatogr.* **1979**, *165*, 31–58.
(8) Frenz, J.; Horvath, C. *J. Chromatogr.* **1983**, *282*, 249–262.
(9) Payne, L. D.; Arenas, R.; Little, E.; Foley, J. P. Presented at the 197th ACS National Meeting, Dallas, April 10, 1989; Paper No. ANYL 6.
(10) McCormick, R. M.; Karger, B. L. *Anal. Chem.* **1980**, *52*, 2249–2257.
(11) McCormick, R. M.; Karger, B. L. *J. Chromatogr.* **1980**, *199*, 259–273.
(12) Yonker, C. R.; Zwier, T. A.; Burke, M. F. *J. Chromatogr.* **1982**, *241*, 257–268.
(13) Yonker, C. R.; Zwier, T. A.; Burke, M. F. *J. Chromatogr.* **1982**, *241*, 269–280.
(14) Gilpin, R. K.; Gangoda, M. E. *J. Chromatogr. Sci.* **1983**, *21*, 352–361.
(15) Gilpin, R. K.; Gangoda, M. E. *Anal. Chem.* **1984**, *56*, 1470–1473.
(16) Marshall, D. B.; McKenna, W. P. *Anal. Chem.* **1984**, *56*, 2090–2093.
(17) Carr, J. W.; Harris, J. M. *Anal. Chem.* **1986**, *58*, 626–631.
(18) Tanaka, N.; Sakagami, K.; Araki, M. *J. Chromatogr.* **1980**, *199*, 327–337.
(19) Scott, R. P. W.; Simpson, C. F. *J. Chromatogr.* **1980**, *197*, 11–20.
(20) Quarry, M. A.; Grob, R. L.; Snyder, L. R. *J. Chromatogr.* **1984**, *285*, 19–51.
(21) Scott, R. P. W.; Simpson, C. F. *Faraday Symp. Chem. Soc.* **1980**, *15*, 69–82.
(22) MacCrehan, W. A.; Schönberger, E. *J. Chromatogr.* **1987**, *417*, 65–78.
(23) MacCrehan, W. A.; Schönberger, E. *Clin. Chem.* **1987**, *33* (19), 1585–1592.

(24) MacCrehan, W. A.; Brown-Thomas, J. M. *Anal. Chem.* **1987**, *59* (3), 477–479.
(25) Dorsey, J. G.; DeEchegaray, M. T.; Landy, J. S. *Anal. Chem.* **1983**, *55*, 924–928.
(26) Foley, J. P.; May, W. E. *Anal. Chem.* **1987**, *59*, 102–109.
(27) Foley, J. P.; May, W. E. *Anal. Chem.* **1987**, *59*, 110–115.
(28) Dill, K. A. *J. Phys. Chem.* **1987**, *91*, 1980–1988.
(29) Dill, K. A.; Naghizadeh, J.; Marqusee, J. A. *Annu. Rev. Phys. Chem.* **1988**, *39*, 425–461.
(30) Dorsey, J. G.; Dill, K. A. *Chem. Rev.* **1989**, *89*, 331–346.
(31) Sentell, K. B.; Dorsey, J. G. *Anal. Chem.* **1989**, *61*, 930–934.
(32) Berendsen, G. E.; de Galen, L. *J. Liq. Chromatogr.* **1978**, *1*, 561–586.
(33) Sentell, K. B.; Barnes, K. W.; Dorsey, J. G. *J. Chromatogr.* **1988**, *455*, 95–104.

RECEIVED for review July 17, 1989. Accepted October 6, 1989. The authors are grateful for support of this work by NIH GM33382 and by Burdick and Jackson BJ 8803.

Immobilized 8-Oxine Units on Different Solid Sorbents for the Uptake of Metal Traces

O. Abollino, E. Mentasti,* V. Porta, and C. Sarzanini

Department of Analytical Chemistry, University of Torino, Via Giuria 5, 10125 Torino, Italy

The sorption of 8-hydroxyquinoline and 8-hydroxyquinoline-5-sulfonic acid on a polystyrene–divinylbenzene resin (Amberlite XAD-2) and on an anion exchange resin (Bio-Rad AG MP-1) has been used for the uptake and enrichment of trace metal ions. The investigated metal ions were Ca(II), Cd(II), Cu(II), Mg(II), Mn(II), Ni(II), Pb(II), and Zn(II). The uptake and recovery yields were determined by use of inductively coupled plasma atomic emission spectroscopy. The behavior of the sorbed ligands was determined in different conditions, and the results have been discussed and compared with those computed according to a model described. The chelating solid substrates have been used for the enrichment of metal traces from environmental samples. Enrichment factors of up to 100, together with low blank levels of the optimized procedures, allow the simple determination of the above elements at concentrations down to a few nanograms per milliliter.

Different solid sorbents (namely polymers, anion exchangers, reversed-phase octadecylsilica, controlled-pore glass) have extensively been used for the immobilization of organic ligands (*1, 2*). Such substrates have been used for the uptake of metal ion traces from aqueous samples and for their enrichment, under different operating mechanisms of ligand and of complex retention, i.e. adsorption (*3–5*), ion exchange (*6*), partition (*7*), ion pair interaction (*8*), chelation (*9–11*).

Among the grafted ligands, 8-hydroxyquinoline (oxine) has been extensively used in different forms, especially grafted to controlled-pore glass (CPG) (*12–18*), or adsorbed on octadecyl reversed-phase silica (silica C-18) (*5, 19, 20*). In this last form standard procedures for the enrichment and subsequent determination of a series of metal traces have been investigated in detail (*2, 21*).

In the present paper we have investigated the grafting procedures of the oxine moiety to organic polymeric supports in order to develop preconcentration procedures. In particular the systems used here are a polystyrene–divinylbenzene (ST–DVB) copolymer and an anion exchange (AE) resin, whose properties allowed metal complexes of the parent ligand oxine (OX) and of its 5-sulfonic acid derivative (SOX), respectively, to retain.

For both systems very low contaminations from the solid supports were experienced during the enrichment procedures, and this favorable condition was given by the low content of metal impurities on both investigated polymeric supports. On the contrary, this is not the case for the other silica-based solid supports, like CPG or silica C-18; with these last, higher blank values are usually found that make the developed procedures not appropriate for applications directed to the analysis of environmental samples (*5, 22*).

The high stability of the complexes formed by the 8-hydroxyquinoline moiety with several metals prompted us to investigate in detail the behavior of Ca(II), Cd(II), Cu(II), Mg(II), Mn(II), Ni(II), Pb(II), and Zn(II). The aim of the present paper is therefore the characterization of the above chelating systems for the uptake of such trace metal ions.

The experimental results have been compared with reference to the theoretical uptake yields which can be computed on the basis of each metal speciation, obtained with the aid of the corresponding stability constants, according to a described model.

EXPERIMENTAL SECTION

Instruments. A Plasma 300 Allied Analytical Systems (Waltham, MA) inductively coupled plasma emission spectrometer (ICP-AES) was used throughout for the determination of the metals in all solutions. The operating conditions of the ICP-AES were as follows: rf power, 1.2 kW; coolant flow rate, 13 L/min; aspiration rate, 1.5 mL/min; nebulizer pressure 26 psi; observation height above the load coil, 12 mm; integration time, 5 s; window slit, 0.067 nm; readings, 2. An Orion EA 920 pHmeter equipped with a combined glass–calomel electrode was used for all pH measurements. All solutions were prepared with high-purity water HPW (Millipore Milli-Q). High-purity acids and ammonia were obtained with a sub-boiling quartz still (K. Kurner, Rosenheim, West Germany). Standard labware and glassware were used throughout and repeatedly cleaned with HNO_3 and rinsed with HPW, according to a published procedure (*23*).

Chemicals. The ligands employed were 8-hydroxyquinoline (OX) and 8-hydroxyquinoline-5-sulfonic acid (SOX). OX ligand is less polar and its dissolution may be easily achieved in a water/methanol (75/25 (v/v)) mixture, while SOX was dissolved in water.

Also the solid supports for these ligands show different properties. For SOX, a macroporous anion exchange resin (AG MP-1, 100–200 mesh, chloride form, Bio-Rad) enabled the immobilization of the ligand through its sulfonato group. OX was supported on Amberlite XAD-2 polymer beads (polystyrene–divinylbenzene copolymer, 20–50 mesh, Fluka). For some experiments (see below), AG MP-1 resin was converted in nitrate form according to the following procedure: 1 g of resin, slurry packed in a polypropylene

Table I. Emission Wavelengths for ICP-AES Determinations of the Elements Investigated and Detection Limits for the Instrumentation Adopted[a]

element	wavelength, nm	detection limit, μg/L
Ca	393.37	0.2
Cd	214.44	1.5
Cu	324.75	1.0
Mg	279.55	0.1
Mn	257.61	1.0
Ni	221.65	4.0
Pb	220.35	25.0
Zn	213.86	2.0

[a] Detection limits are evaluated as twice the standard deviation of the blanks, run in triplicate. For other operative details, see the Experimental Section.

column, was treated with 50 mL of 2.0 M HNO_3.

Stock metal solutions, 1000 mg/L (E. Merck), were diluted daily for obtaining reference and working solutions.

Procedure. For the XAD-2 + OX system, 100.0 mL of solution containing 10.0 μg of a metal (M) was added of the required volume of a 2.0×10^{-3} M solution of OX (for obtaining a 20-fold greater molar concentration with respect to the metal, e.g. 2.0 mL for copper) and brought to the desired pH between 2 and 9. One gram of XAD-2 resin that was previously washed with 6 N HCl, methanol, and HPW was then poured into a Bio-Rad polypropylene (5.0 mL) Econo-Column. The resin was supported by the built-in porous polyethylene support disk. A small portion of washed (HNO_3, HPW) glass wool was placed on top of the resin bed in order to immobilize the beads. The resin was equilibrated with 10 mL of HPW brought to the same pH of the uptake experiment, and finally the metal solution was driven through the column with a peristaltic pump (Gilson Minipuls 4). Sample flow rates were usually 7–10 mL/min. The procedure for the AG MP-1 anion exchange resin + SOX was similar to the one described above, with obvious adaptations.

The column was then washed with HPW portions and the metal was recovered in a 10-mL volumetric flask (enrichment factor 10) with the aid of portions of the proper stripping agent (see below).

A 5.0-mL portion of the stripping agent was poured into the column. The column was closed on both sides, gently shaken a few times, and left to react for 5 min, in order to allow a more intimate contact of the stripping agent with bound metals. The solution was then collected in a 10-mL volumetric flask. Another 4.0-mL portion was added in the same way, and finally additional reagent (~1 mL) was used in order to rinse the resin and to bring to volume the recovered metal in the 10-mL volumetric flask.

After such treatment the resins apparently do not undergo any modification. After proper equilibration at the desired pH, the column may be reused indefinitely. In the present case the resin was discarded after 12–15 experiments.

The determination of the metal in the final solution enabled the evaluation of the recovery yield for each experiment. The metal concentrations in the solutions, before and after uptake by the sorbent, and after recovery by the stripping agent, were determined with ICP-AES (one element at a time for multicomponent mixtures) at the wavelengths reported in Table I, in order to evaluate uptake and recovery yields. Cross check was obtained by comparing the metal remaining in the starting solution after flowing through the column.

The determinations of the metal remained in the starting solution, after passage through the resin, allowed verification of the efficiency of the recovery from the solid sorbent achievable with the stripping agent. Possible differences between the sum of the absolute quantities found in the final solution and in the treated sample and the total amount present in the starting solution may be given by a noncomplete stripping procedure from the sorbent.

Table II. Stability Constants (log *K*) for the Metal Complexes and Acidity Constants (pK_A) of the Ligands OX and SOX, Determined at Ionic Strength = 0.01 M, *t* = 25 °C (*24–26*)

	OX		SOX	
metal	K_1	K_2	K_1	K_2
Ca(II)	3.27	3.27	3.52	3.00
Cd(II)	7.80	6.20	6.90	6.50
Cu(II)	12.1	10.9	11.9	10.1
Mg(II)	4.50	2.00	4.10	3.60
Mn(II)	6.80	5.80	5.70	5.00
Ni(II)	9.90	8.80	9.60	8.70
Pb(II)	9.02	7.00	8.50	7.60
Zn(II)	8.56	7.40	7.45	6.50
H^+	5.0	10.0	3.40	8.35

Experiments were performed also on blank solutions, i.e. on samples containing all the reagents but not the metal, in order to evaluate the absolute blanks of each method, to be subtracted to the values determined in the presence of the metal. All measurements were performed in triplicate by repeating the entire procedure for each replicate; the derived standard deviations are given throughout with the reported experimental results.

RESULTS AND DISCUSSION

The ligands OX and SOX form with the investigated metals (all divalent aquacations) 1:1 and 1:2 metal–ligand complexes with relatively high stability. Table II shows the acid dissociation constants of the ligands (K_1 refers to the pyridine nitrogen and K_2 to the hydroxy group) and the formation constants for the complexes (*24–26*). Thus, SOX may be used for retaining preformed complexes on the anion-exchange resin through the dissociated sulfonato groups while OX can be conveniently used for the uptake of its neutral 1:2 metal complexes on the apolar XAD-2 resin.

XAD-2 + OX System. The concentration and type of reagent for the recovery of copper from the resin were optimized, and 1.0 M HCl proved to be efficient for the recovery of all the metal taken by the resin, as tested with solutions of known composition. For the recovery of Ca(II), Cd(II), Mg(II), Mn(II), Ni(II), Pb(II), and Zn(II), the stripping agent was 2.0 M HCl warmed at 50 °C.

All experiments were performed by adopting a metal to ligand molar ratio of 1:20 as in the scheme outlined above. This value was first optimized in experiments with Cu(II) and then maintained throughout. Such a ratio ensures the existence of conditions for the formation of the ML_2 complex. Higher concentrations of ligand were not tested in order to avoid possible competition by free ligand for the resin sites which would produce a reduction of metal uptake yield. Moreover the constancy of M:L ratio allowed correct comparisons among the investigated metals and between experimental and computed data.

Figure 1 reports the results (percent relative recoveries) obtained for the uptake of the investigated metals using OX ligand and XAD-2 resin. The experimental behavior shown by the continuous lines is reported together with the theoretical behavior (dashed lines) which can be expected by computing (*27*) the distribution of the metal in all the complexes formed with the aid of the stability constants reported in Table II (*24–26*), and assuming that all the neutral species, namely ML_2 species, are retained by XAD-2 resin.

AG MP-1 Anion-Exchange Resin + SOX. In this case the preformed complexes of the single metals are retained by the anion exchanger owing to the interaction with the negatively charged sulfonato group present on the benzene ring of the ligand.

In order to characterize the recovery yields with the system AG MP-1 + SOX, the same procedure outlined for the XAD-2 + OX system was used. For the recovery of Ca(II), Cu(II), Ni(II), and Mg(II) for the resin, 1.0 M HCl was used. The other investigated metals, namely Cd(II), Mn(II), Pb(II), and Zn(II), have an higher tendency to form chloro complexes with chloride ions and therefore, have been released from the resin with 2.0 M HNO_3. In fact the formation of chloro complexes

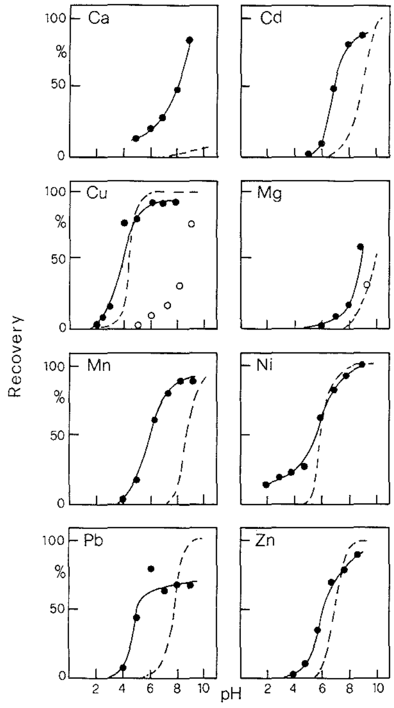

XAD 2 - OX

Figure 1. Percent metal traces recovery as OX complexes, as a function of pH, on XAD-2 resin: starting solution, 100.0 mL; 100 μg/L of metal 1.0 g of resin; OX ligand concentration, 3.0 × 10^{-5} M. Dotted lines represent the theoretical computed behavior (see text). Continuous lines and closed points are the experimental behavior and the open points represent metal retention in absence of ligand.

may produce anionic species, $MCl_n^{(2-n)+}$ with $n > 2$, which would be retained by the resin in a less reversible form. Also for SOX ligand, a ligand to metal ratio of 20:1 was adopted, since lower ratios could render the complexation less effective and higher ratios could give rise to saturation effects of the resin sites by the free ligand.

Volumes and concentrations of the metal subjected to enrichment, of the ligand added, and of the stripping agent solution, the column equilibration, and washing procedure were the same as described for XAD-2 + OX system. When the stripping agent was nitric acid, the anion exchange resin used was previously transformed in nitrate form (see the Experimental Section).

Figure 2 reports the results obtained for the recovery of the different metals with the XAD-2 + SOX system. The relative percent recoveries have been determined at different acidities performing, for all metals, an enrichment factor of 10, from 100-mL samples containing 100 μg/L of a single metal.

Discussion of Behavior. All the metals show a common general trend of high recovery/enrichment yield at the higher pHs and a more or less pronounced decrease at increasing acidities. Generally the recovery is almost zero at pH 3–4, with the exception of Ni(II) and of Cu(II). Only for Pb(II) is the behavior slightly different with a random maximum around pH 6 and a decrease toward pH 9.

With OX + XAD-2 a quantitative recovery (≥95%) was attained for Cu and Ni, while lower values were found for Cd, Mn, Pb, Zn, Ca, and Mg. With AG MP-1 + SOX a quantitative recovery is possible for Cd, Cu, and Ni and almost complete for Zn. For other metals like Mn and Pb, the yield is around 60–65%, while for Ca and Mg the values are much lower. It must be mentioned that the low recovery of Ca and Mg on the anion exchanger is helpful in view of applications to environmental samples. These samples are usually more rich in such alkaline-earth elements, so that on one side their low uptake does not create problems of saturation and on the other it allows an enriched sample to be obtained, which is free from the excess elements that could heavily contribute with their matrix effects to interferences in the determination of the other trace elements present at lower concentration.

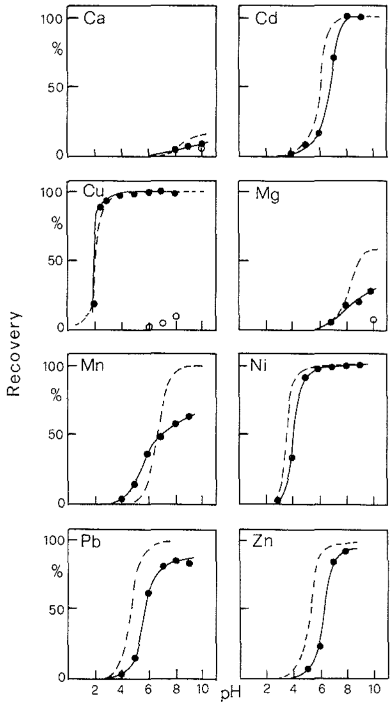

AGMP1 SOX

Figure 2. Percent metal traces recovery as SOX complexes, as a function of pH, on AG MP-1 anion exchange resin: starting solution, 100.0 mL, 100 μg/L of metal; 1.0 g of resin; SOX ligand concentration, 3.0 × 10^{-5} M. Dotted lines represent the theoretical computed behavior (see text). Continuous lines and closed points are the experimental behavior and the open points show the metal retention in absence of ligand.

The experimental values obtained in the present work are compared in Figures 1 and 2 with the theoretical evaluation of the retention and recovery. Considering the metals and the ligand as present in solution in the absence of the solid sorbent (adsorbent or exchanger), it is possible to evaluate the distribution of the species as a function of pH with the formation constants reported in Table II. All OX complexes, whose net charge is zero (namely MOX_2), are assumed to be retained by an adsorbent like XAD-2, while every metal complex formed by SOX is assumed to be retained by the anion exchanger, owing to the interaction with the $-SO_3^-$ groups (it should be mentioned, however, that the retention of 1:1 complexes with SOX might be less effective due to the overall neutral charge of the complex (one positive net charge on the metal center and one negative on the sulfonato groups of the ligand)). Under these assumptions the theoretical recovery yields reported as dashed lines in Figures 1 and 2 have been obtained (*27*).

From the figures it appears that the experimental and computed curves are parallel but not coincident. In the case of AG MP-1 + SOX there is a regularity of behavior (with the exception of Mn at pH <6) since all experimental curves lie at higher pH values than the theoretical ones, so that the computed recovery is generally higher that that experimentally determined. Therefore the immobilization of the ligand on the resin lowers the stability with respect to the complex in solution. This behavior may be explained by considering the presence on the resin bead surface of a positive charge layer which produces a repulsion toward the metal center, with subsequent weakening of the complex. Only for copper the experimental retention is somewhat higher than that computed, especially when recovery yield is below 80%. Also for XAD-2 + OX there is a difference between the experimental and computed behavior. Different cases may be described. For Ca and Mg the experimental curves lie at lower pH values with respect to the computed ones, showing that the retention of these metals is higher than expected. This may be explained considering the formation of neutral hydroxides which do not separate as insoluble species and that may be retained by the sorbent as well. In order to have indirect proof of this hypothesis, measurements were performed on Ca and Mg solutions brought to the desired pH in the absence of added ligand OX or SOX. Also in this case a definite metal uptake on the sorbents has been found (see Figures 1 and 2). In particular the recovery was higher for XAD-2 than for AG MP-1, in agreement with the fact that a neutral species, such as hydroxo species $M(OH)_2$, should be more tightly retained on the polymeric XAD-2 structure than on the anion exchanger AG MP-1, where the positive charge layer makes the retention of a neutral species less operative. Uptake experiments in the absence of ligand showed that at higher pH values copper also is partially retained by XAD-2 and to a much lower extent by AG MP-1, as shown in Figures 1 and 2. For copper, while an almost complete retention and recovery is expected at pH 5.0, a satisfactory experimental behavior is obtained only at pH 9.0. Theoretical and experimental behaviors parallel each other at pH 2–4, while at pH 4.0–8.0 the retention is significantly lower than expected and not quantitative (80–86%).

Considering the other metals, the substrate effect may be different. On one side the concentration of excess ligand retained on the surface of the sorbent is much higher than in solution so that the interaction of each metal with the ligand bound to the sorbent proceeds to a higher extent than the one computed on the basis of the concentration in homogeneous solution. On the other side the interaction of the ligand with the sorbent could produce a less favorable steric disposition of the ligand for the metal complexation. The correct geometric disposition of the ligands required for the formation of a 1:2 M:L species could be prevented by inclusion of the ligands in the cavities of the resins, thus weakening the stability of the complex species. These effects have an inverse effect toward metal uptake and recovery. The balance of all these effects will produce a different behavior for each metal and for each ligand/sorbent system.

The contribution of these effects may vary also as a function of acidity; in fact for Pb, Ni, Mn, Cd, and Zn, the experimental and the computed behavior cross: at the lower pH values the metals are complexed at a lower extent and the effect of the increase of ligand concentration on the sorbent surface predominates, increasing the experimental retention with respect to the one computed. At higher pH values the steric effect becomes more important since the fraction of metal bound to the ligand increases, and the destabilizing effect of the support may reduce the experimental behavior with respect to the computed one. This negative effect should be more important for metals with higher ionic radius, and the anomalous behavior of Pb at the higher pH values could be due to this effect.

Table III. Recovery Efficiency for a Mixture of Cu(II), Ca(II), and Mg(II) (all 100.0 mL, 10 μg/L) with XAD-2 + OX and with AG MP-1 + SOX (for Other Experimental Details, See Text)

metal	recovery, %	
	XAD-2 + OX	AG MP-1 + SOX
Cu(II)	98.5 ± 3.8	98.5 ± 2.7
Ca(II)	80.0 ± 4.7	11.2 ± 2.7
Mg(II)	35.3 ± 5.2	5.7 ± 3.5

Finally one should consider that the computation uses thermodynamic data obtained in different conditions (e.g. ionic strength ranging from 0.5 to 0 M) and apply to equilibrium conditions, which are not completely fulfilled for a system where the flowing solution of the metal and ligand interacts with a immobilized support. In general however if one compares the results for AG MP-1 resin and XAD-2 sorbent, with the exception of Mn and Pb, the yields for transition metals are higher for the anion exchanger. This behavior could be due to the fact that the exchanger is able to retain all complex species, while XAD-2 retains only the neutral ones.

Applications. Measurements have been performed in order to evaluate possible applications to real samples.

Mixture of Metals. In order to explore the possibility of selective recovery of a metal in the presence of calcium and magnesium ions, enrichment procedures on the two resins have been performed by using 100.0-mL solutions containing 100 μg/L of Cu, Ca, and Mg. The same experimental procedures described above were adopted with the only variation of an increased excess concentration of ligand OX or SOX. In the previous measurements a molar ratio M:L 1:20 was adopted and kept constant in order to allow correct comparisons among the investigated metals, and between experimental and computed data. In these measurements, in view of applications to real samples of unknown composition, an higher ligand concentration was adopted in order to allow complete complexation of all the metals present. Therefore 8.0 mL of 2.0×10^{-3} M OX or SOX was added for the experiments with XAD-2 and AG MP-1, respectively, and 2.0 g of each resin was used in order to overcome possible saturation by the ligand. The solutions were then brought to an optimum pH in order to ensure the highest recovery of Cu and the lowest for Ca and Mg. The pH was 8.0 for the adsorbing resin and 6.0 for the anion exchanger. The recovery was obtained with HCl 2.0 M at 50 °C for the first resin and HNO_3 2.0 M for the second. Table III collects the results obtained.

As can be seen the use of SOX with the anion exchanger gives the best results with complete recovery and enrichment of copper and partial removal of Ca and Mg (recovery around or below 10%). For XAD-2 resin + OX the separation is less effective especially for the reasons discussed above, that is retention of Ca and Mg probably as hydroxo species, since with this system a higher pH must be used.

Then experiments on multicomponent mixtures (seven metal traces) were performed. One hundred milliliter solutions containing 100 μg/L of Ca, Cd, Cu, Mg, Mn, Ni, and Pb were added of 13 mL of 2.0×10^{-3} M solutions of OX or SOX. The experiments with XAD-2 and with AG MP-1 were performed respectively at pH 9.0 and 8.0, recovering the metals with 2.0

Table IV. Recovery Efficiency for a Mixture of a Series of Metal Ions (all 100.0 mL, 100 μg/L) with XAD-2 + OX and with AG MP-1 + SOX (for Other Experimental Details, See Text)

metal	recovery, % XAD-2 + OX	recovery, % AG MP-1 + SOX
Ca(II)	102.0 ± 3.9	11.0 ± 2.5
Cd(II)	93.8 ± 4.8	96.7 ± 2.1
Cu(II)	97.2 ± 3.8	101.1 ± 3.8
Mg(II)	61.8 ± 5.3	25.5 ± 2.4
Mn(II)	82.3 ± 3.2	87.1 ± 2.2
Ni(II)	94.4 ± 4.9	97.2 ± 1.6
Pb(II)	83.7 ± 3.3	86.7 ± 1.3

M HCl at 50 °C from the first substrate and with 2.0 M HNO_3 for the second.

From the data reported in Table IV one can notice that on the anion exchanger higher recoveries are obtained than in the experiments performed at the same pH in the presence of a single metal species. The reason for this arises from the higher ligand concentration adopted in the present tests. A comparison for the two systems points out a similar good efficiency but a more selective behavior of the anion exchanger toward transition metals with respect to Ca and Mg.

Effect of Interferents. The effects of possible interferents present in real samples have been tested by investigating the recovery of three different metals, namely Cu, Cd, and Mn, which may be representative of metal ions with different decreasing tendency to be coordinated by the quinolinol moiety. The same metal concentrations (100 μg/L), enrichment factor 10, and stripping agents adopted for the seven metals mixture were adopted, and triplicate measurements were run on test solutions and on metal-free solutions for blank corrections. As interferents the following were considered: a high salinity (NaCl 0.5 and 1.0 M), a ligand competitor (nitrilotriacetic acid, NTA, in molar ratio 1:5, 1:1, and 2:1 with respect to OX or SOX), a nonionic surfactant (polyoxyethylene glycol, POLY, 10 and 100 mg/L), and an excess of alkaline-earth ions (Ca 20 mg/L + Mg 2 mg/L). Table V shows the results obtained, and as can be seen for AG MP-1 + SOX a slight lowering of recovery was observed only in the case of the higher concentration of surfactant. A more severe yield reduction was observed for the XAD-2 + OX system, for the competition with NTA (especially Cd and, at a lower extent, Mn) and for the surfactant POLY, at the higher concentration. However one must consider that 100 mg/L of POLY or NTA in molar concentration around 1×10^{-4} to 1×10^{-3} M represents very high concentrations, unusual in real samples.

A comparison between the anion exchanger and XAD-2 adsorbent points out again that the former gives better results, on the basis of transition-metal selectivity and much lower sensitivity to interferents.

Higher Preconcentration Factors. Experiments were also performed in order to explore the possibility of enriching solutions of lower concentration with a higher preconcentration factor. Solutions of 5 μg/L (1000 mL) were added to OX in molar excess 20:1 and brought to pH 9.0. The sample was then passed at a flow rate of about 10 mL/min through a column containing 1 g of XAD-2 resin. The recovery of copper was effected with 2.0 M HCl at 50 °C into a 10-mL flask. The enrichment factor is then 100 and a theoretical concentration of 0.500 mg/L is expected. Triplicate measurements on blank samples and on copper samples gave the following results: blank, 0.122 ± 0.018 mg/L; copper, 0.608 ± 0.074 mg/L. The experimental recovery is then 0.486 ± 0.092 mg/L with a percent yield of 97.2%, which may be considered as very satisfactory considering the low level investigated. Table VI reports the results for solutions of Cu + Cd + Mn each 5 μg/L, with an enrichment factor of 100 obtained on 1000-mL solutions. The results stand well for both systems.

Natural Waters. The methods have been applied to the analysis of Cd, Cu, Mn, Ni, Pb, and Zn in tap water and in Po River water. Samples of 1 L were used for both systems under the standard addition procedure. For Cd, Cu, Mn, and Zn additions of 1.0, 5.0, and 10.0 μg/L were used, for Ni, 5.0, 10.0, and 20.0 μg/L, and for Cu, 10.0, 20.0, and 30.0 μg/L. Recoveries of the added spikes, evaluated with reference to external standards, were always almost complete thus showing absence of matrix interferences, with the exception of Mn (for river water) and Zn (for tap and river water), for which incoerent data were obtained. The data reported in Table VII were obtained by a linear regression of the standard addition results. The analysis of Po River water was performed only with SOX with the anion exchanger, since the addition of OX ligand to Po River water produced an extensive formation of precipitate of insoluble iron(III) species.

Saline Solutions for Hemodialysis. Finally the enrichment procedure was tested for the analysis of a concentrated salt solution used for the hemodialysis of patients suffering from renal function deficiency. Such a solution has a complex composition (*28*) so that heavy matrix effects prevent an accurate direct analysis of trace metal impurities, which, on the other side, should be accurately evaluated in order to prevent the occurrence of harmful effects. Table VII collects the results obtained with the internal standard addition procedure performed on 1-L samples. The recovery yields for the standard additions were always higher than 90%, thus confirming the accuracy of the procedure and its independence from matrix effects.

CONCLUSIONS

In conclusion the present systems, based on the use of different sorbents, like the anion exchanger AG MP-1 in conjunction with ligand SOX and the apolar polymer XAD-2 in conjunction with OX, allowed quantitative enrichments to

Table V. Effect of Different Interferents on the Recovery Efficiency of Cu(II), Cd(II), and Mn(II) (100 μg/L) (for Other Details, See Text)

	recovery, %					
	XAD-2 + OX			AG MP-1 + SOX		
interferent	Cu(II)	Cd(II)	Mn(II)	Cu(II)	Cd(II)	Mn(II)
no interferent	95.8 ± 2.3	97.3 ± 3.2	98.9 ± 1.6	104.7 ± 1.9	97.0 ± 0.4	99.2 ± 0.3
NaCl 0.5 M	98.3 ± 2.0	97.5 ± 0.9	95.9 ± 2.4	103.3 ± 2.9	99.1 ± 1.1	99.6 ± 0.8
NaCl 1.0 M	94.6 ± 3.4	95.1 ± 4.0	91.2 ± 4.8	106.8 ± 4.3	95.3 ± 0.6	97.2 ± 0.9
[NTA]:[L] = 1:5	99.0 ± 4.1	74.8 ± 0.4	89.6 ± 0.8	104.7 ± 3.9	95.2 ± 0.5	97.1 ± 0.9
[NTA]:[L] = 1:1	89.0 ± 2.2	46.0 ± 1.1	74.5 ± 1.7	102.3 ± 1.1	97.3 ± 1.1	99.4 ± 0.5
[NTA]:[L] = 2:1	89.9 ± 3.5	48.1 ± 3.2	75.6 ± 3.9	101.7 ± 1.8	96.0 ± 1.0	95.6 ± 2.1
POLY 10 mg/L	90.1 ± 1.2	100.7 ± 2.3	92.8 ± 0.8	95.7 ± 1.0	91.8 ± 0.2	88.6 ± 0.6
POLY 100 mg/L	68.8 ± 0.2	77.8 ± 0.2	86.0 ± 0.3	78.5 ± 0.9	75.0 ± 0.8	76.0 ± 0.8
Ca 20, Mg 2 mg/L	95.2 ± 0.4	97.1 ± 5.2	95.6 ± 7.6	93.9 ± 3.4	89.9 ± 3.8	96.5 ± 2.3

Table VI. Percent Recovery Efficiency from 1-L Samples Containing 5 μg of Cu, Cd, and Mn with the Investigated Systems (for Other Details, See Text)

metal	recovery, % XAD-2 + OX	 AG MP-1 + SOX
Cu(II)	109.6 + 2.5	115.6 + 9.8
Cd(II)	94.4 + 1.0	92.4 + 2.0
Mn(II)	94.2 + 0.7	94.9 + 3.6

Table VII. Enrichment with the Described Procedures and ICP-AES Determination of Some Trace Elements in Tap Water (City of Torino), in Po River Water (Collected in the City of Torino), and in a Dialysis Concentrate for Blood Cleanup

metal	concentration, μg/L XAD-2 + OX	 AG MP-1 + SOX
	Tap Water	
Cd(II)	0.3 ± 0.1	0.2 ± 0.1
Cu(II)		4.4 ± 0.5
Mn(II)	4.1 ± 0.3	3.3 ± 0.2
Ni(II)	4.6 ± 0.6	3.2 ± 0.4
Pb(II)		7.2 ± 0.9
Zn(II)		
	River Water	
Cd(II)	*a*	0.12 ± 0.01
Cu(II)	*a*	5.9 ± 0.3
Mn(II)	*a*	
Ni(II)	*a*	6.0 ± 0.4
Pb(II)	*a*	4.1 ± 0.7
Zn(II)	*a*	
	Concentration for Hemodialysis	
Cd(II)		<0.1
Cu(II)		0.43 ± 0.1
Mn(II)		0.21 ± 0.04
Ni(II)		0.44 ± 0.2
Pb(II)		<0.7

[a] Precipitation of Fe(III) as oxine complex prevented the determination from Po River water.

be obtained for a series of metal traces. Even if for some elements the recovery yield is lower than quantitative, analytical applications can anyway be pursued by using correction factors obtained from the recovery yield of samples of known composition or of added spikes. In addition applications to the demetalation of liquid samples, a reduction, even if not quantitative is always of great importance for example in the field of recycling and reclamation of waters or in the cleaning procedures of liquid effluents. The variation of yields as a function of pH allowed a comparison with the behavior expected on the basis of pure thermodynamic metal–ligand interactions. The patterns have been discussed in terms of a model described above. The use of AG MP-1 + SOX appeared superior with respect to XAD-2 + OX, as also pointed out by the effect of interferents on the recovery and enrichment. Applications to the analysis of real samples were also performed.

LITERATURE CITED

(1) Van Grieken, R. *Anal. Chim. Acta* **1982**, *43*, 3.
(2) Van Loon, J. C. "Selected Methods of Trace Metal Analysis"; *Chemical Analysis*; Wiley: New York, 1985; Vol. 80.
(3) Isshiki, K.; Tsuji, F.; Kuwamoto, T.; Nakayama, E. *Anal. Chem.* **1987**, *59*, 2491.
(4) Vanderborght, B. M.; Van Grieken, R. *Anal. Chem.* **1977**, *49*, 311.
(5) Sturgeon, R. E.; Berman, S. S.; Willie, S. N. *Talanta* **1982**, *29*, 167.
(6) Sarzanini, C.; Mentasti, E.; Porta, V.; Gennaro, M. C. *Anal. Chem.* **1987**, *59*, 484.
(7) Sturgeon, R. E.; Berman, S. S.; Desaulniers, A.; Mykytiuk, A.; McLaren, J. W.; Russell, D. S. *Anal. Chem.* **1980**, *52*, 1585.
(8) Porta, V.; Mentasti, E.; Sarzanini, C.; Gennaro, M. C. *Talanta* **1988**, *35*, 167.
(9) Gennaro, M. C.; Mentasti, E.; Sarzanini, C. *Talanta* **1986**, *33*, 620.
(10) Mentasti, E.; Sarzanini, C.; Gennaro, M. C.; Porta, V. *Polyhedron* **1987**, *6*, 1197.
(11) Gennaro, M. C.; Mentasti, E.; Sarzanini, C. *Polyhedron* **1986**, *5*, 1013.
(12) Sugawara, K. F.; Weetall, H. H.; Schucker, G. D. *Anal. Chem.* **1974**, *46*, 489.
(13) Jezorek, J. R.; Freiser, H. *Anal. Chem.* **1979**, *51*, 366.
(14) Sturgeon, R. E.; Berman, S. S.; Willie, S. N.; Desaulniers, J. A. H. *Anal. Chem.* **1981**, *53*, 2337.
(15) Fang, Z.; Ruzicka, J.; Hansen, E. H. *Anal. Chim. Acta* **1984**, *164*, 23.
(16) Fang, Z.; Zhu, Z.; Zhang, S.; Xu, S.; Guo, L.; Sun, L. *Anal. Chim. Acta* **1988**, *214*, 41.
(17) Honjo, T.; Kitayama, H.; Terada, K.; Kiba, T. *Fresenius' Z. Anal. Chem.* **1988**, *330*, 159.
(18) Nakashima, S.; Sturgeon, R. E.; Willie, S. N.; Berman, S. S. *Fresenius' Z. Anal. Chem.* **1988**, *330*, 592.
(19) Watanabe, H.; Goto, K.; Taguchi, S.; Mc Laren, J. W.; Berman, S. S.; Russell, D. S. *Anal. Chem.* **1981**, *53*, 738.
(20) Ruzicka, J.; Arndal, A. *Anal. Chim. Acta* **1989**, *216*, 243.
(21) Sturgeon, R. E.; Berman, S. S.; Willie, S. N. *Talanta* **1982**, *29*, 167.
(22) Willie, S. N.; Sturgeon, R. E.; Berman, S. S. *Anal. Chim. Acta* **1983**, *149*, 59.
(23) Laxen, D. P. H.; Harrison, R. M. *Anal. Chem.* **1981**, *53*, 345.
(24) Sillên, L. G.; Martell, A. E. *Stability Constants o' Metal Ion Complexes*; The Royal Society of Chemistry: London, 1964; Special Publication No. 18.
(25) Sillên, L. G.; Martell, A. E. *Stability Constants of Metal Ion Complexes*; The Royal Society of Chemistry: London, **1971**, Special Publication No. 25.
(26) Martell, A. E.; Smith, R. M. *Critical Stability Constants*; Plenum Press: New York, 1975; Vol. II.
(27) BASECO program, Sammartano, S.; Rigano, C.; Institute of Analytical Chemistry, University of Messina, Italy.
(28) Sarzanini, C.; Mentasti, E.; Gennaro, M. C.; Marengo, E. *Anal. Chem.* **1985**, *57*, 1960.

RECEIVED for review May 22, 1989. Accepted September 11, 1989. The financial support from The Italian Ministry of Education and the National Research Council of Italy is kindly acknowledged.

Anal. Chem. **1990**, *62*, 27–31

Copper Determination in Urine by Flow Injection Analysis with Electrochemical Detection at Platinum Disk Microelectrodes of Various Radii

Darryl L. Luscombe and Alan M. Bond*

Department of Chemical and Analytical Sciences, Deakin University, Geelong, Victoria 3217, Australia

David E. Davey

The South Australian Institute of Technology, The Levels, P.O. Box 1, Ingle Farm, South Australia 5098, Australia

John W. Bixler

Chemistry Department, State University College at Brockport, Brockport, New York 14420

The incorporation of platinum disk microelectrodes of various radii (2.5–50 μm) in a wall-jet flow cell offers reduced limits of detection for the determination of copper in urine by flow injection analysis compared with standard methods based on a conventional sized glassy carbon disk macroelectrode (radius 1.5 mm), in a thin-layer cell. The radius of the platinum disk microelectrode was found to be critical with respect to both the limit of detection and flow rate dependence. An optimal radius value of 28 μm was found with detection limits increasing with both larger and smaller electrode radii. In contrast, as theoretically expected, a diminished flow rate dependence was observed the smaller the radii of the platinum disk microelectrodes. Sample cleanup and preparation is conveniently achieved by the use of Sep-Pak cartridges and formation of a copper dithiocarbamate complex. The metal complex is easily oxidized at platinum disk microelectrodes in acetonitrile, which was the solvent used in the flow injection method of analysis.

INTRODUCTION

The properties that distinguish microelectrodes from conventional sized electrodes in stationary solution measurements include a predominance of radial diffusion to the electrode, yielding a true steady-state response in experimentally accessible times; a reduced requirement for deliberately added supporting electrolyte; a reduced ohmic *iR* drop in solution; a fast cell response time; and the ability to operate by using a simple two-electrode system rather than the more complex potentiostated system due to the low *iR* drop involved (*1–3*). The use of microelectrodes as analytical detectors in flowing rather than stationary solution systems, to which the above benefits apply, has already been demonstrated (*4–9*). The retention of many of the advantages deduced from measurements on stationary solutions in conventional cells, together with a reduced dependency of peak current on flow rate in flowing solutions, makes the use of microelectrodes as electrochemical detectors for chromatography and flow injection analysis (FIA) particularly appealing (*4–9*).

In this paper we will discuss a flow injection analysis procedure for the determination of copper in urine, using electrochemical detection in a wall-jet cell with platinum disk microelectrodes of variable radii over the range of 2.5–50 μm. A comparison with detection at a conventional sized glassy carbon disk electrode (radius 1.5 mm) in a thin-layer cell is presented to demonstrate the advantages of the microelectrode method over a standard method using commercially available instrumentation. Importantly, in this work it is shown that while improved limits of detection are obtained via the use of microdisk electrodes, there is likely to be an optimal radius and that the limit of detection does not become more favorable as the electrode radius is decreased in size as may be deduced from solely considering the theoretically expected faradaic-to-charging current ratio. This feature of microelectrode detectors having an optimal size is an important aspect of their use that has yet to be widely recognized.

EXPERIMENTAL SECTION

Chemicals. Chemicals were of analytical grade purity and used without further purification, unless otherwise stated. Solvents (Mallinckrodt) were of liquid chromatography grade. The water used in this study was obtained from a Millipore water purification system. Acetate buffer was prepared according to Vogel (*10*). Tetraethylammonium perchlorate (Et_4NClO_4) (Southwestern Analytical Chemicals, Inc.) was recrystallized from methanol and then dried and stored in a vacuum desiccator prior to use.

C_{18} Sep-Pak cartridges were obtained from Waters/Millipore Corp. and used as described in Figure 1.

Flow Injection System. The microelectrode-based FIA system consisted of an ICI LC1500 pump (ICI Instruments, Melbourne, Australia), a Rheodyne 7125 sample injector (20-μL loop), and a Metrohm 656 wall-jet flow cell. The microelectrode cell was operated in the two-electrode mode, with a microelectrode as the working electrode and either a Ag/AgCl (3 M KCl) reference or large-area gold disk (radius 2.5 mm) as the second electrode. The gold disk was found to be suitable for use as a pseudo reference electrode if the current was maintained below 1.0 nA to avoid polarization of the electrode. The current was measured with a Keithley 614 electrometer, and the cell voltage was applied by using a home-built precision voltage source, as described previously (*4, 5*). The macroelectrode FIA system consisted of a Waters 6000A pump coupled to a Rheodyne 7125 sample injector (20 or 50 μL loop) and then to a BAS LC4B thin-layer cell detector, using a glassy carbon working electrode (radius 1.5 mm), stainless steel auxiliary electrode, and Ag/AgCl (3 M KCl) reference electrode.

Microelectrode Fabrication. All microdisk electrodes used in this work were fabricated from platinum wire (Goodfellows, Cambridge, England) of nominal diameters 2.5–50 μm. A length of soda glass tubing was collapsed in a flame, leaving a 1–2-mm hole in the end. A 10–15-mm length of the microwire was placed in the hole and then sealed into the glass. Electrical contact was made by using Wood's Metal (mp 72 °C) to solder the microwire to a length of copper wire, and the body of the electrode was filled with polystyrene to immobilize the connection. The end of the electrode was ground on emery paper and then successively finer grades of alumina slurry (5–0.3 μm) until a mirror smooth finish was obtained (*11*).

Microdisk Electrode Calibration. The radii of all microdisk electrodes fabricated as described above were calibrated prior to use. Slow scan rate voltammetry in a conventional cell of a solution of ferrocene (1.0×10^{-3} M) in acetonitrile (0.10 M

0003-2700/90/0362-0027$02.50/0

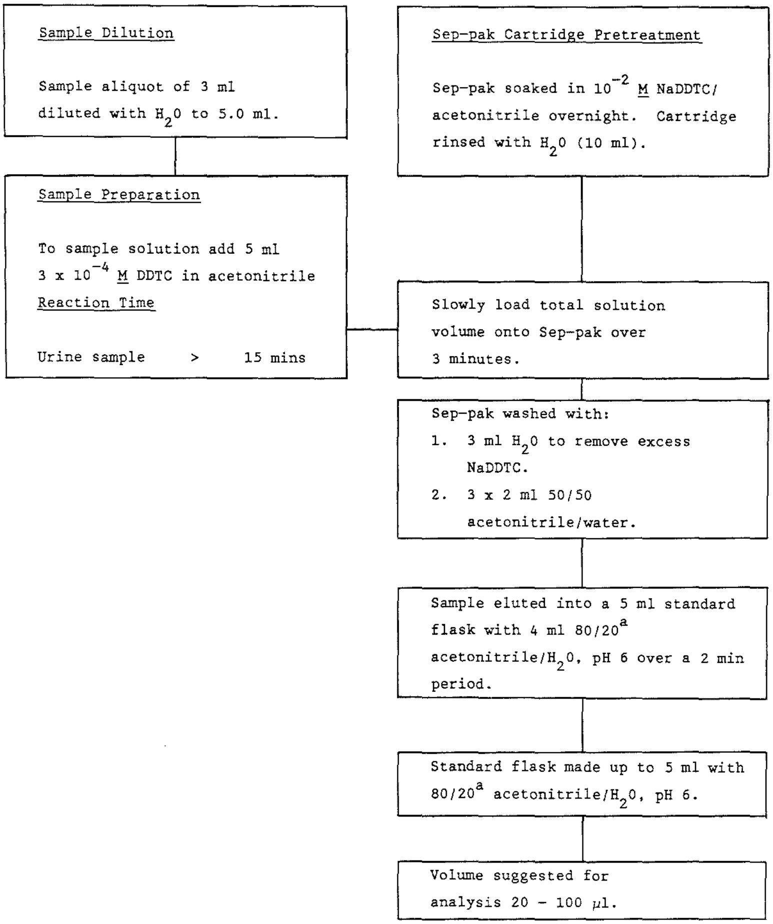

Sample Dilution

Sample aliquot of 3 ml diluted with H_2O to 5.0 ml.

Sample Preparation

To sample solution add 5 ml 3×10^{-4} M DDTC in acetonitrile

Reaction Time

Urine sample > 15 mins

Sep-pak Cartridge Pretreatment

Sep-pak soaked in 10^{-2} M NaDDTC/acetonitrile overnight. Cartridge rinsed with H_2O (10 ml).

Slowly load total solution volume onto Sep-pak over 3 minutes.

Sep-pak washed with:

1. 3 ml H_2O to remove excess NaDDTC.
2. 3 x 2 ml 50/50 acetonitrile/water.

Sample eluted into a 5 ml standard flask with 4 ml $80/20^a$ acetonitrile/H_2O, pH 6 over a 2 min period.

Standard flask made up to 5 ml with $80/20^a$ acetonitrile/H_2O, pH 6.

Volume suggested for analysis 20 - 100 μl.

[a] When microelectrodes were used the sample was eluted with 100% acetonitrile.

Figure 1. Sample preparation and cleanup procedure used for copper in urine by flow injection analysis with electrochemical detection.

Et_4NClO_4) was employed under conditions where a steady-state response is obtained to calibrate the microelectrodes by using the relationship (*12*)

$$i_d = 4nFDCr \qquad (1)$$

where i_d is the diffusion-limited current, n is the number of electrons transferred, F is Faraday's constant, C is the bulk concentration, D is the diffusion coefficient (2.3×10^{-5} cm^2/s (*4*)), and r is radius of the microelectrode.

Procedures. *Urine Collection.* All urine samples were collected as random specimens by the clean-catch/midstream technique described by Schumann (*13*) and acidified and stored as described in ref 14.

Glassware. All glassware used in these determinations was precleaned in an acid bath (2 M HNO_3) for a minimum of 7 days and then throughly rinsed with distilled/deionized water prior to use.

RESULTS AND DISCUSSION

General Methodology. *Determination of Copper as the Diethyldithiocarbamate Complex.* Sodium diethyldithiocarbamate (NaDDTC) and other dithiocarbamate ligands form stable complexes with a wide variety of transition metals (*15*). The nonspecific nature of NaDDTC has meant that careful selection of experimental conditions is necessary to increase the selectivity of the reagent.

In this study, selectivity and sample cleanup are obtained from a combination of the sample preparation procedure and differences in oxidation potentials of the metal–DDTC complexes. For example, from data contained in ref 16 it can be noted that an applied potential of 0.60 V vs Ag/AgCl will selectively oxidize the $Cu(DDTC)_2$ complex, according to a reversible one-electron oxidation reaction

$$Cu(DDTC)_2{}^{+} \rightleftharpoons [Cu(DDTC)_2]^{+} + e^{-} \qquad (1)$$

in the presence of nickel, cobalt, or chromium, which are oxidized at more positive potentials. In the present work, the separation previously performed by the chromatographic column (*14*) is achieved by judicious choice of applied potential.

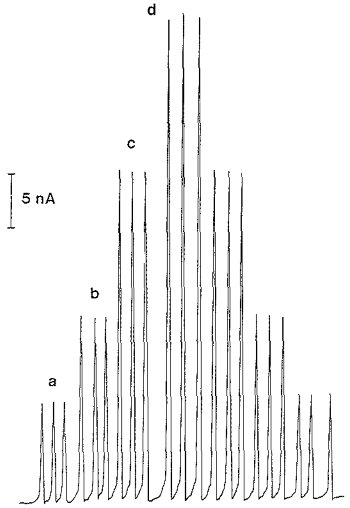

Figure 2. Flow injection response of Cu(DDTC)$_2$ standards in 80/20 acetonitrile/acetate buffer containing 0.2 M NaNO$_3$. Conditions: flow rate, 0.7 mL min^{-1}; sample injection, 50 μL; applied potential, +0.60 V vs Ag/AgCl. The working electrode is a conventional glassy carbon electrode in a thin-layer cell. Concentrations (as Cu) are (a) 10, (b) 20, (c) 40, and (d) 60 ppb.

Sample Determination. In a FIA method where no chromatographic column is employed, no separation of interfering components present in urine is possible during the copper determination. That is, unless a sample cleanup procedure is used, gross interference occurs. A simple and efficient means of sample preparation has been developed using the small disposable solid-phase extraction cartridges (Sep-Pak (Waters)), which are available in a wide range of solid phases. A reversed-phase (C$_{18}$) Sep-Pak was found to be a suitable choice for the sample preparation and cleanup, as detailed in Figure 1. This method, which forms the copper dithiocarbamate complex in an in-situ mode, achieves the equivalent of the chromatography in ref 14 with respect to both cleanup and removal of potentially interfering species. However, the procedure is faster and does not involve dilution.

Macroelectrode Studies. (*a*) *Mobile Solvent Composition.* The optimum mobile solvent composition for FIA experiments when macroelectrode detection with a glassy carbon electrode was employed in a thin-layer cell was found to be 80% acetonitrile/20% acetate buffer (pH = 6.0), with 0.2 M NaNO$_3$ added to increase the conductivity. A decrease in the aqueous component of the mobile solvent leads to a decrease in the limit of detection for copper. The limit of detection (signal-to-noise ratio of 2:1) with 50% acetonitrile was 20 ppb Cu and with 80% acetonitrile was 6 ppb Cu. Concentrations of acetonitrile higher than 80% cause problems with ohmic *iR* drop and cannot be used with a macroelectrode in a thin-layer cell. An example of the FIA response to a standard series of copper solutions is shown in Figure 2. The calibration curves for both the 50/50 and 80/20 (acetonitrile/buffer) mobile solvents are illustrated in Figure 3. Although both mobile solvents yield an excellent linear response, the response per unit concentration of the 80/20 mixture is considerably greater than that of the 50/50 mixture, well above the increase expected due to the flow rate difference present in the two sets of data; hence the lowered limit of detection found with the former. The addition of 5 ppb copper as the Cu(DDTC)$_2$ complex to the mobile solvent (80/20 mixture) was found to improve long-term base-line stability and lowers the detection limit to 3 ppb Cu. This deliberate addition of copper meant that slight variations of background current due to variable copper impurity levels was effectively eliminated. Copper levels in urine are considerably higher than this level, so detection of copper in urine is possible by the procedure of FIA (80/20 solvent mixture) with amperometric detection at a glassy carbon electrode in a thin-layer cell.

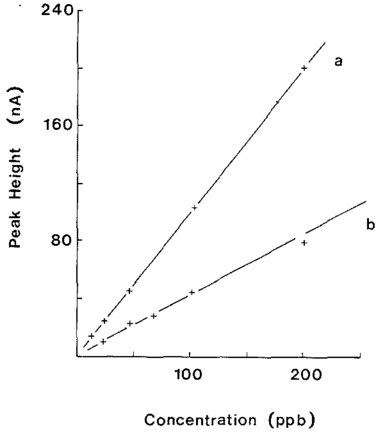

Figure 3. Concentration dependence of FIA peak height for copper with the use of conventional glassy carbon electrode in a thin-layer cell. Conditions: applied potential, +0.60 V vs Ag/AgCl; (a) mobile solvent, 80/20 acetonitrile/acetate buffer containing 0.2 M NaNO$_3$, flow rate, 0.4 mL min^{-1}; (b) mobile solvent, 50/50 acetonitrile/acetate buffer, flow rate, 0.6 mL min^{-1}.

(*b*) *Urine Samples.* Recoveries from deliberately spiked urine samples were determined over the concentration range of 20–100 ppb. For all spiked samples excellent copper recoveries of 100 ± 2% were obtained. Results obtained on three samples obtained from healthy adults (38.8, 40.2, and 37.1 ppb) were also in excellent agreement with data obtained by the previously described chromatographic method (*14*) at the ±5% level, thus validating the procedure developed in this work. The possibility of contamination from the Sep-Pak cartridges was examined and found to be negligible by comparing results from a duplicate series of standards. The first was prepared without the use of Sep-Pak cartridges, and the second according to Figure 1. Within the limits of experimental error no difference was noted, indicating minimal contamination.

Microelectrode Method. (*a*) *Instrumental Considerations.* Most of the measurements with microelectrodes were performed by using a very low impedance 2.5-mm-radius gold disk as reference electrode. If the current exceeded 1.5 nA, the base-line current was found to oscillate before settling out to an equilibrium value. This is attributed to electrode polarization problems. Therefore, as a general rule, the peak current was maintained under 1.0 nA for all microelectrode experiments reported in this paper.

(*b*) *Mobile Solvent Composition.* The effect of mobile solvent composition on detection limits noted for macroelectrode detection was also observed for microelectrodes. However a further decrease in the aqueous component of the mobile solvent and further increase in sensitivity were possible without introducing problems from ohmic *iR* drop. The use of a microelectrode detection system enabled a 100% acetonitrile mobile solvent to be used, with the addition of only 0.001 M Et$_4$NClO$_4$ as the supporting electrolyte.

(*c*) *Analytical Response.* In the analytical problem being considered, FIA provides a simple and efficient means of transferring the samples and standards to the electrochemical cell. The copper concentration may be derived either from

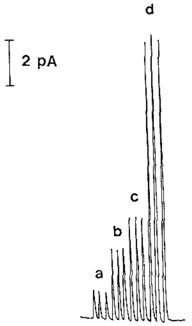

Figure 4. Flow injection response of Cu(DDTC)$_2$ standards in pure acetonitrile containing 0.001 M Et$_4$NClO$_4$, for a 28-μm-radius Pt disk electrode in a wall-jet cell: flow rate, 1.0 mL min^{-1}; applied potential, +0.70 V vs Au pseudo reference electrode. Concentrations of standards (calculated as Cu) are (a) 6.4, (b) 12.8, (c) 25.6, and (d) 64.0 ppb.

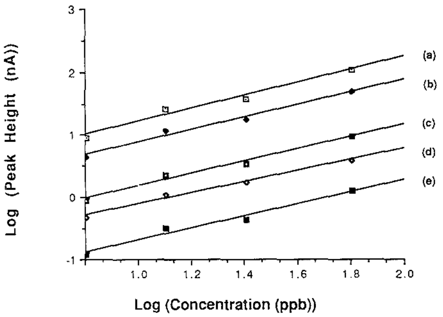

Figure 5. Concentration dependence of FIA peak height for copper observed with a range of Pt microdisk electrodes of different radii: (a) 65.7, (b) 28.1, (c) 13.2, (d) 4.7, (e) 2.5 μm. Concentrations are in parts per billion (calculated as Cu); other conditions are as in Figure 4.

Table I. Detection Limits[a] for the Determination of Copper Using the Microelectrode and Macroelectrode Methods Coupled with Flow Injection Analysis

electrode radius	analytical sensitivity, pA ppm^{-1}	normalized sensitivity, pA ppm^{-1} m^{-2}	lim of detectn, ppb
65.7 μm[b]	1732	1.27×10^{11}	0.83
28.1 μm[b]	768	3.10×10^{11}	0.70
13.2 μm[b]	143	2.61×10^{11}	1.08
4.7 μm[b]	58	8.22×10^{11}	1.40
2.5 μm[b]	20	1.06×10^{12}	3.80
1.5 mm[c]	6.0×10^5	8.45×10^{10}	3.0

[a] Detection limits (S/N ratio of 2:1) and sensitivities calculated in units of concentration of copper added as Cu(DDTC)$_2$. [b] Conditions: platinum microelectrode in a wall-jet cell; mobile solvent, acetonitrile (10^{-3} M Et$_4$NClO$_4$); applied potential, 0.65 V vs Au disk reference electrode; flow rate, 1.0 mL min^{-1}. [c] Conditions: large-area inlaid glassy carbon disk in thin-layer cell; mobile solvent, 80% acetonitrile/20% acetate buffer (0.02 M; pH = 6.0) containing 0.2 M NaNO$_3$; applied potential, 0.60 V vs Ag/AgCl (3 M KCl); flow rate, 1.0 mL min^{-1}.

Table II. Magnitude of Noise and Signal-to-Noise Ratio[a] for Microelectrodes of Different Radii[b] under Conditions of Flow Injection Analysis with a Wall-Jet Cell

electrode radius, μm	noise level, pA	normalized noise, pA m^{-2}	S/N ratio
65.7	0.40	2.95×10^7	65
28.1	0.17	6.85×10^7	70
13.2	0.050	9.13×10^7	45
4.7	0.035	4.96×10^8	31
2.5	0.024	1.27×10^9	13

[a] Signal-to noise ratio calculated for injections of 2×10^{-7} M Cu(DDTC)$_2$ standard. [b] Noise levels calculated as peak-to-peak values, using experimental conditions contained in Figure 4.

the peak height (current) or peak area (charge), as both are a linear function of concentration. A typical FIA microelectrode response to a series of Cu(DDTC)$_2$ standards is shown in Figure 4. The dependence of injected copper concentration on peak height or peak area was determined to be linear for a range of microelectrode sizes, in the concentration range of interest; data for peak height are shown in Figure 5.

It was anticipated that decreasing the size of the electrode would lead to greater analytical sensitivities (more favorable signal-to-noise (S/N) ratios) in flowing systems, as would be predicted for stationary solutions. However, experimental data obtained in this work indicate that decreasing the size of the electrodes below a radius of 28.1 μm leads to a less favorable limit of detection (poorer S/N ratio), as shown in Table I. The area normalized analytical sensitivity did indeed increase as the radius was decreased, but this did not result in a concomitant decrease in detection limits because of the dependence of noise on the electrode radius.

The reason for this behavior is revealed by a detailed examination of the short-term variation in the background current (noise). The background noise was found to vary with electrode radius (Table II), where a decrease in radius corresponds to a decrease in observed noise. However the noise level decreases at a slower rate as the radius is decreased than does the faradaic response, as evidenced by the S/N ratios calculated for the 2×10^{-7} M Cu(DDTC)$_2$ standard. Similar results were obtained for all concentrations of Cu(DDTC)$_2$. An increase in S/N from varying the radius from 65.7 to 28.1 μm is followed by a progressive decrease in S/N as the radius decreases. We can therefore find no analytical benefit in incorporating microelectrodes less than 28.1 μm for the determination of copper in wall-jet type detectors. The higher background found with small-radii electrodes is presumably a result of imperfect sealing and other nonidealities introduced during the fabrication and polishing of the smaller electrodes. The question of noise in flowing solutions is complex (*17, 18*) and needs to be further addressed with respect to microelectrodes.

(*d*) *Flow Rate Effects*. The variation of current with rate of mass transport, or flow rate, is expected to vary with the geometry of the flow cell and the nature of the electrodes employed.

The dependence of peak height on flow rate has the form

$$i_p \propto U^x \tag{2}$$

where i_p is peak current, U is flow rate, and x is flow rate dependence. When a sample of electroactive species is injected into the flowing stream, a transient or peak shaped response is the result. When the electroactive species is present in the mobile solvent, such that a constant uniform concentration of the analyte is flowing into the detector cell, then a steady-state response is observed. The experimentally determined flow rate dependencies for these two kinds of experiments are shown in Table III.

The range of flow rate dependencies observed with the microelectrodes does not correspond to any particular flow model described in the literature (*19–22*). However, the smallest electrode (radius = 2.5 μm) examined is the least dependent on flow rate, as theoretically expected. Thus, while the greater analytical sensitivity is not achieved with the smaller electrodes, the theoretically decreased dependence on

Table III. Exponential Flow Rate Dependencies in a Wall-Jet Cell for a Range of Microelectrodes of Different Radii[a]

	flow rate dependence (x)	
electrode radius, μm	transient response	steady-state response
65.7	0.80	0.90
28.1	1.11	0.85
13.2	0.95	0.61
4.7	0.72	0.59
2.5	0.43	0.40

[a] Flow rate dependence of the form $i \propto U^x$ where U is the flow rate and x is the flow rate dependence. The concentration of copper was 1.0×10^{-6} M $Cu(DDTC)_2$ in acetonitrile (10^{-3} M Et_4NClO_4). The flow rate was varied from 0.4 to 1.6 mL min^{-1}, in 0.2 mL min^{-1} increments.

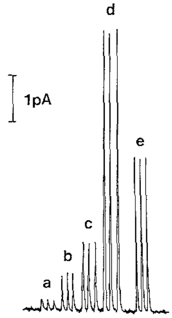

Figure 6. Flow injection response of copper in human urine. Concentrations of standards (calculated as Cu) are (a) 0.7 ppb, (b) 3.2 ppb, (c) 6.4 ppb, (d) 31.8 ppb, (e) diluted urine sample (see Figure 1). Other conditions are as in Figure 4.

flow rate is observed and is a distinct advantage when flow rate variations are introduced into a flowing system by the pump.

(*e*) *Urine Samples.* The results for the determination of copper in a urine sample using FIA with amperometric detection at a 28.1-μm microelectrode are shown in Figure 6. The concentrations determined on individually collected samples on consecutive days were 26.7 ± 2 and 34.4 ± 2 ppb Cu, respectively. These results fall within the limits expected for a normal healthy adult (*23–25*) and are in agreement with results obtained by the high-performance liquid chromatography method described previously (29.1 ± 1.5 ppb) (*14*). In the previous study (*14*), extensive studies on the medical status, sample collection, storage, and sample treatment were undertaken. Similar considerations with respect to sample treatment and storage apply to the present method. Readers are referred to ref 14 for these aspects of urine analysis.

CONCLUSIONS

1. The method for the determination of copper in urine using the sample preparation method described in Figure 1 with electrochemical detection at both conventional glassy carbon electrode–thin-layer cell configurations and microelectrode–wall-jet cell configurations has been found to be simple to perform.

2. The microelectrode method exhibits a considerable improvement in the limit of detection and in some instances decreased dependence on flow rate over that found with the conventional approach. Both methods are sufficiently sensitive for the determination of copper in urine at naturally occurring levels. The absence of the column present in the previously described chromatographic method (*14*) leads to lower detection limits than previously reported. This is a considerable advantage for determining copper in urine of healthy adults.

3. There was found to be limited benefit in using extremely small microelectrodes. An increase in the limit of detection was observed with a decrease in electrode radius below 28.1 μm. However, the dependence of peak current on flow rate does decrease as the electrode radius decreases, and this could be an advantage in some circumstances.

4. The decrease in signal-to-noise ratio with decreasing microelectrode radius is interesting. Data obtained from chromatographic separation and electrochemical detection indicate that the same trend is found when high-performance liquid chromatography is associated with the analytical scheme. It therefore appears that this effect may be a general phenomenon associated with electrochemical detection at microelectrodes.

Registry No. NaDDTC, 148-18-5; Cu, 7440-50-8; Pt, 7440-06-4.

LITERATURE CITED

(1) Bond, A. M.; Oldham, K. B.; Zoski, C. G. *Anal. Chim. Acta* **1989**, *216*, 177–230.
(2) Wightman, R. M.; Wipf, D. O. In *Electroanalytical Chemistry*; Bard, A. J., Ed.; Marcel Dekker: New York, 1988; Vol. 15, pp 267–353.
(3) *Ultramicroelectrodes*; Fleischmann, M., Pons, S., Rolison, D. R., Schmidt, P. P., Eds.; Datatech Systems Publishers: Morganton, NC, 1987.
(4) Bixler, J. W.; Bond, A. M. *Anal. Chem.* **1986**, *58*, 2859–2863.
(5) Bixler, J. W.; Bond, A. M.; Lay, P. A.; Thormann, W.; van den Bosch, P.; Fleischmann, M.; Pons, B. S. *Anal. Chim. Acta* **1986**, *187*, 67–77.
(6) Caudill, W. L.; Howell, J. O.; Wightman, R. M. *Anal. Chem.* **1982**, *54*, 2532–2535.
(7) Khoo, S. B.; Gunasingham, H.; Tay, B. T. *J. Electroanal. Chem. Interfacial Electrochem.* **1987**, *216*, 115–126.
(8) St. Claire, R. L., III; Jorgenson, J. W. *J. Chromatogr. Sci.* **1985**, *23*, 186–191.
(9) Knecht, L. A.; Guthrie, E. J.; Jorgenson, J. W. *Anal. Chem.* **1984**, *56*, 479–482.
(10) Vogel, A. *A Textbook of Quantitative Inorganic Analysis*; Longmans: London, 1968; p 1161.
(11) Bond, A. M.; Luscombe, D. L.; Oldham, K. B.; Zoski, C. G. *J. Electroanal. Chem. Interfacial Electrochem.* **1988**, *249*, 1–14.
(12) Oldham, K. B. *J. Electroanal. Chem. Interfacial Electrochem.* **1987**, *237*, 303–307.
(13) Schumann, G. B. *Urine Sediment Examination*; Waverly Press: Baltimore, 1980; p 13.
(14) Bond, A. M.; Knight, R. W.; Reust, J. B.; Tucker, D. J.; Wallace, G. G. *Anal. Chim. Acta* **1986**, *182*, 47–59.
(15) Fries, J.; Getrost, H. *Organic Reagents for Trace Analysis*; E. Merck: Darmstadt, FRG, 1977; pp 125–152.
(16) Bond, A. M.; Wallace, G. G. *Anal. Chem.* **1982**, *54*, 1706–1712.
(17) Fox, K.; Armstrong-James, M.; Millar, J. *J. Neurosci. Methods* **1980**, *3*, 37–48.
(18) Morgan, D. M.; Weber, S. G. *Anal. Chem.* **1984**, *56*, 2560–2567.
(19) Yamada, J.; Matsuda, H. *J. Electroanal. Chem. Interfacial Electrochem.* **1973**, *44*, 189–198.
(20) Chin, T. S.; Tsang, C. H. *J. Electrochem. Soc.* **1978**, *125*, 1461–1470.
(21) Albery, W. J.; Bruckenstein, S. *J. Electroanal. Chem. Interfacial Electrochem.* **1983**, *144*, 105–112.
(22) Dalhuijsen, A. J.; van der Meer, Th. H.; Hoogendoorn, C. J.; Hoogvliet, J. C.; van Bennekom, W. P. *J. Electroanal. Chem. Interfacial Electrochem.* **1985**, *182*, 295–313.
(23) Sunderman, F. W., Jr. In *Chemical Diagnosis of Disease*; Brown, S. S., et al., Eds.; Elsevier/North Holland Biomedical Press: Amsterdam, 1979; pp 1015–1021.
(24) Piscator, M. In *Handbook on the Toxicology of Metals*; Friberg, L., et al., Eds.; Elsevier/North Holland Biomedical Press: Amsterdam, 1979; pp 411–420.
(25) Sunderman, F. W., Jr.; Roszel, N. O. *Am. J. Clin. Pathol.* **1967**, *48*, 286–300.

RECEIVED for review November 28, 1988. Accepted September 27, 1989.

Surface Acoustic Wave Sensor Response and Molecular Modeling: Selective Binding of Nitrobenzene Derivatives to (Aminopropyl)triethoxysilane

Wolfgang M. Heckl, Francesca M. Marassi, Krishna M. R. Kallury, David C. Stone, and Michael Thompson*

Department of Chemistry, University of Toronto, 80 St. George Street, Toronto, Ontario M5S 1A1, Canada

A number of derivatives of nitrobenzene have been found to bind selectively to a surface acoustic wave sensor treated with (aminopropyl)triethoxysilane. The relative binding affinities, measured by analyzing the frequency shift over time, exhibit response behaviors ranging from reversible to irreversible. These results can be explained in terms of a molecular orbital AM1 study of the binding behavior of the different analytes to the (aminopropyl)triethoxysilane film. The theoretical calculations indicate that differences in hydrogen bond strength and dipole moment are responsible for the observed selectivity.

INTRODUCTION

Piezoelectric devices that can generate and support acoustic waves have attracted considerable attention in the area of chemical and biosensor research (*1*). The majority of applications have employed the bulk acoustic wave (BAW) device together with an adsorptive coating to provide some degree of response selectivity toward the analytes of interest (*2, 3*). Recently the surface acoustic wave (SAW) device has been introduced. A detailed description of the design and operation of such devices may be found in the work of Wohltjen (*4, 5*).

When a suitable radio frequency (rf) signal is applied to the input terminals of a SAW device, a Rayleigh wave is generated that propagates along the surface and gives rise to an alternating voltage on the output terminals. When incorporated into an oscillator circuit, any perturbation of the acoustic wave will result in a change of the wave velocity, frequency, amplitude, and phase. Factors producing such effects include changes of temperature, pressure, deposited mass, and surface conductivity. For example, the frequency shift produced by applying a thin organic film to the surface of a SAW crystal may be approximated by

$$\Delta f = (k_1 + k_2) f_0^2 h \rho \qquad (1)$$

where Δf is the frequency change, k_1 and k_2 are material constants for the crystal, f_0 is the initial frequency, and h and ρ are the film thickness and density, respectively. Since $h\rho$ is the mass per unit area, it can be seen that Δf is proportional to the change in surface mass and the square of the oscillator frequency. One important implication of this is that the higher the frequency, the greater the sensitivity of the device.

In a manner analogous to that for the BAW sensor, the SAW device has been employed with a variety of empirically chosen coatings for the gas-phase detection of organic species (*6–8*), substances of environmental importance (*9–12*), and hydrogen (*13*). An attempt to deal with the problem of marginal selectivity, provided by various coatings, has involved the use of an array of devices with different films deposited on each, followed by the application of pattern recognition techniques for responses of the whole configuration to a number of gases (*14*). Other applications include use as a gas chromatographic detector (*15*), in polymer analysis (*16*), and in immunoassay (*17*), although the importance of Rayleigh waves in the latter experiment has been disputed (*18*).

Although there has been a recent escalation of interest in molecular recognition derived on a synthetic basis (*19*), little of this technology has found application in the realm of chemical sensor science. In molecular recognition, selectivity is usually achieved by means of noncovalent interactions, the most significant being hydrogen bonding (H-bonding) involving hydroxylic and amino functions. Previous work with BAW devices in our laboratory has revealed a selectivity of (aminopropyl)triethoxysilane (APTES) for nitroaromatics (*20*). To investigate this effect more thoroughly, we used the more sensitive SAW system. This approach has some advantages over previous ones. The APTES selective coating is covalently bound to the SAW crystals, giving stability to the sensor. The interaction between APTES and the analytes is believed to be mainly due to H-bonding, a desirable interaction from the point of view of chemical sensors due to its reversibility. The higher sensitivity of the SAW device allows such a weak, reversible interaction to be detected.

In order to understand the mechanism of selective binding on a molecular level, this paper introduces the combination of a new experimental setup with molecular orbital computational methods. Until recently only very large basis set ab initio computations have been successful in calculating hydrogen bonds. However these methods can only be applied to molecules of limited size due to the high cost and long computing time required. The AM1 semiempirical molecular orbital method (*21*), the latest by Dewar, overcomes some of the problems of modified neglect of diatomic overlap (MNDO) (*22*) and is the only effective method for the study of hydrogen bonds on larger size molecules.

EXPERIMENTAL SECTION

Apparatus and Materials. A schematic diagram of the experimental setup used is shown in Figure 1. The SAW crystals were 52-MHz dual delay line devices obtained from Microsensor Systems, Inc. (Springfield, VA). These were mounted inside the gas cell of the CEM-52 RF electronics and power supply system from the same source. This unit includes the necessary components for two oscillators, and a mixer stage that gives the difference frequency (Δf) between the two (Figure 1b). Thus the two sides of the crystal can be used as sample and reference channels, respectively. The change in Δf obtained by loading one side of the crystal with a mass of 1 μg indicated a mass sensitivity of ±14 Hz/ng. The gas chromatograph was a Varian Model 2740 fitted with a gas control system and glass-lined injection splitter (Chromalytic Technology P/L), a 30 m × 0.25 mm Duribond DB1 capillary column (J & W Scientific, Inc., Rancho Cordova, CA), and a flame ionization detector. Chromatographic peaks were observed with a Hewlett-Packard 3390A reporting integrator. The split flow from the injector was diverted to the SAW detector. By measuring the various gas flow rates and the split ratio, it was possible to present known amounts of different sample compounds to the SAW detector in the gas phase. Connections between the injector and the SAW detector were kept as short as possible. The GC was used to confirm successful injection and monitor the

0003-2700/90/0362-0032$02.50/0

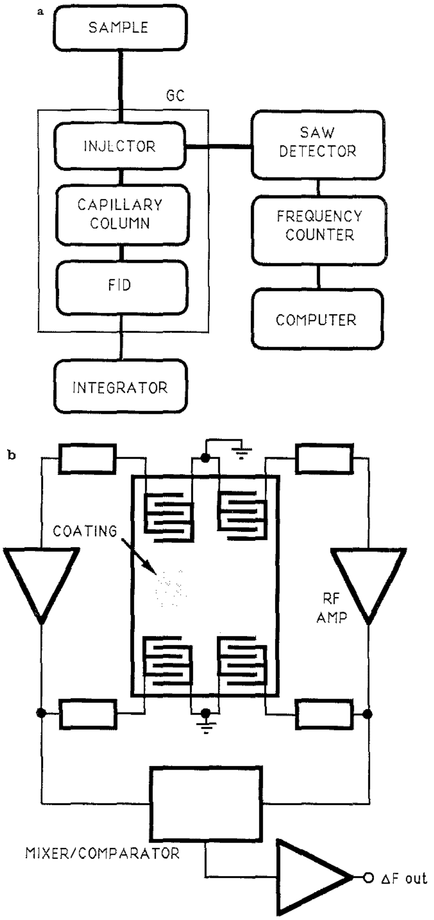

Figure 1. Schematic diagram of the experimental setup: (a) general outline and (b) 52-MHz dual SAW delay line oscillator system diagram (Microsensor Systems, Inc.).

sample for any impurities. Nitrogen was used as the carrier gas, and all gas lines were fitted with moisture and hydrocarbon traps. The difference frequency was measured by using a Hewlett-Packard 5334A frequency counter linked to a personal computer for data acquisition and display.

The following compounds were analyzed: (1) 2-nitroanisole; (2) 2-nitrotoluene; (3) 4-fluoronitrobenzene; (4) nitrobenzene; (5) 3-fluorotoluene; (6) 2-fluorotoluene; (7) anisole; (8) acetone; (9) toluene; (10) benzene. APTES, nitrobenzene, nitroanisole, 2-nitrotoluene, 2-fluorotoluene, 3-fluorotoluene, anisole, and 4-fluoronitrobenzene (Aldrich Chemical Co.) were purified by distillation before use. Chloroform, methanol, acetone, benzene, and toluene (ACS reagent grade) were dried over either phosphorus pentoxide or a molecular sieve as appropriate and were distilled before use.

Surface Coating Procedure. The surface of the SAW crystal was chemically modified through the reaction of APTES with the surface silanol groups of the quartz. The reaction was carried out in a specially constructed cell that left a 5 × 5 mm area of the surface between the electrodes on one side of the crystal exposed to the APTES. This corresponded to the largest area of one delay line that could be chemically treated without affecting the interdigital transducers. The crystal was treated with 5 mL of a 2% solution of APTES in dry toluene (room temperature, 24 h), followed by repeated washing with chloroform and acetone and subsequent vacuum drying for 1 h. The change in Δf observed after treatment with APTES was 4000 ± 100 Hz, corresponding to about 285 ng or 7 layers of APTES. This was in good agreement with the film thickness obtained by ellipsometric measurements. The APTES film was further characterized by X-ray photoelectron spectroscopy (XPS) using an SSX-100 ESCA spectrometer under conditions described previously (*23*). The surface coverage measured by this technique was found to be greater than 90%, and the measured film thickness agrees well with the above results.

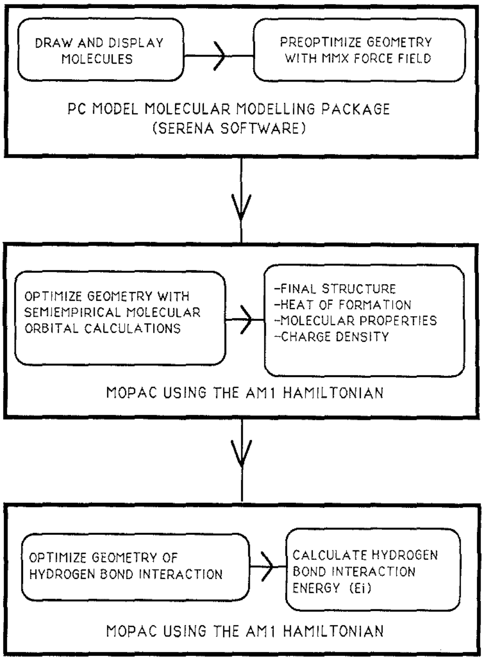

Figure 2. Flow chart of molecular modeling and calculation routines.

Experimental Measurements. A 0.5-μL aliquot of each sample compound, corresponding to a mass of about 400–600 ng, was injected in turn. For all the measurements the injection temperature was 240 °C, the split flow rate was 40 mL/min, and the split ratio was 1:40. The change in Δf with time was recorded by using the computer. Each injection was repeated three times and the complete set of experiments repeated by using a second crystal treated in a manner identical with the first. The crystal was positioned in the holder in such a way that preferential adsorption on the APTES-coated side of the crystal resulted in an increase in Δf.

Computational Methods. The PC Model (*24*) molecular graphics/modeling package was used to construct and display the structures of compounds **1**–**10**. The structures were preoptimized by using the molecular mechanics MMX force field in PC Model. Further geometry optimizations were performed by using the AM1 semiempirical molecular orbital method in MOPAC (*25*). All geometrical parameters were optimized with the exception that the aromatic rings were constrained to be planar. AM1 was then used to study the H-bonding interaction between the APTES terminal amino hydrogens and the compounds under study. In the calculations methylamine was used as a substitute for the APTES propyl function to enconomize on computer time. For the energy calculations of the intermolecularly H-bonded complexes, all geometrical parameters were held fixed except for the bond lengths, angles, and dihedral angles of the amino hydrogens and the H-bond acceptor atoms directly involved in the interaction; these parameters were optimized. The reported H-bond interaction energies (E_i) are all AM1 values. All calculations were

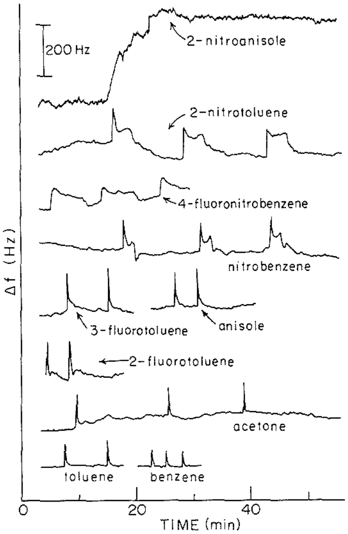

Figure 3. Frequency shift (hertz) over time (min) after multiple injections of the analytes on the APTES-coated SAW surface. Vertical bar represents 200 Hz.

done on the Macintosh II. Figure 2 is a flow chart showing the molecular modeling and calculation routines performed.

RESULTS AND DISCUSSION

Experimental Measurements. The results obtained for the 10 different analytes are shown in Figure 3. The same results were obtained for both crystals. It should be noted that the entire surface of the crystal is exposed to the gas flow, while the area coated with APTES accounts for about 13% of the active area of one delay line (see above). Therefore the observed change in Δf represents the difference in adsorption behavior between the APTES and the bare quartz: If analyte was adsorbed to the same extent by the APTES coating and the bare quartz, no change in Δf would be observed. This means that the value of Δf does not give an absolute measure of the adsorption of analyte by the APTES. However, adsorption on the reference delay line is largely compensated for by adsorption to the untreated area of the sample delay line. Thus the change in Δf provides a good estimate of the extent of adsorption to the APTES film, allowing a comparison to be made between the observed relative binding affinity (RBA) values for the different analytes and their corresponding calculated E_i values. (See also the discussion of the APTES structure below).

Table I. Results of Experimental Measurements and AM1 Calculations for the 10 Analytes Used

compound	exptl rel binding affinity	calcd E_i, kcal/mol	calcd dipole moment, D	bp, °C
1 2-nitroanisole	a	−7.100	6.198	276.8
2 2-nitrotoluene	1.00	−3.349	4.915	221.7
3 4-fluoronitrobenzene	0.93	−3.212	3.737	214.6
4 nitrobenzene	0.83	−3.325	5.238	210.8
5 3-fluorotoluene	0.37	−1.739	1.763	116.0
6 anisole	0.36	−1.876	1.249	155.0
7 2-fluorotoluene	0.31	−1.262	1.394	114.0
8 acetone	0.14	−2.604	2.921	56.2
9 toluene	0.10		0.265	110.6
10 benzene	0.05		0.000	80.1

[a] Irreversible.

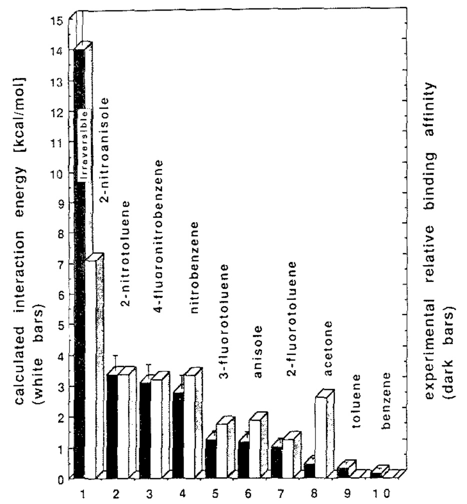

Figure 4. Correlation of the theoretical results to the experimental data.

Acetone, toluene, and benzene show very little preferential adsorption to the APTES coating, the observed peaks being sharp and narrow. The signals obtained for anisole, 2-fluorotoluene, and 3-fluorotoluene indicate a somewhat greater interaction with the APTES coating. The results for nitrobenzene, 4-fluoronitrobenzene, and 2-nitrotoluene show an even greater interaction with the APTES coating, while that for 2-nitroanisole was essentially irreversible and solvent had to be used to remove the compound from the surface of the SAW crystal. To obtain a more objective comparison between the different analytes, a relative binding affinity was calculated. The area under the curve for each peak is a function of the total mass of material passed over the surface of the crystal and was found by cutting and weighing. This area was divided by the molecular weight for each compound. The mean corrected area over three injections was taken to give the RBA for each analyte, and the results are shown in Figure 4 and Table I. These confirm the trend noted from the Δf curves, namely that the compounds tested appear to fall into the following groups: slight, moderate, and large reversible preferential adsorption, and irreversible adsorption.

Theoretical Calculations. The results of the AM1 calculations are included in Table I. Figure 5a shows some of the H-bonding geometries possible between the APTES amino function and nitrobenzene, while the H-bond geometries that gave the highest values of E_i by AM1 are shown in Figure 5b. From this it becomes apparent that the compounds that can form the greatest number of H bonds via their electron lone pair donor functions are the ones with the highest E_i and RBA. Thus 2-nitroanisole with three H bonds has the highest E_i, 2-nitrotoluene, 4-fluoronitrobenzene, and nitrobenzene form two H bonds and have medium E_i, while 3-fluorotoluene, anisole, 2-fluorotoluene, and acetone form one H bond and have a small E_i. This trend is illustrated in Figure 4 where the good agreement between the theoretical E_i values and the experimental RBAs is shown. Discrepancies between theory and experiment may be partly accounted for by the neglect of H-bonding with the π electron systems of the analytes in the calculation. This interaction, which is shown in scheme C of Figure 5a, was not calculated with AM1; therefore no E_i

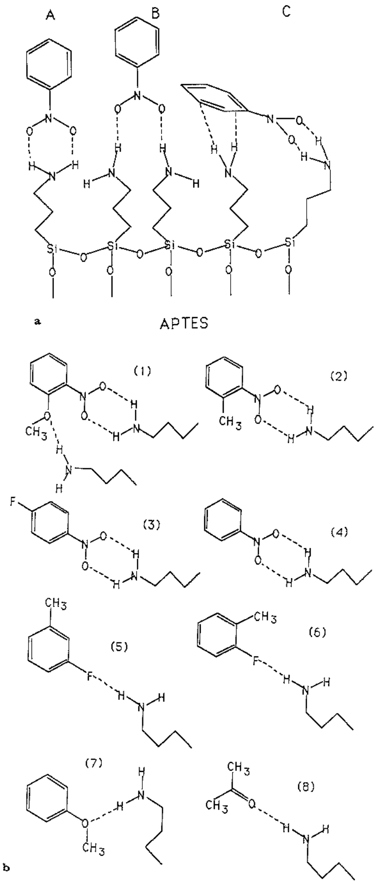

Figure 5. (a) Possible H-bonding geometries of nitrobenzene with APTES. (b) Optimal H-bonding geometries for compounds **1**–**8** with the APTES amino hydrogens.

values for toluene and benzene are available. The AM1 dipole moments of compounds **1**–**10** were also calculated (Table I) and are found to follow the same trend as the RBA and the E_{i} values.

Interpretation of the Results. The experimental RBAs in Table I show that there is a preferential interaction of the compounds with the APTES-coated side of the crystal compared with the bare quartz. Specific adsorption of the analytes to the SAW surface is believed to occur through the following interactions: H-bonding, dipole–dipole, and π- Si d orbital overlap. The energy of specific adsorption, which is reflected by the RBA and which is a result of the above interactions, must depend on three important factors: the nature of the adsorbing surface coating, the density of H-bonding groups available for interaction with the analytes, and the electronic structure of the adsorbate. In addition the boiling point may contribute to the observed RBA of the compounds. The relative importance of these factors with respect to the specific interactions is discussed below.

In recent years several reports (*23*, *26*–*34*) have appeared on the characterization of silica treated with silanizing agents by techniques such as XPS, XRF, NMR, ESR, and IR. The structure of the surface coating was found to depend upon the silanization conditions, the extent of substrate hydration, and the postsilanization treatment. A recent report (*35*) and our own XPS results (*24*) indicate that under anhydrous conditions, at room temperature, the APTES film does not contain many free silanol or ethoxy groups and is mostly in the cross-linked siloxane form. The probable structure of the APTES film is the one resulting from vertical polymerization to give a cagelike three-dimensional multilayer array (*33*). High-resolution XPS studies on the amino N 1s binding energy peak show the presence of two components: one for the neutral, nonbonded amino function and the other for the amino function H-bonded or protonated by the acidic silanols of the APTES and to a lesser extent of the substrate. Thus the APTES coating on our SAW quartz crystal can be described as a vertically cross-linked siloxane with approximately 65% free amino groups and 35% H-bonded or protonated ones.

The H-bonding interaction with the APTES, contributing to the specific adsorption of the analytes, occurs through the amino hydrogens. The possibility of the analytes H-bonding to the APTES and substrate silanol hydrogens is regarded to be minimal due to the low silanol abundance. The few silanols that are present are acidic and become involved in H-bonding with the basic APTES nitrogen. Such H-bonding renders the hydrogens on the amino function more positive and hence more capable of interacting with an electron-rich group on the analytes. H-bonding also occurs with the bare quartz surface hydroxyls, which have an average surface density of 4.6 OH/100 Å^2 for a fully hydroxylated surface (*36*). Indeed the hydroxyl group is a stronger H-bond donor than the primary amine group because the higher electronegativity of the oxygen allows the hydroxyl hydrogen to be more positive; therefore the increased binding to the APTES-coated side must be a result of the higher concentration of H-bond donors in the APTES compared to that of the bare quartz. The APTES coating, consisting of a few layers, forms a thin film providing a greater number of H-bonding sites; thus the analyte molecules diffuse through this film and are more concentrated by it than by the bare quartz. It is this diffusion through the layers that allows the entire analyte molecule to interact with APTES, via both the aromatic ring and its electronegative substituents, thus maximizing the total interaction energy.

The electronic structure of compounds **1**–**10** can be obtained from the electron population analysis, a result of the AM1 molecular orbital calculation. This molecular property is useful in understanding the H-bonding behavior since the specific H-bonding interaction is governed by the local electron distribution in a given adsorbate molecule. Two types of H-bonds can be distinguished: those to lone pair electron donors, such as the acetone oxygen, and those to π electron donors, such as the aromatic rings. IR studies have indicated that the former can be from 2 to 10 times as strong as the latter depending on the particular molecule involved (*36*).

The nitro oxygens in compounds **1**–**4** have lone pair electrons that can be donated for H-bonding. The negative charge on the oxygens was calculated to be of the order of −0.35; thus each nitro group can form two H bonds and the calculations give similar E_{i} values for compounds **2**–**4**. The higher E_{i} of compound **1** is due to a third H bond which it can form with the methoxy group whose oxygen has a charge of −0.18. This extra interaction contributes 3.775 kcal/mol above the E_{i} of nitrobenzene and is believed to be responsible for the irreversible signal of 2-nitroanisole. The π electron density of the aromatic rings of the nitro-substituted compounds **1**–**4** is affected by the other ring substituents and decreases in the order **1**, **2**, **3**, and **4**. This is not surprising since it follows the order of decreasing electron-releasing ability of the substituents, methoxy, methyl, and fluoro; therefore it is expected that the strength of H-bonding to the π system should follow the same trend. H-bonding with the π system increases the total energy of specific adsorption of compound 1 and is probably responsible for differentiating the RBAs of compounds 2–4.

The negative charges on the fluorines and oxygen of compounds 5–7 were calculated to be −0.11, −0.11, and −0.21, respectively; moreover, all these groups are lone pair electron donors and can form one H bond with APTES. The calculated E_i values indicate that the strengths of these H bonds fall approximately in the same range, with the strongest being the one to the most negative group, the anisole methoxy. The electron density of the π ring of compound 5 is slightly greater than that of compound 7 due to the relative positions of the fluoro and methyl groups and to their ortho-, para-directing abilities: In compound 5 the positions para and ortho to both the fluoro and methyl group coincide, while in compound 7 they do not. The strong electron-releasing ability of the methoxy group places the ring electron density of anisole between those of compounds 5 and 7. Therefore the strength of H-bonding to these aromatic systems should decrease in the order **5**, **6**, **7**, the same trend observed in the experimental RBAs. Anisole has an aromatic system with greater electron density than nitrobenzene; however, the former interacts with APTES to a lower extent than does the latter, indicating that the contribution to the total energy of specific adsorption from H-bonding with the π system must be smaller than the contribution from H-bonding with lone pair electrons.

Compounds 1–7 are therefore capable of participating in a dual or multiple interaction with the APTES amino hydrogens through their aromatic nuclei and the lone pair electrons of the ring substituents. Acetone, on the other hand, can be classified as a lone pair electron donor since it is only capable of H-bonding through the lone pair electrons of the oxygen whose AM1 negative charge was calculated to be −0.29. The AM1 results indicate that this interaction, with an E_i of −2.604 kcal/mol, is stronger than those of compounds **5**, **6**, and **7**. Toluene and benzene are π electron donors because they are only capable of H-bonding to APTES via their aromatic rings, and this explains their low RBAs. Furthermore the π aromatic system of toluene is more electron-rich due to the electron-releasing ability of the methyl group; therefore H-bonding to toluene is stronger than H-bonding to benzene. This energy difference is reflected in the relative magnitudes of the experimental RBAs of the two compounds.

Although the total dipole moment is not directly related to the H-bond strength, it does govern the extent of the dipole–dipole interaction. The latter is believed to contribute to the total energy of specific adsorption for those compounds that are substantially polar. Indeed, dipole moments calculated by AM1 are found to follow a trend similar to that of the experimental RBAs. The presence of a small number of protonated amino nitrogens, detected by XPS, renders the APTES more polar and may enhance the importance of electrostatic dipole–dipole interactions.

The extent of specific interaction between the π systems and the Si d orbitals is also determined by the electron density of the π systems, and therefore it should follow the same trend discussed above for H-bonding with the π electron donors. However the donation of π bonding electrons to the vacant d orbitals of Si is sterically hindered by the fact that Si is already tetrahedrally coordinated, and so π Si d bonding is not expected to make a large contribution to the total energy of specific adsorption of the compounds to APTES.

The boiling points of compounds **1**–**10** may influence the degree of their retention by the APTES film due to differences in transport behavior. That is, the low-boiling compounds would have a higher instantaneous concentration in the carrier gas stream than the high-boiling ones. Thus, acetone, with a boiling point of 56.2 °C, appears to be too volatile to be trapped by the APTES cagelike structure under ambient conditions and therefore will show less nonspecific adsorption. This explains the low RBA measured for acetone in spite of its predicted ability to form a stronger H bond than compounds **5**, **6**, and **7**. However, boiling point (or volatility) is not the determining factor in the measured RBA value. As an example, the toluene compounds **5**, **7**, and **9** have very similar boiling points of 116, 114, and 110.6 °C, respectively, but quite different RBAs which follow the same pattern as the calculated E_i values. Therefore it is possible to conclude that the electrostatic interactions discussed above are the major determinants of the specific adsorption of the analytes to APTES. Another example illustrating the minimal importance of the boiling point is the fact that toluene and benzene, with boiling points higher than that of acetone, have lower RBAs than the latter. This is due to the fact that toluene and benzene participate in H-bonding only as π electron donors and have negligible dipole moments, whereas this is not the case for acetone.

The molecular orbital calculations allow us to conclude that the major forces responsible for the observed experimental signals are H-bonding to lone pair electron donors, and less importantly H-bonding to π electron donors and dipole–dipole interactions. Thus, the compounds can be classified into five groups with the RBAs reflecting their H-bonding behavior. Compound 1 constitutes the first group and interacts irreversibly through three lone pair electron donor functions and one aromatic nucleus. Compounds **2**–**4** in the second group and compounds **5**–**7** in the third all form a H bond through their aromatic nucleus, but the former contain two lone pair electron donor functions and have large RBAs, while the latter only contain one such function and have moderate RBAs. Acetone, in the fourth group, with a single lone pair donor function has a small RBA, and finally, compounds **9** and **10**, in group five, are only π electron donors and are characterized by very slight RBAs. This classification is well illustrated by Figure 4 where the five different RBA levels are clearly visible. The fact that H-bonding is the predominant factor in specific adsorption is also demonstrated by the following observation. Treatment of the APTES coating with a 1% methanolic hydrochloric acid solution, followed by alcohol washing, resulted in a 50% reduction of the RBA of nitrobenzene. Reacting the acid-treated APTES with methanolic triethylamine restored the original RBA value. Acid treatment increases the abundance of protonated amines so that the predominant interaction of APTES with the nitrobenzene is not H-bonding but an acid–base proton donation without binding. Thus it is clear that when the ability of APTES to act as a H-bond donor is diminished, the experimental RBA is also greatly diminished.

CONCLUSIONS

This work has been a first attempt at developing a sensor based on the H-bonding interaction between an acceptor analyte and a donor surface. The results show that the SAW sensor can be used as a probe of H-bond strength. This sensor possesses the three major requirements of sensitivity, reversibility, and selectivity. The sensitivity is a result of the high-frequency 52-MHz SAW device, which allows an interaction as weak as the hydrogen bond to be detected. Selectivity can then be obtained by preparing surface coatings with specifically oriented hydrogen bonds of well defined geometry. This can be achieved by the templating technique in conjunction with the molecular modeling design of coatings selective for specific target molecules. Work in this direction is presently under way in our laboratory.

LITERATURE CITED

(1) Bastiaans, G. J. In *Chemical Sensors*; Edmonds, T. E., Ed.; Blackie: Glasgow, U.K., 1988; p 295.

(2) Alder, J. F.; McCallum, J. J. *Analyst* **1983**, *108*, 1169.
(3) Glassford, A. P. M. In *Application of Piezoelectric Quartz Crystal Microbalances*; Lu, C. S., Czanderna, A. W., Eds.; Elsevier: New York, 1984; p 281.
(4) Wohltjen, H.; Dessy, R. *Anal. Chem.* **1979**, *51*, 1458.
(5) Wohltjen, H. *Sens. Actuators* **1984**, *5*, 307.
(6) Wohltjen, H.; Snow, A. W.; Barger, W. R.; Ballantine, D. S. *IEEE Trans. Ultrason. Ferro. Freq. Control* **1987**, *34*, 172.
(7) Grate, J. W.; Snow, A.; Ballantine, D. S.; Wohltjen, H.; Abraham, M. H.; McGill, R. A.; Sasson, P. *Anal. Chem.* **1988**, *60*, 869.
(8) Rose-Pehrsson, S. L.; Grate, J. W.; Ballantine, D. S.; Jurs, P. C. *Anal. Chem.* **1988**, *60*, 2801.
(9) Bryant, A.; Poirier, M.; Riley, G.; Lee, D. L.; Vetelino, J. F. *Sens. Actuators* **1983**, *4*, 105.
(10) Vetelino, J. F.; Lade, R. K.; Falconer, R. S. *IEEE Trans. Ultrason. Ferro. Freq. Control* **1987**, *34*, 156.
(11) Nieuwenhuizen, M. S.; Nederlof, A. J.; Barendsz, A. W. *Anal. Chem.* **1988**, *60*, 230.
(12) Cook, R. L.; MacDuff, R. C.; Sammels, A. F. *Anal. Chim. Acta* **1989**, *217*, 101.
(13) D'Amico, A.; Palma, A.; Verona, E. *Sens. Actuators* **1982**, *3*, 31.
(14) Ballantine, D. S.; Rose, S. L.; Grate, J. W.; Wohltjen, H. *Anal. Chem.* **1986**, *8*, 3058.
(15) Wohltjen, H.; Dessy, R. *Anal. Chem.* **1979**, *51*, 1465.
(16) Wohltjen, H.; Dessy, R. *Anal. Chem.* **1979**, *51*, 1470.
(17) Roederer, J. E.; Bastiaans, G. J. *Anal. Chem.* **1983**, *55*, 2333.
(18) Calabrese, G. S.; Wohltjen, H.; Roy, M. K. *Anal. Chem.* **1987**, *59*, 833.
(19) *Molecular Inclusion and Molecular Recognition*; Topics in Current Chemistry 149; Weber, E., Ed.; Springer Verlag: Berlin, 1988.
(20) Rajaković, L.; Ghaemmaghami, V.; Kallury, K. M. R.; Thompson, M., submitted for publication in *Anal. Chim. Acta*.
(21) Dewar, M. J. S.; Zoebisch, E. G.; Healy, E. F.; Stewart, J. J. P. *J. Am. Chem. Soc.* **1985**, *107*, 3902.
(22) Dewar, M. J. S.; Thiel, W. *J. Am. Chem. Soc.* **1977**, *99*, 4899.
(23) Kallury, K. M. R.; Krull, U. J.; Thompson, M. *Anal. Chem.* **1988**, *60*, 169.
(24) PC Model. Molecular Modelling Software, Serena Software, Bloomington, IN.
(25) Stewart, J. J. P.; Seiler, F. J. MOPAC Version 4.0, QCPE, Bloomington, IN.
(26) Hannicutt, M. L.; Harris, J. M. *Anal. Chem.* **1986**, *58*, 748.
(27) Cukman, D.; Jednacak-Biscan, J.; Veksil, Z.; Haller, W. *J. Colloid Interface Sci.* **1987**, *115*, 357.
(28) Moses, P. R.; Wier, L. M.; Lennox, J. C.; Finklea, H. O.; Lenhard, J. R.; Murray, R. W. *Anal. Chem.* **1978**, *50*, 576.
(29) Willmann, K. W.; Rocklin, R. D.; Nowak, R.; Kuo, K. N.; Shultz, F. A.; Murray, R. W. *J. Am. Chem. Soc.* **1980**, *102*, 7629.
(30) Hair, M. L.; Hertl, W. *J. Phys. Chem.* **1969**, *73*, 2372.
(31) Puglisi, O.; Torris, A.; Marletta, G. *J. Non-Cryst. Solids* **1984**, *68*, 219.
(32) Ratner, B. D.; Rosen, J. J.; Hoffman, A. S.; Scharpen, L. H. In *Surface Contamination*; Mittal, K. L., Ed.; Plenum: New York, 1979.
(33) Sindorf, D. W.; Maciel, G. E. *Anal. Chem.* **1983**, *105*, 3767.
(34) Kelusky, E. C.; Fyfe, C. A. *J. Am. Chem. Soc.* **1986**, *108*, 1746.
(35) Caravajal, G. S.; Leyden, D. E.; Quinting, G. R.; Maciel, G. E. *Anal. Chem.* **1988**, *60*, 1776.
(36) Knozinger, H. In *The Hydrogen Bond: Recent Developments in Theory and Experiments*; Schuster, P., et al., Eds.; North Holland Publ. Co.: Amsterdam, 1976; Chapter 27, p 1264.

RECEIVED for review August 4, 1989. Accepted October 2, 1989. Support for this work from the Institute of Chemical Science and Technology, Canada, and the Natural Sciences and Engineering Research Council of Canada is gratefully acknowledged. In addition, we are indebted to the Deutsche Forschungsgemeinschaft, West Germany, for a postdoctoral stipend to W.M.H. through He 1617/1-1.

How Long Does It Take a Microelectrode To Reach a Voltammetric Steady State?

Cynthia G. Zoski[1] **and Alan M. Bond**

Department of Chemical and Analytical Sciences, Deakin University, Geelong, Victoria 3217, Australia

E. Tracey Allinson and Keith B. Oldham*

Department of Chemistry, Trent University, Peterborough, Ontario K9J 7B8, Canada

Though steady-state conditions offer a number of voltammetric advantages, the degree to which the steady state is attained is often in experimental doubt. A theoretical study of the long-time voltammetric behavior of microelectrodes leads to the conclusion that steady states are reached in similar times by potentiostatic and galvanostatic routes. For reversible processes, the time to reach the steady state is independent of the position of the target point on the voltammetric wave, but for irreversible processes the steady state is attained much faster toward the bottom of the wave than near its plateau. Hemispherical and disk microelectrodes of equivalent size take the same length of time to reach steady states. Experimental confirmation is reported for the reversible oxidation of ferrocene in acetonitrile at a microdisk electrode.

The development of efficient techniques (*1–11*) for fabricating microelectrodes has given a valuable impetus to steady-state voltammetry, because it is only at electrodes that are small in both their superficial dimensions that steady states can be achieved in times short enough to avoid natural convection (*12*). Two geometries are of especial interest: the hemispherical electrode resting on an infinite plane (*12, 13*), and the inlaid disk electrode (*12–14*). The first is important because it possesses the simplifying feature of "uniform accessibility" (*12, 15*); the second, because of its ease of construction (*1, 8–11*).

A feature of steady-state voltammetry (*12*) not shared by the more familiar transient voltammetries is that the interrelationship between current and potential is unique, being totally independent of the experimental method used to achieve the steady state. For example, consider a steady state to be attained by imposing a constant potential E on a microelectrode and waiting (theoretically for an infinite time) until the current has decayed to its final steady value $i(\infty)$. Of course, $i(\infty)$ is a function of the choice of E, $i(\infty) = f\{E\}$, in this potentiostatic steady-state experiment. Now imagine that, in a separate experiment with the same microelectrode in the same solution, this same current $i(\infty)$ is passed constantly through the cell. The electrode potential will drift, but will ultimately acquire a steady value $E(\infty)$ whose magnitude is a function of the applied current, $E(\infty) = g\{i(\infty)\}$, in this galvanostatic steady-state experiment. Uniqueness implies that the function $g\{\}$ is the inverse function of $f\{\}$, so that $E(\infty)$ and E are equal

$$E(\infty) = g\{i(\infty)\} = g\{f\{E\}\} = E \qquad (1)$$

In other words, the shapes of galvanostatic and potentiostatic steady-state voltammograms are identical.

---

[1] Present address: Pastore Chemical Laboratory, University of Rhode Island, Kingston, RI 02881.

0003-2700/90/0362-0037$02.50/0

A voltammetric steady state is a condition that is approached as a limit and is never theoretically attained. Thus when we speak of the time to "reach" a steady state, we actually mean the time that it takes to arrive at some state within a specified closeness to the steady state. With this understanding of what is meant by "reach", this article will address the question of which route—the potentiostatic route or the galvanostatic route—reaches the steady state first. Several related questions will also be addressed: Is the time to reach a steady state affected by the degree of reversibility of the electrode reaction? Are all points on a steady-state voltammogram reached in equal lengths of time? Do inlaid disk microelectrodes and microhemispherical electrodes of equivalent size reach steady states equally promptly, or does one take significantly longer than the other?

Before seeking answers to these various questions, we establish certain "ground rules" concerning the electrodes and the experiments to which they are subjected, as well as giving a description of the steady states themselves.

To establish an equivalency between a hemispherical and an inlaid disk microelectrode, we define (*13*) the "superficial diameter" d, as the distance from one edge of the electrode to the other, measured along the electrode surface. Thus, a microdisk of radius a and a microhemisphere of radius r_0 are of equivalent size when their superficial diameters are equal: $\pi r_0 = d = 2a$.

STEADY-STATE VOLTAMMOGRAMS

Consider the n-electron oxidation reaction

$$\mathrm{R(soln)} \underset{k_\mathrm{b}}{\overset{k_\mathrm{f}}{\rightleftharpoons}} \mathrm{O(soln)} + ne \tag{2}$$

occurring at the interface between a microelectrode and a solution containing a bulk concentration $c_\mathrm{R}{}^\mathrm{b}$ of the electroreactant with species O initially absent. The solution is unstirred and contains excess supporting electrolyte, so that transport occurs solely by diffusion. The diffusion coefficients of O and R are taken as equal, with the symbol D assigned to each. The heterogeneous rate constants k_f and k_b are assumed to obey the Butler–Volmer equations

$$k_\mathrm{f} = k^\circ \exp\{(1-\alpha)nF[E - E^\circ]/RT\} \tag{3}$$

$$k_\mathrm{b} = k^\circ \exp\{-\alpha nF[E - E^\circ]/RT\} \tag{4}$$

in terms of the three constant parameters E°, α, and k°.

The shapes of steady-state voltammograms differ between hemispherical and disk microelectrodes, except when k_f and k_b are both so large that only their ratio is significant. Under such reversible conditions, the steady current and the steady potential at an electrode of superficial diameter d are interrelated by (*13*)

$$i(\infty) = \frac{2nFc_\mathrm{R}{}^\mathrm{b}Dd}{1 + \exp\{nF[E^\circ - E(\infty)]/RT\}} = \frac{i_\mathrm{d}(\infty)}{2}\left[1 + \tanh\left\{\frac{nF[E(\infty) - E^\circ]}{2RT}\right\}\right] \tag{5}$$

Note that we adopt the convention that anodic current is positive. Equation 5 may be rearranged to

$$E(\infty) = E^\circ - \frac{RT}{nF}\ln\left\{\frac{i_\mathrm{d}(\infty) - i(\infty)}{i(\infty)}\right\} = E^\circ - \frac{RT}{nF}\ln\left\{\frac{1-h}{h}\right\} \tag{6}$$

where $i_\mathrm{d}(\infty)$ is the steady-state diffusion-limited current, given by

$$i_\mathrm{d}(\infty) = 2nFc_\mathrm{R}{}^\mathrm{b}Dd \tag{7}$$

and h is the fractional wave height of a steady-state voltammogram

$$h = i(\infty)/i_\mathrm{d}(\infty) = i(\infty)/(2nFc_\mathrm{R}{}^\mathrm{b}Dd) \tag{8}$$

For future use, we take the derivative of eq 5, expressing the slope of the reversible steady-state voltammogram

$$\left(\frac{\mathrm{d}i}{\mathrm{d}E}\right)_\infty = \frac{nFi_\mathrm{d}(\infty)}{4RT}\,\mathrm{sech}^2\left\{\frac{nF[E(\infty) - E^\circ]}{2RT}\right\} = \frac{nF(1-h)i(\infty)}{RT} \tag{9}$$

Equations 1, 6, and 9 apply only to *reversible* steady-state voltammograms, but they hold equally for microdisks and microhemispheres, and they apply whether the steady state is reached potentiostatically or galvanostatically.

The general equation for potentiostatic voltammetry at a spherical electrode (*16, 17*), written for a hemisphere of superficial diameter d reads

$$i(t) = 2nFc_\mathrm{R}{}^\mathrm{b}D^{1/2}k_\mathrm{f}d\left[\frac{1}{\lambda} + \left(\frac{d}{\pi D^{1/2}} - \frac{1}{\lambda}\right)\exp\{\lambda^2 t\}\,\mathrm{erfc}\,\{\lambda t^{1/2}\}\right] \tag{10}$$

where $\lambda = \pi D^{1/2}/d + (k_\mathrm{f} + k_\mathrm{b})/D^{1/2}$. As $t \to \infty$, the exponential-error-function-complement term vanishes, leaving

$$i(\infty) = 2nFc_\mathrm{R}{}^\mathrm{b}D^{1/2}k_\mathrm{f}d/\lambda = k_\mathrm{f}i_\mathrm{d}(\infty)/(\lambda D^{1/2}) \tag{11}$$

It is this equation that, in the $k_\mathrm{f} \to \infty \leftarrow k_\mathrm{b}$ limit, reduces to the reversible steady-state eq 5, after the Butler–Volmer relationships 3 and 4 are adopted.

The equation for an irreversible steady-state voltammogram at a microhemisphere results from setting $k_\mathrm{f} \gg k_\mathrm{b}$ in eq 11, leading to (*13*)

$$i(\infty) = \frac{2nFc_\mathrm{R}{}^\mathrm{b}d}{(\pi/k_\mathrm{f}d) + (1/D)} = \frac{i_\mathrm{d}(\infty)}{1 + (\pi D/k^\circ d)\exp\{(1-\alpha)nF[E^\circ - E(\infty)]/RT\}} \tag{12}$$

or its equivalent inverse

$$E(\infty) = E^\circ - \frac{RT}{(1-\alpha)nF}\ln\left\{\frac{(1-h)}{h}\right\} - \frac{RT}{(1-\alpha)nF}\ln\left\{\frac{k^\circ d}{\pi D}\right\} \tag{13}$$

The slope of the irreversible steady-state voltammogram is

$$\left(\frac{\mathrm{d}i}{\mathrm{d}E}\right)_\infty = \frac{(1-\alpha)nFi_\mathrm{d}(\infty)}{4RT} \times \mathrm{sech}^2\left\{\frac{(1-\alpha)nF[E(\infty) - E_{1/2}(\infty)]}{2RT}\right\} = \frac{(1-\alpha)nF(1-h)i(\infty)}{RT} \tag{14}$$

where the irreversible steady-state half-wave potential $E_{1/2}(\infty)$ results from setting $h = {}^1/_2$ in eq 13.

CRITERIA OF CLOSENESS

Let the curve in Figure 1 represent some steady-state voltammogram and the vertical line be the approach route to that voltammogram in a particular potentiostatic experiment. The label O identifies the point (the "target" point) on the voltammogram that would be reached after an infinite time, whereas P is a point close to O that is actually reached in some finite time t. If $i(\infty)$ and $i(t)$ are the ordinates of points

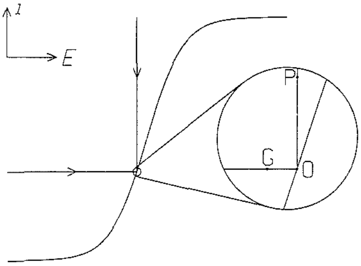

Figure 1. Illustration of the potentiostatic approach of the current and the galvanostatic approach of the potential to a particular "target" point on a steady-state voltammogram.

O and P, then the experiment has come within a certain percentage ϵ of the steady state, if

$$\frac{\epsilon}{100} = \frac{i(t) - i(\infty)}{i(\infty)} \tag{15}$$

Further, t_ϵ^{P} is used to indicate the time at which identity 15 is attained

$$i(t_\epsilon^{\mathrm{P}}) = \frac{100 + \epsilon}{100} i(\infty) \tag{16}$$

The superscript "P" indicates that t_ϵ^{P} is the time to reach a state within ϵ% of the steady state potentiostatically. For example, t_5^{P} is the time at which the potentiostatic current equals 105% of its ultimate value.

Similarly t_ϵ^{G} represents the time required by a galvanostatic experiment to reach a point ϵ% away from the steady state. The horizontal line in Figure 1 represents the course of a galvanostatic experiment that would, ultimately, reach the same target point as in the previously described potentiostatic experiment. G is the point actually reached in time t_ϵ^{G}. Thus G lies on the galvanostatic route at a point such that "G is as close to O as is P", so that the same percentage closeness ϵ is ascribed to each. The most reasonable way of making this comparison of "apples and oranges" is to say that points G and P are equivalently close to O if the slope of the straight line joining G to P in Figure 1 matches the slope of the voltammogram itself at the target point. That is

$$\frac{i(t) - i(\infty)}{E(\infty) - E(t)} = \left(\frac{\mathrm{d}i}{\mathrm{d}E}\right)_\infty \tag{17}$$

where $E(\infty)$ and $E(t)$ are the abscissas of points O and G. Hence, utilizing definition 15, we can associate the time t_ϵ^{G} with a closeness percentage ϵ if, during a galvanostatic approach to the steady state

$$E(t_\epsilon^{\mathrm{G}}) = E(\infty) - \frac{\epsilon i(\infty)}{100}\left(\frac{\mathrm{d}E}{\mathrm{d}i}\right)_\infty \tag{18}$$

The justification for considering 16 and 18 as equivalent criteria for a closeness of ϵ% to a voltammetric steady state comes from noting that a single near-steady-state voltammogram may be drawn through two sets of points, some determined potentiostatically and some galvanostatically provided that a single small value of ϵ attaches to all the experiments.

A criterion superior to 18 would replace $(\mathrm{d}E/\mathrm{d}i)_\infty$, the reciprocal of the voltammogram's slope at the target point, by an average value of $(\mathrm{d}E/\mathrm{d}i)$ over the interval from t to infinity. We do not introduce this refinement but our failure to do so introduces an anomaly into our predictions. Because criterion 18 becomes more inappropriate as $h \rightarrow 1$, we use the phrase "plateau anomaly" to refer to false galvanostatic predictions arising from this cause. The plateau anomaly disappears for small enough values of ϵ; for $\epsilon \leq 5$, it affects only the top one-quarter of the wave, $0.75 \leq h < 1$, and only the top one-tenth seriously.

Table I. Times to Reach a Reversible Steady State at Inlaid Disk (Radius a) and Hemispherical (Radius r_0) Microelectrodes to within 5% and 1% for a Diffusion Coefficient of 10^{-9} m^2 s^{-1} and the Superficial Electrode Diameters Listed

a/μm	0.25	0.50	1.0	2.5	5.0	10	25
r_0/μm	0.16	0.32	0.64	1.6	3.2	6.4	16
d/μm	0.50	1.0	2.0	5.0	10	20	50
t_5/s	0.0032	0.013	0.052	0.32	1.3	5.2	32
t_1/s	0.081	0.32	1.3	8.1	32	132	780

POTENTIOSTATIC APPROACH TO A REVERSIBLE STEADY STATE AT A MICROHEMISPHERE

In this section we examine the relationship governing the approach of the transient current $i(t)$ to the ultimate steady current $i(\infty)$ under potentiostatic conditions; i.e. when the potential of a hemispherical microelectrode is suddenly (at time $t = 0$) stepped from a value at which no current flows to some reaction-inducing value E.

For reversible voltammetry, k_f and k_b are both extremely large and under these conditions eq 10 reduces to

$$i(t) = 2nFc_\mathrm{R}^{\mathrm{b}}D^{1/2}k_\mathrm{f}d\left[\frac{1}{\lambda} + \frac{d}{\pi D^{1/2}}\exp\{\lambda^2 t\}\operatorname{erfc}\{\lambda t^{1/2}\}\right] \tag{19}$$

where λ is redefined as $\lambda = (k_\mathrm{f} + k_\mathrm{b})/D^{1/2}$. For very large $\lambda t^{1/2}$, $\exp\{\lambda^2 t\}\operatorname{erfc}\{\lambda t^{1/2}\}$ is accurately equivalent to $1/(\pi^{1/2}\lambda t^{1/2})$, so that further simplification occurs to

$$i(t) = \frac{2nFc_\mathrm{R}^{\mathrm{b}}Dk_\mathrm{f}d}{k_\mathrm{f} + k_\mathrm{b}}\left[1 + \frac{d}{(\pi^3 Dt)^{1/2}}\right] = i(\infty)\left[1 + \frac{d}{(\pi^3 Dt)^{1/2}}\right] \tag{20}$$

where $i(\infty)$ is given by eq 5. The simplicity of eq 20 means that it is straightforward to extrapolate currents obtained at a series of finite times to obtain $i(\infty)$.

Equation 20 describes the approach to the steady state by a potentiostated microhemispherical electrode under reversible conditions. It may be combined with eq 16, which provides a definition of the time t_ϵ^{P} to approach the steady state potentiostatically to within a closeness of ϵ%, to produce

$$t_\epsilon^{\mathrm{P}} = 10^4 d^2/(\pi^3 \epsilon^2 D) \tag{21}$$

Table I lists times calculated by this formula. It will transpire that eq 21 is obeyed under circumstances other than those currently being considered; Table I is therefore labeled more comprehensively than the present need warrants. The tabulated data confirm the well-known result that electrodes of micrometer dimensions "reach" steady states within seconds but that the time required is crucially dependent on the electrode size.

POTENTIOSTATIC APPROACH TO AN IRREVERSIBLE STEADY STATE AT A MICROHEMISPHERE

Irreversibility of reaction 2 corresponds to the inequality $k_\mathrm{f} \gg k_\mathrm{b}$ at all potentials at which significant current flows. Insertion of $k_\mathrm{f} + k_\mathrm{b} = k_\mathrm{f}$ into eq 10 leads to

$$i(t) = \frac{2nFc_\mathrm{R}^{\mathrm{b}}D^{1/2}k_\mathrm{f}d}{\lambda}\left[1 + \frac{k_\mathrm{f}d}{\pi D}\exp\{\lambda^2 t\}\operatorname{erfc}\{\lambda t^{1/2}\}\right] \tag{22}$$

where now

$$\lambda = (\pi D^{1/2}/d) + (k_f/D^{1/2}) \tag{23}$$

An equation equivalent to 22 is already in the literature (*17*). Combining it with eq 11 for the steady-state current leads to

$$\frac{i(t) - i(\infty)}{i(\infty)} = \frac{k_f d}{\pi D} \exp\{\lambda^2 t\} \operatorname{erfc}\{\lambda t^{1/2}\} = \frac{k_f d}{\pi^{3/2}\lambda D t^{1/2}}\left[1 - \frac{1}{2\lambda^2 t} + \frac{3}{4\lambda^4 t^2} - ...\right] \tag{24}$$

in which we have used an asymptotic expansion (*18*) of the exponential-error-function-complement term. At times long enough that $1/(2\lambda^2 t)$ and subsequent terms are negligible compared with unity (we shall return later to check the implications of this assumption), eq 24 simplifies to

$$\frac{i(t) - i(\infty)}{i(\infty)} = \frac{k_f d}{\pi^{3/2}\lambda D t^{1/2}} = \frac{d}{(\pi^3 D t)^{1/2}[1 + (\pi D/k_f d)]} \tag{25}$$

Unlike the corresponding expression for the reversible case, a potential dependence enters eq 25 via the k_f term. Instead of introducing this dependence explicitly, we utilize the quantity h, defined in eq 8 as the fractional wave height in the steady state, which implicitly depends on potential. Consecutive combinations of eq 15, 25, 12, and 8 lead to

$$\frac{\epsilon}{100} = \frac{i(t) - i(\infty)}{i(\infty)} = \frac{d}{(\pi^3 D t)^{1/2}[1 + (\pi D/k_f d)]} = \frac{i(\infty) d}{(\pi^3 D t)^{1/2} i_d(\infty)} = \frac{hd}{(\pi^3 D t)^{1/2}} \tag{26}$$

which gives

$$t_\epsilon^{\mathrm{P}} = 10^4 h^2 d^2/(\pi^3 \epsilon^2 D) \tag{27}$$

as the time for the potentiostatic approach to reach within ϵ% of an irreversible steady state at a hemispherical microelectrode.

Equation 27 differs from its reversible analogue, eq 21, only by the presence of the h^2 multiplier. On the diffusion plateau of an irreversible steady-state voltammogram, $h = 1$, and so the equations are identical and Table I applies. Elsewhere on the wave, $h < 1$, and therefore the irreversible steady state is reached faster than is the corresponding reversible steady state. For example, at the half-wave point, $h = {}^1/_2$ and the steady state is attained 4 times as fast.

It remains to justify our assumption that $1/(2\lambda^2 t_\epsilon^{\mathrm{P}}) \ll 1$. Using eq 11 and 23 to express λ in terms of h by eliminating k_f, and substituting for t_ϵ^{P} from eq 27, one finds that the inequality is equivalent to

$$\frac{1}{2\lambda^2 t_\epsilon^{\mathrm{P}}} = \frac{\pi(1-h)^2\epsilon^2}{(2 \times 10^4)h^2} \ll 1 \tag{28}$$

For any reasonable value of ϵ, this inequality is satisfied except for very small values of h, corresponding to the foot of the voltammetric wave. With $\epsilon = 5$, for example, the left-hand side of the inequality is less than 0.04, provided $h \geq 0.25$.

GALVANOSTATIC APPROACH TO A REVERSIBLE STEADY STATE AT A MICROHEMISPHERE

Standard methods (*19*) show that during a galvanostatic experiment at a hemispherical electrode of superficial diameter d, the concentrations of R and O at the surface of the microelectrode obey the relationships

$$c_R^b - c_R^s = c_O^s = \frac{i}{2nFDd}\left[1 - \exp\left\{\frac{\pi^2 D t}{d^2}\right\} \operatorname{erfc}\left\{\frac{\pi D^{1/2} t^{1/2}}{d}\right\}\right] \tag{29}$$

The concentrations approach finite steady values provided that the applied current i does not exceed $2nFc_R^bDd$, which we henceforth assume. Otherwise, the system encounters a chronopotentiometric "transition time" (*19*) and reaction 2 ceases to carry all the applied current.

Equation 29 is valid for all degrees of reversibility of reaction 2, but if the reaction is reversible, we may adopt the Nernst equation to arrive at

$$E(t) = E^\circ - \frac{RT}{nF} \ln\left\{\frac{\dfrac{2nFc_R^bDd}{i} - 1 + \exp\{1/(\pi\mu^2)\} \operatorname{erfc}\{1/(\pi^{1/2}\mu)\}}{1 - \exp\{1/(\pi\mu^2)\} \operatorname{erfc}\{1/(\pi^{1/2}\mu)\}}\right\} \tag{30}$$

where the abbreviation

$$\mu = d/(\pi^3 D t)^{1/2} \tag{31}$$

is used. As $t \rightarrow \infty$, the exponential-error-function-complement terms in eq 30 vanish and we arrive at

$$E(\infty) = E^\circ - \frac{RT}{nF} \ln\left\{\frac{i_d(\infty) - i}{i}\right\} \tag{32}$$

in agreement with eq 6 and confirming that the same steady state is achieved galvanostatically and potentiostatically.

In line with definition 8, we can replace $2nFc_R^bDd/i$ in eq 30 by $i_d(\infty)/i$ and hence by $1/h$. When eq 32 is then subtracted from eq 30, the result

$$E(t) - E(\infty) = -\frac{RT}{nF} \times \ln\left\{\left[\frac{(1/h) - 1 + \exp\{1/(\pi\mu^2)\} \operatorname{erfc}\{1/(\pi^{1/2}\mu)\}}{1 - \exp\{1/(\pi\mu^2)\} \operatorname{erfc}\{1/(\pi^{1/2}\mu)\}}\right] \times \left(\frac{h}{1-h}\right)\right\} \tag{33}$$

emerges. This result is exact, but we now embark on a long sequence of approximations and transformations of the logarithmic term in eq 33, which are valid provided μ is sufficiently small. Later we shall reexamine this question and determine conditions under which the overall approximation is acceptable. We start by replacing each of the exponential-error-function-complement terms by μ (*18*)

$$\ln\left\{\left[\frac{(1/h) - 1 + \exp\{1/(\pi\mu 2)\} \operatorname{erfc}\{1/(\pi^{1/2}\mu)\}}{1 - \exp\{1/(\pi\mu 2)\} \operatorname{erfc}\{1/(\pi^{1/2}\mu)\}}\right] \times \left(\frac{h}{1-h}\right)\right\} \simeq \ln\left\{\left[\frac{(1/h) - 1 + \mu}{1 - \mu}\right]\left(\frac{h}{1-h}\right)\right\} = \ln\left\{\frac{1 - h + h\mu}{(1-\mu)(1-h)}\right\} \simeq \ln\left\{\frac{(1 - h + h\mu)(1 + \mu)}{1-h}\right\} = \ln\left\{\frac{1 - h + \mu + h\mu^2}{1-h}\right\} \simeq \ln\left\{\frac{1 - h + \mu}{1-h}\right\} = \ln\left\{1 + \frac{\mu}{1-h}\right\} \simeq \frac{\mu}{1-h} \tag{34}$$

so that

$$E(t) - E(\infty) = \frac{-RT\mu}{nF(1-h)} = \frac{-RTd}{nF(1-h)(\pi^3 D t)^{1/2}} \tag{35}$$

if the approximations are valid. Experimental confirmation

Table II. A Test of Approximation 34 for $\mu = 0.0500$

h	term footnoted	$\mu/(1-h)$
0.010	0.0516	0.0505
0.050	0.0537	0.0526
0.250	0.0675	0.0667
0.500	0.0997	0.100
0.750	0.190	0.200
0.950	0.717	1.00
0.990	1.83	5.00

$\ln \{[((1/h) - 1 + \exp\{1/(\pi\mu^2)\} \operatorname{erfc} \{1/(\pi^{1/2}\mu)\})/(1 - \exp\{1/(\pi\mu^2)\} \operatorname{erfc} \{1/(\pi^{1/2}\mu)\})](h/(1-h))\}$.

of eq 35 would be provided by a linear graph of $E(t)t^{1/2}$ versus $t^{1/2}$.

The criterion of being within ϵ% of a galvanostatic steady state is embodied in eq 18 which, in view of result 9, may be written

$$E(t_\epsilon^{\mathrm{G}}) - E(\infty) = \frac{\epsilon RT}{100nF(1-h)} \tag{36}$$

Comparison of eq 35 and 36 leads to $\epsilon/100 = d/(\pi^3 Dt)^{1/2}$ or

$$t_\epsilon^{\mathrm{G}} = 10^4 d^2/(\pi^3\epsilon^2 D) \tag{37}$$

This formula for t_ϵ^{G} is identical with that for t_ϵ^{P} given in eq 21. Thus, at least when approximation 34 is valid, a galvanostatic steady state is reached at a reversible microhemispherical electrode in the same time that it takes for a potentiostatic steady state to be attained. Table I therefore applies.

In fact, approximation 34 is not valid at all points on the voltammetric wave, but only in its lower reaches. If we treat 5% as the largest error of interest then, from eq 31 and 37, $\mu \le 0.05$. Table II lists values of the exact expression in 34 and of the $\mu/(1-h)$ approximant, for the worst ($\epsilon = 5$) case and for a range of values of h. Notice that the agreement is almost perfect at the half-wave point and is acceptable for $0 < h \le 0.75$. The approximation could be considered to fail for $0.75 < h < 1$, in the sense that eq 37 overestimates the time to reach the steady state. As an example, consider a galvanostatic approach to a reversible steady state with $D = 10^{-9}$ m^2 s^{-1}, $d = 5.0$ μm, and $h = 0.9$. Based on eq 37, Table I predicts that it takes 0.32 s to reach within 5% of the steady state, but the exact equations show that after 0.32 s the steady state is within 4.2%. This discrepancy is not serious and, we believe, is purely an artifact arising from the plateau anomaly discussed earlier.

GALVANOSTATIC APPROACH TO AN IRREVERSIBLE STEADY STATE AT A MICROHEMISPHERE

Equation 29 is valid irrespective of the degree of electrode reversibility. In the irreversible case

$$\frac{\pi i}{2nFd^2} = \frac{i}{nFA} = k_{\mathrm{f}} c_{\mathrm{R}}^{\mathrm{s}} = k_{\mathrm{f}} c_{\mathrm{R}}^{\mathrm{b}} - \frac{ik_{\mathrm{f}}}{2nFDd}[1 - \exp\{1/(\pi\mu^2)\} \operatorname{erfc} \{1/(\pi^{1/2}\mu)\}] \tag{38}$$

where we have utilized abbreviation 31. This equation transforms to

$$1 - \frac{i}{i_{\mathrm{d}}(\infty)}\left[1 - \exp\left\{\frac{1}{\pi\mu^2}\right\} \operatorname{erfc}\left\{\frac{1}{\pi^{1/2}\mu}\right\}\right] = \frac{\pi i}{2nFc_{\mathrm{R}}^{\mathrm{b}} k_{\mathrm{f}} d^2} = \frac{\pi i}{2nFc_{\mathrm{R}}^{\mathrm{b}} k^\circ d^2} \exp\left\{\frac{(1-\alpha)nF}{RT}[E^\circ - E(t)]\right\} \tag{39}$$

by making use of definitions 3 and 7. Following this we transpose to

$$E(t) = E^\circ - \frac{RT}{(1-\alpha)nF} \ln \left\{\frac{2nFc_{\mathrm{R}}^{\mathrm{b}} k^\circ d^2}{\pi i}\right\} - \frac{RT}{(1-\alpha)nF} \ln \left\{1 - h\left[1 - \exp\left\{\frac{1}{\pi\mu^2}\right\} \operatorname{erfc}\left\{\frac{1}{\pi^{1/2}\mu}\right\}\right]\right\} \tag{40}$$

which is an exact equation describing the chronopotentiometric response of an irreversible hemispherical microelectrode to a constant current i. Again, $h = i/i_{\mathrm{d}}(\infty)$ must be less than unity to avoid a transition time.

As $t \to \infty$, the argument of the second logarithm in eq 40 becomes $(1-h)$ and the resulting expression 13 for $E(\infty)$ may be subtracted to yield

$$E(t) = E(\infty) - \frac{RT}{(1-\alpha)nF} \ln \left\{\frac{1 - h[1 - \exp\{1/(\pi\mu^2)\} \operatorname{erfc} \{1/(\pi^{1/2}\mu)\}]}{1-h}\right\} \tag{41}$$

Again, a sequence of approximations, akin to eq 34 but mercifully briefer, may now be applied to the logarithmic term in eq 41

$$\ln \left\{\frac{1 - h[1 - \exp\{1/(\pi\mu^2)\} \operatorname{erfc} \{1/(\pi^{1/2}\mu)\}]}{1-h}\right\} \simeq \ln\left\{\frac{1 - h(1-\mu)}{1-h}\right\} = \ln\left\{1 + \frac{h\mu}{1-h}\right\} \simeq \frac{h\mu}{1-h} \tag{42}$$

by which we arrive at

$$E(t) - E(\infty) = \frac{-RTh\mu}{(1-\alpha)nF(1-h)} = \frac{-RThd}{\pi^{3/2}(1-\alpha)nF(1-h)D^{1/2}t^{1/2}} \tag{43}$$

Subject to the validity of approximation 42, this is the equation that describes the galvanostatic approach to the steady state at an irreversible microhemisphere.

Equation 18 may be rephrased via eq 14 and 43 to express $\epsilon/100$ in terms of $(\mathrm{d}i/\mathrm{d}E)_\infty$ and $E(\infty) - E(t)$ as

$$\frac{\epsilon}{100} = \frac{E(\infty) - E(t_\epsilon^{\mathrm{G}})}{i(\infty)}\left(\frac{\mathrm{d}i}{\mathrm{d}E}\right)_\infty = \frac{hd}{(\pi^3 Dt)^{1/2}} \tag{44}$$

and hence

$$t_\epsilon^{\mathrm{G}} = 10^4 h^2 d^2/(\pi^3\epsilon^2 D) \tag{45}$$

Once more we see that this galvanostatic result is identical with that obtained in a potentiostatic experiment, as given in eq 27.

Table III tests approximation 42 in the same way that Table II tested approximation 34. Again, the discrepancy is serious only in the upper reaches of the wave, where it can be attributed to the plateau anomaly.

POTENTIOSTATIC APPROACH TO A REVERSIBLE STEADY STATE AT A MICRODISK

Several workers (*20–23*) have derived expressions for the transient behavior of an inlaid disk microelectrode when subjected to a concentration-polarizing potential step. The long-time version of these expressions is (*22*)

$$i_{\mathrm{d}}(t) = i_{\mathrm{d}}(\infty)\left[1 + \frac{d}{(\pi^3 Dt)^{1/2}} + \frac{0.151d^3}{(\pi^3 Dt)^{3/2}} + \ldots\right] \tag{46}$$

when applied to a microdisk of superficial diameter d. By use

Table III. A Test of Approximation 42 for $\mu = 0.0500$

h	term footnoted	$h\mu/(1 - h)$
0.010	0.000503	0.000505
0.050	0.00262	0.00263
0.250	0.0165	0.0167
0.500	0.0486	0.0500
0.750	0.139	0.150
0.950	0.666	0.950
0.990	1.78	4.95

$\ln \{(1 - h[1 - \exp\{1/(\pi\mu^2)\} \operatorname{erfc} \{1/(\pi^{1/2}\mu)\}])/(2 - h)\}$.

of a general theorem (*24*), the long-time response to a potential step of any magnitude is

$$i(t) = \frac{i_d(\infty)}{1 + \exp\{nF(E^\circ - E)/RT\}}\left[1 + \frac{d}{(\pi^3 Dt)^{1/2}}\left(1 + \frac{0.151d^2}{\pi^3 Dt} + ...\right)\right] \quad (47)$$

provided that the reaction is fully reversible.

We will assume, for the time being, that $1 \gg 0.151d^2/(\pi^3 Dt)$ and later examine the consequences of this assumption. Comparing the resulting simplified eq 47 with its even simpler $t \to \infty$ limit, we find that

$$i(t) = i(\infty)[1 + d/(\pi^3 Dt)^{1/2}] \quad (48)$$

describes the approach of the potentiostatic current to its ultimate value. Accordingly, making use of criterion 15, one arrives at $\epsilon/100 = [i(t) - i(\infty)]/i(\infty) = d/(\pi^3 Dt)^{1/2}$ whence

$$t_\epsilon^{\mathrm{P}} = 10^4 d^2/(\pi^3 \epsilon^2 D) \quad (49)$$

This is identical with the corresponding result, eq 21, for a microhemispherical electrode of identical superficial diameter, showing that the two electrodes reach their steady states simultaneously. Table I again applies.

Now we can examine the validity of truncating the expansion in eq 47 after two terms. To validate this requires

$$1 \gg 0.151d^2/(\pi^3 Dt_\epsilon^{\mathrm{P}}) = (0.151 \times 10^{-4})\epsilon^2 \quad (50)$$

which is amply satisfied for any percentage ϵ of interest.

GALVANOSTATIC APPROACH TO A REVERSIBLE STEADY STATE AT A MICRODISK

Aoki et al. (*25*) derived the equation

$$E(t) = E^\circ - \frac{RT}{nF} \times \ln\left\{\frac{[i_d(\infty)/i] - 1 + d/(\pi^3 Dt)^{1/2} - 0.863d^3/(\pi^3 Dt)^{3/2} + ...}{1 - d/(\pi^3 Dt)^{1/2} + 0.863d^3/(\pi^3 Dt)^{3/2} + ...}\right\} \quad (51)$$

to describe the long-time chronopotentiometric relationship at an inlaid disk microelectrode of diameter d provided that the electrode reaction obeys Nernst's law. The corresponding steady-state potential $E(\infty)$, given by eq 6, can also be found by setting $t = \infty$ in eq 51. If this expression for $E(\infty)$ is then subtracted from eq 51, one obtains

$$E(t) - E(\infty) = \frac{-RT}{nF} \times \ln\left\{\left[\frac{\frac{1}{h} - 1 + \frac{d}{(\pi^3 Dt)^{1/2}}\left(1 - \frac{0.863d^2}{\pi^3 Dt} + ...\right)}{1 - \frac{d}{(\pi^3 Dt)^{1/2}}\left(1 - \frac{0.863d^2}{\pi^3 Dt} + ...\right)}\right]\left(\frac{h}{1 - h}\right)\right\} \quad (52)$$

Table IV. Comparison of the Exact Logarithmic Term in Eq 52 with the $\mu/(1 - h)$ Approximant for $\mu = 0.0500$

h	term footnoted	$\mu/(1 - h)$
0.010	0.0517	0.0505
0.050	0.0538	0.0526
0.250	0.0678	0.0667
0.500	0.0999	0.100
0.750	0.191	0.200
0.950	0.718	1.00
0.990	1.83	5.00

$\ln \{[((1/h) - 1 + \mu(1 - 0.863\mu^2))/(1 - \mu(1 - 0.863\mu^2))](h/(1 - h))\}$.

where $h = i/i_d(\infty)$. The definition, eq 31, of μ aids the simplification of the logarithmic term in eq 52 to $\mu/(1 - h)$, valid for small μ. The approximations mirror those in scheme 34 and lead to an identical result. From this point, the derivation parallels that in eq 35 and 36 leading to a result identical with 37, namely

$$t_\epsilon^{\mathrm{G}} = 10^4 d^2/(\pi^3 \epsilon^2 D) \quad (53)$$

To validate these approximations, we have prepared Table IV comparing the starting and end points. The results are very similar to those in Table II and we draw a similar conclusion: that the approximation is discrepant toward the top of the voltammetric wave but that this is due to the plateau anomaly rather than representing the failure of result 53.

EXPERIMENTAL SECTION

The reversible (*26*, *27*) oxidation of ferrocene

$$(C_5H_5)_2Fe \rightarrow (C_5H_5)_2Fe^+ + e^- \quad (54)$$

in acetonitrile containing $(C_2H_5)_4NBF_4$ was employed to test the potentiostatic and galvanostatic approach to a reversible steady state. See ref 28 for details of the solutions and electrodes.

A Pine Instrument Co. RDE3 potentiostat was used in potentiostatic experiments to apply a range of constant potentials. A battery-powered Keithley 485 picoammeter in the working electrode lead served as the current monitor: its analogue output was recorded as a function of time using a Hewlett-Packard 7046A xy plotter. In the galvanostatic experiments, a range of constant currents were applied with a PARC 363 potentiostat/galvanostat and the resulting potentials were recorded as a function of time on the xy plotter. Current or potential data at regular time intervals were read directly from the plotter graphs.

ANALYSIS OF EXPERIMENTAL RESULTS

The predicted approach of the potentiostatic current to the steady value for a reversible electrooxidation at a microdisk electrode can be written, from eq 48, in the form

$$i(t)t^{1/2} = i(\infty)t^{1/2} + i(\infty)d/(\pi^3 D)^{1/2} \quad (55)$$

This equation shows that a graph of $i(t)t^{1/2}$ versus $t^{1/2}$ should yield a straight line of slope $i(\infty)$, which may be extrapolated to intersect the $i(t)t^{1/2}$ axis at $i(\infty)d/(\pi^3 D)^{1/2}$. Thus the quantity

$$\frac{\pi^{3/2}(\text{intercept})}{\text{slope}} = d/D^{1/2} \quad (56)$$

should be constant for a given electrode. Moreover, from expression 7

$$i_d(\infty)/2nFc_R^{\mathrm{b}} = Dd \quad (57)$$

thus enabling the product of the diffusion coefficient and electrode diameter to be determined. Relationships 56 and 57 provide a route for separate determinations of the diffusion coefficient D and the electrode diameter d. The constancy of quantities determined in this way provides confirmation of the theory, but we are not advocating this approach as an experimental method for measuring either D or d.

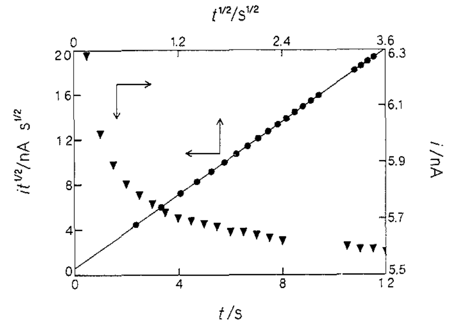

Figure 2. A current–time transient (shown by triangles), to which the right-hand and bottom scales relate, for ferrocene oxidation. The data were obtained at a 25.0 μm diameter disk electrode after stepping the potential from −100 to +100.4 mV. The left-hand and upper scales relate to the current–time transient plotted as $i(t)t^{1/2}$ versus $t^{1/2}$ and shown as solid dots. A value of $i(\infty)$ of 5.40 nA was determined from the slope of the solid line which has a correlation coefficient of 0.999 96. Extrapolation to the $i(t)t^{1/2}$ axis gives a value of $i(\infty)d/(\pi^3 D)^{1/2}$ of 0.609 nA $s^{1/2}$.

Table V. Experimental Parameters and Calculated Results from the Slopes and Intercepts of $i(t)t^{1/2}$ versus $t^{1/2}$ Graphs of Potentiostatic Current–Time Data[a]

d/μm	E/mV	$i(\infty)$/nA	$(d/D^{1/2})/s^{1/2}$	$D/10^{-9}$ m^2 s^{-1}	d^{calc}/μm
25.0	100.4	5.40	0.628	2.29	30.0
25.0	150.0	11.2	0.706	2.12	32.5
25.0	200.4	13.4	0.624	2.30	29.9
25.0	349.6	13.4	0.645	2.25	30.6
25.0	450.3	13.4	0.663	2.21	31.2
76.2	100.0	15.2	1.40	2.76	73.4
76.2	119.0	23.1	1.51	2.61	77.4
76.2	150.0	30.3	1.68	2.45	83.0
76.2	200.0	32.8	1.40	2.75	73.6
76.2	350.5	40.1	1.46	2.67	75.8
76.2	450.1	41.3	1.56	2.56	79.0

[a] The concentration of ferrocene was 1.01 mM for all entries except the final two for which the ferrocene concentration was 1.04 mM. The potential was stepped from −100 mV to the stated E values. d^{calc} is a calculated disk diameter, distinct from the true value reported in the first column.

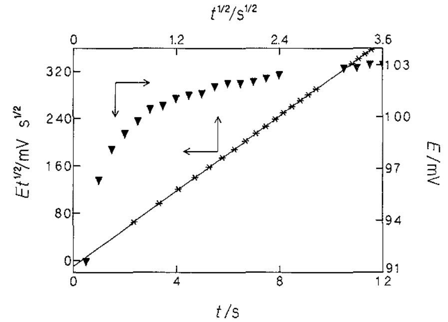

Figure 3. A potential–time transient (shown by triangles), to which the right-hand and bottom scales relate, for ferrocene oxidation. The data were acquired at a 25.0 μm diameter disk electrode after imposing a constant current of 7.00 nA. The left-hand and upper scales relate to the potential–time transient plotted as $E(t)t^{1/2}$ versus $t^{1/2}$ and shown as asterisks. A value of $E(\infty)$ of 105.7 mV was determined from the slope of the regression line through the points (correlation coefficient 0.999 97). Extrapolation to the $E(t)t^{1/2}$ axis gives a value for $RTd/[nF(1-h)(\pi^3 D)^{1/2}]$ of -9.5 mV $s^{1/2}$.

Table VI. Experimental Parameters and Calculated Results from the Slopes and Intercepts of $E(t)t^{1/2}$ versus $t^{1/2}$ Graphs of Galvanostatic Potential–Time Data[a]

d/μm	i/nA	h	$E(\infty)$/mV	$(d/D^{1/2})/$ $s^{1/2}$	$D/10^{-9}$ m^2 s^{-1}	d^{calc}/μm
25.0	5.00	0.346	85.7	0.645	2.25	30.6
25.0	7.00	0.484	105.7	1.06	1.62	42.5
25.0	10.00	0.691	143.2	0.604	2.35	29.3
25.0	12.00	0.830	170.2	1.06	1.62	42.5
76.2	15.00	0.379	92.2	1.61	2.51	80.7
76.2	20.00	0.506	118.9	3.45	1.51	134
76.2	26.00	0.658	147.7	2.69	1.78	114

[a] The concentration of ferrocene was 1.09 mM for experiments conducted at 25.0-μm disks and 1.01 mM for those at disks of 76.2-μm diameter. The significance of d^{calc} is as reported in Table V.

Figure 2 shows a representative example of a current–time transient obtained at a 25.0 μm diameter disk electrode. The result of graphing these data according to eq 55 is shown in this same figure. The remarkable linearity of the current–time data plotted as $i(t)t^{1/2}$ versus $t^{1/2}$ provides confirmation that eq 55 accurately predicts the potentiostatic approach of the current to a reversible steady state at a microdisk electrode. Nevertheless, the small magnitude of the intercept means that a large relative error attaches to this measurement.

Data relating to this, and other, potentiostatic experiments have been assembled into Table V. The first two columns in this table list the microdisk diameters and the magnitudes of the potential steps applied. The third column tabulates the steady current values determined from the slopes of graphs resembling that of Figure 2. A diffusion-limited steady current $i_d(\infty)$ of 13.4 nA for the 25.0-μm disk and 40.7 nA for the 76.2-μm disk is found at the more positive applied potentials. Each $i_d(\infty)$ value leads (via expression 57) to a Dd product of 6.88×10^{-14} m^3 s^{-1} and 2.03×10^{-13} m^3 s^{-1} for the 25.0- and 76.2-μm disk electrodes, respectively. The fourth column of Table V lists $d/D^{1/2}$ values which are reasonably constant for each electrode diameter, calculated by using expression 56. The remaining two columns tabulate the diffusion coefficient and disk diameter calculated from the experimental dD and $d/D^{1/2}$ values. An average diffusion coefficient of $(2.5 \pm 0.2) \times 10^{-9}$ m^2 s^{-1} is in excellent agreement with the literature value of 2.3×10^{-9} m^2 s^{-1} (*29*), though there is some unexpected correlation of the experimental D value with disk size. The disk diameter, similarly calculated from Dd and $d/D^{1/2}$, is significantly larger than the true value for the smaller disk but agrees well for the larger disk.

From eq 35, the approach of the galvanostatic potential to the steady value for a reversible electrooxidation at a microdisk electrode may be written as

$$E(t)t^{1/2} = E(\infty)t^{1/2} - RTd/[nF(1-h)(\pi^3 D)^{1/2}] \qquad (58)$$

Thus a graph of $E(t)t^{1/2}$ versus $t^{1/2}$ should be linear and may be extrapolated to intersect the $E(t)t^{1/2}$ axis at $-RTd/[nF(1-h)(\pi^3 D)^{1/2}]$. From this intercept one may calculate the ratio

$$\frac{-\pi^{3/2}nF(1-h)(\text{intercept})}{RT} = d/D^{1/2} \qquad (59)$$

which should be constant for a given electrode. The steady potential $E(\infty)$ may be found from the slope.

Figure 3 is a graph of the data acquired at a 25.0-μm disk electrode for a representative galvanostatic experiment. When plotted as $E(t)t^{1/2}$ versus $t^{1/2}$, these data superbly portray the linearity predicted by eq 58. Again, however, the small magnitude of the intercept leads to a significant relative error in its measurement.

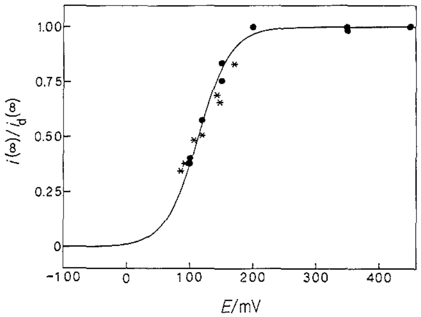

Figure 4. Graphical portrayal of the extrapolated steady-state currents and potentials tabulated in Tables V and VI. Data from potentiostatic experiments are shown as solid dots and those from galvanostatic experiments as asterisks. The reversible steady-state voltammogram shown by the solid line was drawn according to eq 5. The $i(\infty)$ values have been normalized for small concentration differences between experiments.

Table VI is a tabulation of data calculated from $E(t)t^{1/2}$ versus $t^{1/2}$ graphs similar to that in Figure 3 for galvanostatic experiments using different applied constant currents. The first two columns report the disk diameters and the magnitudes of the applied constant current. The third column, the fractional wave height, is calculated from the ratio of the applied constant current and the potentiostatically determined diffusion-limited current (adjusted for any concentration difference). The steady potential $E(\infty)$ is found from the slope of graphs similar to that in Figure 3, while the $d/D^{1/2}$ ratio is calculated from the extrapolated intercept according to eq 59. This ratio, in combination with the potentiostatically determined Dd product, leads to the remaining two columns of this table. Noticeable is that the separately determined values for D and d, based upon extrapolated intercepts, are much less reproducible than those reported in Table V for the potentiostatic experiments.

Evidence that the steady values $i(\infty)$ and $E(\infty)$, determined from the slopes of linear plots such as shown in Figures 2 or 3, correspond to true steady-state values is provided by Figure 4. This figure shows a theoretical reversible steady-state voltammogram around which are plotted the steady currents and potentials obtained respectively from extrapolations of potentiostatic and galvanostatic experimental data. The points obtained potentiostatically are in good agreement with the theoretical voltammogram in spite of the long extrapolations involved. We attribute this concordance to the fact that eq 55 is indeed valid during the approach to a steady-state voltammogram. The agreement of the galvanostatic data with the theoretical voltammogram is not as good but certainly verifies that the same voltammogram is reached by both routes.

Our experiments show that the potentiostatic and galvanostatic approach to the steady state for a reversible oxidation occurring at a microdisk may be predicted by eq 55 and 58, respectively. Equations 21, 37, 49, and 53, which define the time t_ϵ to approach within a closeness ϵ% of the steady state, follow from eq 55 and 58 and thus must be valid though we have not calculated these times directly. We have, however, reported in Tables V and VI the experimental values of $d/D^{1/2}$ which are equal to $0.01\pi^{3/2}\epsilon t_\epsilon^{1/2}$ and from which t_ϵ may be calculated if desired.

SUMMARY

We have established theoretically that the time taken to attain a reversible voltammetric steady state within ϵ% is given by the formula $10^4d^2/(\pi^3\epsilon^2D)$ for both hemispherical and disk microelectrodes of superficial diameter d, irrespective of whether the route to the steady state is potentiostatic or galvanostatic. This formula does not contain any term reflecting the position of the target point on the voltammogram, indicating that all points on the wave are reached equally fast. Experiments conducted at a microdisk electrode have verified this prediction.

The transient behavior of irreversible processes at microdisk electrodes is a topic apparently absent from the literature and our examination of the approach to an irreversible steady state is therefore limited to hemispherical microelectrodes. For these systems, we find that $10^4h^2d^2/(\pi^3\epsilon^2D)$ is the time that must elapse before an ϵ% approach to the steady state is attained, whether that approach be potentiostatic or galvanostatic. The presence of the h^2 factor means that the time to reach an irreversible steady state does depend on the position along the wave of the particular target point. For example, an irreversible half-wave point is reached 4 times faster than a point on its plateau and 4 times faster than the half-wave point of an otherwise similar reversible system.

Note that our criterion of closeness of approach to the steady state is based on a *relative* discrepancy from the steady-state current (that is, $[i(t) - i(\infty)]/i(\infty)$, or its galvanostatic equivalent). The *absolute* discrepancy ($i(t) - i(\infty)$ or its equivalent) will, of course, be greater the higher the target point is on the voltammetric wave, even for a reversible system.

To date it has been rare for microelectrode experiments to be carried out potentiostatically and almost unheard of for them to be performed galvanostatically. Rather the majority of near-steady-state experiments are carried out potentiodynamically, using a measurement technique borrowed from classical cyclic voltammetry to which our theory is not directly applicable. Nevertheless, our findings are valuable in two respects. First, the fact that the time to reach an irreversible steady state depends on the location of the target point, whereas this is not true for reversible systems, suggests that potentiodynamic near-steady-state voltammograms may lie strictly parallel to their truly steady-state counterparts when the microelectrode reaction is reversible (*28*), but that the wave shape may be distorted for irreversible systems. Second, we wish to advocate the greater use of potentiostatic and galvanostatic studies of the steady state at microelectrodes. Such studies would be ideal, for example, in determining the kinetics of ultrafast electron-transfer reactions by a method published recently (*30*). In that method, accurate values of the steady-state half-wave potential are needed for a series of microdisk electrodes of differing sizes. An ideal way to measure such a half-wave potential accurately involves two experiments: a potentiostatic experiment in the plateau region to determine $i_d(\infty)$, followed by a galvanostatic experiment employing $i = i_d(\infty)/2$ to arrive at $E_{1/2}(\infty)$.

ACKNOWLEDGMENT

We are pleased to acknowledge discussion with Christa Colyer and Jan Myland.

LITERATURE CITED

(1) Wightman, R. M.; Wipf, D. O. *Electroanalytical Chemistry*; Bard, A. J., Ed.; Marcel Dekker, Inc.: New York, 1989, Vol. 15, 268.
(2) Wehmeyer, K. R.; Wightman, R. M. *Anal. Chem.* **1985**, *57*, 1989.
(3) Guminski, C.; Roslonek, H.; Galus, Z. *J. Electroanal. Chem.* **1983**, *158*, 357.
(4) Golas, J.; Galus, Z.; Osteryoung, J. *Anal. Chem.* **1987**, *59*, 389.
(5) Scharifker, B.; Hills, G. *J. Electroanal. Chem.* **1981**, *130*, 81.
(6) Bindra, P.; Brown, A. P.; Fleischmann, M.; Pletcher, D. *J. Electroanal. Chem.* **1975**, *58*, 31.
(7) Ciszokowska, C.; Stojek, Z. *J. Electroanal. Chem.* **1985**, *191*, 101.
(8) Baer, C. D.; Stone, N. J.; Sweigart, D. A. *Anal. Chem.* **1988**, *60*, 188.
(9) Rolison, D. R. In *Ultramicroelectrodes*; Fleischmann, M.; Pons, S.; Rolison, D.; Schmidt, P. P., Eds.; Datatech Systems Publishers: Morganton, NC, 1987; Chapter 3.
(10) Bond, A. M.; Luscombe, D.; Oldham, K. B.; Zoski, C. G. *J. Electroanal. Chem.* **1988**, *249*, 1.

(11) Bond, A. M.; Fleischmann, M.; Robinson, J. *J. Electroanal. Chem.* **1984**, *168*, 299.
(12) Bond, A. M.; Oldham, K. B.; Zoski, C. G. *Electrochim. Acta* **1989**, *216*, 177.
(13) Oldham, K. B.; Zoski, C. G. *J. Electroanal. Chem.* **1988**, *256*, 11.
(14) Bond, A. M.; Oldham, K. B.; Zoski, C. G. *J. Electroanal. Chem.* **1988**, *245*, 71.
(15) Oldham, K. B. *J. Electroanal. Chem.* **1981**, *122*, 1.
(16) Delmastro, J. R.; Smith, D. E. *J. Phys. Chem.* **1967**, *71*, 2138.
(17) Bond, A. M.; Oldham, K. B. *J. Electroanal. Chem.* **1983**, *158*, 193.
(18) Spanier, J.; Oldham, K. B. *An Atlas of Functions*; Hemisphere Publishing Corp.: Washington, DC, and Springer-Verlag: Berlin, 1987; Chapter 41.
(19) MacDonald, D. D. *Transient Techniques in Electrochemistry*; Plenum Press: New York and London, 1977; Chapter 5.
(20) Aoki, K.; Osteryoung, J. *J. Electroanal. Chem.* **1981**, *122*, 19.
(21) Aoki, K.; Osteryoung, J. *J. Electroanal. Chem.* **1981**, *125*, 315.
(22) Shoup, D.; Szabo, A. *J. Electroanal. Chem.* **1982**, *140*, 237.
(23) Aoki, K.; Osteryoung, J. *J. Electroanal. Chem.* **1984**, *160*, 335.
(24) Cope, D. K.; Tallman, D. E. *J. Electroanal. Chem.* **1987**, *235*, 97.
(25) Aoki, K.; Akimoto, K.; Tokuda, K.; Matsuda, H.; Osteryoung, J. *J. Electroanal. Chem.* **1985**, *182*, 281.
(26) Bond, A. M.; Henderson, T. L. E.; Mann, T. F.; Mann, D. R.; Thormann, W.; Zoski, C. G. *Anal. Chem.* **1988**, *60*, 1878.
(27) Wipf, D. O.; Kristensen, E. W.; Deakin, M. R.; Wightman, R. M. *Anal. Chem.* **1988**, *60*, 306.
(28) Zoski, C. G.; Bond, A. M.; Colyer, C. L.; Myland, J. C.; Oldham, K. B. *J. Electroanal. Chem.* **1989**, *263*, 1.
(29) Sharp, M. *Electrochim. Acta* **1983**, *28*, 301.
(30) Oldham, K. B.; Zoski, C. G.; Bond, A. M.; Sweigart, D. A. *J. Electroanal. Chem.* **1988**, *248*, 467.

RECEIVED for review May 31, 1989. Accepted October 3, 1989. Financial support was received from the Natural Sciences and Engineering Research Council of Canada and from the Australian Research Grants Committee.

Infrared Spectroscopic Determination of pH Changes in Diffusionally Decoupled Thin-Layer Electrochemical Cells

I. T. Bae, Daniel A. Scherson,* and Ernest B. Yeager

Case Center for Electrochemical Sciences and the Department of Chemistry, Case Western Reserve University, Cleveland, Ohio 44106

In situ Fourier transform reflection absorption infrared spectroscopy has been employed as a probe of the local pH in the thin layer of electrolyte solution trapped between the electrode and the optical window. The method is based on the differences in the spectral properties of certain bases and their conjugated acids, which makes it possible to determine pH changes on the basis of the relative integrated intensities of the two species. Illustrations are given for the carbonate/bicarbonate and acetate/acetic acid systems and the oxidation of CO in alkaline media.

INTRODUCTION

In situ reflection absorption infrared spectroscopy has provided much insight into a variety of interfacial processes, including adsorbate–substrate interactions and their dependence on potential, as well as the mechanism of a growing number of electrode reactions (*1–3*). Crucial to the successful application of this spectroscopic technique is a reduction in the volume of electrolyte in the path of the infrared beam. This makes it possible to minimize the spectral contributions due to the solvent, particularly in the case of aqueous media, and thus achieve substantial gains in sensitivity. Such conditions are attained in practice by placing the electrode as close as possible to the optical window so as to reach average electrolyte thicknesses of the order of a few micrometers (*4*). In this geometry, ionic migration in an electric field becomes the predominant form of mass transport in and out of the layer, which within the time required for the measurements to be completed may be regarded as diffusionally decoupled from the bulk solution in the reservoir. This effect makes it essential to account for possible spectral contributions of ions exhibiting IR active normal modes in order to interpret correctly the spectral data. Illustrations of this phenomenon have been provided by Weaver and co-workers (*5*) in their studies of ionic specific adsorption, and most recently by Bae et al. (*6*), who examined quantitatively the changes in the local concentration of anions associated with the formation and reduction of oxide films on Pt and Au electrodes.

The in situ Fourier transform infrared reflection absorption spectroscopy (FTIRRAS) experiments to be described in this communication will show that a quantitative measure of local pH changes in the thin electrolyte layer can be obtained by incorporating judiciously chosen IR active species in the solution. Based on this approach, it has been possible to determine that depending on the magnitude of the current and the solution composition, the local pH can differ by many units from that in the bulk reservoir.

EXPERIMENTAL SECTION

All experiments were conducted at room temperature in a specially designed electrochemical cell described in detail elsewhere (*7*) using a flat platinum foil (4N, Johnson Matthey) of ellipsoidal shape cast in Kel-F as the electrode. The incident angle of the IR beam on the flat CaF_2 window was 70°.

Sodium acetate and sodium carbonate solutions were prepared with ultrapurified water and reagent grade chemicals (Fisher Chemicals). All potentials are given with respect to the saturated calomel reference electrode SCE.

The adsorption of CO on the Pt surface was effected by introducing a 0.1 N NaOH solution saturated with CO (4N, Matheson) into the spectroelectrochemical cell. During this process, the electrode was polarized at a potential of −0.80 V vs SCE and placed away from the optical window. After 20 min the solution was purged with N_2 (3N, Air Products) for the same period of time, and the electrode was then pushed against the window prior to recording the in situ FTIRRAS spectra.

Each of the spectra presented in this work was acquired while the potential was being swept in a linear fashion at 2 $mV{\cdot}s^{-1}$ and represents an average of 200 (carbonate/bicarbonate) or 300 scans (acetate/acetic acid) obtained in a potential region spanning about 115 and 170 mV, respectively.

RESULTS AND DISCUSSION

A series of normalized spectra obtained for a Pt electrode in 0.1 M Na_2CO_3 during a potential sweep between −0.4 and +0.72 V are shown in Figure 1A. The reference spectrum was acquired by collecting 200 scans at −0.4 V, prior to the initiation of the sweep in the positive direction. The spectra are characterized by three prominent bands at 1640, 1403, and

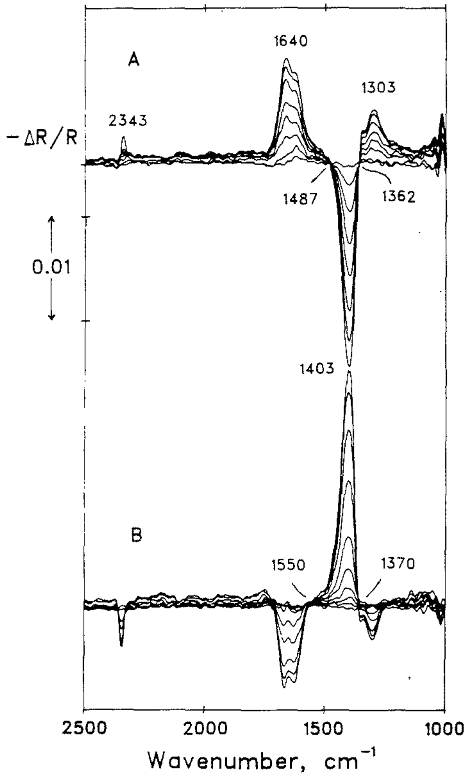

Figure 1. A. Series of normalized spectra obtained for a Pt electrode in 0.1 M Na_2CO_3 during a potential sweep between -0.4 and +0.72 V. Each of the spectra was acquired during a potential sweep at 2 mV·s^{-1} and thus corresponds to an average over a range of approximately 115 mV. The absolute magnitude of the intensity of all peaks grows as the potential is driven toward more positive values. The reference spectrum for this series was obtained by collecting 200 scans at -0.40 V. B. Same as A for reverse potential sweep in the region between +0.71 and -0.73 V. The reference spectrum in this case was the spectrum obtained at the most anodic potential in the sweep in the positive direction in series A in this figure. Other conditions are specified in A.

1303 cm^{-1}. In separate measurements, the solution-phase FTIR spectrum of 0.5 M Na_2CO_3 in aqueous media was found to display a strong band at 1396 cm^{-1} (ν_3 of D_{3h}) (*8*) and a weaker band at 1651 cm^{-1} attributed to OH bending of structurally modified water by concentrated carbonate. (*9*) Two peaks were also observed for 0.5 M $NaHCO_3$ (1362 and 1663 cm^{-1}), which correspond to ν_2 and ν_4 of C_{2v}, respectively, with intensities comparable although smaller than those of the carbonate species. On this basis, the positive- (1640 and 1303 cm^{-1}) and negative-going (1403 cm^{-1}) features in Figure 1A can be ascribed predominantly to bicarbonate and carbonate, respectively. The presence of two well-defined isosbestic points at about 1487 and 1362 cm^{-1} affords evidence for a quantitative conversion of carbonate into bicarbonate induced by the increase in the hydronium ion concentration due to surface oxidation.

Essentially mirror images of these spectra were obtained upon reversing the potential sweep, using the average spectrum acquired in the most positive potential region displayed in series A as the reference. These are shown in B in the same figure. The direct correspondence between the two sets of data is to be expected since the hydronium ions generated during surface oxidation are subsequently consumed during the reduction of the oxide, transforming bicarbonate into carbonate.

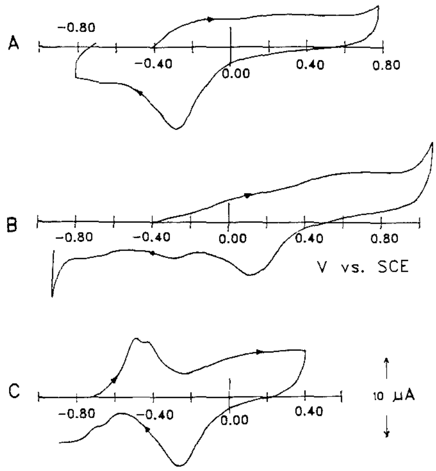

Figure 2. Cyclic voltammetry of a Pt electrode obtained in the thin-layer cell while the FTIRRAS spectra were recorded (A) in 0.1 M Na_2CO_3, (B) in 0.1 M CH_3CO_2Na, and (C) with a monolayer of preadsorbed CO in 0.1 M NaOH (see text for details). Conditions: scan rate, 2 mV·s^{-1}; electrode area, 2.0 cm^2.

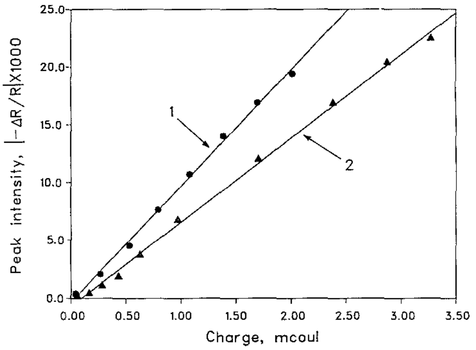

Figure 3. Infrared peak intensity of the 1403-cm^{-1} band plotted as a function of the integrated charge obtained from the voltammetric curve recorded during the actual experiment (see curve A in Figure 2) in the positive (1) and negative (2) directions.

The infrared peak intensity of the 1403-cm^{-1} band plotted as a function of the integrated charge obtained from the voltammetric curve recorded during the actual experiment (see curve A, Figure 2) yielded straight lines with zero intercept and slopes of 10.1 $(\Delta R/R)\cdot C^{-1}$ and 7.2 $(\Delta R/R)\cdot C^{-1}$ for the sweeps in the positive and negative directions, respectively (see Figure 3). The linearity of the plots indicates that the Beer–Lambert law is obeyed. The differences in the values of the slopes for the forward and backward sweeps are due to differences in the background intensity for the two spectra used as reference. This gives rise to a relative shift in the frequency associated with the isosbestic points, $\Delta\nu_{isos}$(forward) = 125 cm^{-1} and $\Delta\nu_{isos}$(reverse) = 180 cm^{-1}. The integrated intensities per coulomb yielded essentially identical values for the forward and reverse sweeps, 1260 ± 80 and 1300 ± 60

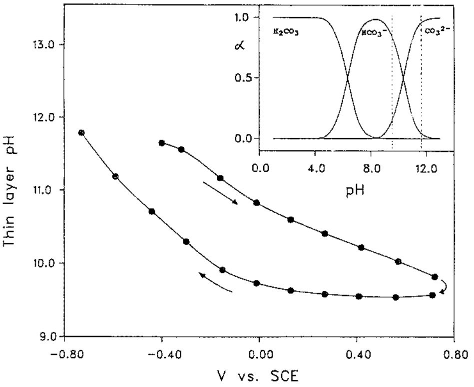

Figure 4. Average pH of the Na_2CO_3 solution vs potential based on the experimental data in Figures 1 and 2. The initial pH of the Na_2CO_3 solution is 11.6 and the charge at −0.40 V is assumed to be zero. All transport numbers were obtained from the literature. The arrows in the figure indicate the direction of the potential sweep. Insert: Fraction of H_2CO_3, HCO_3^-, and CO_3^{2-} evaluated strictly from acid–base equilibria. The region associated with the spectroscopic measurements is indicated by the dashed lines.

$(\Delta R/R) \cdot C^{-1} \cdot cm^{-1}$, respectively.

The change in the average pH of the thin layer as a function of potential can be calculated on the basis of the values of the integrated change, provided the thickness of the electrolyte d and the transport numbers of all relevant species are known. The magnitude of d was estimated on the basis of the following:

(i) The relative separation of the Newton rings formed at the electrode–electrolyte–window interface (*10*). These measurements were conducted with a He–Ne laser source and yielded values in the range between 0.3 and 1.8 μm, for the 1st- and 6th-order red rings, respectively (*4*).

(ii) A comparison between the theoretical and experimental spectra of water using routines developed in this laboratory. These calculations were based on the classical Drude–Fresnel equations as applied to the CaF_2/water/Pt system, using accepted optical constants for each of the phases (*11*, *12*). An analogous analysis has been reported recently be Bethune et al. (*13*).

From the results obtained it was concluded that the average value of d was about 1.0 μm (*2*).

The effective average concentration of hydronium ions was evaluated as a function of potential by using as the initial pH that of the original 0.1 M Na_2CO_3 solution, i.e. 11.6, and the results are displayed in Figure 4. In these experiments, the electrode was pushed against the window at −0.40 V, a potential corresponding to a zero of charge. The changes in the concentrations of cations and anions in the thin-layer cell were calculated from the charge q passed through the working electrode and the transport numbers (*8*).

A simple way of calculating the final pH of the solution consists in estimating first a transport corrected concentration $c_i^t = c_i^0 + t_i/z_i(q/FdA)$ for $i = CO_3^{2-}$, HCO_3^-, and OH^-, where q/FdA is the equivalent hydronium ion-to-charge passed. Hence, if $[OH^-] < q/dFA < [CO_3^{2-}]$ the concentration of cabonate and bicarbonate after reaction with hydronium ions can be shown to be given by $[CO_3^{2-}] = [CO_3^{2-}]^t - (q/FdA - [OH^-]^t)$ and $[HCO_3^-] = [HCO_3^-]^t + (q/FdA - [OH^-]^t)$ with $[OH^-]$ being negligible. These formulas can then be replaced in the expression for the equilibrium constant for dissociation of HCO_3^-, yielding after rearrangement and equation for $[H^+]$ in terms of c_i^t and q/dFA. The values of the transport numbers used in the calculations for 0.1 M Na_2CO_3 are the following: $Na^+ = 0.412$, $CO_3^{2-} = 0.543$, $HCO_3^- = 0.008$, and $OH^- = 0.037$.

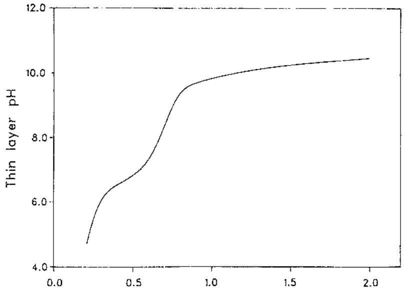

Figure 5. Plot of the pH of a 0.1 M Na_2CO_3 aqueous solution as a function of the electrolyte thickness assuming a total charge passed during a sweep in the positive direction of 2.0 mC. This value corresponds approximately to the charge obtained experimentally for a sweep between −0.40 and +0.72 V vs SCE.

The transport numbers at the concentration prevailing at the edge of the thin-layer call are the critical values, and these are taken to be those corresponding to the electrolyte in the bulk reservoir. The changes in pH associated with modifications in the concentrations of carbonate and bicarbonate based strictly on acid–base equilibria are shown in the insert of Figure 4, in which the region associated with the spectroscopic measurements is indicated by the dashed lines. The effect of the thickness of the electrolyte, d, on the pH changes attending the passage of charge (2.0 mC) is shown in Figure 5. As indicated, smaller values of d lead to a decrease in the pH. With thin layers of nonuniform thicknesses, local variations in pH many also be encountered, although a quantitative treatment of such effects is more complicated. This provides and explanation for the CO_2 peak observed in Figure 1.

The pH changes induced by the formation and subsequent reduction of an oxide layer were also monitored by using a 0.1 M CH_3CO_2Na solution ($pK_a = 1.73 \times 10^{-5}$, initial pH = 8.9). In this case $CH_3CO_2^-$ is converted into its conjugate acid by the reaction with hydronium ions produced during oxidation of the metal. The positive-going bands at 1713, 1373, and 1280 cm^{-1} in Figure 6 are attributed to the asymmetric and symmetric stretchings of O–C–O and the single CO bond of the nonionized acetic acid (*8*, *14*, *15*), whereas the negative-going bands at 1418 and 1550 cm^{-1} are associated with the symmetric and asymmetric stretching modes of the resonant $-CO_2^-$ group, respectively (*8*, *14*, *15*). As was the case with the carbonate solution, this series of spectra also exhibit isosbestic points in the potential sweeps, both in the positive and negative directions.

An interesting aspect of these results is that in contrast to information reported in the literature (*16*, *17*), a substantial fraction (equivalent to about half a monolayer of CO oxidation) of acetic acid and/or acetate undergoes oxidation at moderately low potentials. This is clearly indicated by the appearence of the characteristic CO_2 band at 2343 cm^{-1}. A more quantitative treatment of these data has not been pursued. Based strictly on the spectral data and the cyclic voltammetry in curve B of Figure 2, however, which obviously includes the effects of the HCO_3/CO_2 system, the final pH can be estimated to be about 4.0.

The results of the experiments involving CO oxidation in 0.1 M NaOH are shown in Figure 7. This process is of special interest as the adsorption of a CO-type species is believed to interfere with the continuous oxidation of methanol, formaldehyde, and formic acid, as well as a variety of other organic

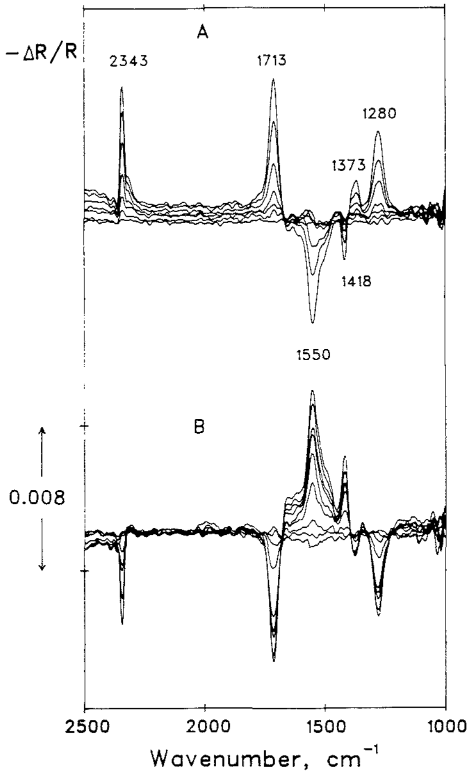

Figure 6. A. Series of normalized spectra obtained for a Pt electrode in 0.1 M $NaCH_3CO_2$ during a potential sweep between −0.4 and +0.99 V. Each of the spectra was acquired during a potential sweep at 2 $mV{\cdot}s^{-1}$ and thus corresponds to an average over a range of approximately 210 mV. The absolute magnitude of the intensity of all peaks grows as the potential is driven toward more positive values. The reference spectrum for this series was obtained by collecting 300 scans at −0.40 V. B. Same as A for reverse potential sweep in the region between +0.76 and −0.88 V. The reference spectrum in this case was the spectrum obtained at the most anodic potential in the sweep in the positive direction in series A in this figure. Other conditions are specified in A.

compounds, at small overpotentials (*2, 16–19*). In this case, each of the spectra was collected over a period of 80 s and represents the average of 200 scans recorded while the potential was swept in the positive direction at a rate of 2 $mV{\cdot}s^{-1}$ in a continuous fashion from −0.8 to +0.32 V.

The lack of any spectral features for the spectrum acquired during the first time interval is consistent with the fact that no current is observed in the highly distorted cyclic voltammetry in the region between −0.8 and about −0.65 V, shown in curve C of Figure 2. Clear defined spectroscopic features were observed, however, for potentials positive to the onset of CO oxidation. These include the negative-going bands at 2017 and 1828 cm^{-1} attributed to linear and bridged CO, respectively (*2, 3, 20*), as well as the positive-going bands at 1639 and 1389 cm^{-1}. These features grow until a potential of −0.21 V is reached, which corresponds precisely to the end of CO oxidation as can be inferred from the cyclic voltammetry. Based on the magnitude of the charge evaluated from the cyclic voltammetry, the expected pH at this potential is only 0.05 unit smaller than that of the original solution. This implies that the positive-going bands in the spectrum correspond to carbonate (arising from the oxidation of adsorbed CO), as the concentration of bicarbonate at this pH as shown in the insert of Figure 4 is negligible.

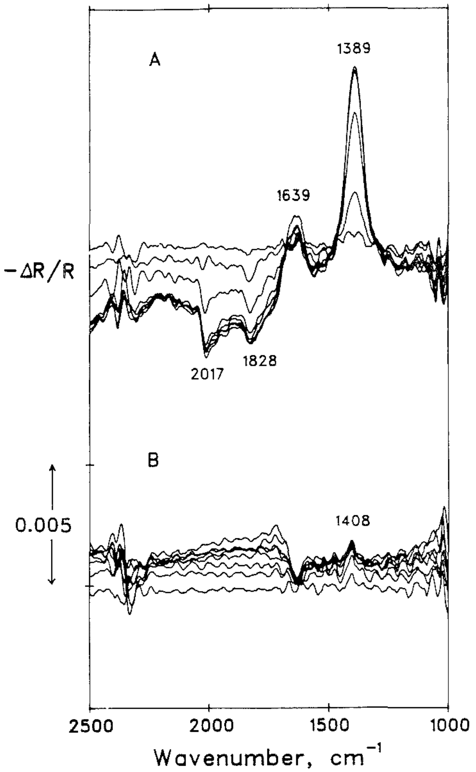

Figure 7. A. Series of normalized spectra obtained for a monolayer of CO adsorbed on Pt in 0.1 M NaOH, during a potential sweep between −0.8 and +0.32 V. Each of the spectra was acquired during a potential sweep at 2 $mV{\cdot}s^{-1}$ and thus corresponds to an average over a range of approximately 150 mV. The reference spectrum for this series was obtained by collecting 200 scans at −0.80 V. B. Same as A for reverse potential sweep in the region between +0.17 and 0.90 V. The reference spectrum in this case was the spectrum obtained at the most anodic potential in the sweep in the positive direction in series A in this figure. Other conditions are specified in A.

As the potential is driven in the negative direction (see B in Figure 7), the reference spectrum in this case having been obtained in the most positive potential region in series A, no further features other than the ubiquitous water-related peak at 1650 cm^{-1} were observed. It may be noted that the change in pH induced by the reduction of the oxide for such strongly alkaline solution is too small to give rise to observable changes (except a very minor peak at 1408 cm^{-1}) in the amount of carbonate in solution.

It follows from the previous discussion that the effects presented in this work can be essentially avoided by using either concentrated acid or base, by reducing the concentration of electroactive species, or by increasing the buffer capacity. Care must be exercised, however, in choosing conditions that would enable the desired signals to be detected with minimum interference from other ions in the solution.

SUMMARY

The experiments presented in this work have indicated that changes in pH associated with certain faradaic processes in thin-layer cells of the type employed in in situ FTIRRAS can be monitored by adding to the electrolyte acids or bases exhibiting distinct spectral features in the infrared region. Illustrations were provided for the formation and reduction of oxide layers on Pt surfaces in 0.1 M Na_2CO_3 and 0.1 M CH_3CO_2Na aqueous solutions. Also probed was the formation of carbonate ions generated by the oxidation of CO adsorbed on a Pt electrode in strongly alkaline media, in which case the reduction of the oxide leads to negligible changes in pH and thus in very small changes in the concentration of carbonate ions in the layer.

The described method is applicable for monitoring changes in pH during the oxidation or reduction of a variety of species, provided that the overall reaction is accompanied by the generation or consumption of hydronium ions and that the pH markers are not involved in the redox process.

LITERATURE CITED

(1) Parsons, R.; VanderNoot, T. *J. Electroanal. Chem. Interfacial Electrochem.* **1988**, *257*, 9.
(2) Ashley, K.; Pons, S. *Chem. Rev.* **1988**, *88*, 673.
(3) Bewick, A.; Pons, S. In *Advances in Infrared and Raman Spectroscopy*; Clark, R. J. H., Hester, R. E., Eds.; Heyden: London, 1985; Vol. 12.
(4) Bae, I. T. Ph.D. Dissertation, Case Western Reserve University, Cleveland, OH, 1989.
(5) Corrigan, D. S.; Weaver, M. J. *J .Electroanal. Chem. Interfacial Electrochem.* **1988**, *239*, 55.
(6) Bae, I. T.; Xing, X.; Yeager, E. B.; Scherson, D. *Anal. Chem.* **1989**, *61*, 1164.
(7) Bae, I. T.; Xing, X.; Liu, C.; Yeager, E. B., submitted for publication in *J. Electroanal. Chem. Interfacial Electrochem.*
(8) Nakamoto, K. *Infrared and Raman Spectra of Inorganic and Coordinated Compounds*; Wiley: New York, 1986; p 126.
(9) Irish, D. H.; Brooker, M. H. In *Advances in Infrared and Raman Spectroscopy*; Clark, R. J. H., Hester, R. E., Eds.; Heyden: London, 1976; Vol. 2, p 262.
(10) Born, M.; Wolf, E. *Principles of Optics*, 6th ed.; Pergamon Press: Oxford, England, 1980; p 282.
(11) Lynch, D. W.; Hunter, W. R. In *Handbook of Optical Constants of Solids*; Palik, E. K., Ed.; Academic Press: London, 1965.
(12) Rusk, A. N.; Williams, D.; Querry, M. R. *J. Opt. Soc. Am.* **1971**, *61*, 895.
(13) Bethune, D. S.; Luntz, A. C.; Sass, J. K.; Roe, D. K. *Surf. Sci.* **1988**, *88*, 3322.
(14) Pouchert, C. J. *The Aldrich Library of Infrared Spectra*, 3rd ed.; Aldrich Chemical Co.: Milwaukee, WI, 1981.
(15) Socrates, G. *Infrared Characteristic Group Frequencies*; Wiley-Interscience: Chichester, U.K., 1980; p 138.
(16) Corrigan, D. S.; Krauskopf, E. K.; Rice, L. M.; Wieckowski, A.; Weaver, M. J. *J. Phys. Chem.* **1988**, *92*, 1596.
(17) Leung, L. H.; Weaver, M. J. *J. Phys. Chem.* **1988**, *92*, 4019.
(18) Kunimatsu, K.; Kita, H. *J. Electroanal. Chem. Interfacial Electrochem.* **1987**, *218*, 155.
(19) Corrigan, D. A.; Weaver, M. J. *J. Electroanal. Chem. Interfacial Electrochem.* **1988**, *241*, 143.
(20) Beden, B.; Bewick, A.; Kunimatsu, K.; Lamy, C. *J. Electroanal. Chem. Interfacial Electrochem.* **1982**, *142*, 345.

RECEIVED for review July 14, 1989. Accepted October 13, 1989. This work was supported by the Gas Research Institute. Additional funding was provided by the Department of Energy through a subcontract from Lawrence Berkeley Laboratory. The purchase of the FTIR instruments was made possible by a grant from the U.S. Office of Naval Research.

Multivariate Analysis of Carbon-13 Nuclear Magnetic Resonance Spectra. Identification and Quantification of Average Structures in Petroleum Distillates

Trond Brekke,* Tanja Barth, Olav M. Kvalheim, and Einar Sletten

Department of Chemistry, University of Bergen, Bergen N-5007, Norway

The $\{C_{10}, C_{11}, \ldots, C_{25}\}$ fractions from two North Sea crude oils are investigated. For each fraction CH_n (n = 1, 2, 3) ^{13}C nuclear magnetic resonance subspectra are obtained with the use of distortionless enhancement by polarization transfer subspectral editing. The combined spectral profiles for each fraction, consisting of 9651 data points, are reduced to 1024 pooled variables by using a "soft" maximum entropy criterion. A principal component analysis is performed. Two principal components account for 85.9% of the variance in the reduced data. Spectral assignments show that the two principal components are related to variations in the abundances of *n*-alkanes and isoalkanes. After the variables are divided by their means, the second principal component discriminates between the two oils in all fractions. The loading profile for this principal component shows that the two oils differ mainly in the content of saturated isoprenoid structures. The content of the saturated isoprenoid structures is quantified by using the marker-object projection technique, with the spectrum of pure pristane as a marker object.

INTRODUCTION

The ^{13}C nuclear magnetic resonance (NMR) chemical shift is an extremely sensitive probe for the characterization of the carbon skeleton of organic molecules. This makes ^{13}C NMR an attractive method for the analysis of petroleum. The number of constituents in petroleum increases exponentially with molecular weight (*1*), so that single-constituent detection is feasible only in the lighter fractions (*2–4*). The large number of constituents in the heavier fractions, combined with an increasing viscosity, leads to extensive spectral overlap that prohibits a ready analysis on the single-constituent level. However, since similar structures give similar chemical shifts, the patterns in such spectra correspond to average structures in the samples (*5–9*). Additional structural information is obtained by the use of designed pulse sequences like gated spin-echo (GASPE) (*10*) and distortionless enhancement by polarization transfer (DEPT) (*11*) for the determination of resonance multiplicities. Furthermore, under appropriate experimental conditions, the NMR response becomes uniform for all carbons in the sample, resulting in a quantitative spectrum (*12–16*).

The present data consists of two objects (oils), each represented by a series of ^{13}C DEPT NMR spectra of the C_{10}–C_{25} fractions. As such, the two series of fraction spectra may be recognized as an example of *bilinear data*. Each of the two objects can thus be represented by a data matrix (rather than an array) with boiling point intervals in one dimension and spectral responses in the second. Methods for the analysis of such data have been developed as a response to the advent

0003-2700/90/0362-0049$02.50/0

Table I. Sample Names, Lengths of Dominating n-Alkane, and Distillation Cutoff Temperatures

sample	fractn	cutoff temp, °C
A1, B1	C_{10}	181.2, 182.0
A2, B2	C_{11}	201.1, 199.4
A3, B3	C_{12}	221.4, 221.0
A4, B4	C_{13}	242.0, 240.2
A5, B5	C_{14}	260.0, 261.2
A6, B6	C_{15}	277.4, 276.4
A7, B7	C_{16}	292.5, 290.4
A8, B8	C_{17}	309.2, 306.5
A9, B9	C_{18}	322.8, 320.5
A10, B10	C_{19}	334.1, 333.4
A11, B11	C_{20}	346.2, 345.8
A12, B12	C_{21}	358.0, 357.2
A13, B13	C_{22}	370.2, 369.0
A14, B14	C_{23}	380.8, 378.8
A15, B15	C_{24}	392.0, 391.0
A16, B16	C_{25}	402.9, 402.0

of hyphenated measuring techniques such as gas chromatography–mass spectroscopy and liquid chromatography–ultraviolet spectroscopy (*17*). However, most methods are designed for a quantitative calibration and prediction of the individual sample constituents, which is not possible from the present data.

A second approach, which we shall adopt, is based on the assumption that all samples are composed of a common set of structural units. This is a reasonable assumption since the bulk of biological matter, from which fossil hydrocarbons originate, is known to be composed of repeated units such as $-CH_2O-$ (sugars, starches, cellulose, etc.), isoprenoid units (chlorophyll, essential oils, etc.), and n-alkyl chains (fats and oils). The diversity of petroleum constituents is also limited by geochemical/geophysical processes that favor the stable and nonpolar structures. Since similar structures give similar chemical shifts, it is possible to prepare a data matrix where each row represents a distillate fraction and each column represents a structural unit. This arrangement permits us to analyze each fraction as an individual sample.

As our main analytical tool, we use principal component (PC) analysis. PC analysis has found a number of applications in the analysis of ^{13}C NMR data (*18–23*). For the present data, PC analysis is used to extract peak correlations in order to reveal average structures in the samples. We also propose the use of marker-object projections (MOP) (*24*) for the quantification of such average structures in the fractions.

THEORETICAL SECTION

The data are arranged in a matrix, $\mathbf{X}'$, with n spectra (rows) and p' intensities (columns).

Data Reduction. In raw spectroscopic data the number of variables, p', is generally too large for an exhaustive analysis. It is thus necessary to reduce the number of variables. The best way to achieve this is by applying the maximum entropy criterion, which ensures that a maximum of the information for any given number of reduced variables is retained (*25*). However, as a strict maximum entropy criterion produces a completely flat average spectrum, the raw spectral features are obscured. To avoid this, the following algorithm developed by Karstang and Eastgate (*26*) for a similar reduction of X-ray diffraction data was employed:

(1) Calculate the average intensities of all spectra.

(2) Calculate the total intensity (sum) for the average spectrum.

(3) Calculate δ = sum/reduced number of variables required.

(4) Beginning at the first average variable, add consecutive variable intensities until the partial sum is equal to or greater than δ. This summed interval defines a reduced variable. Continue this process until the whole average spectrum is processed.

(5) Calculate the corresponding intensities of the reduced variables for the individual spectra.

When the partial sums are allowed to exceed δ in (4), a deviation from the strict maximum entropy definition is introduced. Hence, the name "soft" maximum entropy is used. The effect is that the more intense data points are left unchanged, while the less intense data points are summed together. Thus, the main features in the raw spectra are retained in the reduced spectra. Provided that the consecutive variables in a reduced variable belong to the same peak, and hence span the same PC dimension, no chemical component information is lost.

Principal Component Analysis. Principal component (PC) analysis is now a well-established tool for the interpretation of chemical data. All basic features of the PC method are thoroughly documented together with numerous chemical examples (*18–23*, *27–29*). This section provides only a brief description of the features necessary for the interpretations in the present work.

The major step in a PC analysis is the extraction of the eigenvectors from the variance–covariance matrix to get uncorrelated new variables called principal components (PCs) that span a maximum of the variance in the data set. Since the PCs are linear combinations of all the original variables, they can be viewed as composite average variables. The explanatory importance of a PC is measured by its proportion of variance relative to the total variance contained in the original data. If the original variables are highly correlated, the first few PCs are sufficient to reproduce the systematic variance in the data, so that the data can be approximated with a PC model with F product terms:

$$\mathbf{X} = \mathbf{1}\bar{\mathbf{X}} + \mathbf{TB} + \mathbf{E} \quad (1)$$

Here, $\mathbf{X}$ is the $n \times p$ data table with n spectra and p (reduced) variables; $\bar{\mathbf{X}}$ is the $1 \times p$ matrix of the mean values of each variable; $\mathbf{1}$ is a $n \times 1$ matrix of 1's; $\mathbf{B}$ is the $F \times p$ matrix of variable coefficients (loadings) for the first F PCs; $\mathbf{T}$ is the $n \times F$ matrix of coordinates (scores) for the samples in the space spanned by the first F PCs; and $\mathbf{E}$ is the $n \times p$ matrix of residuals. The amount of variance explained by the PCs decreases in the order Var(PC1) > Var(PC2) > Var(PC3), etc.

One of the nice features of PC analysis is that nearly every result can be presented graphically. The scores along the PCs reveal the relationship among the samples. This information is displayed in a score plot where the sample scores are plotted in a plane spanned by two PCs. Since the PCs are orthogonal, the Euclidian distances can be used to measure sample similarities quantitatively.

A variable's contribution to a PC is directly proportional to the squared loading. Thus the relative importance of a variable to the interpretation of a PC is given by its loading. Furthermore, correlated variables have similar loadings. Thus, variables representing a common chemical structure may be identified by similarities in their loadings (*30*). Traditionally, the variable relations are displayed in two-dimensional loading plots in the same manner as sample relations are displayed in score plots. However, the large number of variables in the present data makes such loading plots less useful. Instead, we have chosen to display the variable relations as loading profiles directly comparable to the reduced spectra.

Marker-Object Projection. The content of an anticipated constituent, or structural unit in a mixture, may be quantified by calculating the scalar product, or marker-object projection (MOP), between the mixture spectrum and the neat-liquid spectrum of the anticipated constituent:

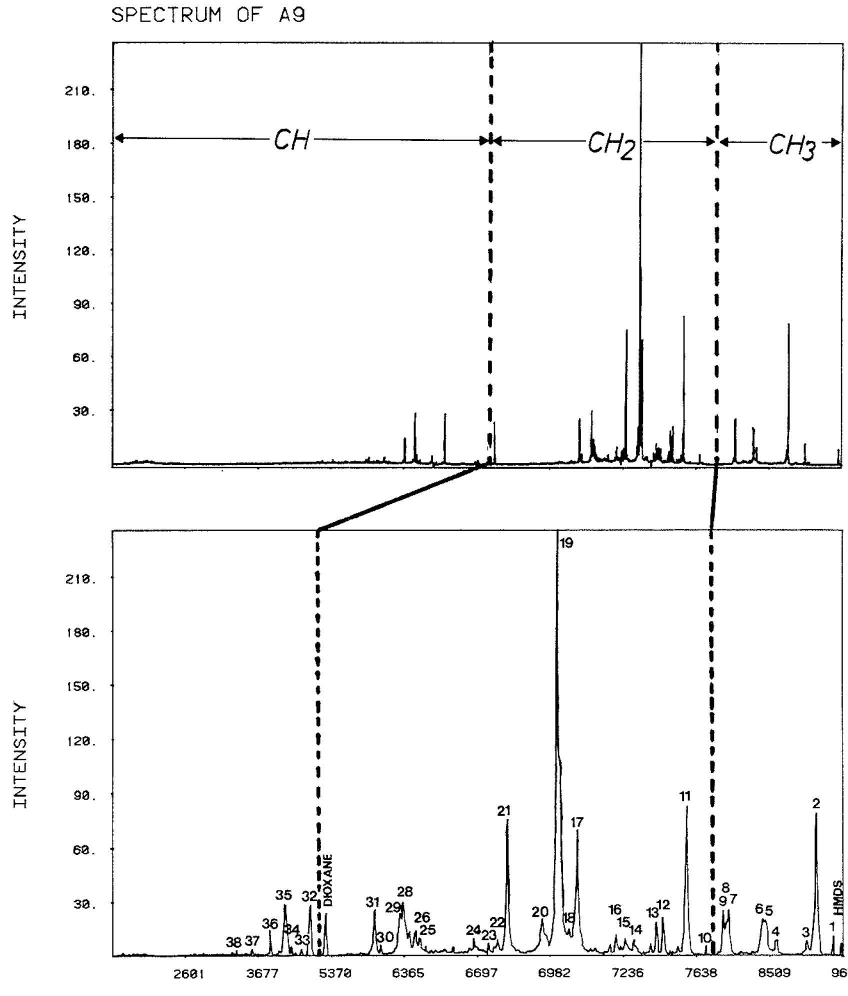

Figure 1. Spectrum of a C_{18} fraction (sample A9) before (above) and after data reduction. The CH, CH_2, and CH_3 subspectra are separated by using the DEPT technique and recombined as indicated in the Experimental Section. The most intense peaks are numbered for assignment purposes. The variable numbers in the bottom scale refer to the raw spectrum before data reduction.

$$\mathrm{MOP} = \mathbf{O}\cdot\mathbf{M} = \sum_{j=1}^{p} o_j m_j \qquad (2)$$

where **O** and **M** are the vectors of intensities in the sample spectrum (object) and neat-liquid spectrum (marker object), respectively, and p is the number of data points in the spectra. Thus, only nonzero elements in **M** will contribute with nonzero products to eq 2. For the purpose of quantification two conditions must be fulfilled: (1) the marker-object spectrum must be present, at least partly, as a resolved subspectrum in the mixture spectrum; (2) the total intensities in the spectra must be normalized. Other applications of the MOP technique are reported elsewhere (*24, 30*).

EXPERIMENTAL SECTION

Samples. The $\{C_{10}, C_{11}, C_{12}, \ldots, C_{25}\}$ distillate fractions were collected from two crude oils produced from different wells in the North Sea. The boiling point ranges are given in Table I. NMR samples were prepared from 1.7216 ± 0.0005 g of distillate with 20 ± 0.2 μL of hexamethyldisilane (HMDS) and 20 ± 0.2 μL of dioxane as internal standards and diluted 1:1 in $CDCl_3$. To obtain a uniform spectral response, ferric acetylacetonate was added to give a 0.03 M concentration of Fe^{3+} ion in the samples. The use of paramagnetic relaxation agents introduces severe line broadening in the spectra, but this is compatible with the present complex mixtures, which anyway exhibit extensive peak overlap.

NMR. The NMR measurements were performed on a Bruker AM-400 spectrometer immediately after sample preparation. "WALTZ-16" proton-decoupled ^{13}C DEPT spectra were obtained by using three different values for the proton pulse, θ: $\theta_1 = 45°$, $\theta_2 = 90°$, $\theta_3 = 135°$ (*11, 31*). This gave three spectra for each sample. To obtain comparable intensities between the spectra, 32, 64, and 32 scans were collected for the three values of θ, respectively. The relaxation delay was set to 10 s, and the evolution period, τ, was 0.0071 s, assuming an average ^{13}C–^{1}H one-bond coupling constant of 140 Hz. The free induction decays

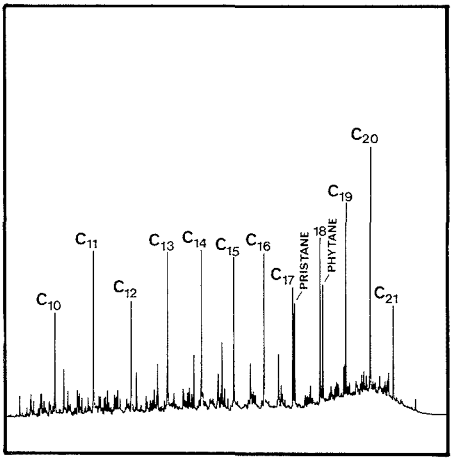

Figure 2. Gas chromatogram of the combined fractions C_{10}–C_{21} (samples A1–A12). Labels refer to *n*-alkanes. Appreciable amounts of pristane and phytane were detected in the C_{17} (sample A8) and C_{18} (sample A9) fractions, respectively.

(FIDs) were sampled in 32K data points over a 20 000-Hz spectral range. Data acquisition was performed at ambient temperature (ca. 20 ± 0.2 °C).

Spectral Processing. Separate FIDs, FID CH_n, for the CH, CH_2, and CH_3 carbons were generated by linear combination of FID θ_1, FID θ_2, and FID θ_3 acquired for the three values of θ:

$$\text{FID CH}_2 = \text{FID } \theta_1 - 1.20(\text{FID } \theta_2)$$

$$\text{FID CHCH}_3 = \text{FID } \theta_1 + 1.20(\text{FID } \theta_2)$$

$$\text{FID CH} = \text{FID } \theta_2 - 0.22(\text{FID CHCH}_3)$$

$$\text{FID CH}_3 = \text{FID CHCH}_3 - 0.78(\text{FID } \theta_2)$$

The coefficients were obtained empirically. To reduce base-line noise, the FIDs were multiplied with an exponential factor corresponding to an additional line broadening of 2 Hz in the Fourier transformed spectra.

After Fourier transformation the spectra were manually phased, and a first-order base-line correction was applied. The spectra were referenced by using a peak at 28.04 ppm for the CH subspectra, a peak at 22.80 ppm for the CH_2 subspectra, and a peak at 14.5 ppm for the CH_3 subspectra. In this way the large solvent shift differences introduced by using one chemical shift reference for all carbon types are eliminated (*30*). The spectral ranges that exhibited more than base-line intensity were transferred to a Micro-VAX II computer. In the final raw data matrix, each of the 32 samples was characterized by 5030 CH data points, 2970 CH_2 data points, and 1651 CH_3 data points (Figure 1).

Data Pretreatment, Reduction, and Analysis. The spectral intensities were normalized to internal HMDS and dioxane. The number of variables was reduced to 1032 by using the soft maximum entropy procedure described in the theoretical section. Principal component analysis and marker-object projections were applied to the normalized and reduced data. Principal component analysis was performed both before and after dividing the variables by their respective means as specified in the discussion. The whole procedure for scaling, variable reduction, and data analysis was performed by using the SIRIUS program implemented on a Micro-VAX II computer (*32*).

Gas Chromatography. Samples A1–A12 (C_{10}–C_{21} fractions) and B8 (C_{17} fraction) were analyzed by gas chromatography (GC) for comparison with the NMR spectra. The chromatographic analysis was performed on Carlo Erba Fractovap 2900 equipment with a 40-m fused silica capillary column with a stationary phase of 5% phenyl methyl silicone and a flame ionization detector. The distillate fractions were dissolved in hexane (1 μL:2 mL) before analysis. Main peaks were identified by comparison with standards (*n*-alkanes, pristane, phytane). The pattern of peaks in the chromatograms is typical for petroleum fractions. *n*-Alkanes dominate, and branched alkanes are found at lower concentrations. Pristane and phytane are found in concentrations equal to those of the *n*-alkanes in this series. A chromatogram of the combined fractions, A1–A12, is shown in Figure 2 to illustrate the sample compositions. The pristane concentrations in the C_{17} fractions were calculated as area percentage of the base-line-corrected pristane peak to total area of components in the fraction, including the components eluted in the unresolved envelope.

Table II. Assignment of the Main Peaks in the Spectra

	peak no.	chem shift, ppm	peak assignments
CH_3	HMDS	−2.50	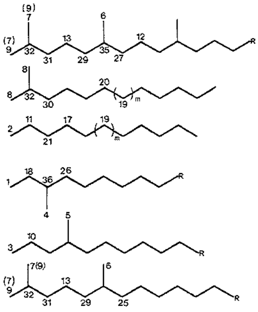
	1	11.44	
	2	14.16	
	3	14.45	
	4	19.30	
	5	19.69	
	6	19.75	
	7	22.65	
	8	22.69	
	9	22.74	
CH_2	10	20.22	
	11	22.80	
	12	24.56	
	13	24.91	
	14	26.55	
	15	26.86	
	16	27.21	
	17	29.50	
	18	29.65	
	19	29.84	
	20	30.17	
	21	32.05	
	22	32.37	
	23	32.80	
	24	33.55	
	25	37.04	
	26	37.21	
	27	37.38	
	28	37.48	
	29	37.54	
	30	39.16	
	31	39.45	
	dioxane	67.11	
CH	32	28.04	
	33	30.15	
	34	32.57	
	35	32.84	
	36	34.48	
	37	37.78	
	38	40.27	

RESULTS AND DISCUSSION

The raw spectrum and the corresponding reduced spectrum of the C_{18} fraction (sample A9) are shown in Figure 1. As described in the Experimental Section, each sample spectrum consists of a CH_3 subspectrum, a CH_2 subspectrum, and a CH subspectrum. Note how the data reduction procedure expands the spectral features in regions of high intensity, as seen in the CH_2 subspectrum, and pools the intensities in ranges of low intensity, as seen in the CH subspectrum. Thus, the spectral features are retained although the number of variables is reduced by an order of magnitude.

Some representative spectra are shown in Figure 3. Note that all spectra exhibit the same pattern. The similarity between corresponding fraction spectra for the two oils is striking. Visual inspection reveals virtually no significant difference between the two oils. By integration of the raw spectral profiles we found that the systematic pattern con-

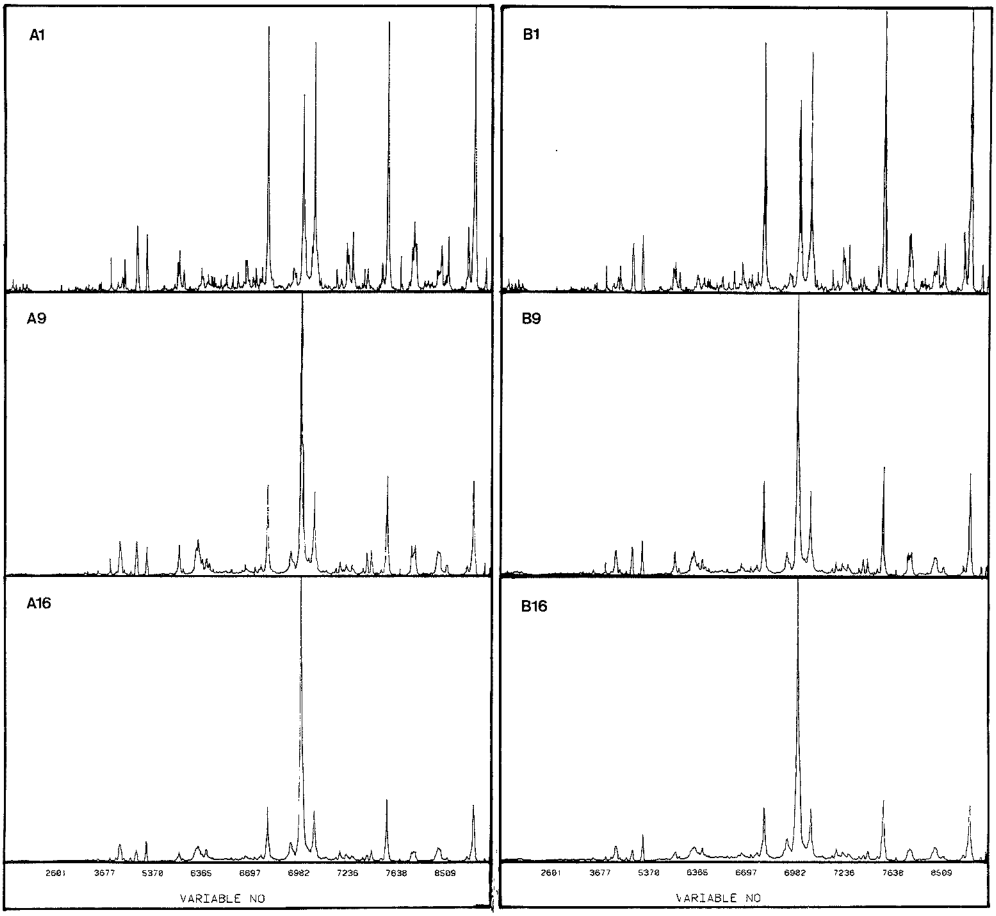

Figure 3. Spectra of the C_{10}, C_{18}, and C_{25} fractions of the two oils A and B.

stitutes roughly 70–90% of the total intensity in the spectra, consistent with the assumption that all samples are composed of the same structural units (*6, 7*).

Assignments. Ward et al. (*5*) and Netzel et al. (*6*) have reported ^{13}C spectra of shale oil fractions that are very similar in appearance to the present spectra of petroleum fractions. We chose to use the A9 spectrum (C_{18} fraction) for the assignment of the main structures in the samples. Assignments are given in Table II. The presence of *n*-alkanes, pristane (2,6,10,14-tetramethylpentadecane), and phytane (2,6,10,14-tetramethylhexadecane) is confirmed by GC (Figure 2), while the other structures are assigned by comparison to literature data (*5, 6*). Correlation between variables revealed in the PC analysis is also a strong indication that the peaks represent a common molecular structure (*18, 30, 33*).

The intense and well-defined peaks are due to *n*-alkanes and isoalkanes. The unassigned peaks in the range 26.50–27.30 ppm (peaks 14, 15, and 16) are probably due to methylene carbons with a methyl substituent in γ-position on one side and a long unbranched chain on the other. The unassigned peak at 37.48 (peak 28) is probably due to a structure similar to the ones assigned to peaks 25, 26, 27, and 29. The rest of the unassigned peaks (peaks 22, 23, 24, 33, 34, 37, and 38) are also seen to be of some importance in the PC loadings, but the assignments of these less intense peaks are not clear. The absence of well-defined patterns in the less intense spectral ranges reflects a greater diversity in carbon environments. It is likely that this diversity is caused by bridging and geometrical isomerism in cyclic structures (aromatics, naphthenes, and cycloalkanes). Most of the unassigned intensity is found in the CH subspectrum, and the fraction of unassigned intensity increases toward higher boiling fractions.

Principal Component Analysis. The two first principal components (PCs) describe 72.5% and 13.4% of the variance in the spectra, respectively. The first point to note is thus the dramatic reduction in dimensionality in the data, from 9651 variables in the raw spectra to two PCs that describe 85.9% of the variance. There are two sources for the large redundancy in the data: (1) Each constituent is represented by many peaks in the ^{13}C NMR spectrum; (2) petroleum constituents correlate due to similarities in source, evolution, migration, and other geochemical processes. The third and subsequent PCs each described less than 6% of the variance in the data and were partly obscured by residual solvent shift effects (see below). These PCs are not considered further.

A plot of the sample scores in the plane spanned by the first two PCs and the corresponding loading profiles are given in Figure 4. The scores for the first PC are seen to describe a

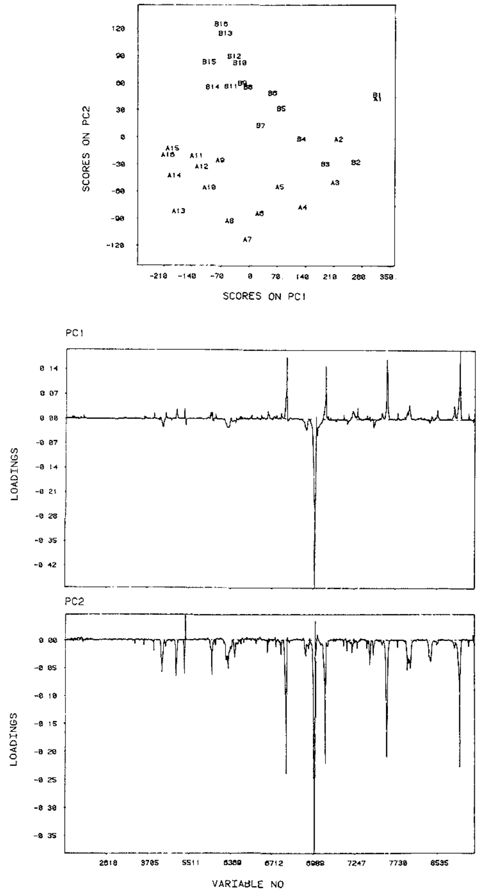

Figure 4. Plot of the sample scores in the plane spanned by the first two PCs (above) and the corresponding loading profiles.

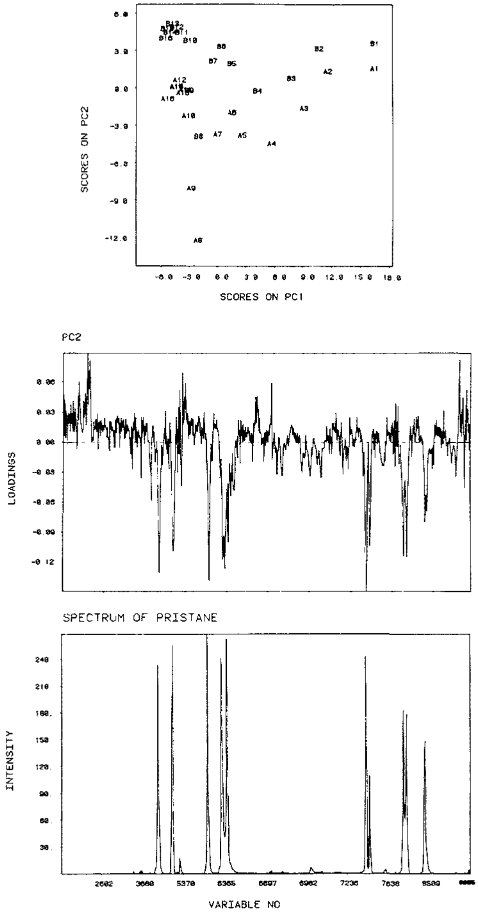

Figure 5. Plot of the sample scores in the plane spanned by the first two PCs (above) and the corresponding loading profile for PC2 (middle) after mean-scaling of the variables. The spectrum of pure pristane is shown for comparison with the PC2 loading profile.

variation related to the boiling points of the fractions. The loading profiles can be directly related to the spectral profiles in Figure 3. The dominant feature in the loading profile for PC1 is the negative correlation between the peak representing the carbons in the middle of unbranched alkane chains (peak 19) and the peaks representing the end carbons of unbranched alkane chains (peaks 2, 11, 21, and 17). The PC1 loadings for peaks 6, 12, 20, 25–27, and 35 correlate with that for peak 19. These peaks all represent central parts of large isoalkanes. In other words, PC1 describes a decrease in chain length. The lack of variance in the scores for the heavier distillate cuts can be explained by a general decrease in the relative contents of *n*-alkyl chains, or by the decreasing relative effect of adding one more carbon to an ever longer chain.

The aromatic and, presumably, the saturated cyclic resonances contribute with small, but generally positive loadings to PC2. The loading for peak 19 is less dominating in PC2 than in PC1, indicating that long *n*-alkyl chains contribute less to this PC. Consistent with this observation, peak 19 is seen to have two loading components in PC2 due to a small chemical shift difference between carbon 5 and the other central carbons of long *n*-alkyl chains. This component can be seen as a shoulder on peak 19 in the spectra. Peaks representing isoalkanes, particularly those that are derived from isoprenoid structures (Table II), are seen to contribute appreciably to PC2 as well. PC2 thus primarily describes a variation from low to high contents of substituted/branched alkanes. The scores along PC2 discriminate between the two oils although they tend to be similar in the C_{10}–C_{12} fractions. This is an interesting observation because the concentration of constituents with saturated isoprenoid structure is known to be highest in the early stages of the petroleum generation process. In petroleum from similar source rocks, the amounts of pristane and phytane relative to those of the *n*-alkanes are thus believed to be related to the maturity of the source rock (*34*).

Appreciable amounts of pristane and phytane were detected by gas chromatography in the C_{17} and C_{18} fractions, respectively (Figure 2). The spectrum of pristane is shown at the bottom of Figure 5. Due to the presence of pristane in the C_{17} fraction the peaks that represent the pristane structure are very intense in the A8 and B8 spectra, giving relatively large variances in these variables. By division of the variables by their means, the impact of variables with relatively large variances is enhanced at the cost of variables with relatively

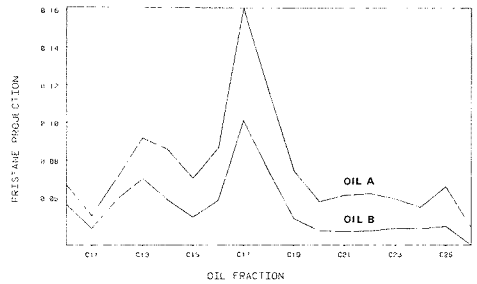

Figure 6. Scalar product between the fraction spectra and the pristane spectrum scaled to unity for pure pristane. The vertical scale times 100 thus gives the percent concentrations of pristane-like structures in the fractions. The residue fractions for the oils are included as the sample points at the rightmost frame of the figure.

low variances. After such a scaling of the variables, the two first PCs described 46.9% and 17.2% of the variance, respectively. Again, from the scores it is seen that PC1 reflects a decrease in boiling points of the fractions, while PC2 now discriminates between the two oils also in the C_{10}–C_{12} fractions. From a comparison between the loading profile for PC2 and the spectrum of pure pristane (bottom of Figure 5) it is evident that PC2 is related to the content of components with structures similar to that of pristane. The scores for PC2 tell us that the pristane spectrum represents a feature that accounts for the difference between the two oils in all fractions, not only the one actually containing pristane. It is evident that the pristane spectrum is representative for a wide range of constituents with saturated isoprenoid structure. The relatively large negative scores for samples A8 and A9 (the C_{17} and C_{18} fractions in oil A) are consistent with the high content of pristane and phytane, respectively, in these samples.

A ready interpretation of the loading profiles requires that the ^{13}C NMR solvent shift differences are minimized. This is a major problem in complex ^{13}C NMR spectra. Solvent shifts result in a displacement of intensity from one data point in one spectrum to a neighboring data point in another spectrum. Such intensity variations have a disturbing impact on the principal components, as seen in the PC2 loading profile for dioxane in Figure 4. ^{13}C NMR solvent shifts in hydrocarbon mixtures are discussed elsewhere (*3, 23, 30*). Apart from a suspicious spike in the middle of the loading profile for peak 19, the loadings for the rest of the variables show that separate referencing of the three CH_n ($n = 1, 2, 3$) DEPT subspectra reduces the solvent shift differences to an acceptable level.

Validation of the Analysis. The assumption that all samples are composed of the same structural units in varying amounts is crucial. Mathematically, the assumption is equivalent to stating that all samples are described within the same multivariate space. In order to test this, separate PC decompositions of the spectra for the two oils A and B were performed. $PC1_A$ and $PC1_B$ accounted for 81.7% and 80.8%, respectively, of the variance in the two series of spectra, while 8.1% and 6.4% of the variance were described by $PC2_A$ and $PC2_B$, respectively. The congruence (*35*), or scalar product, between the normalized loading vectors for the two components PC_A and PC_B was calculated. Since the loading vectors are scaled to unit length, the congruence between pairs of PCs is a number between +1 and −1, with ±1 showing perfect overlap. Congruences of 0.93 between $PC1_A$ and $PC1_B$ and 0.81 between $PC2_A$ and $PC2_B$, the two major PCs for the two oils, confirm that the two oils are, mainly, confined to the same multivariate space. We have also seen that this assumption leads to chemically meaningful results, a strong evidence of its validity.

Quantification of Pristane Structures. The correlation between the "pristane" variables seen in the loadings for PC2 in the mean-scaled data gives us a unique possibility for a simple quantification of a statistically and chemically well-defined and important feature in this extremely complex system. Since all spectra are normalized to internal standards (HMDS and dioxane), their intensities are directly comparable. This means that the spectrum of pure pristane represents a unit vector for pristane relative to the fraction spectra. By projecting the fraction spectra onto the pristane spectrum (the scalar product between each fraction spectrum and the pristane spectrum) and dividing by the squared norm of the pristane spectrum, we get a number between zero and 1, with 1 for pure pristane. The results are shown in Figure 6.

Figure 6 shows that pristane-like structures are present in all samples, as expected from the PC analysis above. The two oils are systematically separated, oil A being richer in pristane-like structures than oil B in all fractions. The maximum around the C_{17} fraction is mainly due to the presence of pristane itself, but similar structures will contribute also for this fraction. Our analysis thus gives 16.1% "pristane" in oil A, and 10.3% in oil B, compared to 11.5% and 7.5% pure pristane as obtained from GC. There is a tendency of "peaking" at every fourth fraction. This pattern may be due to the presence of constituents that are built from an integral number of saturated isoprenoid units. From symmetry considerations (see Table II), it is evident that the spectra of these constituents will overlap completely with the spectrum of pristane, resulting in a larger scalar product than for those structures that are partly different from pristane. The residue fractions (containing all constituents above C_{25}) are included in this analysis and are seen to have a relatively low content of pristane-like structures.

Conclusions. The result suggests ^{13}C NMR as an alternative to chromatographic methods for the analysis of the heavier petroleum fractions. The large number of possible constituents makes chromatographic profiles less useful for these fractions, especially if isoconstituents are believed to be present in significant amounts. The fact that NMR gives average structures in petroleum samples is no drawback, since geochemical processes often relate to compound classes rather than to single constituents.

Principal component analysis in combination with data reduction by use of a maximum entropy criterion is a very efficient and objective means of extracting the essential information in complex ^{13}C NMR spectra. The analysis provides specific information on straight-chain and isoalkane structures in particular, while the spectral representation of the cyclic hydrocarbons, including aromatics, naphthenes, and cycloalkanes, is more complex. Marker-object projection offers a mathematically simple method for the quantification of structural units that are identified in the PC analysis.

ACKNOWLEDGMENT

Bo Nordén at the University of Umeå and Nils Å. Frøystein at the University of Bergen are thanked for supplying the software connection between the NMR spectrometer and the VAX computer. Terje V. Karstang at the University of Bergen is thanked for updating the SIRIUS program to our specific desires. Norsk Hydro Research Center in Bergen is thanked for supplying the petroleum distillates.

LITERATURE CITED

(1) Klemens, A. *Mat. Naturwissenschaft. Unterricht* **1983**, *36*, 29–35.
(2) Allerhand, A.; Maple, R. M. *Anal. Chem.* **1987**, *59*, 441A–452A.
(3) Brekke, T.; Aksnes, D. W.; Sletten, E.; Stöcker, M. *Anal. Chem.* **1988**, *60*, 591–596.

(4) Laude, D. A.; Wilkins, C. L. *Anal. Chem.* **1986**, *58*, 2820–2824.
(5) Ward, R. L.; Burnham, A. K. *Fuel* **1984**, *63*, 909–914.
(6) Netzel, D. A.; McKay, D. R.; Heppner, R. A.; Guffey, D. G.; Cooke, S. D.; Varie, D. L.; Linn, D. E. *Fuel* **1981**, *60*, 307–320.
(7) Petrakis, L.; Allan, D. K.; Gavalas, G. R.; Gates, B. C. *Anal. Chem.* **1983**, *55*, 1557–1564.
(8) Forsyth, D. A.; Hediger, M.; Mahmoud, S. S.; Giessen, B. C. *Anal. Chem.* **1982**, *54*, 1896–1898.
(9) Lindeman, L. P.; Adams, J. Q. *Anal. Chem.* **1971**, *43*, 1245–1252.
(10) Cookson, D. J.; Smith, B. E. *Fuel* **1983**, *62*, 34–43.
(11) Barron, P. F.; Bendall, M. R.; Armstrong, L. G.; Atkins, A. R. *Fuel* **1984**, *63*, 1276–1279.
(12) Bouquet, M.; Bailleul, A. *Fuel* **1986**, *65*, 1240–1246.
(13) Gillet, S.; Delpuech, J.-J. *J. Magn. Reson.* **1980**, *38*, 433–445.
(14) Gillet, S.; Delpuech, J.-J.; Valentin, P.; Escalier, J.-C. *Anal. Chem.* **1980**, *52*, 813–817.
(15) Gillet, S.; Rubini, P.; Delpuech, J.-J.; Escalier, J.-C.; Valentin, P. *Fuel* **1981**, *60*, 221–225.
(16) Gillet, S.; Rubini, P.; Delpuech, J.-J.; Escalier, J.-C.; Valentin, P. *Fuel* **1981**, *60*, 226–230.
(17) Øhman, J. Calibration and Background Correction with Partial Least Squares Regression in Liquid Chromatography. Ph.D. Thesis, University of Umeå, Sweden, 1988.
(18) Kvalheim, O. M.; Aksnes, D. W.; Brekke, T.; Eide, M. O.; Sletten, E.; Telnæs, N. *Anal. Chem.* **1985**, *57*, 2858–2864.
(19) Johnels, D.; Edlund, U.; Grahn, H.; Hellberg, S.; Sjöström, M.; Wold, S.; Clementi, S.; Dunn, W. J., III. *J. Chem. Soc., Perkin Trans. 2* **1983**, 863–871.
(20) Johnels, D.; Edlund, U.; Wold, S. *J. Chem. Soc., Perkin Trans. 2* **1985**, 1339–1343.
(21) Grahn, H.; Masino, C. J.; Nordên, B.; Edlund, U. *Magn. Reson. Chem.* **1988**, *26*, 1097–1102.
(22) Hearmon, R. A.; Scrivens, J. H.; Jennings, K. R.; Farncombe, M. J. *Chemom. Intell. Lab. Syst.* **1987**, *1*, 167–176.
(23) Brekke, T.; Kvalheim, O. M.; Sletten, E. *Anal. Chim. Acta* **1989**, *223*, 123–134.
(24) Kvalheim, O. M. *Chemom. Intell. Lab. Syst.* **1987**, *2*, 283–290.
(25) Full, W. E.; Ehrlich, R.; Kennedy, S. K. *J. Sediment. Petrol.* **1984**, *54*, 117–126.
(26) Karstang, T. V.; Eastgate, R. J. *Chemom. Intell. Lab. Syst.* **1987**, *2*, 209–219.
(27) Wold, S.; Esbensen, K.; Geladi, P. *Chemom. Intell. Lab. Syst.* **1987**, *2*, 37–52.
(28) Kvalheim, O. M. *Chemom. Intell. Lab. Syst.* **1988**, *4*, 11–25.
(29) Joliffe, I. T. *Principal Component Analysis*; Springer Verlag: Berlin, 1986.
(30) Brekke, T.; Kvalheim, O. M.; Sletten, E. *Chemom. Intell. Lab. Syst.*, in press.
(31) Doddrell, D. M.; Pegg, D. T.; Bendall, M. R. *J. Magn. Reson.* **1982**, *48*, 323–327.
(32) Kvalheim, O. M.; Karstang, T. V. *Chemom. Intell. Lab. Syst.* **1987**, *2*, 235–237.
(33) Windig, W. *Chemom. Intell. Lab. Syst.* **1988**, *4*, 201–213.
(34) Waples, D. W. *Geochemistry in Petroleum Exploration*; D. Reidel Publ. Co.: Boston, MA, 1985; p 51.
(35) Kvalheim, O. M. *Chemom. Intell. Lab. Syst.* **1987**, *2*, 127–136.

RECEIVED for review June 19, 1989. Accepted October 2, 1989. This work was supported by the Norwegian Council for Science and the Humanities (NAVF).

Simultaneous Monitoring for Parent Ions of Targeted Daughter Ions: A Method for Rapid Screening Using Mass Spectrometry/Mass Spectrometry

Scott A. McLuckey,* Gary L. Glish, and Barry C. Grant

Analytical Chemistry Division, Oak Ridge National Laboratory, Oak Ridge, Tennessee 37831-6365

A novel method of operation possible with some, but not all, types of instruments capable of mass spectrometry/mass spectrometry is demonstrated. The method involves operating the first stage mass analyzer as a high-pass filter while a second stage of mass analysis is used to detect the daughter ions from a targeted compound class that fall below the arbitrary cutoff mass. This method can be employed in those cases where a parent ion scan is useful. The present method, with some sacrifice in specificity, provides a roughly 10-fold increase in parent ion transmission relative to that for either conventional daughter ion analysis or the parent ion scan. This mode of operation is demonstrated with anions derived from 2,4-dinitrotoluene (DNT), 1,3,5-trinitroazacyclohexane (RDX), a heterocyclic nitramine, and pentaerythritol tetranitrate (PETN), a nitrate ester.

INTRODUCTION

Mass spectrometry/mass spectrometry (MS/MS) has been recognized to be particularly useful for the analysis of targeted compounds in mixtures (*1–4*). Compound classes can also be targeted provided ions derived from members of the class undergo a similar reaction between stages of mass analysis. These reactions include, for example, those that result in a particular daughter ion, those that involve the loss (or gain) of a particular chemical moiety, and those that involve a change in charge state. One or more of various scanning modes can be used to detect selectively ions that undergo the reaction. Common scan modes that have been used to screen rapidly for members of a targeted compound class include the parent ion scan, for ions of a class that fragment to a common daughter ion, and the neutral loss scan, for ions of a class that lose a common neutral fragment upon dissociation. Scan modes have also been employed to screen for ions that readily undergo a charge-changing reaction, such as the so-called E/2 scan for singly charged ions formed in the ion source of a mass spectrometer that are converted to doubly charged ions prior to an electric sector. Each of these modes of operation, as well as others, has been shown to be useful for appropriate applications (*1–4*). For example, Gallegos demonstrated the usefulness of the parent ion scan in organic mixture analysis by the accelerating voltage technique for decompositions of metastable ions in the first field-free region of a sector mass spectrometer (*5, 6*). Hunt et al. demonstrated, early in the application of triple quadrupole MS/MS to analytical problems, the rapid screening for several compound classes in environmental samples by using parent ion scans and neutral loss scans (*7–9*). Indeed, these types of rapid screening scans are now widely accepted and are standard features in most commercial MS/MS instruments.

We report here a method of operation possible with some, but not all, MS/MS instruments that, at some sacrifice in specificity, can increase parent ion transmission and reduce analysis time in rapid screening applications. These applications are restricted to those in which parent ions derived from the targeted compound class or classes fragment to a

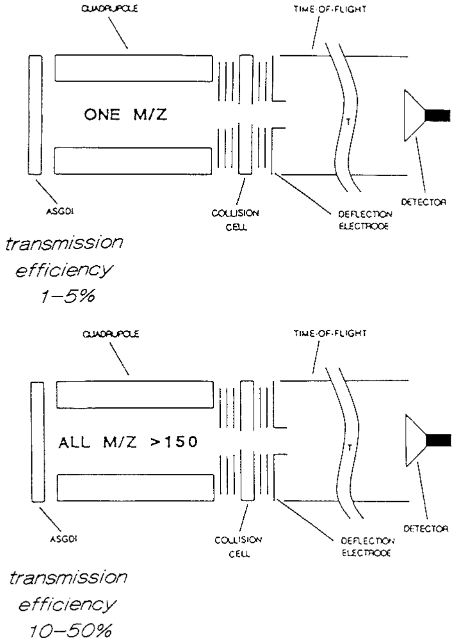

Figure 1. Schematic diagrams demonstrating the conventional daughter ion MS/MS mode (top) and the rf-only QTOF daughter mode (bottom).

common daughter ion. This method of operation is demonstrated with a quadrupole/time-of-flight (QTOF) MS/MS instrument but should also be possible with any beam-type tandem mass spectrometer in which the first mass spectrometer is a quadrupole mass filter and with trapping instruments such as the quadrupole ion trap and the Fourier transform ion cyclotron resonance spectrometer. The method under discussion, very simple in implementation in the QTOF instrument, is shown schematically in Figure 1 along with the method for obtaining a conventional daughter ion MS/MS spectrum for comparison. In the present method, the quadrupole mass filter is operated in the "total ion" or radio frequency voltage (rf-only) mode with the rf voltage maintained at a level sufficient to reject ions that issue from the ion source below some predetermined m/z value. A target gas is admitted into the collision cell, and the TOF portion of the instrument is operated in the usual way. The resulting TOF spectrum contains both parent ions, which appear at masses above the cutoff of the quadrupole mass filter, and daughter ions resulting from dissociation of the parent ions that pass through the quadrupole. Daughter ions can appear both above and below the quadrupole cutoff mass. This mode of operation is useful only if the ions derived from the targeted compound class show a common daughter ion with a mass that falls below the cutoff of the quadrupole mass filter. Thus, it can be employed in any instance in which a parent ion scan is useful. This constitutes, therefore, a degraded form of MS/MS in which a high-pass mass filter serves as the first stage of mass spectrometry. Therefore, the parent ion–daughter ion relationship is not defined by the experiment, resulting in a loss in specificity relative to that of a conventional MS/MS parent ion scan. However, the principal advantages of this method of operation are (i) increased transmission of the parent ions by operating in the rf-only mode relative to operating in the mass analysis (i.e., rf/dc (direct current)) mode and (ii) more favorable duty cycle resulting from eliminating the need for scanning the quadrupole or hopping the quadrupole through a series of masses.

EXPERIMENTAL SECTION

Data were acquired by using a linear quadrupole/time-of-flight tandem mass spectrometer. The instrument is based on an early prototype (*10*) and employs an Extrel Model 7-270-9 mass filter powered by Extrel C50 electronics with a mass range of 500 daltons. Details of the data system, the instrument, and its operation have been described (*11*). The QTOF spectrometer is fitted with an atmospheric sampling glow discharge ionization (ASGDI) source, which has been described recently (*12*). For these studies the ASGDI source was operated for negative ion analysis. The outer aperture plate/electrode was held at −385 V, and the inner aperture plate/electrode was held at ground potential. The pressure in the ion source was held at 0.7 Torr, and ambient air was drawn into the ionization region at a rate of 4–5 mL/s. 2,4-Dinitrotoluene samples were admitted by allowing the headspace vapor over a solid sample to be drawn into the ion source along with the ambient air. Samples containing pentaerythritol tetranitrate (PETN) and 1,3,5-trinitroazacyclohexane (RDX) were admitted, as described in the text, via quartz sampling tubes placed into a heated block leading to the ion source inlet aperture. Crystalline PETN and C-4, a military explosive composition containing RDX, were obtained from Sandia National Laboratories. The SEMTEX-H sample, a plastic explosive containing both RDX and PETN, was provided by the Forensic Science Research Unit of the FBI Academy.

To demonstrate the high-pass filter mode of operation, the quadrupole mass filter was operated with a constant rf voltage level of approximately 2000 V peak-to-peak (the frequency applied to the quadrupole is 1.2 MHz). This level effectively prevents ions of mass less than 150 daltons from passing through the quadrupole (transmission $< 0.01\%$). In the conventional mode of operation the quadrupole was operated at unit mass resolution up to approximately m/z 400, where resolution is defined as $M/\Delta M$ at half-height. The TOF part of the measurements was common to both modes and has been described in detail (*11*). All TOF spectra were accumulated for 10 s at a rate of 20 kHz. Air was used as the collision gas and was admitted to a pressure sufficient to attenuate the ion beam issuing from the collision cell by about 50%. This results in collection efficiencies, defined as the ratio of the ion flux leaving the collision cell to that entering the collision cell, ranging between 0.2 and 0.3. The pressure within the 1-cm collision cell under these conditions is estimated to be a few milliTorr. Anions were detected with a conversion dynode/electron multiplier detector.

Detection limits for RDX were measured when the QTOF instrument was moved to Sandia National Laboratories in Albuquerque, NM, for tests. Known concentrations of RDX were admitted into the ion source via a quartz tube heated to 450 K from a calibrated vapor generator, which has been described (*13*). No effort was made to generate full response curves in these studies since the lower limit of detection was the quantity of interest. The lower limit of detection, taken as 5 times the standard deviation of the background noise, was arbitrarily chosen to be measured by using a 10-s period for acquiring the TOF spectrum for the modes that employ the TOF measurement, as this was deemed the longest reasonable time for many operational scenarios.

RESULTS AND DISCUSSION

The capability of the quadrupole mass filter to serve as a high-pass filter has been used by Hunt et al. in conjunction with injection of ions from an external ion source into an ion cyclotron resonance (ICR) spectrometer (*14*). In this application, the quadrupole is used to reject the low-mass ions formed from the matrix in a desorption ionization experiment to minimize space charge problems that might otherwise be encountered in the ICR cell. Of course, any of the quadrupoles in a triple-quadrupole mass spectrometer can be used in the rf-only mode, and this is often done. The center quadrupole is typically operated in the rf-only mode, and mass spectra are obtained by operating two of the quadrupoles in the rf-only mode. As a rule, however, the quadrupoles are operated so as to avoid any severe mass discrimination. A method intermediate between the conventional daughter ion MS/MS spectrum and the method emphasized here has been used by Hunt et al. in the sequence analysis of polypeptides using a triple-quadrupole mass spectrometer (*15*). The first quadrupole was operated by using a mass resolving power low enough to pass a window of several mass units, allowing for the simultaneous acquisition of the MS/MS spectra of both an unlabeled compound and its trideutero analogue.

The approach described here emphasizes the capability of the quadrupole mass filter to act as a high-pass filter in real-time rapid screening for members of targeted classes of compounds present in trace quantities. This method of operation has been found to be useful in the rapid screening of ambient air for the presence of trace levels of organic explosives. This application is one where it is most important to determine if *any* of the targeted compounds are present at the lowest level detectable. Once the presence of one or more of the targeted compounds is indicated, more specific, though less sensitive, MS/MS methods can be used, if so desired, to identify unambigously the compound(s). Therefore the explosives detection application below is used to illustrate this method.

Most organic explosives contain several NO_2 or NO_3 groups which give the molecules relatively high electron affinities. The analysis of the anions derived from the explosives molecules affords an important degree of selectivity since most organic molecules do not form stable anions (*16*). Most of the organic explosives fall into one or more of the following compound classes: nitroaromatic compounds, nitrate esters, and nitramines. The high-mass anions derived from members of each of these compound classes via glow discharge ionization show common intense daughter ions in their MS/MS spectra. For example, nitroaromatic anions typically show intense daughter ion signals due to NO_2^-, anions of nitrate esters dissociate predominantly to give NO_3^-, and the most intense parent ions derived from the heterocyclic nitramines tend to dissociate to both NO_2^- and $CH_2NCH_2NNO_2^-$. These daughter ions can therefore be used to indicate the possible presence of organic explosives.

The effective removal of the abundant low-mass ions that issue from the ASGDI source is illustrated in Figure 2. This figure compares the normalized TOF mass spectra acquired when the rf voltage of the quadrupole mass filter is low enough to transmit ions with *m/z* values greater than 10 and when the rf is held at a level that transmits ions only of *m/z* values greater than about 150. (Note that an intense anion is present at *m/z* 46. This signal is predominantly due to NO_2^- formed by the discharge in air. The fact that NO_2^- is formed from the air matrix and constitutes a major fraction of the background ion signal precludes the use of single-ion monitoring at *m/z* 46 for the detection of trace levels of explosives.) The ion at *m/z* 182 (which falls at a channel number of 295 in the TOF spectra) is the molecular anion of 2,4-dinitrotoluene (DNT) and arises from residual DNT present in a sampling tube attached to the ion source.

A major advantage of this mode is the improvement in transmission for any given parent ion in going from the mass analysis mode to the rf-only mode. With the QTOF quadrupole, transmission increases by a factor of 4–15 depending upon the resolution of the quadrupole when both rf and dc voltages are applied and on the rf voltage level used in the rf-only mode. It should be recognized that transmission through the quadrupole is not equal for all ions of mass greater than the nominal cutoff mass. The rf-only quadrupole is not a perfect high-pass filter. Each mass ion falls within a different part of the stability region, and even for ions of the same mass,

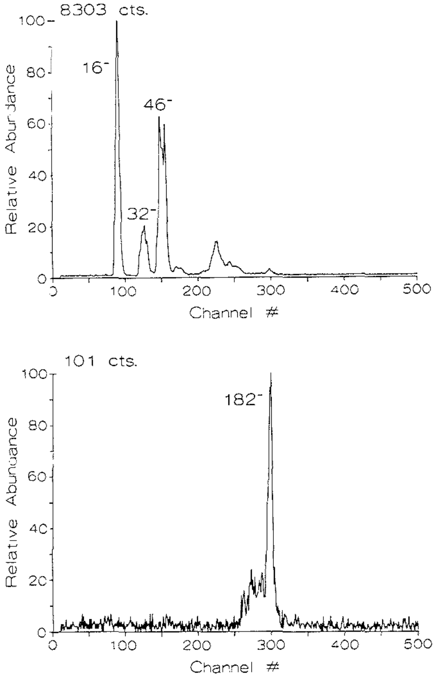

Figure 2. Comparison of (top) the TOF spectrum obtained when the quadrupole is operated in the rf-only mode at a level that transmits all ions above *m/z* 10 with (bottom) the TOF spectrum obtained when the rf level of the quadrupole is set to pass only those ions with *m/z* ratios greater than ≈150.

transmission is known to depend significantly on the kinetic energy of the ion and the angle and position at which it enters the quadrupole (*17*). It has been predicted (*18*) and shown (*19*) that higher order multipoles (e.g., hexapoles and octapoles) are less prone to severe mass and kinetic energy discrimination effects.

Figure 3a shows the TOF spectrum obtained when vapors of 2,4-dinitrotoluene were admitted into the ion source and when the quadrupole was used to pass only *m/z* 182, the mass of the molecular anion. Figure 3b shows the TOF spectrum obtained when the quadrupole was used as a high-pass filter with masses less than 150 daltons effectively rejected. In this case, the increase in signal for *m/z* 182 is roughly a factor of 12. Figure 3c shows the TOF spectrum that results when air is admitted into the collision cell under the same conditions used to obtain the spectrum of Figure 3b, i.e., when the quadrupole is operated as a high-pass filter. An intense peak arises from the NO_2^- daughter ion, which is common in the MS/MS spectra of anions derived from nitroaromatic compounds and heterocyclic nitramines (*20, 21*). In this example, the target gas attenuated the total ion current by about 75% (collection efficiency = 0.25). The spectrum of Figure 3c indicates a fragmentation efficiency of 0.63, which, with a collection efficiency of 0.25, yields an overall collision-induced dissociation efficiency of 0.16.

In addition to the ion transmission improvement shown above, a second major advantage of the present mode relative to a mode that requires the first stage mass spectrometer to be scanned is the improvement in duty cycle. When several parent ions are of interest, in the usual method of operation the rf/dc voltages applied to the quadrupole must be scanned

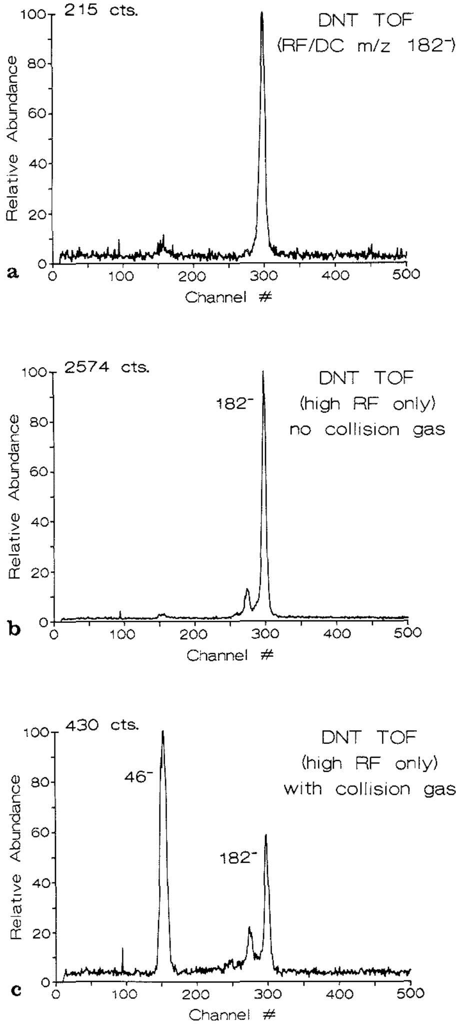

Figure 3. TOF spectra obtained for DNT when (a) the quadrupole is set to pass only ions of m/z 182 and in the absence of collision gas, (b) the quadrupole is set to pass all ions above $m/z \approx 150$ and in the absence of collision gas, and (c) collison gas is added and the quadrupole is operated as in b.

or they must be "hopped" to sequentially pass the different parent ion masses to the collision cell. A TOF spectrum must then be acquired at each parent mass. The duty cycle of the quadrupole therefore varies with the number of parent ions to be monitored as $1/n$ where n is the number of parent ions monitored. Therefore, for any particular rapid screening application, the improvement in duty cycle provided by the present mode of operation can be anticipated since the duty cycle of the first stage of the analysis is unity.

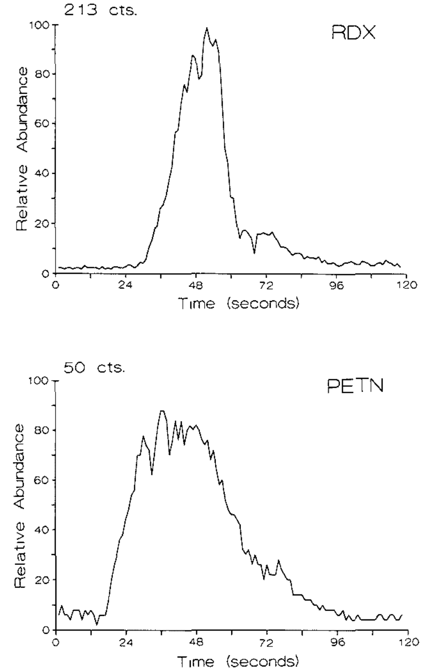

Figure 4. Desorption profiles of RDX and PETN from quartz sampling tubes admitted into a block heated to 450 K leading to the inlet of the ASGDI source. Profiles were determined in the single-ion monitoring mode by using m/z 176 for RDX and m/z 240 for PETN.

The duty cycle advantage is particularly important when there are many possible parent ions and when all of the sample compounds are introduced into the ion source either simultaneously or with significant overlap. Our most commonly used method for sampling and introducing explosives into the QTOF instrument provides an example. Often a hand-held vacuum cleaner is used to draw an air sample through a quartz tube from some object to be investigated. The quartz tube is then admitted into a block maintained at a temperature of 450 K, which is connected to the inlet of the ion source. Molecules of explosives thermally desorb from the quartz surface and are drawn into the ion source. The temperature of the heated block can be adjusted to give some separation in the times at which different explosives evolve from the tube. There is still significant overlap for most of the compounds of interest, however, at a block temperature sufficiently high (450 K) to keep the total analysis time less than 60 s. As an example, Figure 4 shows the normalized desorption profiles of approximately 20 pg each of RDX and PETN from quartz tubes separately admitted into the heated block. The desorption profiles were obtained by monitoring the most intense high-mass ion ($m/z > 150$) that appears for each of these explosives as a function of time. For RDX this ion appears at m/z 176 and corresponds to $(M - NO_2)^-$ while for PETN it appears at m/z 240 and corresponds to $(M - CH_2ONO_2)^-$. The point here is that there is significant overlap in these profiles. Several other possible explosives of interest also desorb over a similar time period including, for example, tetryl and picric acid.

In many explosives detection scenarios it is desirable to minimize the analysis time. It is therefore preferable to admit all of the sample over as short a period as feasible. However, the rapid desorption of all material present on the sampling tube is not optimal for the conventional mode of operation. Much of an explosive may desorb while the quadrupole is set to pass ions of m/z values other than those of the particular explosive that is present. Figure 5 illustrates the capability of the present mode of operation to simultaneously monitor for any explosives with parent ions with $m/z > 150$ when a "real-world" scenario is used. The figure shows the TOF

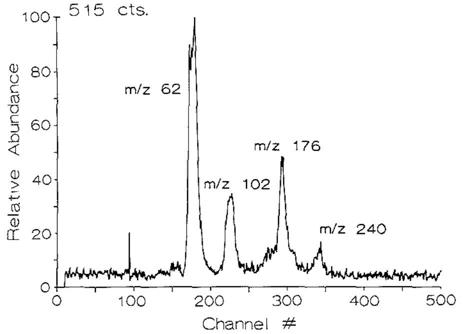

Figure 5. TOF spectrum obtained from a sampling of an envelope contaminated by SEMTEX-H, using the quadrupole as a high-pass filter with a target gas admitted into the collision cell. Signals at *m/z* 176, 102, and 46 are derived from RDX and signals at *m/z* 240 and 62 are derived from PETN.

spectrum acquired with the quadrupole in the rf-only mode with a low-mass cutoff of ≈150 and collision gas admitted into the collision cell after an envelope containing the plastic explosive SEMTEX-H, a mixture of RDX and PETN, was sampled by drawing air through the quartz sampling tube while the tube was drawn across the outside of the envelope. The spectrum shows daughter ions characteristic of both explosives. The fragments at *m/z* 102 (loss of CH_2NNO_2 from the ion at *m/z* 176) and at *m/z* 46 (NO_2^-), which appears as a small signal centered at channel no. 155, are characteristic of the parent anion from RDX, and the *m/z* 62 anion (NO_3^-) is characteristic of the parent anion from PETN.

A variation on this mode, as mentioned above, is to operate the quadrupole in a manner such that the rf/dc scan line intersects a broad region of the stability diagram rather than the apex so that it passes a wide range of ions (*15*) (i.e., use the quadrupole as a mass filter with very poor mass resolution). This situation is intermediate between the rf-only mode and the rf/dc mode with unit mass resolution. Such a mode is useful if the parent ions of interest fall within a fairly narrow mass range and may be helpful when extensive chemical noise is present in the mass spectrum, particularly at masses higher than those of the ions of interest. It has been noted that, with the quadrupole in the QTOF instrument, the improvement in transmission over that observed in the normal rf/dc mode for an ion of a particular *m/z* ratio is similar when the quadrupole is operated in the rf-only mode and when the mass resolution is degraded sufficiently to pass at least a range of 5 daltons or so.

The limits of detection for RDX obtained with several modes of operation have been compared. When the quadrupole was set to pass *m/z* 176 only and the TOF was turned off (i.e., in the single-ion-monitoring mode of operation), the detection limit defined as 5 times the standard deviation of the noise was ≈3 parts per trillion by volume in air. With the use of the conventional daughter ion MS/MS mode (i.e., adding collision gas to the collision cell and turning the TOF on), the detection limit for a 10-s TOF spectrum, defined as 5 times the standard deviation of the noise for the *m/z* 102 daughter ion, was 30 parts per trillion. During this period, ≈9 pg of RDX in air was sampled. By use of degraded mass resolution with the quadrupole, the detection limit, obtained under conditions otherwise identical with those used for the conventional daughter ion experiment, was determined to be 3 parts per trillion (≈900 fg of RDX in air). The detection limit obtained with the quadrupole in the rf-only mode was not measured but is expected to be similar to that obtained with degraded mass resolution since parent ion transmission is similar. No significant difference in noise levels in the mass region below the low-mass cutoff of the first stage of mass filtering for the three modes of operation has been observed. Of the three modes of operation, the conventional daughter ion mode is most specific but least sensitive. The rf/dc mode with less than unit mass resolution has greater specificity than does the rf-only high-pass filter method and comparable sensitivity when the compound(s) of interest fall within the transmitted mass window. However, when the targeted compound classes give ions over a wider mass range than the transmitted mass window (such as the example in Figure 5), much of the favorable duty cycle advantage of the rf-only method is lost.

The present mode of operation can also be implemented on several other types of instruments used for MS/MS studies. Implementation of this mode on a triple-quadrupole mass spectrometer, for example, would be straightforward and would offer advantages over the QTOF geometry in many applications. For example, the mass resolution of a quadrupole is better by a factor of 20–30 than the mass resolution that is generally obtained for negative ions in the TOF portion of the QTOF system. This provides greater specificity for the daughter ions. Furthermore, although the transmission through the TOF is roughly a factor of 10 greater than the transmission through a quadrupole operated in the rf/dc mode, the duty cycle of the TOF is 0.5% (ions are deflected out of the path to the detector 99.5% of the time). The duty cycle of the quadrupole can be varied depending upon the number of daughter ions of interest of different mass. When only one daughter ion is of interest, the duty cycle of the quadrupole can be unity. An advantage of the QTOF system is that a mass spectrum is obtained and possible parent ions can be identified directly from that spectrum. This is seen in Figure 5 in which the parent ions at *m/z* 240 and 176 are observed along with the targeted daughter ions.

A procedure analogous to the present mode of operation should also be possible with ion trapping intruments. In the Fourier transform ion cyclotron resonance instrument, the analogous experiment would involve an ion creation pulse, the ejection of low-mass ions, the selective excitation of masses of targeted parent ions perhaps via the selected waveform inverse Fourier transform technique (*22*), and the subsequent acquisition of the mass spectrum obtained in the usual way (*23*). This procedure would allow several parent ions to be monitored following a single ionization pulse as opposed to acquiring MS/MS spectra from one parent ion at a time, each requiring a separate ionization pulse. A similar procedure, in principle, can be used with a quadrupole ion trap, but the capability for kinetically exciting several different mass parent ions simultaneously is not currently available with rf ion traps. Different parent ions can, however, be excited sequentially following a single ionization period. It should be recognized that the advantage of greater transmission efficiency obtained with beam instruments is not realized with the trapping instruments. The primary advantage for the trapping instruments may be realized in the more efficient use of the ions that are formed. Another important difference between the beam and trapping instruments is that kinetic excitation for collisional activation is mass dependent in the trapping instruments so that the specificity of the analysis can be comparable to that of a conventional MS/MS experiment. The fact that kinetic excitation is mass dependent, however, requires that some choice be made regarding which *m/z* values are excited. The unselective excitation afforded in the beam instruments (all parent ions are subjected to collisional activation) does not allow for flexibility in this regard, but it makes the detection of an unanticipated member of a compound class more likely than with a trapping instrument in which some of the high-mass ions are not excited. (A less selective means of activation, such as some form of photoexcitation, may be feasible in the trapping instruments as an alternative to collisional activation.)

The loss in specificity in using the rf-only QTOF daughter mode in beam instruments is likely to limit its applicability to problems that can be addressed with selective ionization methods such as negative chemical ionization. Universal ionization methods, such as electron ionization, would probably result in excessive chemical noise when complex mixtures are analyzed, resulting in poor detection limits and frequent false positives. However, this mode of operation is intended to be used for targeted compound classes in cases where extremely low limits of detection are required. A selective ionization method is usually desirable in such cases under any circumstances. This mode of operation is useful as a first screen in those cases when many samples are to be analyzed in a limited amount of time. The detection of trace levels of explosives in air is one such case.

ACKNOWLEDGMENT

We gratefully acknowledge Frank C. Conrad and Dave W. Hannum of Sandia National Laboratories for their assistance in the RDX measurements and for helpful discussions.

LITERATURE CITED

(1) Busch, K. L.; Glish, G. L.; McLuckey, S. A. *Mass Spectrometry/Mass Spectrometry: Principles and Applications of Tandem Mass Spectrometry*; VCH Publishers: New York, 1988.
(2) McLafferty, F. W., Ed. *Tandem Mass Spectrometry*; John Wiley and Sons: New York, 1983.
(3) McLafferty, F. W. *Science* **1981**, *214*, 280.
(4) Yost, R. A.; Fetterolf, D. D. *Mass Spectrom. Rev.* **1983**, *2*, 1.
(5) Gallegos, E. J. *Anal. Chem.* **1975**, *47*, 1524.
(6) Gallegos, E. J. *High Performance Mass Spectrometry: Chemical Applications*; Gross, M. L., Ed.; ACS Symposium Series 70; American Chemical Society: Washington, DC, 1978; p 274.
(7) Hunt, D. F.; Shabanowitz, J.; Harvey, T. M.; Coates, M. L. *J. Chromatogr. Chromatogr. Rev.* **1983**, *271*, 931.
(8) Hunt, D. F.; Shabanowitz, J.; Harvey, T. M.; Coates, M. L. *Anal. Chem.* **1985**, *57*, 525.
(9) Hunt, D. F.; Shabanowitz, J.; Giordani, A. B. *Anal. Chem.* **1980**, *52*, 386.
(10) Glish, G. L.; Goeringer, D. E. *Anal. Chem.* **1984**, *56*, 2291.
(11) Glish, G. L.; McLuckey, S. A.; McKown, H. S. *Anal. Instrum.* **1987**, *16*, 191.
(12) McLuckey, S. A.; Glish, G. L.; Asano, K. G.; Grant, B. C. *Anal. Chem.* **1988**, *60*, 2220.
(13) Dionne, B. C.; Rounbehler, D. P.; Achter, E. K.; Hobbs, J. R.; Fine, D. H. *J. Energy Mater.* **1986**, *4*, 447.
(14) Hunt, D. F.; Shabanowitz, J.; Yates, J. R., III; Zhu, N. Z.; Russell, D. H.; Castro, M. E. *Proc. Natl. Acad. Sci. U.S.A.* **1987**, *84*, 620.
(15) Hunt, D. F.; Buko, A. M.; Ballard, J. M.; Shabanowitz, J.; Giordani, A. B. *Biomed. Mass Spectrom.* **1981**, *8*, 397.
(16) Harrison, A. G. *Chemical Ionization Mass Spectrometry*; CRC Press: Boca Raton, FL; 1983.
(17) Dawson, P. H.; Fulford, J. E. *Int. J. Mass Spectrom. Ion Phys.* **1982**, *42*, 195.
(18) Hagg, C.; Szabo, I. *Int. J. Mass Spectrom. Ion Processes* **1986**, *73*, 295.
(19) Syka, J. E. P.; Szabo, I. Presented at the 36th ASMS Conference on Mass Spectrometry and Allied Topics, June 5–10, 1988, San Francisco, CA.
(20) McLuckey, S. A.; Glish, G. L.; Carter, J. A. *J. Forensic Sci.* **1985**, *30*, 773.
(21) Yinon, J.; Harvan, D. J.; Hass, J. R. *Org. Mass Spectrom.* **1982**, *17*, 321.
(22) Marshall, A. G.; Wang, T.-C. L.; Ricca, T. L. *J. Am. Chem. Soc.* **1985**, *107*, 7893.
(23) Gross, M. L.; Rempel, D. L. *Science* **1984**, *226*, 261.

RECEIVED for review August 21, 1989. Accepted October 18, 1989. This research was sponsored by the U.S. DOE Office of Safeguards and Security under Contract DE-AC05-840R21400 with Martin Marietta Energy Systems, Inc.

Laser Desorption/Fourier Transform Ion Cyclotron Resonance Mass Spectrometry of Polymer Additives

Bruce Asamoto,* Judy R. Young, and Robert J. Citerin

BP Research, Warrensville Research Center, 4440 Warrensville Center Road, Cleveland, Ohio 44128-2837

Laser desorption/Fourier transform ion cyclotron resonance mass spectrometry is found to be a viable method for identifying polymer additives in polyethylene extracts. Reference spectra were obtained for 18 antioxidants, 7 UV absorbers, and 4 amide waxes. The spectra were found to contain intense quasimolecular ions (Na^+ and K^+ adducts) and also structurally informative fragments, depending on conditions used. The molecular weights of several additives in the diethyl ether extracts of three commercial polyethylenes were determined by using the characteristic Na^+/K^+ adduct pairs observed in the laser desorption spectra. Two additives were identified as phenolic antioxidants.

INTRODUCTION

The analysis of additives in polymers is often difficult for numerous reasons. Additives are usually present at less than percent level concentrations in the polymer matrix. This necessitates an extraction to remove the additive from the polymer matrix, often followed by a chromatographic separation. Even after extraction, gas chromatographic separation is difficult because of the reactive nature and high molecular weight of many additives. Thin-layer chromatography (*1*) and high-performance liquid chromatography (*1–5*) with refractive index and UV absorption detection have been used successfully but both are limited in resolution and the ability to identify unknown components. Supercritical fluid chromatography with off-line Fourier transform infrared detection (*6*) provides functional group information of an unknown additive but, due to the chemical similarity of many additives, may not be able to identify the exact additive used. Liquid chromatography in tandem with mass spectrometry has been used by Vargo and Olson (*7*) to provide enhanced compound identification capability. The molecular weight information provided by mass spectrometry is complementary to the functional group information provided by infrared spectroscopy. Lattimer et al. (*8, 9*) have investigated several mass spectrometric techniques for use on rubber additives. These studies include direct mass spectrometric analysis of the rubber as well as analysis of the rubber extracts. Recently,

---

*Author to whom correspondence should be addressed.

0003-2700/90/0362-0061$02.50/0 © 1989 American Chemical Society

Marshall et al. (*10*) have applied laser desorption/Fourier transform ion cyclotron resonance (LD/FT-ICR) mass spectrometry to identify dyes in poly(methyl methacrylate) polymers. Blease et al. (*11*) and Wilkins et al. (*12*) have also reported the spectra of several additives using LD/FT-ICR.

LD/FT-ICR has numerous features that make it a powerful method for the identification of polymer additives. FT-ICR can achieve both high resolution and high mass accuracy. This can be used to obtain an accurate molecular weight from which a molecular formula can be calculated. Switching from positive to negative ion mass spectral acquisition (for more information) can be done simply through a software command. At low laser power density, predominately molecular or quasimolecular ions are formed, while at higher power density, extensive mass spectrometric fragmentation can be obtained for structural information. It is also possible to select a particular parent ion for fragmentation by collision-induced dissociation (*13*, *14*). Through all these options, a wealth of information can be obtained by using LD/FT-ICR to help identify the numerous additives that may be present.

The purpose of this study was to devise a scheme using only wide bandwidth positive/negative ion LD/FT-ICR mass spectrometry for the identification of additives in polymer extracts. The bandwidth affects the sampling rate, which determines the lowest mass observable. At typical sampling rates of 800 and 400 kHz used in this study, the lower mass limit was 56 and 112 daltons, respectively. The use of a wider bandwidth is offset somewhat by the reduced resolution (typically 3000 at 500 daltons with a bandwidth of 400 kHz and 64K data points).

Three polyethylenes were selected for analysis, from a wash bottle, garbage can, and tarp. Extracts of the polyethylenes were analyzed without a prior chromatographic separation. This is feasible because LD/FT-ICR spectra of mixtures are less complex than electron impact spectra due to the reduced fragmentation. The identification of molecular ions, which will be discussed, is also simpler than for electron impact (EI) spectra. Polyethylenes usually contain antioxidants, UV absorbers and stabilizers, and slip agents (*15*), as well as other additive types. Reference spectra were obtained of additives representative of these types to aid in identifying characteristic ions.

EXPERIMENTAL SECTION

The additive samples were obtained from Ciba-Geigy (Hawthorne, NY), Uniroyal Chemicals (Middlebury, CT), Borg-Warner Chemicals (Morgantown, WV), and Chem Service, Inc. (West Chester, PA). Probe samples were prepared by dissolving 10–20 mg in 1 mL of a suitable solvent (methylene chloride or methanol). Approximately 30 μL of solution was placed on the probe tip, a $^3/_4$ in. diameter stainless steel disk. After the solvent was evaporated in air, the probe tip was mounted on the end of the Nicolet solid probe. Alternatively, a nebulizer (Meinhard Model TR-20-C1) was used to deposit approximately 300 μg of additive on the probe tip.

Polymer Extracts. Three polyethylene samples, from a wash bottle, a garbage can, and a tarp, were selected for analysis. The polymers (10–15 g) were extracted for 8 h with a Soxhlet apparatus using approximately 150 mL of diethyl ether. Between 50 and 150 mg of residue was obtained from the extract, consisting of both additive and low molecular weight polymer. Some of the low molecular weight polymer was removed by redissolving the extract residue in chloroform and precipitating the polymer with acetone. The precipitate was filtered out with a 0.5-μm Teflon filter. The solvent was evaporated from the extract, and the residues were redissolved in methylene chloride and deposited on the probe tip with a nebulizer.

Mass Spectrometry. The spectra were obtained on a Nicolet FTMS-2000 fitted with a Tachisto Model 216 pulsed CO_2 laser. Pulse energy was measured by sampling the pulse with a germanium beam splitter, which transmits roughly 50% of the power to a Scientech 365 energy meter and reflects the remaining 50% along the vendor-designed optical path to the circular probe tip. The focal point is located off-center, so that the probe can be rotated to expose a fresh sample surface. The energy was varied between 2 and 20 mJ, with 10 mJ being typical. Ths spot size at various energies was measured by observing the ablation of black ink on the probe tip with optical microscopy. It was found that as the pulse energy was increased, by opening an intercavity aperture in the laser, the spot size also increased. Energy per ablated area remained fairly constant (though the maximum energy density probably increases at the center of the spot). For this reason, power density at the sample was varied by moving the probe tip in or out along the magnet axis, which focuses or defocuses the beam at the probe tip while not changing the total energy. Two positions were used, a "focused" position, which ablated an area of approximately 0.35 × 0.15 mm, and a defocused position, which ablated an area of 0.7 × 0.4 mm, at 5-mJ pulse energy. These areas are probably smaller than the actual analysis area, since spectra can be obtained when no ablation is visible. The spot sizes correspond to maximum power densities of approximately 5×10^8 and 1×10^8 W/cm^2, respectively. The amount of sample vaporized per shot was on the order of 100 ng.

To obtain spectra, the trap plates were typically 2 V, and spectra were acquired in the source cell of the dual-cell Fourier transform mass spectrometer (FTMS). A delay of 3–10 s was used after the laser shot to allow neutrals to be pumped out (ions remain trapped in the cell) before detection. Laser power was set to be sufficient to give good intensity spectra without saturating the analog-to-digital converter. Spectra were usually not averaged, since adequate signal to noise could be obtained with one laser shot, and due to space charge effects, peaks could change position slightly on the mass scale. For both additives and extracts, several spectra were obtained at each of four conditions; positive ion focused, positive ion defocused, negative ion focused, and negative ion defocused. In some cases, for very easily ionized samples, the trap plate voltages were reduced to as low as 0.6 V to reduce the number of ions trapped. A bandwidth of either 800 or 400 kHz was typically used. At a magnet field of 2.9 T, these gave lower mass limits of 56 and 112 daltons, respectively. Spectra were usually acquired with 64K data points and zero-filled once.

To test reproducibility, a set of five spectra of Tinuvin 326 was obtained on two separate days. The laser pulse energy was maintained between 2 and 3 mJ. For both samples, approximately 300 μg of Tinuvin 326 was deposited on the probe tip. The focused probe position was used.

RESULTS AND DISCUSSION

General trends were apparent in appearance of the LD/FT-ICR spectra. The most pronounced trend was the expected dependence of fragmentation on power. This is shown for Irganox MD-1024 in Figure 1. With a defocused laser, quasimolecular ions were generally the most abundant ions. These ions usually consisted of proton, Na^+, and K^+ adducts. Sodium and potassium are common sample and system contaminants and appear in most of the positive ion spectra. They were never intentionally added to the sample. In the focused position, the quasimolecular ions decreased and fragment ions increased in intensity. Carbon clusters and other noncharacteristic fragment ions reported by others (*16*) were not observed at the power densities used. In some cases the preferred type of cationization was observed to change from K^+ at low power densities to Na^+ and H^+ at higher power densities.

At constant laser power density, the greatest variability in the additive spectra was observed in the relative intensities of the quasimolecular ions, which appeared to vary randomly with some additives. Some additives, such as Tinuvin 326 (see below), were fairly reproducible. The difference in the behavior between additives may be caused by different degrees of alkali-metal contaminants or differences in sample thickness. (For more thorough discussions on mechanisms of ion formation in LD mass spectrometry, see ref 16–19).

Figure 2 shows a typical spectrum of Tinuvin 326, a chlorinated UV stabilizer, under focused conditions. The char-

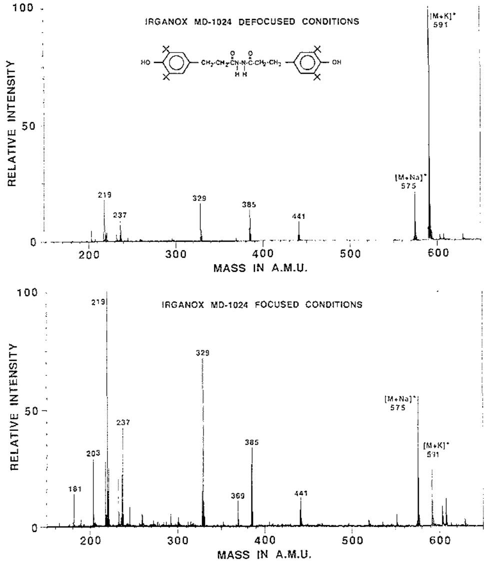

Figure 1. Irganox MD-1024 positive ion spectra under defocused (top) and focused (bottom) conditions.

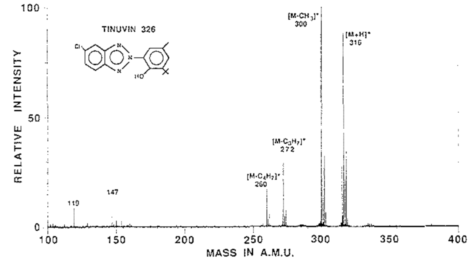

Figure 2. Typical positive ion spectrum of Tinuvin 326 under focused conditions.

acteristic isotope pattern for a singly chlorinated compound is observed in the molecular and fragment ions. Except in the case noted below, this compound did not show Na^+ or K^+ adducts. Table I shows the reproducibility obtained for five repeat spectra on two different days. For each spectrum, the probe was rotated to expose a fresh surface. All peak intensities were normalized to m/z 316 ($[M + H]^+$), though this was not always the base peak. Laser pulse energy was held constant between 2 and 3 mJ. There was no correlation between the total spectral intensity or the fragmentation and the laser pulse energy in this range. The above results demonstrate the best reproducibility obtained; typical spectral variability, especially on the polymer extracts, is much worse. It was also observed that when the same spot was hit a second time, the spectrum change dramatically. The most intense ion became $[M + Na]^+$, and $[M + K]^+$ averaged greater than 50% (Figure 3). These peaks are present at less than 10% of the base peak in "first shot" spectra. This effect was sometimes observed for other additives and may be due to sample depletion at the center of the analysis spot, where the laser power density is the highest.

Table I. Reproducibility of Tinuvin 326 Laser Desorption Spectra[a]

	relative intensity		relative σ_{n-1}, %	
m/z	day 1	day 2	day 1	day 2
119	10	8	18	47
147	15	9	30	26
260	16	4	35	41
272	33	15	20	14
300	110	80	23	14
315	45	54	26	39
316	100	100		

[a] Laser pulse energy was between 2 and 3 mJ. Approximately 300 μg was deposited on the sample disk. The average base peak intensities were 158 on day 1 and 182 on day 2 (arbitrary units).

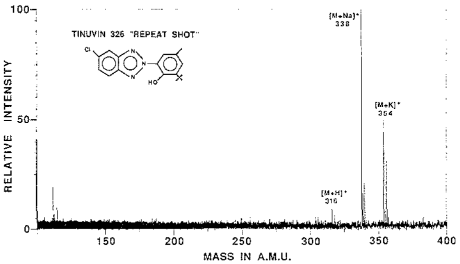

Figure 3. Positive ion LD spectrum of Tinuvin 326 when a second spectrum is obtained from the same spot.

Polymer Additive Spectra. The list of additives is given in Table II and their structures are shown in Chart I. The mass spectra of the additives are listed in Tables III through VIII. The masses and normalized intensities are from a single spectrum which appeared to be representative of the several spectra which were acquired for each compound. Both focused and defocused spectra were selected for the tables, depending on which contained structurally important fragment ions as well as molecular ions. The mass spectra of most additives were simple and easy to rationalize. At low power density, quasimolecular ions were often the only ions present in the positive ion spectra. Cluster ions of the type $[2M + K]^+$ or $[2M + Na]^+$ generally were not observed. Negative ion spectra often contained $[M - H]^-$ as the base peak.

Phenolic Antioxidants. Tables III and IV list the positive and negative ion mass spectra of phenolic antioxidants. The major fragment in the positive ion spectrum was usually due to cleavage β to the alkyl phenol when the group next to the ring was at least CH_2CH_2, resulting in the following fragment:

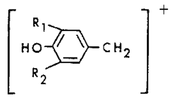

For dibutyl phenols, this fragment appears at $m/z = 219$, while for methyl butyl phenols, the fragment appears at $m/z = 177$. In cases where only a single bridging group (S and CH_2 for Ultranox 236 and Ultranox 246, respectively) was present, this fragment was not observed. Ultranox 236 and 246 were also the only antioxidants to show a significant M^+. In the negative ion spectra, $Ar{-}C_2H_2^-$ ($m/z = 231$ for dibutylphenols, $m/z = 189$ for methylbutylphenols) and loss of $Ar{-}CH_2$ was usually observed, where Ar is the alkyl phenol radical. The fragment Ar^- ($m/z = 205$ for dibutylphenols, $m/z = 163$ for methylbutylphenols) was sometimes present at low intensity. Irganox MD-1024, Irganox 259, and Irganox 1098 show elimination of isobutylene from the phenol. Elimination of one through four isobutylenes from the $[M + H]^+$ of Irganox MD-1024 (Figure 1) is indicated by fragments at m/z 497 (present but too weak to be observed in Figure 1), 441, 385, and 329. Loss

Table II. Chemical Names of Polymer Additives

no.[a]	trade name	MW	chemical name
			Phenolic Antioxidants
1	Irganox 245	586	tri(ethylene glycol)bis-3-(3-*tert*-butyl-4-hydroxy-5-methylphenyl)propionate
2	Irganox 259	638	1,6-hexamethylene bis-(3,5-di-*tert*-butyl-4-hydroxyhydrocinnamate)
3	Irganox 1010	1176	pentaerythritol tetrakis[3-(3,5-di-*tert*-butyl-4-hydroxyphenyl)propionate]
4	Irganox MD-1024	552	*N,N*-bis[1-oxo-3-(3,5-di-*tert*-butyl-4-hydroxyphenyl)propane]hydrazine
5	Irganox 1035	642	2,2-thiodiethylene bis[3-(3,5-di-*tert*-butyl-4-hydroxyphenyl)propionate
6	Irganox 1076 Naugard 76	530	octadecyl 3–(3,5–di–*tert*–butyl–4–hydroxyphenyl)propionate
7	Irganox 1098	636	*N,N'*-hexamethylene bis(3,5-di-*tert*-butyl-4-hydroxyhydrocinnamamide)
8	Irganox 3114	783	tris(3,5-di-*tert*-butyl-4-hydroxybenzyl) isocyanurate
9	Naugard BHT Ultranox 226	220	2,6-di-*tert*-butyl-4-methylphenol
10	Ultranox 236	358	4,4'-thiobis(2-*tert*-butyl-5-methylphenol)
11	Ultranox 246	340	2,2'-methylenebis(4-methyl-6-*tert*-butylphenol)
			Thioester Antioxidants
12	Naugard DLTDP	514	dilauryl thiodipropionate
13	Naugard DSTDP	682	distearyl thiodipropionate
			Phosphite Antioxidants
14	Polygard Weston TNPP	688	tris(nonylphenyl) phosphite
15	Naugard 524	646	tris(2,4-di-*tert*-butylphenyl) phosphite
			UV Stabilizers
16	Tinuvin P	225	2-(2-hydroxy-5-methylphenyl)-2*H*-benzotriazole
17	Tinuvin 144	684	2-*tert*-butyl-2-(4-hydroxy-3,5-di-*tert*-butylbenzyl)[bis(methyl-2,2,6,6-tetramethyl-4-piperidinyl)]dipropionate
18	Tinuvin 320	323	2-(2-hydroxy-3,5-di-*tert*-butylphenyl)-2*H*-benzotriazole
19	Tinuvin 326	315	2-(3-*tert*-butyl-2-hydroxy-5-methylphenyl)-2*H*-5-chlorobenzotriazole
20	Tinuvin 328	351	2-(2-hydroxy-3,5-di-*tert*-amylphenyl)-2*H*-benzotriazole
21	Tinuvin 440	435	8-acetyl-3-dodecyl-7,7,9,9-tetramethyl-1,3,8-triazaspiro(4,5)decane-2,4-dione
22	Tinuvin 770	480	bis(2,2,6,6-tetramethyl-4-piperidinyl) sebacate
			Waxes
23	Acrawax EBS wax	592	*N,N'*-ethylenebis(stearamide)
24	Oleamide	281	
25	Stearamide	283	

[a] Numbers correspond to structure numbers in Chart I.

Table III. Positive Ion Mass Spectra of Phenol Antioxidants

	$[M + K]^+$	$[M + Na]^+$									
Irganox 245	625 (75)	609 (30)	205 (100)	161 (45)	243 (40)	177 (35)	375 (30)	287 (20)			
Irganox 259	677 (100)	661 (40)	219 (20)	414 (15)	506 (10)						
Irganox 1010[a]	1215 (100)	1199 (30)	219 (35)	921 (20)	785 (15)	495 (15)	840 (10)	693 (10)	551 (10)		
Irganox MD-1024	591 (30)	575 (60)	219 (100)	329 (75)	237 (45)	385 (35)	203 (30)	441 (20)			
Irganox 1035[a]	681 (85)	665 (55)	331 (100)	379 (35)	252 (35)	219 (30)	193 (15)				
Irganox 1076[a]	569 (100)	553 (25)	290 (30)	320 (20)	258 (15)	607 (15)	531 (10)[c]	219 (8)			
Irganox 1098	675 (70)	659 (35)	525 (100)	469 (50)	321 (40)	582 (35)	413 (35)	219 (15)	377 (15)	613 (15)	637 (10)[c]
Irganox 3114[a]	822 (10)	783 (8)	219 (100)	436 (35)	203 (20)	346 (15)	260 (10)				
Naugard 76[b]	569 (100)	553 (70)	113 (50)								
Naugard BHT	259 (100)	243 (80)	215 (40)								
Ultranox 226	259 (100)	243 (17)	221 (10)	463 (9)	492 (21)						
Ultranox 236[a]	397 (10)	381 (15)	358 (100)[c]	343 (50)							
Ultranox 246	379 (100)	363 (25)	340 (20)[c]	392 (15)	332 (15)	177 (10)					

[a] Indicates spectrum acquired under defocused conditions. [b] Identical with Irganox 1076. [c] Indicates $[M + H]^+$ or M^+.

of H_2 is also observed at m/z 551.

UV Absorbers. Tables V and VI list the typical positive and negative ion spectra of seven UV absorbers. The UV absorbers were either hindered amines or benzotriazoles. The UV absorbers showed a greater tendency for protonation over alkali-metal cationization than the phenols. Alkyl losses were observed for Tinuvin 320, Tinuvin 326, Tinuvin 328, and Tinuvin 440.

Thioester Antioxidants. The positive ion focused spectrum of DSTDP is shown in Figure 4. The major fragment ion seen in Naugard DSTDP is due to the loss of $[-OC_{18}H_{37}]$ (m/z = 413). Similarly, m/z = 329 is seen for Naugard DLTDP. Molecular ions were weak or not observed in the positive ion

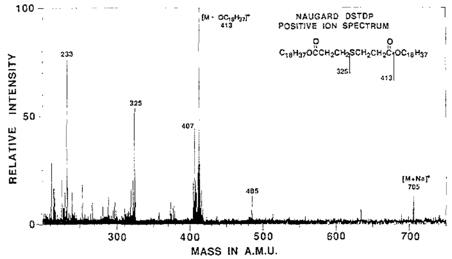

Figure 4. Positive ion LD spectrum of DSTDP under focused conditions.

Table IV. Negative Ion Mass Spectra of Phenol Antioxidants

	$[M - H]^-$	M^-										
Irganox 245	585 (30)	586 (10)	367 (100)	189 (65)	163 (20)	235 (15)						
Irganox 259	637 (100)	638 (45)	377 (30)	419 (25)[c]	231 (15)	277 (10)	205 (10)					
Irganox 1010	1175 (15)	1176 (15)	205 (100)	479 (65)	751 (50)	533 (45)	521 (40)	697 (40)	915 (30)	957 (30)[c]	969 (30)	231 (20)
Irganox MD-1024	551 (30)	552 (15)	231 (100)	258 (85)	276 (55)	331 (50)	333 (40)[c]	387 (30)				
Irganox 1035[a]	641 (30)	642 (10)	277 (100)	363 (85)	381 (55)	231 (40)	339 (25)	163 (25)	205 (20)	423 (20)[c]		
Irganox 1076[a]	529 (100)	530 (30)	231 (20)									
Irganox 1098	635 (100)	636 (50)	231 (50)	417 (35)[c]	375 (30)							
Irganox 3114			564 (100)[c]	346 (45)	230 (30)	194 (25)						
Naugard 76[b]	529 (100)	530 (35)	79 (70)	231 (65)	146 (20)							
Naugard BHT	219 (100)	220 (15)										
Ultranox 226	219 (100)	220 (15)										
Ultranox 236[a]	357 (100)	358 (25)	219 (15)	194 (10)	163 (5)							
Ultranox 246	339 (100)	340 (25)	163 (40)[c]									

[a] Indicates spectrum acquired under defocused conditions. [b] Same as Irganox 1076. [c] Indicates loss of

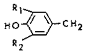

Table V. Positive Ion Mass Spectra of UV Absorbers

additive	MW	$[M + K]^+$	$[M + Na]^+$	$[M + H]^+$				
Tinuvin P	225			226 (15)	225 (100)[a]			
Tinuvin 144[b]	684	723 (100)	707 (5)	685 (5)	154 (35)	339 (10)		
Tinuvin 320	323	362 (80)	346 (60)	324 (100)	323 (60)[a]	308 (30)		
Tinuvin 326	315			316 (95)	300 (100)	315 (40)[a]	272 (15)	260 (15)
Tinuvin 328[b]	351	390 (10)	374 (25)	350 (100)	322 (80)	351 (50)[a]	378 (10)	282 (10)
Tinuvin 440	435		458 (5)	436 (10)	378 (100)	335 (20)	321 (20)	
Tinuvin 770	480	519 (100)	503 (35)	481 (35)	140 (50)	124 (30)	364 (30)	

[a] Indicates $M^{+\bullet}$. [b] Indicates defocused conditions.

Table VI. Negative Ion Mass Spectra of UV Absorbers

additive	$[M - H]^-$						
Tinuvin P	224 (100)	225 (15)					
Tinuvin 144		465 (100)	466 (30)	315 (20)	245 (20)	205 (20)	
Tinuvin 320	322 (60)	323 (100)	324 (20)				
Tinuvin 326	314 (100)	316 (40)	315 (30)	152 (10)			
Tinuvin 328	350 (100)	351 (40)	352 (10)				
Tinuvin 440	434 (40)	392 (100)	393 (25)				
Tinuvin 770[a]	479 (5)	322 (100)	150 (60)	194 (50)	144 (35)	255 (25)	213 (20)

[a] Indicates defocused conditions.

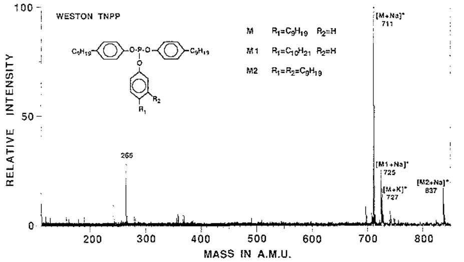

Figure 5. Positive ion LD spectrum of Weston TNPP under defocused laser conditions.

focused spectra. The negative ion spectra of both thioesters were weak and did not show molecular ions.

Phosphites. Weston TNPP and Polygard are both nonylphenyl phosphites. The positive ion defocused spectrum of Weston TNPP is shown in Figure 5. The major peaks are due to the Na^+ and K^+ adducts at m/z = 711 and 727. Impurities observed are the substitution of a decyl for a nonyl chain ($[M + Na]^+ = 725$) and the presence of an extra nonyl chain ($[M + Na]^+ = 837$). The negative ion spectrum is dominated by a nonylphenoxy fragment at m/z = 219. The fragment at m/z = 345 is further indication of the presence of two nonyl groups on one ring. The positive ion focused

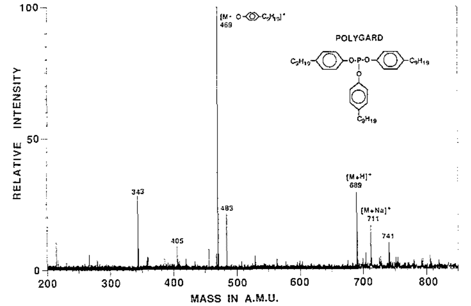

Figure 6. Positive ion LD spectrum of Polygard under focused laser conditions.

Table VII. Positive Ion Mass Spectra of Miscellaneous Additives

additive	MW	$[M + K]^+$	$[M + Na]^+$	$[M + H]^+$					
Naugard DLTDP	514	553 (100)	537 (35)		313 (10)				
Naugard DSTDP	682		705 (11)		413 (100)	233 (75)	325 (54)	407 (45)	485 (14)
Weston TNPP	688	727 (17)	711 (100)		265 (30)	725 (25)	837 (17)		
Naugard Polygard	688		711 (17)	689 (32)	469 (100)	343 (28)	483 (21)		
Naugard 524	646			647 (60)	441 (100)	385 (40)	329 (20)	591 (5)	
Oleamide	281	320 (45)	304 (100)	282 (9)	334 (38)	585 (9)			
Stearamide	283	322 (30)	306 (100)	284 (5)	335 (75)				
Acrawax[a]	592	631 (60)	615 (18)		365 (100)				
	564	603 (67)	587 (16)						
	536	575 (25)	559 (4)						
EBS Wax[a]	592	631 (34)	615 (7)						
	564	603 (100)	587 (30)						
	536	575 (76)	559 (15)						

[a] These compounds are mixed stearyl/palmityl diamides; hence three sets of molecular ions are observed due to the possibly stearyl/palmityl combinations.

Table VIII. Negative Ion Mass Spectra of Miscellaneous Additives

additive	$[M - H]^-$	M^-									
Naugard DLTDP			254 (100)	135 (82)	169 (80)	242 (64)	194 (55)	232 (36)	359 (21)	332 (18)	387 (15)
Naugard DSTDP			214 (100)	136 (36)	177 (10)	254 (3)					
Weston TNPP			219 (100)	135 (33)	345 (23)						
Naugard Polygard			219 (100)	345 (13)	233 (8)						
Naugard 524			283 (100)	79 (78)	268 (66)	205 (38)	473 (25)				
Oleamide	280 (100)	281 (53)	254 (29)								
Stearamide[b]											
Acrawax[a]	591 (7)		283 (100)	255 (23)	325 (18)	297 (12)					
	563 (7)										
	535 (3)										
EBS Wax[a]	591 (9)		255 (100)	283 (88)	507 (8)						
	563 (26)										
	535 (25)	536 (7)									

[a] These compounds are mixed stearyl/palmityl diamides; hence three sets of molecular ions are given to account for the possibly stearyl/palmityl combinations. [b] Spectrum not obtained.

spectrum of Polygard (Figure 6) had less intense molecular ions and a large fragment at $m/z = 469$, due to loss of an alkyl phenoxy group. The positive ion focused spectrum of Naugard 524 shows a strong $[M + H]^+$ at $m/z = 647$. The base peak at $m/z = 441$ is presumably due to the elimination of the alkyl phenol (206 daltons) from the quasimolecular ion.

Amide Waxes. The positive ion spectra of the amide waxes are dominated by the K^+ and Na^+ adducts. The oleamide also shows a peak due to $M + K + CH_2$ and a peak at $m/z = 585$, due to the $[2M + Na]^+$. The waxes Glyco Acrawax and Borg-Warner EBS Wax (Figure 7) are both mixed stearic and palmitic acid diamides. Two overlapping sets of three peaks are seen in the molecular ion region. The three peaks due to the K^+ adducts are offset by 16 daltons from the three Na^+ adducts. Three peaks (each separated by 28 daltons) are observed for each adduct because of the possible combinations of stearyl and palmityl chains. This characteristic pattern of peaks has been useful in identifying these waxes in other samples (*20*).

Polymer Extracts. A scheme was developed for the determination of molecular weights and identification of additives which exploits the facile formation of quasimolecular ions in laser desorption. First, the positive ion spectra are examined for quasimolecular ion candidates. The main criterion for consideration is the appearance of masses 16 daltons apart, corresponding to the Na^+ and K^+ adducts, which usually appear together in our reference spectra. Other mass differences which may indicate a molecular weight are 22 daltons ($[M + H]^+$ vs $[M + Na]^+$) and 38 daltons ($[M + H]^+$ vs $[M + K]^+$). The presence of an ion at 1 dalton less than the proposed molecular weight in the negative ion spectrum then provides further verification. If reference spectra were available for the proposed additive, the extract spectra would then be searched for major fragment ions. Since it is believed that, due to matrix effects, the appearance of a molecular ion or extent of fragmentation can vary considerably, the absence of a negative molecular ion or fragment ions did not necessarily rule out an identification or proposed molecular weight.

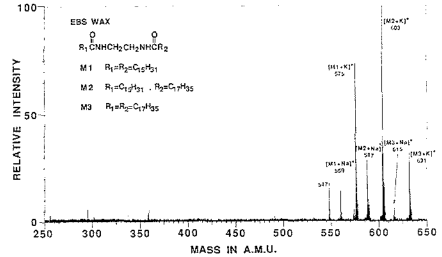

Figure 7. Positive ion LD spectrum of the diamide EBS Wax. The pattern of peaks separated by 28 daltons arises from the three possible combinations of stearyl and palmityl groups.

Misidentification of a Na^+/K^+ adduct pair can occur if two peaks have the expected 16 daltons separation by chance combinations of other formulas. These misidentifications can be reduced if the exact mass separation is measured. For example, two peaks differing in molecular formula by an oxygen would also have a mass separation of 16 daltons. This case can be distinguished from the Na^+/K^+ adduct pair by precisely measuring the mass difference, which will be 15.995 daltons for oxygen versus 15.974 daltons for the Na^+/K^+ adduct pair.

Though molecular weights can easily be obtained, the weakness of this strategy for identification is the need for a

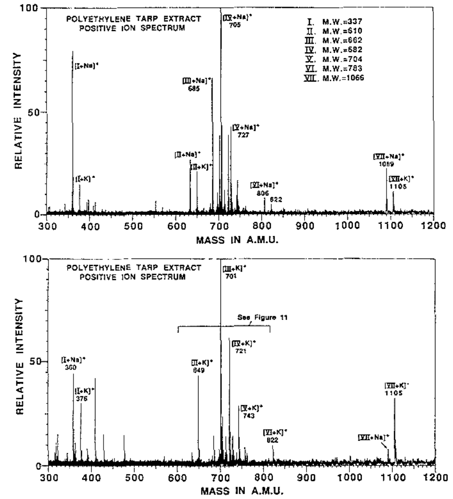

Figure 8. Positive ion LD spectra of the polyethylene tarp extract under defocused conditions.

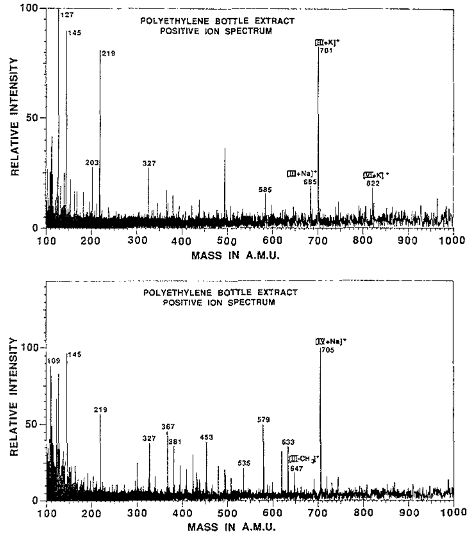

Figure 9. Positive ion LD spectra of the polyethylene bottle extract under defocused conditions.

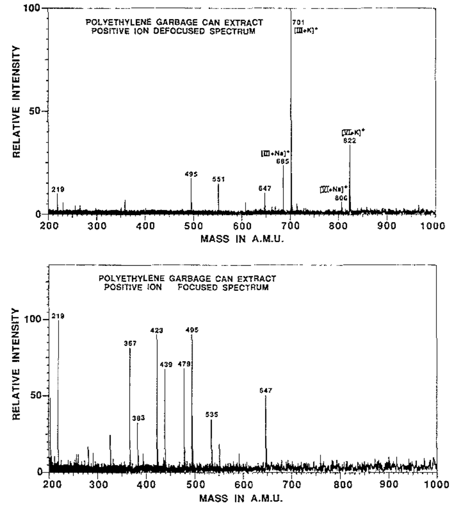

Figure 10. Positive ion LD spectra of the polyethylene can extract. Top spectrum was obtained under defocused conditions. The bottom spectrum was obtained under focused conditions.

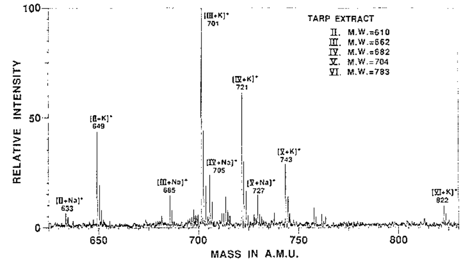

Figure 11. Expansion of lower spectrum in Figure 8.

database of additive molecular weights, as well as spectra for confirmation. For the polymer chemist who is familiar with the additives which may be in a particular polymer, this presents less of a problem. For an analytical chemical unfamiliar with additive use, the probability of exact identification is less, since hundreds of additives are in common use.

Figure 8 shows two defocused positive ion spectra of a polyethylene tarp extract. These spectra demonstrate some of the variability observed in laser desorption. The cationization changes from mostly Na^+ in the top spectrum to mostly K^+ in the bottom spectrum. This is clearly seen for the m/z = 633/649, 806/822, and 1089/1105 Na^+/K^+ pairs. The spectra were obtained under almost identical instrument conditions from the same sample disk (but different spot) on the same day, implying that matrix effects are not the cause of the variability. As discussed previously, the laser pulse power (15 mJ for the top spectrum and 9 mJ for the bottom spectrum) can be loosely correlated with type of cationization, though this correlation was not strictly observed for all other spectra obtained the same day.

Two defocused positive ion spectra of the polyethylene bottle extract appear in Figure 9. Several ions appear in the bottom spectrum which are not visible in the top spectrum (for example, in the 600 to 650 daltons region). The pulse energy for the top spectrum was 18 mJ versus 35 mJ for the bottom spectrum. All other instrumental parameters were identical.

A focused and defocused spectrum of the polyethylene garbage can extract is shown in Figure 10, demonstrating the differences between these conditions. In the focused mode, the molecular ions are much less intense relative to lower mass ions. The pattern of peaks observed in the bottom spectrum (two sets of peaks 16 daltons apart with each member 56 daltons apart) is believed to be due to sequential elimination of butylene from a dibutylphenol type antioxidant. This was observed in the reference spectrum of Irganox MD-1024 (Figure 1). The "richness" of the tarp spectra (Figure 8) relative to the bottle and can spectra (Figures 9 and 10, respectively) may be due to a higher extraction efficiency for the tarp, which was of negligible thickness relative to the others, which were several millimeters thick.

Table IX lists the proposed molecular weights of additives present based on the Na^+/K^+ adduct ions observed in the

Table IX. Proposed Molecular Weights for Unknown Additives

	I	II	III	IV	V	VI	VII
mol wt	337	610	662	682	704	783	1066
M + Na	360	633	685	705	727	806	1089
M + K	376	649	701	721	743	822	1105
tarp	×	×	×	×	×	×	×
bottle			×			×	
can			×			×	

^{a}× indicates presence in the polyethylene extract.

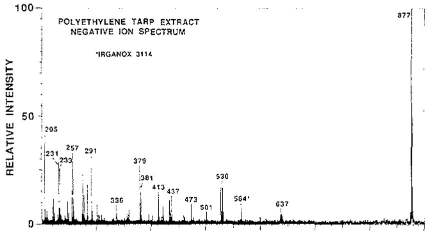

Figure 12. Negative ion LD spectrum of polyethylene tarp extract obtained under focused conditions. Peaks due to Irganox 3114 are indicated by an asterisk.

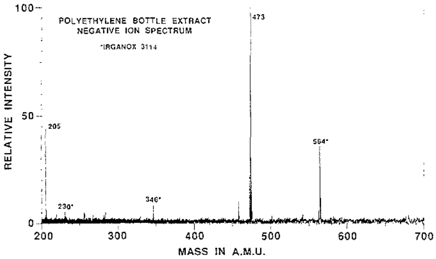

Figure 13. Negative ion LD spectrum of polyethylene bottle extract. Peaks due to Irganox 3114 are indicated by an asterisk.

extract spectra. An expanded view of the lower spectrum in Figure 8 is shown in Figure 11. The Na^+/K^+ quasimolecular ion pairs visible in this region are 633/649, 685/701, 705/721, 727/743, and 806/822, indicating molecular weights of 610, 662, 682, 704, and 783. It does not seem likely that these proposed molecular weights are due to cationized dimers, both because of the mixed nature of the matrix and because our instrument conditions did not appear to favor dimer formation in the analysis of the reference additives. Mass 682 corresponds to the molecular weight of DSTDP and 783 corresponds to the molecular weight of Irganox 3114. The molecular ion candidate at $m/z = 727$ may be due to $[682 + 2Na - H]^+$. The ion at $m/z = 647$ is believed to be due to loss of CH_3 from the unknown of molecular weight 662.

The negative ion spectrum of the tarp extract (Figure 12) shows a mass at $m/z = 336$. Assuming that this ion is due to an unknown $[M - H]^-$ this supports a molecular weight of 337, which has been proposed based on evidence in the positive ion spectrum. Otherwise, no other molecular weight confirmation was offered by the negative ion spectra (Figures 12–14). (In other unpublished work in this laboratory, the negative ion spectra have provided very useful supporting evidence for proposed molecular weights.)

Four fragment ions characteristic of Irganox 3114 at $m/z = 194$, 230, 346, and 564 were observed in the negative ion spectra, leading to the conclusion that Irganox 3114 is present

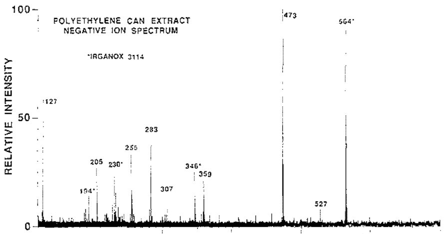

Figure 14. Negative ion LD spectrum of polyethylene can extract. Peaks due to Irganox 3114 are indicated by an asterisk.

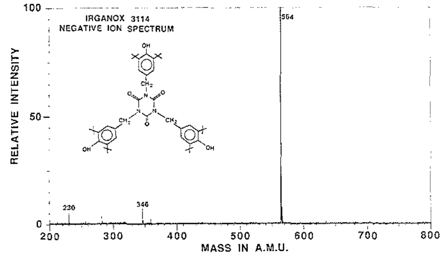

Figure 15. Negative ion LD spectrum of Irganox 3114.

in all three extracts. The negative ion spectrum of Irganox 3114 is shown in Figure 15 for comparison. The presence of DSTDP could not be confirmed. The negative ion spectra also show fragment ions characteristic of stearate and palmitate salts or esters (283 and 255, respectively), a phenolic additive other than Irganox 3114 ($m/z = 205$, $C_{14}H_{21}O$), and I^- (a system contaminant). A major ion in the tarp negative ion spectrum (Figure 12) at $m/z = 877$ was not identified.

To demonstrate the exact mass capability of FT-ICR, an attempt was made to determine the molecular formula of the negative ion at $m/z = 473$, which was the base peak in the bottle and garbage can extract spectra. The spectrum in Figure 14 was calibrated internally by using four known masses ($m/z = 127$, I^-; 205, $C_{14}H_{21}O^-$; 283, $C_{18}H_{35}O_2^-$, and 564, $C_{33}H_{46}N_3O_5^-$). The average error for the calibration masses was 2 ppm. On the basis of the calibration, a mass of 473.2813 daltons was determined for the unknown. A search of possible formulas with C, H, N, O, and P yielded seven formulas within 10 ppm of the measured mass. The most likely formula is believed to be $C_{28}H_{42}O_4P$, which has a mass of 473.2826 daltons (2.8 ppm error). This fits the structure

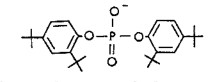

This is a reasonable oxidation/hydrolysis product of Naugard 524, which is a phosphite triester (MW = 646). One can then propose that additive III (MW = 662) is a phosphate triester

Chart I.

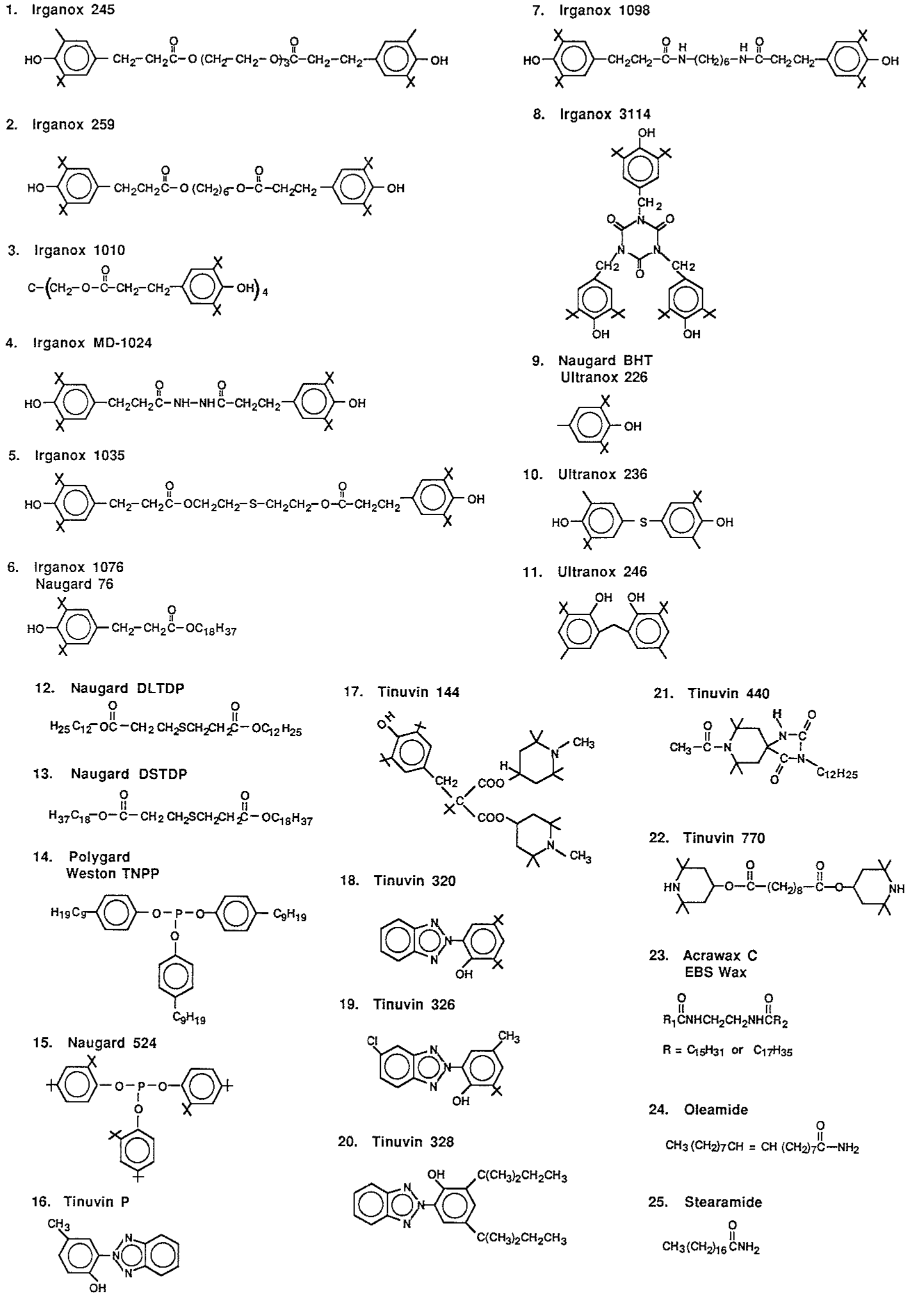

1. Irganox 245
2. Irganox 259
3. Irganox 1010
4. Irganox MD-1024
5. Irganox 1035
6. Irganox 1076 Naugard 76
7. Irganox 1098
8. Irganox 3114
9. Naugard BHT Ultranox 226
10. Ultranox 236
11. Ultranox 246
12. Naugard DLTDP
13. Naugard DSTDP
14. Polygard Weston TNPP
15. Naugard 524
16. Tinuvin P
17. Tinuvin 144
18. Tinuvin 320
19. Tinuvin 326
20. Tinuvin 328
21. Tinuvin 440
22. Tinuvin 770
23. Acrawax C EBS Wax
24. Oleamide
25. Stearamide

$R = C_{15}H_{31}$ or $C_{17}H_{35}$

resulting from the oxidation of Naugard 524 (*21*).

To improve the signal-to-noise and reproducibility of analysis, alternate sampling/ionization methods are now being investigated. These include probe introduction followed by electron impact (EI) ionization and LD for desorbing neutrals followed by EI ionization (as done by Marshall (*9*)). Direct analysis of polymer films would be particularly desirable because of the large reduction in sample preparation time.

CONCLUSIONS

By use of laser desorption FT-ICR seven molecular weights for additives in three polyethylene extracts were proposed.

Irganox 3114 was identified in all three extracts, based on the quasimolecular ions observed in the positive ion spectra and fragment ions in the negative ion spectra. Naugard 524 is believed to be present based on a fragment in the negative ion spectrum, which was determined by exact mass measurement to be a reasonable oxidation/hydrolysis product of Naugard 524, and the presence in the positive ion spectrum of quasimolecular ions corresponding to the phosphate oxidation product of Naugard 524. DSTDP is tentatively identified in the tarp extract. A database containing molecular weights of likely additives would be very useful, since most additives were found to give strong quasimolecular ions under defocused laser desorption conditions. While reference spectra are not needed, they can provide strong confirmation of an additive identity through fragment ion information.

LITERATURE CITED

(1) Sevini, F.; Marcato, B. *J. Chromatogr.* **1983**, *260*, 507-512.
(2) Haney, M. A.; Dark, W. A. *J. Chromatogr. Sci.* **1980**, *18*, 655-659.
(3) Munteanu, D.; Isfan, A.; Isfan, C.; Tincul, I. *Chromatographia* **1987**, *23*, 7-14.
(4) Perlstein, P. *Anal. Chim. Acta* **1983**, 21-27.
(5) Schabron, J. F.; Fenska, L. E. *Anal. Chem.* **1980**, *52*, 1411-1415.
(6) Raynor, M. W.; Barle, K. D.; Davies, I. L.; Williams, A.; Clifford, A. A.; Chalmers, J. M.; Cook, B. W. *Anal. Chem.* **1988**, *60*, 427-433.
(7) Vargo, J. D.; Olson, K. L. *Anal. Chem.* **1985**, *57*, 672-675.
(8) Lattimer, R. P.; Harris, R. E.; Rhee, C. K. *Anal. Chem.* **1986**, *58*, 3188-3195.
(9) Lattimer, R. P.; Harris, R. E. *Mass Spectrom. Rev.* **1985**, *4*, 369-390.
(10) Hsu, A. T.; Marshall, A. G. *Anal. Chem.* **1988**, *60*, 932-937.
(11) Blease, T. G.; Scrivens, J. H.; Monaghan, J. J.; Weil, D. Presented at the 36th ASMS Conference on Mass Spectrometry and Allied Topics, San Francisco, CA, June 5-10th, 1988; paper MPB 73.
(12) Wilkins, C. L.; Laude, D.; Pentoney, S.; Griffiths, P. R.; The University of California, Riverside, private communication, 1987.
(13) Cody, R. B. *Anal. Chem.* **1988**, *60*, 917-923.
(14) Wise, M. B. *Anal. Chem.* **1987**, *59*, 2289-2293.
(15) Kresser, T. O. J. *Polyolefin Plastics*; Van Nostrand Reinhold: New York, 1969; pp 56-63.
(16) Wilk, Z. A.; Viswanadham, S. K.; Sharkey, A. G.; Hercules, D. M. *Anal. Chem.* **1988**, *60*, 2338-2346.
(17) Chiarelli, M. P.; Gross, M. L. I. *J. Mass Spectrom. Ion Processes* **1987**, *78*, 37-52.
(18) Cotter, R. J.; Tabet, J.-C. *Am. Lab.* **1984**, *4*, 86-99.
(19) Hercules, D. M. *Microchem. J.* **1988**, *38*, 3-23.
(20) Asamoto, B. *Spectroscopy* **1988**, *6*, 38-46.
(21) *Stabilization of Polymers and Stabilizer Processes*; Gould, R. F., Ed.; Advances in Chemistry 85; American Chemical Society: Washington, DC, 1968; p 209.

RECEIVED for review October 3, 1989. Accepted October 18, 1989.

Precise Relative Ion Abundances from Fourier Transform Ion Cyclotron Resonance Magnitude-Mode Mass Spectra

Zhenmin Liang and Alan G. Marshall*,[1]

Department of Chemistry, The Ohio State University, 120 West 18th Avenue, Columbus, Ohio 43210

The area under a correctly phased absorption-mode spectral peak is a direct measure of the number of oscillators (ions, spins, molecules) in Fourier transform spectrometry (ion cyclotron resonance, magnetic resonance, interferometry absorbance). However, phase correction can prove difficult when (as in broad-band Fourier transform ion cyclotron resonance (FT/ICR)) detection is considerably time-delayed after excitation. In the absence of noise, Huang, Rempel, and Gross showed that a "complex area" method yields the correct absorption-mode peak area, for an unphased noiseless spectrum. In this paper, we show that the number of oscillators may also be obtained from a least-squares fit to a magnitude-mode (i.e., phase-independent) spectrum. In the presence of noise and in the absence of peak overlap, the magnitude-mode method offers precision superior to that based on magnitude-mode peak height, "complex area", or even direct digital integration of a correctly phased absorption-mode peak, as demonstrated by both theoretical derivation and experimental FT/ICR results. The present method thus appears to offer the best available determination of the relative abundances of ions of different mass-to-charge ratio in FT/ICR mass spectrometry.

INTRODUCTION

One of the most fundamental uses of Fourier transform (FT) spectroscopy is to determine the relative numbers of different species from relative spectral peak "intensities". Most FT spectroscopists use absorption-mode spectral peak *height* as a measure of the number of oscillators at that frequency. [In FT/interferometry, the detector measures light *energy*, not its *electric field*. However, because of the (nonlinear) square-law detection process, an FT of an interferogram nevertheless yields a complex intensity spectrum which when correctly phased yields absorption-mode and dispersion-mode (not "power") spectra (*1*).] Unfortunately, relative oscillator abundances are related to relative peak heights only if all spectral peaks have identical *widths*. In a frequency-domain spectrum obtained by discrete Fourier transformation (FFT) of the time-domain response immediately following a delta-function excitation, the absorption-mode spectral peak relative *areas* are directly proportional to the time-domain relative initial *amplitudes* of the time-domain sinusoidal signals, which in turn are proportional to the numbers of oscillators at those frequencies (*1*). In other words, one should use FT absorption-mode spectral peak *areas* rather than peak *heights* as the proper measure of relative abundances of spectral components.

However, it is not always possible to phase-correct a complex FT spectrum to obtain its pure absorption-mode component. For example, when the time-domain detection must be delayed by more than half of one sampling period after excitation (e.g., to avoid feed-through of the excitation signal into the detector channel), then the failure of the FFT algorithm to accommodate a phase variation of more than 2π radians throughout the spectral range results in FFT spectral phase discontinuities ["phase-wrap" (*1*, *2*)] which produce unavoidable auxiliary "wiggles" in each spectral peak, even for a perfectly phased spectrum. The phase-wrap "wiggles"

---

* To whom correspondence should be addressed.

[1] Also a member of the Department of Biochemistry.

0003-2700/90/0362-0070$02.50/0

have the same form as those from "Gibb's oscillations" resulting from truncation of a time-domain exponentially damped sinusoid before FFT, but the "phase-wrap" effect is unique to the *discrete* FT, whereas "Gibb's oscillations" are present even in *analog* FT of a continuous time-domain signal (*1, 2*). Other instrumental anomalies can produce nonlinear phase shift as a function of frequency. In such cases, the phase-independent magnitude-mode spectral display is usually preferred.

Unfortunately, even in the absence of peak overlap (which is more pronounced for magnitude-mode than for absorption-mode display), magnitude-mode peak height is not a good measure of relative oscillator abundances since peak widths commonly vary significantly. Moreover, magnitude-mode peak area is unsuitable, because (a) if the domain of integration is extended to infinity, magnitude-mode peak area diverges to infinity for a simple Lorentz line shape (*3*), and (b) if the domain of integration is truncated to a finite frequency range, then the relative peak areas will be accurate only if all of the peak widths are the same. Thus, directly integrated magnitude-mode peak relative areas offer a poor measure of relative oscillator abundances.

Although three-point interpolation of a noiseless magnitude-mode FT spectrum can yield the frequency of the peak maximum exactly (*4, 5*), the peak height and area are not so easily estimated, and both estimates are corrupted by noise (*6, 7*). In addition, the apparent frequency and height of a magnitude-mode peak can be shifted significantly by the presence of nearby peaks, to a greater extent than for absorption-mode spectra (because of the dispersion-mode contribution to the magnitude-mode spectrum) (*8, 9*).

Another set of difficulties with magnitude-mode display relates to the nature of magnitude-mode noise. First, since magnitude-mode noise is everywhere positive-valued, noise can quickly overwhelm the signal if the peak area computation is extended very far away from the center of the magnitude-mode spectral peak. Furthermore, magnitude-mode noise (in the absence of signal) follows a Rayleigh rather than Gaussian distribution (*10*). Moreover, magnitude-mode noise contributes only positive errors in spectral segments containing no signal (i.e., "base line") but contributes both positive and negative errors in spectral segments where signals (i.e., "peaks") are present. In work to be reported separately, statistical criteria used to analyze the noise in signal-containing segments of a magnitude-mode spectrum show that such noise is *not* well-described by a Rayleigh distribution (*11*).

In an effort to circumvent the problems posed by magnitude-mode spectral analysis, Huang, Rempel, and Gross proposed a "complex area" method, to calculate the absorption peak area from unphased (noiseless) spectra (*12*). Alternatively, comparison of FT spectra of partial segments of a discrete time-domain signal (*13, 14*) also provides a means for correcting for spectral peak height variations due to differences in peak width. Noest and Kort (*15*) have suggested a time-domain apodization function designed to produce spectral peaks with broad and flat peak maxima, to reduce errors due to discrete sampling. The value of linear prediction (*16*) and/or maximum-entropy methods for analysis of FT/ICR mass spectra is discussed elsewhere (*17*). Apparent relative abundances of ions in FT/ICR can of course also be affected by various experimental factors, including *z*-axis ejection (*18–20*), collisional relaxation of ions to the center of the ion trap (*21*), incomplete ejection of unwanted ions (*21*), and phase and amplitude errors (*22*).

Under quite general conditions (white noise whose root-mean-square magnitude is independent of signal magnitude), we have shown that the precision of a determination of spectral peak height, peak width, or peak center frequency by least-squares fit to an absorption-mode or magnitude-mode spectrum is proportional to the frequency-domain signal-to-noise ratio (SNR) and to the square root of the number of data points (K) per line width (*23*)

$$P(a_i) = c(a_i)\ \mathrm{SNR}\ K^{1/2} \tag{1}$$

in which a_i is the spectral peak height, peak width, or peak center frequency and $c(a_i)$ is a line shape-dependent constant factor.

We begin this paper by extending that treatment to show that the precision of the *number of oscillators* determined by least-squares fit to a magnitude-mode spectrum (or by digital integration of the absorption spectrum, or by the above-cited complex area method) is also proportional to SNR and $K^{1/2}$, with an appropriate value of $c(a_i)$ in eq 1. By comparing the proportionality constants, $c(a_i)$, we are then able to evaluate the relative precision of each of the above methods for peak area determination. Finally, we compare simulated and experimental FT/ICR spectra to demonstrate the validity of our analysis. [We shall report separately on the closely related problem of precision in determination of the same parameters (peak height, width, frequency, and number of oscillators) from a discrete *time-domain* signal, including the effect of time-domain zero-filling (*11*).]

THEORY

Magnitude-Mode Noise. Magnitude-mode spectral noise differs fundamentally from noise in absorption-mode or dispersion-mode spectra. Although noise in signal-free segments of a magnitude-mode spectrum follows a Rayleigh distribution (*10*), magnitude-mode noise at or near peaks more than 2 standard deviations above the base line is more nearly Gaussian-distributed (*11*). In a separate paper, we shall discuss magnitude-mode noise in detail, and show that a least-squares fit to a magnitude-mode spectral peak may be performed with high precision under the assumption that the noise in the vicinity of the peak is Gaussian-distributed about a zero mean value (*11*).

Precision of Peak Area Measurements. *1. Least-Squares Fit to a Frequency-Domain Spectrum.* The number of oscillators can be determined by numerical integration (of either a phased absorption-mode peak or "complex area" (*12*)) or from a least-squares fits to either the absorption-mode peak or magnitude-mode spectrum. In any case, we begin from the absorption-mode, Abs(ν), and magnitude-mode, Mag(ν), Lorentzian frequency-domain spectra corresponding to the Fourier transform of an unapodized time-domain exponentially damped sinusoid, $f(t)$

$$f(t) = N_0 \exp(-t/\tau) \sin(2\pi\nu_0 t) \tag{2}$$

$$\mathrm{Abs}(\nu) = \frac{N_0\tau}{2[1 + (2\pi\tau)^2(\nu - \nu_0)^2]} = \frac{N_0\tau}{2[1 + u^2]} \tag{3}$$

$$\mathrm{Mag}(\nu) = \frac{N_0\tau}{2(1 + (2\pi\tau)^2(\nu - \nu_0)^2)^{1/2}} = \frac{N_0\tau}{2(1 + u^2)^{1/2}} \tag{4}$$

in which $u = 2\pi\tau(\nu - \nu_0)$; N_0 is the time-domain signal initial magnitude, which is proportional to the number of ions having that ICR frequency; $N_0/4$ is the area under the Lorentzian absorption-mode spectra peak; $N_0\tau/2$ is the Lorentzian absorption-mode peak height; $\tau = 1/\pi\,\Delta\nu_{1/2}$, time-domain ICR signal damping constant (see eq 2); $\Delta\nu_{1/2}$ is the absorption-mode full peak width at half maximum peak height; and ν_0

is the ICR frequency, the frequency at the absorption-mode or magnitude-mode peak maximum.

The object of this paper is to be able to predict, from a *single* FT magnitude-mode spectrum, the *precision* of the determined number of oscillators (i.e., a measure of the range of values that would have been obtained from a *large number* of such measurements). Precision, $P(N_0)$, in determination of number of oscillators may be defined as the reciprocal of the relative standard error

$$P(N_0) = N_0/\sigma(N_0) \tag{5}$$

in which $\sigma(N_0)$ is the standard deviation that would be obtained from many independent determinations of N_0. If the absorption-mode spectral noise is "white" (i.e., independent of frequency) and independent of signal (i.e., "detector-limited") and if the time- and frequency-scales are perfectly precise (i.e., noise is present only in the ordinate, not in the abscissa), then the precision, $P(a_i)$, in a determination of spectral parameter, a_i, from a least-squares fit of the spectrum to a given line shape can be shown to be (*23*)

$$P(a_i) = c(a_i)\,(\mathrm{SNR})\,K^{1/2} \tag{1}$$

in which $c(a_i)$ is a line-shape-dependent constant, K is the number of data points per (full) line width at half-maximum peak height, and SNR is the spectral signal-to-noise ratio, which for Lorentzian line shape takes the form

$$\mathrm{SNR} = N_0\tau/2\sigma \tag{6}$$

in which σ is the standard deviation of the absorption-mode spectral base-line noise.

Reference 23 presents a general method for deriving $c(a_i)$ for $a_i = \nu_0$, peak height, or peak width, for Lorentzian or Gaussian absorption-mode and magnitude-mode spectra. In this work, we have applied that method to three-parameter (N_0, ν_0, and τ) least-squares fits to Lorentzian absorption-mode and magnitude-mode line shapes to yield

$$c(N_0) = \left(\frac{\pi}{8}\right)^{1/2} \tag{7a}$$

for Lorentzian absorption-mode line shape and

$$c(N_0) = \left(\frac{\pi}{6(3)^{1/2}}\right)^{1/2} \tag{7b}$$

for Lorentzian magnitude-mode line shape.

In the special case that τ is known accurately (e.g., from measurement of the width of a peak of high SNR in a spectrum for which all of the peaks have the same line width), then it can be shown that the resulting precision in a two-parameter (N_0 and ν_0) least-squares determination of N_0 increases by a factor of $2^{1/2}$ for an absorption-mode and $3^{1/2}$ for a magnitude-mode Lorentzian, compared to a three-parameter fit (N_0, ν_0, and τ).

Finally, it is worth noting that because the magnitude-mode Lorentzian line width (at half-maximum peak height) is broader than the absorption-mode Lorentzian line width by a factor of $3^{1/2}$, the number of data points per line width increases by $3^{1/2}$ and the precision as defined above therefore increases by $K^{1/2} = 3^{1/4}$ for magnitude-mode. Therefore, if we choose to express K as number of points per frequency increment rather than number of points per line width (to facilitate comparison of absorption-mode and magnitude-mode precision), then $C(N_0)$ for magnitude-mode fits should be increased by the factor $3^{1/4}$ (see below).

2. Digital Integration of a Phase-Corrected Absorption-Mode Spectral Peak. From the standpoint of precision, a numerical integration (independent of algorithm) of an absorption-mode spectrum is equivalent to summing up all of the absorption values within the integral limit and multiplying by the discrete frequency interval, $\Delta\nu$, between successive frequency-domain absorption-mode data. Therefore, the deviation, δ, in such an integral is defined by

$$\begin{aligned}\delta &= \sum_{i=0}^{n}\,[\mathrm{Abs}(\nu_i) + N(\nu_i)]\,\Delta\nu - \sum_{i=0}^{n}\,\mathrm{Abs}(\nu_i)\,\Delta\nu \\ &= \sum_{i=0}^{n}\,N(\nu_i)\,\Delta\nu\end{aligned} \tag{8}$$

in which $\mathrm{Abs}(\nu_i)$ and $N(\nu_i)$ are the (absorption-mode) signal and noise values at (discrete) frequency ν_i, and noise is assumed independent of signal. δ is normally distributed with zero mean and standard deviation

$$\sigma(\mathrm{area}) = n^{1/2}\sigma\,\Delta\nu \tag{9}$$

in which n is the number of absorption-mode data points in the integration domain (*24*). Next, since N_0 and absorption-mode peak area differ by a constant (see eq 4 ff)

$$P(N_0) = \frac{N_0}{\sigma(N_0)} = \frac{\text{absorption area}}{\sigma(\text{absorption area})} \tag{10}$$

Then, since the absorption-mode peak area is $N_0/4$, we can use eq 9 to obtain

$$P(N_0) = \frac{\text{absorption area}}{\sigma(\text{absorption area})} = \frac{N_0}{4n^{1/2}\sigma\,\Delta\nu} \tag{11}$$

Next, solve eq 6 for N_0 and substitute for N_0 in eq 11; then substitute for $\tau = 1/(\pi\,\Delta\nu_{1/2})$ to obtain the following expression for the precision in determination of N_0 from a measurement of absorption-mode Lorentzian peak area

$$P(N_0) = \frac{\pi}{2h^{1/2}}(\mathrm{SNR})K^{1/2} \tag{12a}$$

in which

$$h = n/K \tag{12b}$$

is the domain of integration (in multiples of $\Delta\nu_{1/2}$) and we have used the identity

$$K(\text{points/line width}) = \frac{\Delta\nu_{1/2}(\text{Hz/line width})}{\Delta\nu(\text{Hz/point})} \tag{12c}$$

For eq 12a to be valid, the domain of numerical integration should be chosen so as to include, say, >95% of the true absorption-mode peak area.

3. "Complex Area". The "complex" area method consists of adding the areas (each treated as mathematically real quantities) of the real, $R(\nu_i)$, and imaginary, $I(\nu_i)$, spectra obtained by discrete FT of a time-domain discrete signal (*12*). In this case, the deviation in the resultant area is given by

$$\begin{aligned}\delta &= \Delta\nu\Big(\Big(\Big[\sum_{i=1}^{n} R(\nu_i) + N_\mathrm{R}(\nu_i)\Big]^2 + \Big[\sum_{i=1}^{n} I(\nu_i) + N_\mathrm{I}(\nu_i)\Big]^2\Big)^{1/2} - \\ &\qquad \Big(\Big[\sum_{i=1}^{n} R(\nu_i)\Big]^2 + \Big[\sum_{i=1}^{n} I(\nu_i)\Big]^2\Big)^{1/2}\Big) \\ &\approx \Delta\nu\Big(\Big[\sum_{i=1}^{n} R(\nu_i)\Big]^2 + \Big[\sum_{i=1}^{n} I(\nu_i)^2 + 2N'_\mathrm{R}(\nu_i)\Big[\sum_{i=1}^{n} R(\nu_i)\Big] + \\ &\quad 2N'_\mathrm{I}(\nu_i)\Big[\sum_{i=1}^{n} I(\nu_i)\Big]\Big)^{1/2} - \Big(\Big[\sum_{i=1}^{n} R(\nu_i)\Big]^2 + \Big[\sum_{i=1}^{n} I(\nu_i)\Big]^2\Big)^{1/2}\end{aligned} \tag{13}$$

in which

$$N'_\mathrm{R}(\nu_i) = \sum_{i=1}^{n} N_\mathrm{R}(\nu_i) \tag{14a}$$

and

$$N'_{\mathrm{I}}(\nu_i) = \sum_{i=1}^{n} N_{\mathrm{I}}(\nu_i) \tag{14b}$$

represent randomly distributed Gaussian noise (with standard deviation $\sigma n^{1/2}$) in the real and imaginary spectral components of the complex FFT of $f(t)$ (*24*), and we have used the approximation

$$2N'_{\mathrm{R}}(\nu_i)\sum_{i=1}^{n} R(\nu_i) + 2N'_{\mathrm{I}}(\nu_i)\sum_{i=1}^{n} R(\nu_i) \gg N'_{\mathrm{R}}(\nu_i)^2 + N'_{\mathrm{I}}(\nu_i)^2 \tag{15}$$

If equation 13 is next expanded in a Taylor series and only the first two terms are kept—neglect of the remaining terms produces negligible error in practical circumstances—then eq 13 may be simplified to give

$$\delta = \frac{N_{\mathrm{R}}(\nu_i)\sum_{i=1}^{n} R(\nu_i) + N_{\mathrm{I}}(\nu_i)\sum_{i=1}^{n} I(\nu_i)}{([\sum_{i=1}^{n} R(\nu_i)]^2 + [\sum_{i=1}^{n} I(\nu_i)]^2)^{1/2}} \tag{16}$$

In other words, δ may be described by a normal distribution with zero mean and standard deviation, $\sigma n^{1/2}$, which is the same as for direct numerical integration of a perfectly phased absorption-mode spectrum (*19*). Thus, for numerical integration of either phased absorption-mode or "complex area", the precision in determination of absorption-mode peak are is given by

$$P(N_{\mathrm{O}}) = \frac{\pi}{2h^{1/2}}(\mathrm{SNR})K^{1/2} \tag{12a}$$

EXPERIMENTAL SECTION

Simulated Data. Data simulation was conducted with a 20 bit/word Nicolet 1280 computer. Gaussian noise was created by converting uniform random numbers into a Gaussian distributed random number file (*25*). The histogram of the Gaussian random numbers closely resembled that for experimentally acquired Gaussian noise, and the FFT spectrum of the random number sequence showed no peaks [demonstrating that the noise was "white" (i.e., independent of frequency)]. Random noise was added to each time-domain simulated signal, and least-squares fit to a magnitude-mode Lorentzian line shape was performed on the FFT spectrum of the time-domain simulated signal-plus-noise.

Experimental Data. FT/ICR experimental time-domain signals of I_2^+ were acquired with a Nicolet FTMS-2000 mass spectrometer operating in heterodyne mode at 3 T. Iodine crystals were introduced with a solid probe which had been cooled to ~10 °C, and I_2^+ ions were formed by electron ionization (70 eV). The number of points per line width in the FFT spectrum was adjusted by varying the sampling frequency (32 kHz < Nyquist bandwidth < 100 kHz) while keeping the number of time-domain data points constant (4K or 8K). Alternatively, the time-domain damping constant was varied [by addition of argon gas to a neutral pressure between 10^{-6} Torr ($\tau \approx 20$ ms) and 10^{-7} Torr ($\tau \approx 200$ ms)] at fixed sampling rate and number of time-domain data points, to cover the same abscissa range in Figures 3 and 4 (see Results and Discussion). Signal-to-noise ratio was additionally varied by varying the electron emission current. The number of points per line width in the FFT spectrum was adjusted by varying the sampling frequency at constant time-domain acquisition period. The standard deviation for ion relative abundance (determined from FT/ICR mass spectral peak area) was computed from 15 spectra acquired independently under identical conditions. The (single-peak) spectra were phase corrected before performing absorption-mode least-squares fit or numerical integration.

Least-squares fits to both magnitude-mode and absorption-mode spectra were performed with a grid search algorithm (*25*). An initial estimate for the fit parameters (peak area, peak center frequency, and peak width) was obtained by visual approximation from the magnitude-mode spectrum. A representative experimental FT/ICR magnitude-mode discrete spectrum and best-fit Lorentzian are shown in Figure 5 (see Results and Discussion). Numerical integration of the phase-corrected absorption-mode spectrum was performed by use of Simpson's rule (*25*). Complex area was obtained as described by Gross (*12*).

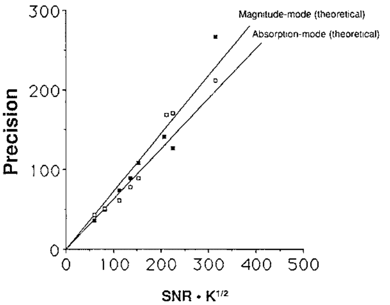

Figure 1. Precision in determination of number of oscillators, N_{O}, as a function of the ratio, SNR, of frequency-domain peak height to root mean square spectral base-line noise, and number of data points, K, per full peak width at half-maximum absorption-mode peak height: □, direct least-squares fit to absorption-mode spectrum; ■, direct least-squares fit to magnitude-mode spectrum. Straight lines are theoretical predictions based on a *single* (simulated) data set. Plotted data represent averages over 30 trials of the same simulated spectrum with different random noise of the same root mean square deviation.

RESULTS AND DISCUSSION

Computer-Simulated Spectra. The predicted precision in determination of number of oscillators was computed from eq 1 and 7 (based on fits to absorption-mode or magnitude-mode Lorentzian peak shape) or eq 12a (for direct integration of phased absorption-mode or "complex area") for simulated spectra with various frequency-domain signal-to-noise ratios (SNR) and K values. Those predictions were tested by determining the standard deviation for various spectral parameters (absorption-mode peak area, ν_0, and τ) from 30 simulated spectra of the same spectral peak height, ν_0, and τ, with different added random noise of the same root-mean-square deviation.

Figure 1 compares the precision, $P(N_{\mathrm{O}})$, in determination of the number of oscillators predicted from a single spectrum to that actually computed from the standard deviation of 30 such measurements of the FFT spectra of simulated time-domain damped exponential sinusoidal signals to which random time-domain noise has been added. In the figure, $P(N_{\mathrm{O}})$ based on three-parameter (peak area, ν_0, and τ) fits to Lorentzian absorption-mode and magnitude-mode spectra is plotted as a function of the product of frequency-domain peak height-to-noise ratio (SNR) and $K^{1/2}$. For absorption mode, K is the number of points per full absorption-mode peak width at half-maximum peak height. For magnitude mode, K is redefined as $3^{1/4}$ times the number of points per absorption-mode peak width, in order that the absorption-mode and magnitude-mode plots may be compared on the basis of points per hertz rather than points per line width. Figure 2 shows the corresponding plots of precision vs $(\mathrm{SNR})(K/h)^{1/2}$ for numerical integration of a correctly phased Lorentzian absorption-mode spectrum or a "complex area" integration; in each case, the domain of integration is extended to include 95% of the peak area.

According to the theory, N_{O} determined from least-squares fit to a magnitude mode spectrum is ~15% more precise than N_{O} determined from least-squares fit to the corresponding absorption-mode spectrum, because (a) the number of points per peak width increases by $3^{1/2}$ in proceeding from absorption-mode to magnitude-mode Lorentzian line shape (so that K increases by $3^{1/2}$ and the precision increases by $K^{1/2}$, for a net increase in precision of ~30%) and (b) the magni-

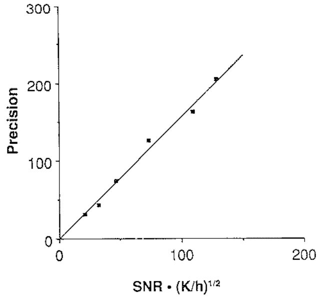

Figure 2. As in Figure 1, except that the number of data points per line width has been divided by the number of line widths, h, over which peak area is measured: □, N_0 determined from the sum of the areas of the real and imaginary components of the complex FFT spectrum (*12*); ■, N_0 determined from (phased) absorption-mode spectral peak area by direct numerical integration. Note: the open and solid squares overlap so closely that they cannot be resolved in this display.

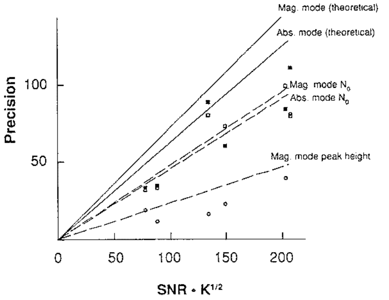

Figure 3. Same as Figure 1, but for experimental FT/ICR mass spectral data: □, direct least-squares fit to absorption-mode spectrum; ■, direct least-squares fit to magnitude-mode spectrum; O, N_0 determined from peak height of least-squares fit to magnitude-mode spectrum; ——, theoretically predicted behavior for the stated experimental SNR and K values; - - -, straight line passing through the origin which best fits the plotted points.

tude-mode peak shape is different from absorption mode, leading to a different value of $c(a)$. (The magnitude-mode fit extends to frequencies at which the spectral signal has dropped to twice the root-mean-square base-line noise.)

To compare the precision of the least-squares fits to the direct numerical integration methods, we must fix the domain of integration, h. For example, if the direct integration is to include 95% or more of the absorption-mode peak area, h must be greater than 12.7 absorption-mode Lorentzian line widths. Under those conditions, *the magnitude-mode least-squares fit is 60% more precise than numerical integration of either the phase corrected spectrum or the "complex area" method.* The simulated spectral data analyzed in Figures 1 and 2 thus confirm the theoretical predictions of eq 1 and 7 (for least-squares fits) and eq 12a (for direct integration).

One might argue that when only *relative* abundances are required, the integration width need not extend to include 95% of the absorption-mode peak area, thereby increasing the precision of the direct integratioin method. However, partial integration presents two practical problems. First, unless the peak widths (i.e., τ values) of all of the peaks are identical, systematic errors in relative abundances will be introduced. Second, the increase in precision, area/σ(area), by reduction in integration domain, h, will be small, because a decrease in h reduces the computed area as well as the imprecision in area measurement: $\sigma(\text{area}) \propto h^{1/2}$.

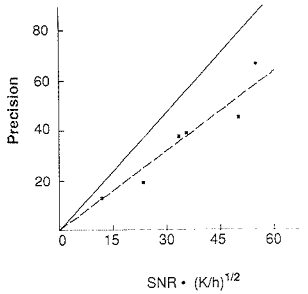

Figure 4. Same as Figure 2, but for experimental FT/ICR data. Again, the open and solid squares overlap in this display; ——, theoretically predicted behavior for the stated experimental SNR and K values; - - -, straight line passing through the origin which best fits the plotted points.

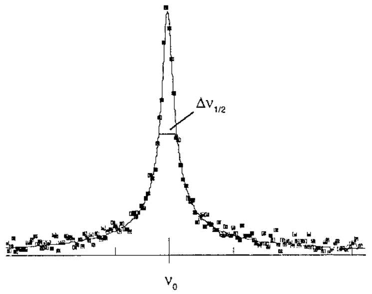

Figure 5. Representative discrete magnitude-mode FT/ICR mass spectrum, with best-fit magnitude-mode Lorentzian smooth curve drawn through the points.

Experimental FT-ICR Spectra Figures 3 and 4 present experimental FT/ICR mass spectral data for I_2^+ ions, plotted as for the simulated data of Figures 1 and 2. Figure 5 shows a typical experimental magnitude-mode FT/ICR discrete mass spectrum along with a best-fit to magnitude-mode Lorentz line shape. The theoretical lines in Figures 3 and 4 represent predicted precision based on SNR and K for a *single* spectrum, and the data points represent the actual precision in N_0 determined from a *series* of 15 independent measurements. Although the slopes of plots of peak area precision vs SNR $K^{1/2}$ from experimental data are 20–30% lower than those predicted for the theoretical ones, the data still give straight-line plots with correlation coefficients of ≥0.9. The differences between experiment and theory are probably due mainly to variation in number of ions from one experiment to the next, due to variation in electron beam current. Nevertheless, Figures 3 and 4 show that the precision in N_0 determined from least-squares fit to a magnitude spectrum is slightly better than that for N_0 determined from a least-squares fit to the corresponding absorption-mode spectrum and is ~60% better than that for N_0 determined by "complex area" or direct numerical integration of a phased absorption-mode spectrum (for integration domain extended to include 95% of the peak area).

Finally, Figure 3 (open circles) illustrates the disadvantage of the use of peak *height* as a measure of relative abundances. Although theory predicts (compare the present results with those in ref 23) that the precision in peak *height* should be as good as that for peak *area* (provided that all spectral peak *widths* are equal), Figure 3 shows that for experimental FT/ICR data, relative abundance computed from least-squares fit to spectral data points whose magnitude exceeded

$\sim 2\sigma$ is twice as precise as relative abundance obtained simply from peak *height* of the same least-squares-fitted magnitude-mode spectrum.

Althought the present computations are restricted to *unapodized* magnitude-mode Lorentzian line shapes, the same qualitative conclusions should apply to other line shapes, with revised values of $c(a_i)$ in eq 1 (see ref 23 for examples).

CONCLUSION

In this paper, we have developed expressions for the precision of number of oscillators, N_O, obtained by various treatments of FFT absorption-mode and magnitude-mode Lorentzian spectra. We find that both theoretical and experimental FT/ICR relative abundance precision based on least-squares fit to the magnitude-mode spectrum is slightly more precise than that obtained from least-squares fit to the corresponding (if available) phased absorption-mode spectrum. Although both of the above methods are distinctly superior in precision to determination of N_O by direct numerical integration of the complex or phased imaginary (i.e., pure absorption-mode) FFT spectrum, the magnitude-mode approach has the (major) advantage that it is not necessary to phase-correct the spectrum in order to determine relative abundances. (It is worth noting that the "complex area" computation requires twice as much memory as a magnitude-mode least-squares fit.) Experimental FT/ICR precision in N_O is somewhat (~20%) lower, for all algorithms, than that predicted theoretically. Finally, peak *area* is in general superior to peak *height* as a measure of relative abundances.

LITERATURE CITED

(1) Marshall, A. G.; Verdun, F. R. *Fourier Transforms in Optical, NMR, and Mass Spectroscopy*; Elsevier: Amsterdam, 1989.
(2) Craig, E.; Marshall, A. G. *J. Magn. Reson.* **1988**, *76*, 458–475.
(3) Shaw, D. *Fourier Transform N.M.R. Spectroscopy*, 2nd ed.; Elsevier: Amsterdam, 1984; p 171.
(4) Giancaspro, C.; Comisarow, M. B. *Appl. Spectrosc.* **1983**, *37*, 153–166.
(5) Keefe, C. D.; Comisarow, M. B. *Appl. Spectrosc.* **1989**, *43*, 605–607.
(6) Chan, S. O.; Comisarow, M. B. *J. Magn. Reson.* **1983**, *54*, 201–215.
(7) Verdun, F. R.; Giancaspro, C.; Marshall, A. G. *Appl. Spectrosc.* **1988**, *42*, 715–721.
(8) Lee, J. P.; Chow, K. H.; Comisarow, M. B. *Anal. Chem.* **1988**, *60*, 2212–2218.
(9) Chow, K. H.; Comisarow, M. B. *Int. J. Mass Spectrom. Ion Processes* **1989**, *89*, 187–203.
(10) Hanna, D. A. 33rd American Society of Mass Spectrometry Annual Conference on Mass Spectrometry and Allied Topics, San Diego, CA, May, 1985; Collected Abstracts, pp 435–436.
(11) Liang, Z.; Marshall, A. G. 37th American Society of Mass Spectrometry Annual Conference on Mass Spectrometry and Allied Topics, Miami Beach, FL, May 1989; Collected Abstracts, pp 1234–1235. Dunbar, R. C., private communication.
(12) Huang, S. K.; Rempel, D. L.; Gross, M. L. American Society of Mass Spectrometry 32nd Annual Conference on Mass Spectrometry and Allied Topics, San Antonio, TX, May 1984; Collected Abstracts, pp 596–597.
(13) de Koning, L. J.; Kort, C. W. F.; Pinske, F. A.; Nibbering, N. M. M. *Int. J. Mass Spectrom. Ion Processes*, in press.
(14) Mitchell, D. W.; DeLong, S. E. *Int. J. Mass Spectrom. Ion Processes*, in press.
(15) Noest, A. J.; Kort, C. W. F. *Comput. Chem.* **1982**, *6*, 115–119.
(16) Rahbee, A. *Int. J. Mass Spectrom. Ion Processes* **1986**, *72*, 1–14.
(17) Meier, J. E.; Marshall, A. G. *Anal. Chem.*, in press.
(18) Rempel, D. L.; Huang, S. K.; Gross, M. L. *Int. J. Mass Spectrom. Ion Processes* **1986**, *70*, 163–184.
(19) Van der Hart, W. J.; Van de Guchte, W. J. *Int. J. Mass Spectrom. Ion Processes* **1988**, *82*, 17–31.
(20) Wang, M.; Marshall, A. G. 37th Amer. Soc. Mass Spectrom. Annual Conf. on Mass Spectrom. & Allied Topics, Miami Beach, FL, May, 1989; Collected Abstracts, pp 1226–1227; Hanson, C. D.; Castro, M. E.; Russell, D. H. *Ibid.* pp 1274–1275.
(21) Moini, M.; Eyler, J. R. *Int. J. Mass Spectrom. Ion Processes* **1989**, *87*, 29–40.
(22) Poretti, M.; Rapin, J.; Gäumann, T. *Int. J. Mass Spectrom. Ion Processes* **1986**, *72*, 187–194.
(23) Chen, L.; Cottrell, C. E.; Marshall, A. G. *Chemom. Intell. Lab. Syst.* **1986**, *1*, 51–58.
(24) Devore, J. L. *Probability and Statistics for Engineering and the Sciences*; Brooks/Cole: Monterey, CA, 1982; p 197.
(25) Press, W. H.; et al. *Numerical Recipes*; Cambridge University: New York, 1986; pp 191–203.

RECEIVED for review June 13, 1989. Accepted October 18, 1989. This work was supported by grants (to A.G.M.) from the U.S.A. Public Health Service (N.I.H. GM-31683) and The Ohio State University.

Anal. Chem. 1990, 62, 76–81

Determination of Organic Acids in Dilute Hydrocarbon Solution Using Poly(ethylenimine)-Coated Piezoelectric Crystals

John M. Charlesworth

DSTO, Materials Research Laboratory, P.O. Box 50, Ascot Vale, Victoria, Australia 3032

Some of the factors that influence the resonant frequency of oscillating 10-MHz AT-cut quartz crystals in liquids are investigated. The relationship between the measured frequency shifts and the physical properties of the liquids are examined, and reasons for departure from ideal behavior are discussed. The sorption characteristics of crystals coated with a polymer film (poly(ethylenimine)) containing basic functional groups are reported. These coated crystals are shown to behave as selective detectors for a range of organic acids in dilute hydrocarbon solution. The lower limit for reliable measurement using a crystal coated with a 40-kHz load of poly(ethylenimine) is estimated to be approximately 25 ppm of phenol in *n*-heptane. Fick's law appears to govern the rate of uptake of mass by the polymer film; however some strong acids show irreversible sorption. The crystals function reliably under solvent flow conditions, where the response time is determined by the thickness of the coating and the flow cell volume. Sensors of this type may find application in areas such as high-performance liquid chromatography detection, industrial process stream analysis, and fuel-quality monitoring.

INTRODUCTION

The use of AT-cut quartz piezoelectric crystals for the analytical determination of low levels of organic compounds in gases is now an accepted technique. Several recent reviews provide useful background information on the development of these devices (*1–4*). In most gas-phase applications, at least one face of the crystal is coated with a material capable of interacting with the compounds to be detected. Following the uptake of additional mass by the exposed coating the oscillation frequency is reduced linearly in accordance with the Sauerbrey expression

$$\Delta f = -k_1 \, \Delta m \qquad (1)$$

where Δf is the frequency change, k_1 is a constant dependent on the oscillation frequency of the crystal and the coating sensitivity and loading, and Δm is the change in mass. King (*5*) has estimated that under ideal conditions the detection limit is around 10^{-12} g for a 15-MHz crystal.

Extending this approach to the liquid phase was originally considered to be unfeasible because it was assumed that a quartz crystal would not reliably oscillate when immersed in a liquid, due to the large energy losses at the interface between phases. Initial experimental findings appeared to confirm this belief, and as a consequence early liquid-phase measurements were restricted to washing and drying the coated crystal, following exposure to the solution, and then determining the frequency change (*6, 7*). Both the precision and repeatability of such measurements are understandably poor due to the difficulty in reproducibly removing solvent and the uptake of atmospheric moisture following drying.

Recently it has been shown that it is possible for AT-cut quartz crystals to achieve stable oscillation in solution (*7*), and simple TTL based circuitry has been designed to facilitate such measurements (*8*). Furthermore, several workers have provided detailed theoretical explanations for the behavior of piezoelectric crystals in contact with liquids. Kanazawa and Gordon (*9, 10*) have developed a simple physical model which considers the coupling of the shear wave in the quartz to a damped shear wave in the fluid, assuming negligible fluid elasticity. This allows the following relationship to be derived, relating the change in oscillation frequency to the material parameters describing the liquid and the quartz

$$\Delta f = -2f_o^{3/2}(\eta_l\rho_l/\pi\rho_q\mu_q)^{1/2} \qquad (2)$$

where f_o is the oscillation frequency of the dry crystal, η_l and ρ_l are the absolute viscosity and density of the liquid, and μ_q and ρ_q are the elastic modulus and the density of the quartz, respectively. Bruckenstein and Shay (*8*) have derived a similar, though not identical, expression based on an analogy between the oscillating boundary layer adjacent to each crystal face and the thickness of an ac polarographic diffusion layer. The expression is

$$\Delta f = -(2.26 \times 10^{-6})nf_o^{3/2}(\eta_l\rho_l)^{1/2} \qquad (3)$$

where n has a value of one or two depending on the number of faces of the crystal in contact with the solution. Hager (*11*) has developed a slightly different equation by considering the viscous energy losses and fluid velocity at the crystal surface. This worker reports the relationship

$$\Delta f = -k_2(\eta_l\rho_l)^{1/2} + k_3\epsilon_l \qquad (4)$$

where k_2 and k_3 are proportionality constants and ϵ_l is the dielectric constant of the liquid.

Taking a more empirical approach, Muramatsu et al. (*12*) have demonstrated a linear relationship between Δf and $(\eta_l\rho_l)^{1/2}$ for alcohol–water solutions. Nonideal behavior was observed when high-viscosity liquids were used and when both faces of the crystal were in contact with water. By contrast Nomura and Okuhara (*13*) reported frequency shifts for oscillators immersed in 17 organic liquids and suggested that the following relationship most appropriately describes the frequency changes:

$$\Delta f = -k_4\rho_l^{1/2} - k_5\eta_l^{1/2} + k_6 \qquad (5)$$

where k_4, k_5, and k_6 are empirical proportionality constants.

In other work, Yao and Zhou (*14*) have measured the oscillation behavior of quartz crystals in contact with aqueous electrolytes, water–organic mixtures, and 47 pure organic liquid. They have observed a relationship resembling the Nomura expression (eq 5), with the exception that two additional terms are included to take into account dielectric and conductance effects.

Liquid phase measurement involving the use of piezoelectric crystals coated with a reactive or absorbing layer were first reported by Konash and Bastiaans (*7*) as part of their attempt to develop a mass detector for liquid chromatography. These workers used 7-MHz quartz crstals, surface bonded with octadecyltrichlorosilane and docosodimethyl(dimethylamino)silane on the crystals face exposed to the solvent flow. It was found that changes in oscillation frequency under these simulated LC conditions were slight. For example, injection of

0003-2700/90/0362-0076$02.50/0

0.2-cm^3 aliquots of 10% solutions of carbon tetrachloride and toluene in aqueous methanol produced only around a 40–128 Hz frequency change. After an allowance was made for solvent density effects, it was estimated that less than 0.005% of the available solute was absorbed by the coatings.

Nomura et al. (*15–17*) used coated quartz crystals for the selective sorption of ionic species from solution. In particular, copper oleate coating was used for the determination of 3–40 μM solutions of lead (*15*), poly(vinylpyridine) coating was used for the measurement of 5–35 μM solutions of copper(II) (*16*), and silicone oil was used for the determination of 5–100 μM solutions of iron(III) (*17*). In each of these examples maximum frequency changes were less than about 0.5 kHz, and reactivation of the coating was necessary between determinations. The response time was of the order of several minutes.

More encouraging results involving liquid phase measurements with coated crystals have been obtained recently by Okahata et al. (*18*). These workers showed that a lipid-bilayer coated piezoelectric crystal provides a very sensitive and rapid indicator of bitter substances in aqueous solution. For instance a 19.3 ppm solution of strychnine produced a 0.5-kHz response and desorbed reversibly in a total period of about 1 min.

The present work was intended to determine whether piezoelectric crystals coated with a lipophobic polymer incorporating basic functional groups in its structure could be used as microsensors for the measurement of low levels of organic acids in nonpolar liquid hydrocarbons. The study was also designed to provide more data on the factors that determine the oscillation frequency of AT-cut quartz crystals immersed in liquids and to extend the preliminary study by Konash and Bastiaans (*7*) on the use of coated piezoelectric crystals as selective LC detectors.

EXPERIMENTAL SECTION

Low temperature coefficient 10-MHz AT-cut quartz crystals (Code No. LJ01E) were obtained from Hy-Q International Pty Ltd, Melbourne. The crystals were 5.0 mm in diameter and 0.125 mm thick and had centrally deposited silver electrodes 3 mm in diameter on each face. To enable measurements in a static sealed system, the crystals together with base and electrical leads were attached with epoxy adhesive to a quickfit adaptor fitting into a 50-cm^3 Pyrex cell. Measurements under solvent flow conditions, simulating those in an LC detection situation were performed by using crystals sealed into stainless steel flow cells with capillary inlet and outlet lines. In order to achieve a liquid-tight seal, the base of the crystal holder was fixed in position with a small clamp and a thin smear of epoxy adhesive. Two cells were tested: one with a dead volume of approximately 100 μL, in which the edge of the crystal faced the direction of solvent flow (flow cell A), and a second cell with a dead volume of approximately 50 μL in which the solvent flow was directed at the crystal face (flow cell B). Solvent was forced through the cells with a Varian 8500 syringe-type pulseless HPLC pump attached to a Valco HPLC injection valve equipped with a 100-μL sample loop.

The electrical circuit used to measure the crystal oscillation frequency was essentially the same as that published by Bruckenstein and Shay (*8*). This consisted of an oscillator circuit with one reference and one working crystal and a circuit to measure the difference in frequency. An SN7490N decade divider reduced the differential frequency to below 20 kHz and this signal was fed to a Hewlett-Packard 5381A frequency counter and to a DGH 15 bit D 1601 frequency-to-digital converter interfaced to the RS 232 C port of an XT microcomputer. Data were logged at chosen intervals by using software written for the purpose and then scaled and plotted on screen as a function of time. Collection of frequency values with a precision of 0.1 Hz for the dry crystal was achieved by these means.

The majority of frequency measurements were performed under ambient conditions at 22.5 ± 0.5 °C in an atmosphere with a relative humidity of 40–60%. When necessary, the cell temperature was maintained at 20 ± 0.1 °C and the relative humidity was set by exposing the coated crystal to the vapors above an appropriately saturated salt solution.

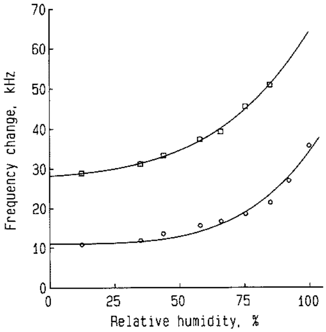

Figure 1. Dependence of frequency change on relative humidity at 22.5 °C for a 10-MHz quartz crystal coated with poly(ethylenimine) at dry loading levels of 11 kHz (○) and 27 kHz (□).

Crystal Coating Method. Poly(ethylenimine) was obtained from Aldrich as a 50% solution in water. ^{15}N NMR analysis in our laboratory revealed that the material was highly branched, containing around 50% secondary and 25% each of primary and tertiary amine groups. The solution was diluted to 5–20 g L^{-1} and a 0.05–1.0-μL aliquot applied with a microliter syringe to the center of the crystal. The droplet was spread with the tip of the syringe needle to cover the entire silver electrode. The liquid layer was then dried with a hot air blower for approximately 10–20 s and allowed to equilibrate by the uptake of atmospheric moisture. Figure 1 illustrates the change in frequency as a function of relative humidity at two levels of poly(ethylenimine) loading. At high humidities (>70%) the sensitivity to moisture increases rapidly, while below 50% humidity the frequency increase is small, corresponding to an uptake of around 25% water at the midpoint of the humidity range at 22.5 °C. All crystal loading determinations, measured by the frequency change due to the coating, contain a contribution from the sorbed water.

RESULTS AND DISCUSSION

Uncoated Crystals. Table I lists the measured frequency shifts at 20 °C for a range of polar, aromatic, and nonpolar liquids together with relevant density and viscosity data. As an example of the stability of oscillation in these liquids, the standard deviation for 1000 frequency measurements taken at 1-s intervals was found to be 8 Hz for oscillation in hexane and 13 Hz for oscillation in carbon tetrachloride.

From eq 3, using a value of 2 for n, the predicted slope of a plot of frequency change against $(\eta_l\rho_l)^{1/2}$ for a 10-MHz crystal is 1.429×10^5 s$^{-1/2}$ g^{-1} cm^2. Accordingly, for a crystal immersed in water at 20 °C, the natural oscillation frequency should be reduced by 14.29 kHz. The experimental value is 15.21 kHz for oscillation in water, which compares favorably with the theoretical prediction.

The data for the pure organic liquids listed in Table I are plotted in Figure 2 as a function of $(\eta_l\rho_l)^{1/2}$. It is clear that for the polar and aromatic molecules the relationship is very close to linear, giving a best fit slope of 1.52×10^5 s$^{-1/2}$ g^{-4} cm^2. For the nonpolar materials, exemplified by the n-alkanes ranging from C5 to C16, the behavior shows positive deviation from ideality. The dielectric constants for the polar compounds are higher than those of the n-alkanes and therefore, according to eq 4, the predicted trend in frequency changes as a function of dielectric constant is opposite to that observed. Attempts to obtain a definitive quantitative relationship between frequency change and dielectric constant have so far proven negative although it does seem likely that the deviation from linearity could be related to the strength of the interfacial bond between the surface of the crystal, or the deposited substrate, and the contacting liquid. For measurements of viscosity at low shear rates, it is assumed that coupling between the liquid and the surface providing the shearing force

Table I. Frequency Change and Physical Property Data for Liquids at 20 °C

liquid	density (ρ), g cm^{-3}	viscosity (η), cP	$(\eta\rho)^{1/2}$, g s$^{1/2}$ cm^{-2}	Δf, kHz
methyl acetate	0.9330	0.381	0.0596	10.11
ethyl acelate	0.9003	0.455	0.0640	10.51
propyl acetate	0.8878	0.590	0.0724	11.37
butyl acetate	0.8822	0.732	0.0804	11.77
diethyl ether	0.7138	0.233	0.0408	7.75
cyclohexene	0.8102	0.660	0.0731	11.20
m-xylene	0.8642	0.620	0.0732	11.28
toluene	0.8669	0.590	0.0715	11.34
cyclohexane	0.7786	0.930	0.0851	12.20
chloroform	1.4832	0.580	0.0928	15.60
carbon tetrachloride	1.5940	0.969	0.1243	18.57
1-propanol	0.8060	2.256	0.1348	20.91
1-butanol	0.8098	2.948	0.1545	21.70
pentane	0.6262	0.240	0.0388	6.55
hexane	0.6603	0.326	0.0464	7.31
heptane	0.6838	0.409	0.0529	8.06
octane	0.7025	0.542	0.0617	9.12
nonane	0.7176	0.711	0.0714	9.98
decane	0.7300	0.920	0.0820	11.05
undecane	0.7402	1.17	0.0931	12.05
dodecane	0.7490	1.35 (25 °C)	0.1043	12.65
tridecane	0.7560	1.55 (23.3 °C)	0.1157	14.17
tetradecane	0.7630	2.18	0.1290	15.30
glycerol/water				
% glycerol, 0	0.9982	1.002	0.1000	15.21
20	1.0459	1.737	0.1348	18.65
40	1.0984	3.653	0.2010	24.43
48	1.1200	5.413	0.2462	27.65
60	1.1530	10.681	0.3509	32.96
68	1.1755	18.455	0.4658	36.60
72	1.1866	27.624	0.5725	38.62
76	1.1976	40.575	0.6971	40.80
80	1.2085	59.905	0.8509	43.30
82	1.2148	69.523	0.9190	44.30

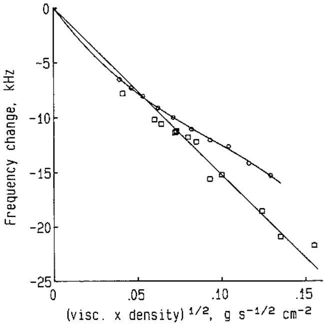

Figure 2. Frequency change versus $(\eta_l\rho_l)^{1/2}$ for a 10-MHz crystal immersed in polar and aromatic liquids (□) and *n*-alkanes ranging from C5 to C14 (○). Details of individual liquids are given in Table I.

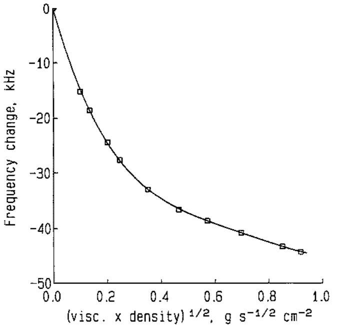

Figure 3. Change in the oscillation frequency of a 10-MHz crystal as a function of $(\eta_l\rho_l)^{1/2}$ following immersion in glycerol/water mixtures.

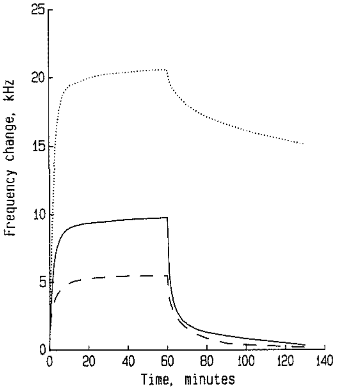

Figure 4. Frequency change of poly(ethylenimine)-coated crystals as a function of time for sorption/desorption of benzoic acid and phenol dissolved in *n*-heptane: 0.5 g L^{-1} phenol (——), 0.25 g L^{-1} phenol (– –), and 0.5 g L^{-1} benzoic acid (···). The coating load corresponds to 17.92 kHz for phenol and 16.12 kHz for benzoic acid, both at 40% relative humidity and 22.5 °C.

is sufficient to prevent slippage (*19*). At the high shear rates involved in the present system, nonpolar liquids such as the *n*-alkanes would not be expected to adhere to the shearing surface as well as the more polar molecules, which show ideal behavior. The presence of a surface effect was suggested by studying the changes in oscillation behavior induced by depositing a layer of poly(ethylenimine) on the crystal face. For the coated crystal the frequency shift was measured to be 6230 Hz for oscillation in *n*-heptane compared to 8060 Hz for the uncoated crystal resonating in the same liquid. However, it must also be pointed out that if the acoustic wave is attenuated by the coating, it may not propagate as far into the liquid as would the wave emanating from an uncoated crystal.

The data in Table I also include frequency shifts for a 10-MHz quartz crystal immersed in water–glycerol mixtures containing up to 82% (w/v) glycerol. Above this limit, which corresponds to a value of 0.9 g s$^{-1/2}$ cm^{-2} for $(\eta_l\rho_l)^{1/2}$, the crystal would not reliably oscillate. These data, plotted in Figure 3, show a pronounced nonlinear dependence on $(\eta_l\rho_l)^{1/2}$, confirming some of the previously reported results relating to the oscillation behavior of quartz crystals in high-viscosity solvents (*12*). An adequate mechanistic explanation for this effect has not yet been advanced (*20*).

Coated Crystals. Figure 4 illustrates the results of sorption/desorption experiments in which poly(ethylenimine) coated crystals were immersed in dilute heptane solutions of phenol and benzoic acid. Neutral solutes such as ethanol, acetone, and toluene produced little or no frequency change at these concentrations. The pronounced interaction between acidic molecules and the basic substrate is obvious. Furthermore the uptake of the organic acid by the polymer coating is faster than the corresponding desorption process, particularly in the case of the benzoic acid, which undergoes partially irreversible sorption. Proton transfer resulting in salt formation is the most probable explanation for this effect given that the pK_a of benzoic acid is much lower than that of phenol.

The rate of sorption and desorption of solute molecules is a significant factor in determining whether a reliable and

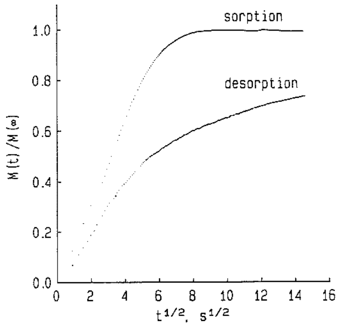

Figure 5. Fickian diffusion plots for sorption and desorption of 1 g L^{-1} phenol in *n*-heptane using a crystal coated with a 17.40-kHz load of poly(ethylenimine) at 40% relative humidity and 22.5 °C.

responsive detector can be designed for use under solvent flow conditions typical of those that occur in an HPLC application. The kinetics of these sorption/desorption processes are often represened by Fick's diffusion equation, the solution of which for a polymer sheet with one side exposed to a liquid leads to the expression (*21*)

$$M(t)/M(\infty) = 4\left(\frac{D(c)t}{\pi l^2}\right)^{1/2} \qquad (6)$$

where $M(t)$ and $M(\infty)$ are the masses of liquid absorbed per unit volume of polymer at time t and at equilibrium, respectively, l is the thickness of the polymer sheet, $D(c)$ is the concentration-dependent diffusion constant, and c is the solute concentration at the film surface. $D(c)$ is assumed to be linearly related to c.

For a film of uniform thickness, eq 6 predicts a linear rate of absorption, provided c is constant, when fractional sorption is plotted against $t^{1/2}$. An example of the application of eq 6 to the present system is given in Figure 5. These data relate to a crystal with one face coated with a loading of 17.40 kHz of poly(ethylenimine), immersed in a 1 g L^{-1} phenol solution. The sorption curve shows Fickian response up to approximately 80% of equilibrium capacity, while the desorption curve is linear to around 40% of the total recovery. The diffusion constant for the desorption is approximately 60% of that for the sorption process.

It has been shown that for coated AT-cut quartz crystals the film thickness is related to frequency decrease by the expression (*20*)

$$l = N_q\rho_q\Delta f/\rho_c f_o^2 \qquad (7)$$

where N_q is the quartz crystal frequency constant (1.668×10^5 Hz cm^{-1}), ρ_q is the quartz density (2.69 g cm^{-3}), and ρ_c is the density of the coating. The gradients of sorption curves of the type shown in Figure 5, for crystals coated with varying film thickness, were linearly related to reciprocal film thickness, further confirming that the detector response time characteristics are largely diffusion controlled.

As expected from thermodynamic considerations, the equilibrium sorption capacity, plotted in Figure 6, is directly proportional to the solute concentration and the coating load. Triplicate measurements obtained by using a crystal coated with a 41.26-kHz load of poly(ethylenimine) (38.5% relative humidity at 22.5 °C) gave average readings of 20.08 ± 0.65 and 1.24 ± 0.38 kHz following immersion in 500 and 25 ppm phenol solutions, respectively. The lower limit for reliable detection is therefore estimated to be around the 10–50 ppm range. Since it is possible to measure frequency changes with much greater precision than 100 Hz, the elimination of extraneous electrical effects by enclosure of the cell and circuitry in a Faraday cage (*8*) and improvements in coating methods would presumably lower the detection limit.

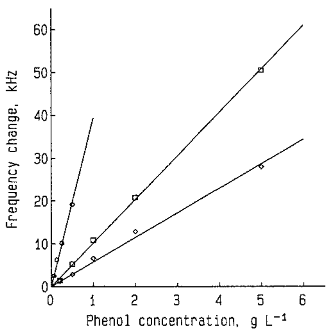

Figure 6. Plots of frequency change at equilibrium as a function of phenol concentration in *n*-heptane: 42.3-kHz load at 40% relative humidity 22.5 °C (○), 20.25 kHz load at 65% relative humidity 22.5 °C (□), and 11.83 kHz load at 65% relative humidity 22.5 °C (◇).

Table II. Response Characteristics of Poly(ethylenimine)-Coated Crystals to Organic Acids at 40–45% Relative Humidity, 22.5 °C

solution (0.5 g L^{-1} in *n*-heptane)	pK_a (25 °C, H_2O)	Δf/coating load
monochloroacetic acid	2.85	2.5
2,4-dinitrophenol	3.96	0.6
benzoic acid	4.19	1.3
phenylacetic acid	4.28	2.5
acetic acid	4.75	0.9
propionic acid	4.87	1.0
butyric acid	4.81	1.1
valeric acid	4.82	1.3
hexanoic acid	4.88	2.5
nonanoic acid	4.96	9.2
2,4,5-trichlorophenol	6.00	0.2
o-nitrophenol	7.17	0.5
β-naphthol	9.51	1.7
phenol	9.89	0.5
o-cresol	10.20	0.3

The sensitivity of poly(ethylenimine) toward other acids was studied by using a range of some commonly occurring organic molecules soluble in *n*-heptane. Stable equilibrium sorption values were taken as the frequency change after 30 min of immersion of coated crystals in 0.5 g L^{-1} solutions of each acid. These data are presented in Table II. The sensitivity factors listed in Table II are defined as the frequency change following uptake of solute, divided by the coating load. As a measure of the strength of each acid, pK_a (H_2O, 25 °C) values are also listed. These results appear to show little correlation between acid strength and sorption capacity. This is most clearly indicated by the data for the *n*-alkyl carboxylic acids ranging from C2 to C9. These compounds have approximately equal dissociation constants in water, yet they have vastly different sensitivity factors. Evidently as the size of the hydrophobic part of the molecule increases, so does the strength of solvation of poly(ethylenimine). Conversely the least sensitive acidic compound tested was 2,4,5-trichlorophenol, which is one of the larger and more polar of the organic molecules examined. The frequency shift may also be due to changes in the viscoelastic behavior within the swollen polymer which influences the manner in which the shear wave is coupled between the crystal and the coating or solution. Acid–base pairing would therefore not appear to be the only cause of interaction between polymer and solute, although it does appear to have the major effect. These data also highlight the potential for applying the present method as a simple and

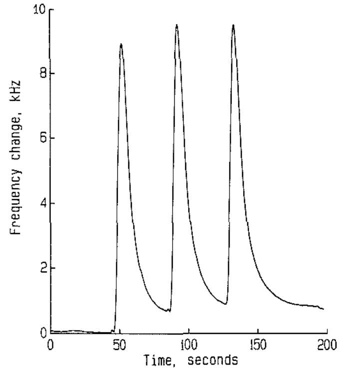

Figure 7. Flow cell detector response obtained by using a crystal coated on both sides with an average 5.25-kHz load of poly(ethylenimine). Repeat injections of 100-μL aliquots of 5 g L^{-1} solutions of phenol in *n*-heptane were made at intervals of 45-s at a flow rate of 2.1 cm^3 min^{-1}.

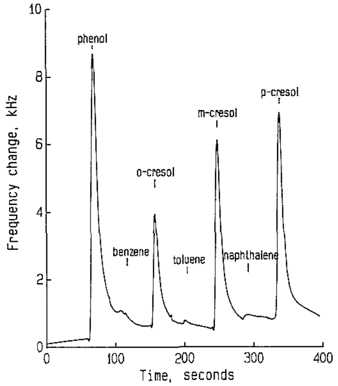

Figure 8. Flow cell detector response obtained by using a crystal coated on both sides with a 5.25-kHz load of poly(ethylenimine). Aliquots of 100 μL of 5 g L^{-1} solutions of each compound in *n*-heptane were injected at 45-s intervals at a flow rate of 2.1 cm^3 min^{-1}.

rapid general means of measuring the interaction between film-forming polymers and solvents or solutes. In particular the method offers the possibility for simultaneous determination of both the kinetic and thermodynamic factors involved in sorption, using only microgram quantities of each material.

HPLC Applications. In terms of designing an optimized detector for an HPLC application, it is apparent that a balance must be maintained between rapid response time, requiring a low film thickness, and high sensitivity, requiring a high film thickness. It must also be recognized that the response time will vary with concentration because the diffusion constant is concentration dependent. High solute concentations will result in a much more rapid uptake of material than will occur at low solute concentrations. This will lead to a complex pattern of behavior when detecting material eluting from a liquid chromatography column since a time-dependent concentation profile will always be present. Strong dependence of response on flow rate would also be expected.

Some examples of measurements illustrating the reproducibility and magnitude of response to different species are shown in Figures 7 and 8. These results were obtained by using flow cell B, at a flow rate of 2.1 cm^3 min^{-1}, fitted with a crystal coated with an average load of 5.25 kHz of poly(ethylenimine) on each face. The data in Figure 7 confirm that successive injections of 100-μL aliquots of 5 g L^{-1} phenol solution produce reproducible peaks, with a slight drift in the base line caused by slow desorption. The pronounced peak asymmetry is due to the lower rate of desorption compared to sorption. Figure 8 presents the results of sequential injections of 100-μL aliquots of 5 g L^{-1} solutions of phenol, the three cresol isomers, and three neutral aromatic species. As expected, the detector shows a selective response in favor of the acidic compounds, the magnitude of which varies with the structure of the sorbed species.

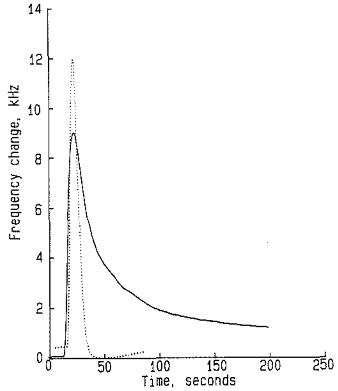

Figure 9. Comparison between peak shapes produced using flow cell A (——) coated on one side with a 13.20-kHz load of poly(ethylenimine) and flow cell B (···) coated on each face with an average load of 5.25 kHz of poly(ethylenimine). Aliquots of 100 μL of 10 g L^{-1} solutions of phenol in *n*-heptane were injected at a flow rate of 2.1 cm^3 min^{-1}.

Improvements in the detector resonse can be achieved by optimizing the cell geometry and coating thickness. Figure 9 shows a comparison between the peaks produced by injection of 100-μL aliquots of 10 g L^{-1} phenol solutions into flow cell A, fitted with a crystal coated on one side only with a 13.2 kHz loading of poly(ethylenimine), and flow cell B fitted with a crystal on which both sides have been coated with a total load of 10.5 kHz of poly(ethylenimine). The reduction in cell volume and the use of a thinner layer of coating combine to improve sensitivity and reduce peak width greatly.

CONCLUSIONS

Piezoelectric crystals coated with a layer of the lipophobic basic polymer, poly(ethylenimine) have been shown to function as versatile sorption detectors for low concentrations of organic acids dissolved in nonpolar hydrocarbons. Reproducible oscillation behavior for coated crystals immersed in liquids has been achieved under both static and flowing conditions. The method offers potential not only as an analytical tool but also for the provision of thermodynamic and kinetic information regarding polymer–solute and polymer–solvent interactions. In terms of the application of these devices as liquid chromatography detectors, some improvement in response time would be required in order to allow for the short residence time of eluting components in the flow cell. The chemical and physical structure of the coating, the film thickness, and the flow cell volume and geometry all influence the response time and scope for further optimization of these parameters is available. In addition the individual response characteristics of each type of acidic compound could be utilized by employing an array of crystals each coated with a different basic polymer. Data analysis techniques such as pattern recognition could then be used for more thorough identification of species present in complex mixtures. This approach has been successfully applied in the case of crystals oscillating in the gas phase, using the array method combined with multivariate analysis (*22–24*). This is particularly appropriate in systems in which no prior separation step has been performed. Industrial process stream monitoring and petroleum and fuel quality measurements are potential areas for the exploitation of these devices.

LITERATURE CITED

(1) Hlavay, J.; Guilbault, G. G. *Anal. Chem.* **1977**, *49*, 1890–1898.
(2) Janata, J.; Bezegh, A. *Anal. Chem.* **1988**, *60*, 62R–74R.
(3) Alder, J. F.; McCallum, J. J. *Analyst* **1983**, *108*, 1169–1189.
(4) Guilbault, G. G.; Jordan, J. M. *CRC Crit. Rev. Anal.* Chem. **1988**, *1*, 1–28.
(5) King, W. H. *Anal. Chem.* **1964**, *36*, 1735–1739.
(6) Mieure, J. P.; Jones, J. L. *Talanta* **1969**, *16*, 149–150.
(7) Konash, P. L.; Bastiaans, G. J. *Anal. Chem.* **1980**, *52*, 1929–1931.
(8) Bruckenstein, S.; Shay, M. *Electrochim. Acta* **1985**, *30*, 1295–1300.
(9) Kanazawa, K. K.; Gordon, J. G. *Anal. Chem.* **1985**, *57*, 1771–1772.
(10) Kanazawa, K. K.; Gordon, J. G. *Anal. Chim. Acta* **1985**, *175*, 99–105.
(11) Hager, H. E. *Chem. Eng. Commun.* **1986**, *43*, 25–38.
(12) Muramatsu, H.; Tamiya, E.; Karube, I. *Anal. Chem.* **1988**, *60*, 2142–2146.
(13) Nomura, T.; Okuhara, M. *Anal. Chim. Acta* **1982**, *142*, 281–284.
(14) Yao, S. Z.; Zhou, T. A. *Anal. Chim. Acta* **1988**, *212*, 61–72.
(15) Nomura, T.; Okuhara, T.; Hasegawa, T. *Anal. Chim. Acta* **1986**, 261–265.
(16) Nomura, T.; Sakai, M. *Anal. Chim. Acta* **1986**, *183*, 301–305.
(17) Nomura, T.; Ando, M. *Anal. Chim. Acta* **1985**, *172*, 353–357.
(18) Okahata, Y.; Ebatao, H.; Taguchi, K. *J. Chem. Soc., Chem. Commun.* **1987**, 1363–1367.
(19) Van Wazer, J. R.; Lyons, J. W.; Kim, K. Y.; Colwell, R. E. *Viscosity and Flow Measurement*; Interscience: New York, 1963.
(20) Lu, C. S.; Lewis, O. *J. Appl. Phys.* **1972**, *43*, 4385–4390.
(21) Park, G. S. *Diffusion in Polymers*; Crank, J., Park, G. S., Eds.; Academic Press: New York, 1968; Chapter 5.
(22) Carey, W. P.; Beebe, K. R.; Kowalski, B. R.; Illman, D. L.; Hirschfeld, T. *Anal. Chem.* **1986**, *58*, 149–153.
(23) Carey, W. P.; Beebe, K. R.; Kowalski, B. R. *Anal. Chem.* **1987**, *59*, 1529–1534.
(24) Carey, W. P.; Kowalski, B. R. *Anal. Chem.* **1988**, *60*, 541–544.

RECEIVED for review June 14, 1989. Accepted October 16, 1989.

Simultaneous Multielement Determination of Trace Metals Using 10 mL of Seawater by Inductively Coupled Plasma Atomic Emission Spectrometry with Gallium Coprecipitation and Microsampling Technique

Tasuku Akagi*,[1] **and Hiroki Haraguchi**[2]

Department of Chemistry, Faculty of Science, University of Tokyo, Hongo, Bunkyo-ku, Tokyo 113, Japan, and Department of Applied Chemistry, Faculty of Engineering, Nagoya University, Furo-cho, Chikusa-ku, Nagoya 464, Japan

By use of a 10-mL sample, the concentrations of several trace elements in seawater were determined simultaneously by inductively coupled plasma atomic emission spectrometry. The techniques employed were coprecipitation with gallium hydroxide and microsample introduction. A preconcentration factor of 200 times was achieved by dissolving gallium precipitate with 50 μL of nitric acid. The solution of one drop size (50 μL) was introduced into the plasma via a cross-flow nebulizer. Integration time and sample volume were examined in detail for the optimization of the measurement conditions of the microsampling technique. With internal standardization using gallium, the concentrations of Al, Ti, Cr, Mn, Fe, Co, Ni, Cu, Zn, Y, and Pb were determined. The detection limits of these elements ranged from 500 (Pb) to 10 ng/L (Cu and Zn). The precisions of most elements for unacidified coastal seawater are about 10%, and accuracy for Mn, which is the only element measurable for an acidified seawater standard, is fairly good. The analytical procedure of the present method is so simple that about 50 samples could be preconcentrated and analyzed in 1 h. This method was applied to the analysis of some natural seawaters, and it was found that this method was effective, especially for the analysis of seawaters where the available sample volume was very small.

INTRODUCTION

So far the volume of seawater required for trace metal analysis has been usually about the liter level. Recently marine chemists have paid much attention to some local phenomena occurring at hydrothermal vents and in deep sea biological communities. In such cases, the amount of the water sampled is quite small and maximum information is sought. Thus, the portion of the sample assigned to trace metal analysis is often limited. The development of a method to determine trace metal concentrations using small amounts of seawater is desirable.

Inductively coupled plasma atomic emission spectrometry (ICP-AES) enables us to determine various trace metals in solution simultaneously. Some preconcentration prior to ICP analysis is, however, necessary to determine the low concentrations of trace elements in seawater containing interfering salts. A variety of preconcentration techniques have been proposed for seawater analysis by ICP-AES (*1–5*). The present authors developed the coprecipitation method for trace metals in seawater by using gallium as a coprecipitation reagent followed by ICP-AES measurement (*1*) and found that this method is a unique coprecipitation technique associated with magnesium in seawater (*6*). Although the gallium coprecipitation has several unique advantages (little spectral interference in ICP-AES measurements and little contamination from a hydroxide solution for pH adjustment), it requires 1 L of seawater sample.

Microsampling techniques have been used for the introduction of the microliter volume solution into ICP-AES (*7–9*).

---

[1] Present address: Department of Earth Sciences, The Open University, Walton Hall, Milton Keynes MK7 6AA, England.

[2] Nagoya University.

0003-2700/90/0362-0081$02.50/0

Table I. Instrumental Components and Operating Conditions

spectrometer	Jarrell-Ash Plasma Atomcomp MK II
frequency	27.12 MHz
rf output power	1.1 kW
coolant gas	argon, 15 L/min
auxiliary gas	argon, 0.5 L/min
carrier gas	argon, 1.0 L/min
observation height	17 mm above work coil
nebulizer	cross-flow
polychromator	Paschen-Runge (75 cm focal length)
grating	2400 grooves/mm
reciprocal linear dispersion	0.54 nm/mm at 270 nm
entrance slit width	25 μm
exit slit width	50 μm
monochromator	Ebert (50 cm focal length)

Table II. Wavelength and Detection Limit of the Elements

			detection limit, μg/L			
			microsampling[b]			
element		wavelength, nm	50 μL	100 μL	continuous	with preconcn and microsampling[c]
Al	I	308.2	70	40	20	0.35
Ti	II	334.9	9	10	2.7	0.05
V	II	292.4	30	20	3.3	0.45
Cr	II	205.5[a]	30	40	25	0.15
Mn	II	257.6	6	6	1.5	0.04
Fe	II	259.9	9	10	6.3	0.05
Co	II	228.6	20	13	4.2	0.11
Ni	II	231.6	60	35	31	0.32
Cu	I	324.7	5	4	2.4	0.016
Zn	I	213.8[a]	5	5	2.4	0.015
Y	II	371.0	7	5	1	0.040
Mo	I	202.0	9	20	14	3
Cd	I	228.8	20	8	7.2	0.24
Pb	II	220.3	90	90	70	0.45

[a] Second-order lines used. [b] Integration time of 5 s. [c] Final sample volume is 50 μL and integration time is 5 s.

Uchida et al. evaluated the microsampling technique for ICP-AES (*7*) and they reported that internal standardization improved the precision of analytical results.

In the present paper, the microsampling technique is applied to the solution preconcentrated by the gallium coprecipitation method. After careful examination of the effectiveness of gallium as an internal reference element and optimization of the experimental procedure, it has been found that the combined technique of gallium coprecipitation and microsample introduction can be successfully applied to the determination of trace metals using only 10 mL of seawater.

EXPERIMENTAL SECTION

Chemicals and Apparatus. Almost all chemicals used were the same as used in the previous study (*1*). Gallium solutions of 250 μg/mL were prepared by dissolving 99.99% pure metal (Wako Chemical Co., Ltd.) in HCl. Sodium hydroxide (Suprapur grade, Merk Co., Ltd.) was used for the preparation of 0.1 M NaOH solution.

An ICP-AES system, Jarrell-Ash AtomComp Mk II, was operated under the conditions listed in Table I. The analytical wavelengths of analytes are shown in Table II. For pipetting the gallium and NaOH solutions, an Eppendorf micropipet of changeable volume (100–1000 μL) was used. All glass and polyethylene ware used were well cleaned by soaking them in 1:1 HNO_3 solution for a week, followed by rinsing with pure water.

Seawater Samples. Coastal seawaters from Tokyo Bay and hydrothermal waters from the Loihi Seamount, HI, were used in the analysis of natural seawater. The coastal and hydrothermal waters were collected in the cruises by research vessels, *Tansei-Maru* and *Hakuho-Maru*, from the Ocean Research Institute, the University of Tokyo. In the recovery test, artificial seawater prepared by following the prescription by Kester et al. (*10*) was used.

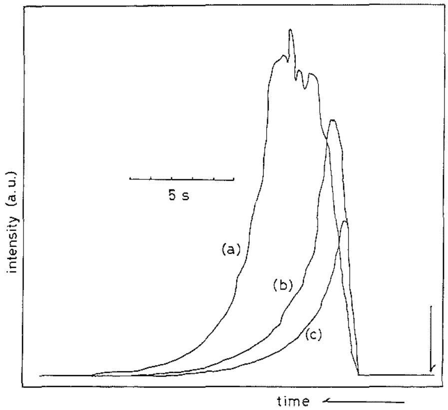

Figure 1. Peak profiles obtained for various volumes of samples containing 1 mg of Ga/mL at Ga I 417.2 nm. The arrow in the figure indicates time of sample injection. Sample volumes aspirated were 100 μL (a), 50 μL (b), and 25 μL (c).

Recommended Procedure. Exactly 10 mL of unacidified seawater was placed into a centrifugation glass tube with a pipet. Two hundred microliters of 250 μg/mL gallium solution was added, followed by agitation. Gallium dissolves in the solution. Then a certain amount of 0.1 M NaOH solution, which was previously determined with a pH meter using reference seawater, was added in order to adjust the pH of the sample solution to 9.1. After the sample solution was shaken for homogenization, the test tube was centrifuged at 3000 rpm for 30 min. A small amount of jellylike precipitate adhered to the bottom of the tube. After the supernatant fluid was removed, 5 mL of pure water was carefully poured into the tube and discarded. The precipitate remained adhering to the tube. Finally, 50 μL of 1 M HNO_3 solution was added in order to dissolve the precipitate just before the ICP-AES measurement. The end of a capillary tube leading to a nebulizer was placed at the bottom of the centrifugation tube, and the emission signals were integrated for 5 s. After the 50-μL sample was aspirated, the capillary tube was immediately returned to pure water.

RESULTS AND DISCUSSION

Peak Profile of Gallium Obtained by Microsampling. The peak profiles obtained by aspirating microliter volumes of gallium solution were examined. This experiment was necessary to determine the timing of the start of integration in the ICP-AES measurement. The observed peak profiles are shown in Figure 1, for which the concentration of gallium in the solution was 300 μg/mL and the emission intensity of Ga was monitored at Ga I 417.2 nm. The peak height increased with the volume aspirated. When more than 100 μL of sample was introduced, the peak reached a plateau, as can be seen in Figure 1. The width of the peak also varied with the sample volume and became larger when the volume was increased. From these results, a time of 3 s after the sample aspiration was chosen to start the integration.

Influence of Air Aspiration to Background Intensity. In the case of the microsampling technique, air was often aspirated together with sample solution when the end of capillary tube was moved from one solution to another. Thus, the influence of air aspiration for various periods on ICP background intensity was investigated. Figure 2 shows the results of the experiment, where the changes in background intensity are given as the equivalent concentrations of analytes.

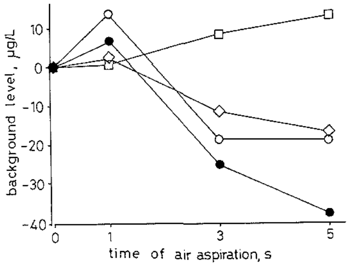

Figure 2. Effect of air aspiration on background intensity in ICP-AES: (○) Ni II 231.6 nm, (●) Cu I 324.7 nm, (□) Zn I 213.8 nm, and (◇) Y II 371.0 nm.

The background intensity was influenced by air aspiration. With an air aspiration of 1 s, all the analytes showed increases in background intensity. The increase might be due to discharge temperature enhancement caused by the interruption of water aspiration. When the length of air aspiration was more than 1 s, the background intensities for all the elements except Zn decreased with air aspiration time. However, the changes in the background levels for all the elements with 1-s air aspiration were within the range of the detection limits obtained by the microsampling method (see Table II). In the case of the microsampling technique, the air aspiration time could be shortened to less than 1 s with some practice, and thus the influence of air aspiration to analytical results became negligible.

Dependence of Detection Limit on Integration Time and Sample Volume. To optimize integration time and sample volume in the microsampling technique, the detection limit was examined. The detection limits were calculated for the concentrations of analytes corresponding to 3 times the standard deviations of the background intensities. These intensities were obtained by aspirating microsamples (containing 500 μg/mL of Ga and 500 μg/mL of Mg) 10 times. The sample volumes examined were 50 and 100 μL. The integration times studied were 15, 10, 7, 5, 3, and 2 s. Almost all the elements investigated gave the smallest detection limits when the integration time was 5 or 3 s regardless of the sample volume. In Table II the detection limits for integration time of 5 s are shown. Roughly speaking, the detection limits obtained at the integration times of 15 and 2 s were 2 times poorer than those of 5 s. These may be due to the inefficient detection of the transient emission signals from the analytes and the relatively large variation of background intensity. For 3-s integration times, careful timing of sample aspiration was required. Thus, 5 s was chosen. Generally the detection limit for the sample volume of 100 μL was slightly better than those of 50 μL. Taking the preconcentration ratio into consideration for the detection limit, the 50-μL sample volume is advantageous over 100 μL. Thus the natural samples were concentrated to 50 μL.

The detection limits obtained by usual continuous nebulization are also shown in Table II. The detection limits of most elements obtained by the microsampling method were 3 times poorer than those for the continuous nebulization method.

The detection limits for seawater obtained under the optimized conditions are shown in Table II. They were estimated by dividing the detection limits obtained under the optimized conditions by the preconcentration factor for each element. The preconcentration factors were about 200 for most elements except for some elements with poor recoveries such as V, Mo, and Cd as shown in the later section. These detection limits were low enough to detect Al, Ti, Mn, Fe, Co, Cu, Zn, and Y in coastal seawater (*1*, *11*).

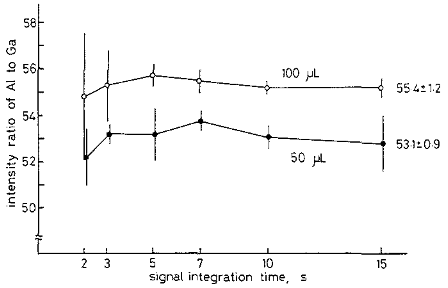

Figure 3. Intensity ratio of Al to Ga with changes of signal integration time and sample volume in microsampling technique. A test solution of 5 mg of Al/L and 250 mg of Ga/L was used. The figure put on the right of each line is the mean and standard deviation of all the data for each line.

Internal Standardization Using Gallium and Recovery of Analytes. As Uchida et al. pointed out (*7*), the use of internal standardization improves the precision of analytical results in the microsampling technique. In the present study, the usefulness of gallium as an internal reference element was examined by considering the following experimental conditions and procedures. Firstly, in the coprecipitation preconcentration a definite amount of gallium was added to the sample. Secondly, the recovery of gallium in the coprecipitation procedure was quantitatively estimated, and finally, the concentration of gallium in natural seawater was negligibly low compared to that added (*12*).

In the case of microsampling technique, small variations in integration time and sample volume aspirated alter the signal intensities of the analytes. We anticipated that the internal standardization will compensate for these variations. The ratios of the intensities of the analytes to that of gallium were examined under various conditions by using the test solution which contained analytes and gallium at certain concentrations. Under the same experimental conditions used in the estimation of the detection limit, the test was done for sample volumes of 100 and 50 μL and integration times of 15, 10, 7, 5, 3, and 2 s. As an example, the results for Al are shown in Figure 3. The fluctuation of gallium intensity, as an indication of deviations in aspirated volume and integration time, was large with short integration time. It sometimes fluctuated as much as 30%, but the intensity ratio of aluminum to gallium only gave a small fluctuation. The ratios were almost constant against change in integration time. The ratios for sample volume of 100 μL were slightly higher than those for sample volume of 50 μL. Such differences were observed for other elements. The differences seem to observe the rule that with larger volumes higher ratios are obtained for the elements measured at atomic lines and lower ratios for those at ionic lines. The differences in the ratios for most elements between 100 and 50 μL are smaller than 5%, but those for V, Ni, Cd, and Pb are 6–9%. We neglected these differences because the variation in sample volume is fairly small. These experimental results indicate that gallium is a useful internal reference element for compensation of aspirated volume and integration time variations.

As long as the initial sample volume and the gallium concentration added is exactly known, the change of the preconcentration factors of analytes can be corrected by using the gallium concentration in the preconcentrated sample. Thus, the standard deviations of recoveries of the analytes were examined after the correction by the internal standardization. The artificial seawater spiked with analyte elements was treated by the same coprecipitation procedure. The results of the recovery and its standard deviation are sum-

Table III. Recoveries[a] of Analytes after Internal Standardization with Gallium Obtained by the Gallium Coprecipitation and Microsampling Technique

element	recovery ± std dev, %	element	recovery ± std dev, %
Al	101.0 ± 2.1	Ni	93.5 ± 3.9
Ti	98.8 ± 0.6	Cu	94.0 ± 4.7
V	33.5 ± 4.2	Zn	98.3 ± 5.6
Cr	100.7 ± 7.9	Y	91.0 ± 5.4
Mn	78.3 ± 8.9	Mo	1.3 ± 0.4
Fe	95.9 ± 6.3	Cd	42.4 ± 7.2
Co	92.4 ± 4.6	Pb	98.8 ± 11.2

[a] Number of replicate analyses was five.

Table IV. Concentrations[a] of Metal Impurities in Artificial Seawater Obtained by the Gallium Coprecipitation and Microsampling Technique

element	concn ± std dev, μg/L	element	concn ± std dev, μg/L
Al	4.5 ± 0.5	Ni	2.2 ± 0.3
Ti	0.59 ± 0.1	Cu	0.51 ± 0.04
Cr	0.30 ± 0.3	Zn	12.5 ± 0.6
Mn	5.6 ± 1.2	Y	0.22 ± 0.06
Fe	1.5 ± 0.2	Cd	0.54 ± 0.13
Co	0.58 ± 0.18	Pb	3.9 ± 0.6

[a] Number of replicate analyses was four.

Table V. Analytical Results[a] for Coastal Seawater Obtained by the Gallium Coprecipitation and Microsampling Technique

element	concn ± std dev, μg/L	element	concn ± std dev, μg/L
Al	4.4 ± 0.4	Cu	0.05 ± 0.01
Ti	0.84 ± 0.5	Zn	2.4 ± 0.3
Mn	16 ± 2	Y	0.14 ± 0.05
Fe	3.1 ± 0.2	Cd	0.19 ± 0.1
Co	3.8 ± 0.4	Pb	5.9 ± 0.8
Ni	5.5 ± 0.5		

[a] Number of replicate analyses was two.

Table VI. Analytical Results for Hydrothermal Waters from Loihi Seamount, HI, by the Gallium Coprecipitation and Microsampling Technique

	concentration, μg/L		
depth, m	Fe	Mn	Ni
744	1.7	–[a]	2.1
793	1.7	–[a]	1.1
843	2.3	–[a]	17
893	2.2	0.08	2.5
917	3.6	–[a]	2.4
942	4.5	0.06	32
967	2.2	0.10	71
992	11	0.30	45
1016	2.5	–[a]	72
1041	29	0.74	51
1066	43	1.6	61
1091	29	0.68	1.0
1116	49	0.45	84
1140	31	0.45	2.7
1190	13	0.17	1.2

[a] Not detected.

marized in Table III. In this experiment, the standard deviation of the concentration of gallium in five preconcentrated solutions was 110 μg/mL, with an average concentration of 280 μg/mL. Although the gallium concentration showed such a large fluctuation, the standard deviation of recovery of each analyte obtained after the internal standardization was very small. The recovery values for these analytes were almost identical with those obtained by the conventional gallium coprecipitation method using 1 L of seawater. These results suggested that the internal standardization using gallium was effective enough to compensate the analytical variation caused by the deviations of preconcentration ratio and/or recovery.

Contamination from the Preconcentration Procedure. The contaminations caused by NaOH and gallium solutions were determined (*1*). They were less than the concentrations corresponding to the detection limits (Table II) except for Fe from NaOH and Cr from gallium. The contamination due to centrifugation in a glass tube was also estimated by repeating the centrifugation procedure with a new tube each time. Contaminations of Ti, Co, Y, Cd, and Pb were detected. The contamination levels for Ti, Co, Y, Cd, and Pb from a single centrifugation corresponding to the original sample were 5, 10, 5, 10, and 30 ng/L, respectively. They were less than the detection limits shown in Table II.

Precision and Accuracy. The precision of the present method was examined by using artificial seawater. The analytical results and their standard deviations are shown in Table IV. The precisions obtained were around 10% for these trace elements at microgram-per-liter or sub-microgram-per-liter levels. The precisions for V, Cr, Mo, and Cd were not as good probably due to their nonquantitative recoveries. The poor precision for Y could be due to the insufficient detection limit of Y.

As we pointed out in the previous papers (*1*, *6*), gallium dissolves in unacidified seawater. This property of gallium enables us to use unacidified samples and to reduce, therefore, the amount of hydroxide solution in pH adjustment as well as serious contamination from hydroxide solution. Unfortunately, all the seawater standards are acidified, and they are not suitable for the accuracy test of the present method. When we analyzed coastal seawater standard, CASS-1, using Suprapur grade sodium hydroxide from Merck, only Mn can be measured without serious contamination from sodium hydroxide. The analytical result for Mn in CASS-1 was 2.7 μg/L, with standard deviation of 0.3 (n = 3), which is slightly higher than the certified value of 2.27 ± 0.17 μg/L. The contamination from the sodium hydroxide estimated by the previous impurity test corresponding to the sample is 0.3 μg/L, which explains well the difference between the obtained and certified values. We wish to mention that the accuracy of the gallium coprecipitation method using a 1-L sample has been examined by comparison with the chelating exchange method (*4*, *13*).

Application to Natural Seawater Analysis. The present method was applied to natural seawater analysis. In Table V, the analytical results of seawaters from the Tamagawa River estuary in Tokyo Bay are given. The results of the duplicate analyses were consistent. These concentrations seemed slightly higher compared with those reported earlier for different samples of Tamagawa River estuary (*11*). The seawater samples were preconcentrated without filtration. The concentrations obtained by the present method appear to reflect the total concentration, because not only dissolved species but suspended particles precipitated in the coprecipitation procedure and might be introduced into ICP. In this coastal area, most trace elements were contained in suspended particles (*14*, *15*).

The present technique was applied to the analysis of limited-volume seawater samples. The samples were seawater collected near the hydrothermal vents of Loihi Seamount, HI, and were analyzed without filtration. The analytical results are given in Table VI. Although the samples were acidified to pH 2 with nitric acid, the clear depth profiles of Fe, Mn, and Ni are observed as shown in Figure 4. The same sea-

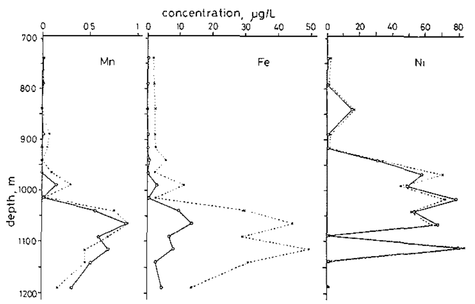

Figure 4. Vertical distributions of Mn, Fe, and Ni in seawaters collected near the Loihi Seamount, HI: (–O–) data obtained for filtered samples by the conventional gallium coprecipitation method (ref 16), (---X---) data obtained for unfiltered samples by the present gallium coprecipitation method with microsampling technique.

waters were also analyzed with the conventional gallium coprecipitation method using 1 L of filtered sample (*1*), and results (*16*) also are given in Figure 4. The profiles show several anomalies in the concentration of Fe, Mn, and Ni and are very similar to that of CH_4 and ^3He concentrations (*16*). The depths of the anomalies were consistent with those of the hydrothermal vents (*16*). Compared with the results obtained by using both the present and previous methods, the concentration levels for Mn and Ni obtained by both were very similar at every depth. While the shape of the depth profile of Fe by the present method was very similar to that by the previous conventional method using 1 L of seawater, the concentration level obtained by using the present method was about 2 or 3 times higher than those obtained previously. The present method was applied to the unfiltered samples and the previous method to the filtered ones. In both cases, the acidified samples were used. The comparison between the results obtained by both the methods seems to provide some important implications on the chemical species of these metals. The significant amount of Fe in the hydrothermal waters may have existed in silicate particles, which are barely soluble by acid. On the other hand, Mn and Ni may exist in particles soluble by acid or in solution.

The present method was almost free from the time-consuming procedure of precleaning of sample bottles. Moreover, the time required for the analysis was much shorter than that by any other techniques. With the present method, preconcentration and ICP-AES measurements of 50 samples could be carried out in 1 h. This method is suitable for on-board preconcentration and subsequent on-land measurement.

ACKNOWLEDGMENT

We express sincere thanks to Professor H. Sakai, the Ocean Research Institute, University of Tokyo, and Professor H. Tsubota, Faculty of Integrated Arts and Science, Hiroshima University, for their help in sampling.

LITERATURE CITED

(1) Akagi, T.; Fuwa, K.; Haraguchi, H. *Anal. Chim. Acta* **1985**, *177*, 139.
(2) Akagi, T.; Nojiri, Y.; Matsui, M.; Haraguchi, H. *Appl. Spectrosc.* **1985**, *39*, 662.
(3) Watanabe, H.; Goto, K.; Taguchi, S. McLaren, J. W.; Berman, S. S.; Russell, D. S. *Anal. Chim.* **1981**, *53*, 738.
(4) Chu, J. C.; Akagi, T.; Haraguchi, H. *Bull. Chem. Soc. Jpn.* **1985**, *58*, 3229.
(5) McLeod, C. W.; Otsuki, A.; Okamoto, K.; Haraguchi, H.; Fuwa, K. *Analyst (London)* **1981**, *106*, 419.
(6) Akagi, T.; Fuwa, K.; Haraguchi, H. *Bull. Chem. Soc. Jpn.* **1989**, *62*, 3823.
(7) Uchida, H.; Nojiri, Y.; Haraguchi, H.; Fuwa, K. *Anal. Chim. Acta* **1981**, *123*, 57.
(8) Greenfield, S.; Smith, P. B. *Anal. Chim. Acta* **1972**, *59*, 341.
(9) Knisely, R. N.; Fassel, V. A.; Butler, C. C. *Clin. Chem.* **1973**, 19, 807.
(10) Kester, D. R.; Duedall, I. W.; Connors, D. N.; Pytkowicz, R. M. *Limnol. Oceanogr.* **1967**, *12*, 176.
(11) Akagi, T.; Haraguchi, H. *Chikyukagaku (Geochemistry)* **1984**, *18*, 81.
(12) Q.-Hunt, M. S.; Turekian, K. K. *Trans. Am. Geophys. Union* **1983**, *64*, 130.
(13) Akagi, T.; Kodama, T.; Haraguchi, H.; Fuwa, K.; Tsubota, H. *Geochem. J.* **1986**, *20*, 127.
(14) Burton, J.; Culkin, F.; Riley, J. P. *Geochim. Cosmochim. Acta* **1959**, *16*, 151.
(15) Akagi, T.; Haraguchi, H. *Chem. Lett.* **1986**, 1141.
(16) Sakai, H.; Tsubota, H.; Nakai, T.; Ishibashi, J.; Akagi, T.; Gamo, T.; Tilbrook, B.; Igarashi, G.; Kodera, M.; Shitashima, K.; Nakamura, S.; Fujioka, K.; Watanabe, M.; McMurtry, G.; Malahoff, A.; Ozima, M. *Geochem. J.* **1987**, *21*, 11.

RECEIVED for review July 3, 1989. Accepted October 15, 1989. This research was supported by Grant-in-Aid (No. 63602019) from the Ministry of Education, Science and Culture, Japan.

TECHNICAL NOTES

Determination of Urinary Mercury with an Automated Micro Batch Analyzer

Liu Ping and Purnendu K. Dasgupta*

Department of Chemistry and Biochemistry, Texas Tech University, Lubbock, Texas 79409-1061

Recently, we have described a new method to determine the total Hg content of water and urine samples by fast low-temperature digestion of the sample by Fenton's reagent ($FeSO_4 + H_2O_2$) to convert all forms of Hg in the sample into inorganic Hg prior to reduction by $NaBH_4$ and air purging to deliver the elemental Hg to a conductometric gold film sensor (*1*). Excellent agreement was established for reference water, wastewater, and urine standards and for blind comparisons of worker urine samples with the values of total Hg as determined by conventional acid digestion and cold vapor atomic absorption spectrometry. In terms of occupational health related measurements, the measurement of Hg in body fluids is routinely needed because of its wide industrial use. An automated version of the new procedure would be particularly useful to meet the need of busy industrial hygiene laboratories. Because the method involves the formation of a precipitate, $Fe(OH)_3$, at one point in the process, neither flow injection nor segmented flow analytical schemes can be easily adapted. The procedure, however, was easily adapted to an automated micro batch analyzer (AMBA) recently developed in this laboratory (*2*, *3*). The operation and performance of this automated urinary Hg analyzer are described in this note.

EXPERIMENTAL SECTION

Reagents and Instrumentation. The experimental system

0003-2700/90/0362-0085$02.50/0

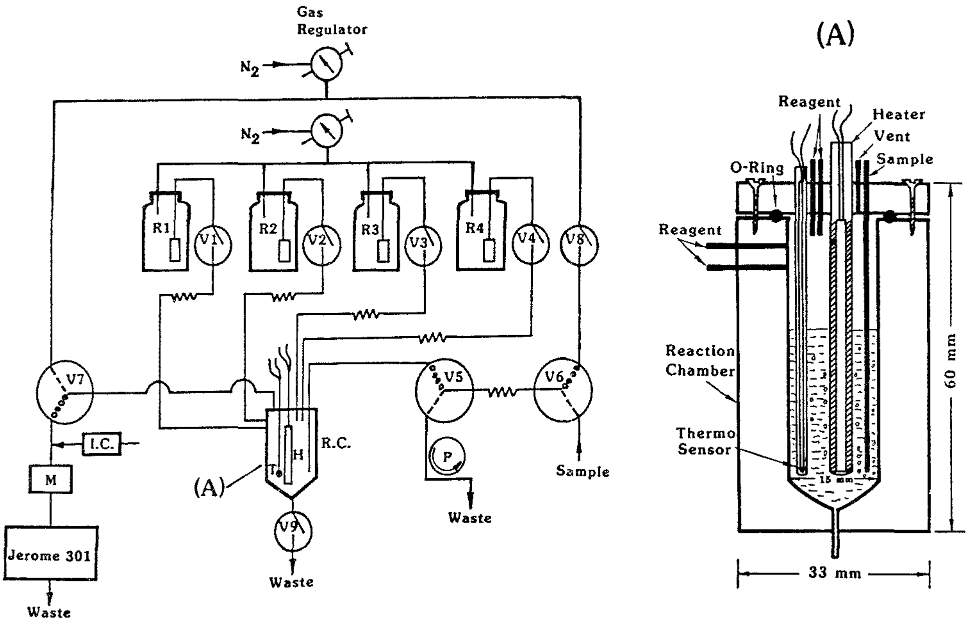

Figure 1. Instrument schematic: R1–R4, pressurized liquid reservoirs; V1–V9, logic-addressable valves; M, alkaline cartridge filter; IC, iodized charcoal filter; T, thermistor; H, heater; RC, reaction chamber; P, peristaltic pump.

Table I. Reagent Composition and Delivery Lines

reagent	composition	delivery line
R1	$NaBH_4$ (Fisher), 2% (w/v) prepared daily	0.71 mm i.d., 1.4 m
R2	0.25 M H_2SO_4	0.86 mm i.d., 1.3 m
R3	H_2O_2, 5% (v/v)	0.86 mm i.d., 1.3 m
R4	$FeSO_4(NH_4)_2SO_4 \cdot 6H_2O$ satd + 1% (w/v) $NH_2OH \cdot HCl$ +1 mL conc H_2SO_4/100 mL	0.86 mm i.d., 1.4 m; sheathed with nylon tube to exclude oxygen

is schematically shown in Figure 1. The heart of the system is the reaction chamber RC, shown in detail in the inset. Different liquids (R1–R4) are delivered from N_2-pressurized reservoirs (5.6 psi) via PTFE tubes and electrically actuated on/off valves V1–V4. The reagent compositions and delivery line details are given in Table I. The rinse solution tube enters through the upper side walls of the chamber, the terminus being exactly atop the $NaBH_4$ delivery tube, such that during rinsing, any lingering drops of the latter are washed down. The other lines enter through the top of RC. The R4 delivery line terminates in a 26-gauge hypodermic stainless steel needle tip, covered externally by the PTFE tube. The fine orifice improves reproducible dispensing of small reagent aliquots. The urine sample from the autosampler is aspirated by a peristaltic pump into the loop (203 ± 0.7 μL, gravimetrically determined for water as sample, $n = 5$) of V5/V6 (dashed ports connected). Next, V5/V6 is turned off to switch to the inject mode (dotted ports connected), V8 is turned on, and 2.5 psi N_2 blows the sample into RC. The sample delivery tube protrudes 42 mm from the top into the chamber. A cartridge heater ($^1/_8 \times 1^1/_4$ in., Watlow, St. Louis, MO) sheathed in a Pyrex sleeve and a precalibrated thermistor (type P30, Thermometrics, Edison, NJ) sealed in a 1.5 mm o.d. glass tube also enter from the top to depths of 38 and 36 mm, respectively. The heater is operated at 80 V and a simple thermostating circuitry maintains the temperature at 50 ± 0.5 °C during digestion.

The chamber is machined from 1.5 in. PTFE rod; the lid is affixed to the top by three screws and an O-ring seal. The tubes are push-fit to the chamber. A double three-way large orifice (1.5 mm) valve (type 360-T-041, Neptune Research, Inc., Maplewood, NJ) constitutes V7/V9; the latter is used here in the two-way mode. The other valves (all of inert construction) and their control by a programmable microprocessor driven process controller (Micromaster LS, Minarik Electric, Los Angeles, CA) have been previously described (*2, 3*). The eight relay outputs of the controller were assigned as V1, V2, V3/V4, V5/V6/autosampler (see below), V7/V9, V8, heater, and flash desorption pulse to the Jerome 301 mercury monitor (Arizona Instruments, Jerome division, Jerome, AZ).

The sources and preparation of various mercury standard solutions and urinary mercury standards have been previously described (*1*). The air inlet to the Hg monitor is protected by a small cartridge filter M filled with an alkaline adsorbent (Mallcosorb, Mallinckrodt Inc.). The sensor film of the monitor is thermally regenerated daily before use.

Autosampler Construction. An inexpensive autosampler (under $800) was made by modifying a commercial fraction collector (Model 2110, Bio-Rad Laboratories, Richmond, CA). The fraction collector advances one tube in response to an external signal, e.g., a contact closure. The sampler intake is a 0.5 mm i.d. 1.5 mm o.d. Tefzel tube (Dionex Corp., Sunnyvale, CA), sharpened to a point at the tip and thermally shaped to provide a stiff straight 10 cm end. This is firmly attached to the threaded end of the piston of a miniature double acting pneumatic actuator of 4 in. displacement (type SDR-05-4-B, Clippard Instruments, Cincinnati, OH) controlled by two air solenoid valves operated with 5 psi air. The fraction collector is affixed on a baseboard provided with a standard $^1/_2$ in. diameter laboratory support rod and the probe tip is positioned by clamps to occupy the location of the drop forming head. With the actuator retracted, the probe tip is clear of the sample tubes (13 × 100 mm culture tubes, covered optionally with Parafilm), permitting free rotation of the sample tray. With the actuator extended, the probe tip punctures the Parafilm cover and descends, to within a few millimeters of the bottom of the sample tube. In operation, as the control output

Table II. Operation Sequence

time, s	H[a]	V_1	V_2	V_3	V_4	V_5	V_6	V_7	V_8	V_9	function
0.0–15.0						on	on				sample loaded into loop
15.0–20.0									on		sample delivered to chamber
20.0–35.0						on	on				distilled water loaded into loop
35.0–42.0				on	on				on		Fenton's reagent and distilled water delivered to chamber
42.0–282.0	on								on		digestion at 50 °C
282.0–283.0				on	on				on		Fenton's reagent delivered to chamber
283.0–285.8		on							on		sodium borohydride delivered to chamber
285.8–405.8									on		mercury vapor collected on gold coil
405.8–406.0									on		collector coil flash heated, mercury carried to gold film sensor
406.0–420.0								on	on	on	contents of chamber discarded
420.0–429.0			on						on		rinse solution delivered to chamber
429.0–443.0								on	on	on	contents of chamber discarded
443.0–452.0			on						on		rinse solution delivered to chamber
452.0–466.0								on	on	on	contents of chamber discarded

[a] Denotes heater circuit.

governing V5/V6 turns on, the probe tip descends into the sample tube. An auxiliary relay also turns on, providing power to the peristaltic type sample aspiration pump P, and the sample is loaded into V5/V6. As the control output goes off, the probe retracts, the sample pump stops, and the sample tray advances one tube. With some flow restriction to the vent port of the appropriate air solenoid, the probe tip descends relatively slowly, while its retraction remains fast. However, since the suction pump starts at the same time the actuator is activated, this results in air being aspirated into the tube prior to the sample, thus resulting in a segment of air between individual samples which minimizes carryover.

RESULTS AND DISCUSSION

Operation. The temporal sequence of events appears in Table II. Following the delivery of the sample into the chamber, water is aspirated into the sample loop and delivered into RC. This procedure greatly reduces sample carryover. Next, 2.5 mL of H_2O_2 and 0.1 mL of Fe(II) solution are delivered simultaneously. Following a 4-min digestion period, a second smaller shot (250 μL of H_2O_2 and 10 μL of Fe(II)) of Fenton's reagent is added. This repeat addition is done for the following reason. For an occasional sample, the H_2O_2 is totally consumed during the digestion step. Under these conditions, the addition of the alkaline reducing reagent causes immediate formation of some $Fe(OH)_2$, as evidenced from greenish black color of the resulting precipitate. In our experience, the loss of reproducibility in the recovery of Hg is associated with the formation of $Fe(OH)_2$. If additional H_2O_2 or Fenton's reagent is added following the digestion period, no precipitation of $Fe(OH)_2$ occurs.

The second shot of Fenton's reagent is followed by the addition of 1 mL of $NaBH_4$. Note that except for the initial sample loading period, V8 remains continuously on, admitting 2.5 psi N_2 and the gas bubbles through the solution at a rate of 60 mL/min. This bubbling mixes the solution and the exit gas proceeds through V7 (dotted port connected), through the alkaline filter M into the gold-plated collection coil of the Jerome 301 mercury monitor. Elemental Hg is liberated as soon as the $NaBH_4$ is added and the N_2 carrier gas purges it from the solution onto the collector. The air aspiration pump of the Hg monitor is internally set at 1.1 L/min. To provide its remaining aspiration requirement, room air, freed from any mercury by an iodized charcoal filter cartridge (IC), is drawn through a makeup tee. The liberated Hg is collected for 2 min; preliminary experiments established that this period is sufficient to essentially quantitatively collect the Hg. Following the collection period, a momentary pulse applied to the Jerome 301 causes the instrument to go into a flash desorption step wherein the collector is electrically heated and the liberated Hg passes over to the gold film conductometric sensor and the resulting peak is recorded on a strip chart recorder (*1*).

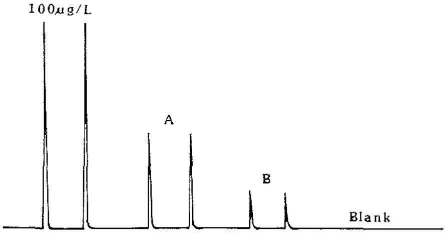

Figure 2. Typical system output.

Finally, the drain valve V9 is turned on and V7 is simultaneously switched, disconnecting the Hg monitor from the system and allowing the pressurized N_2 to force the contents of RC to waste. The chamber is then washed twice with several milliliters of the rinse solution, the contents being discarded each time. At the conclusion of this step, the system is ready to receive another sample.

Performance. The instrument output was found to be linear with mercury concentration in the sample from the limit of detection to the highest concentration studied (200 μg/L), with a correlation coefficient better than 0.999 and a near-zero intercept (equivalent to the calculated response from a 0.5 μg/L sample). Based on a S/N value of 3 as the limit of detection (LOD) (*4*), the LOD is 500 pg of Hg or 2.5 μg/L for a 200-μL sample. The LOD is proportionately decreased for a higher sample volume. Figure 2 shows typical instrument performance for duplicate sample injections, from left to right: 100 μg/L aqueous standard, reference urine sample A, reference urine sample B, blank. The stated Hg content of the reference samples were 50 ± 10 and 20 ± 6 μg/L; the measured values (48.0 ± 0.6 and 20.5 ± 0.3, respectively, $n = 3$) were in excellent agreement. Over the period the instrument has been in operation, the worst-case precision of the determination has been observed to be 2.4% (100 μg/L sample, $n = 7$).

The reaction chamber RC in this application is deliberately much larger than that used in previous AMBA systems (capacity 6.5 vs 1.5 mL in ref 2 and 3) which have been used for microtitrations (using potentiometric, colorimetric or conductometric sensors), for colorimetric or fluorometric measurements in homogeneous solution, or in systems involving solvent extraction and volatile analyte distillation. The detector used for the present dedicated application system is mass-sensitive. Consequently, the ability to handle a larger sample volume in the reaction chamber translates to a better concentration LOD. Although sample volumes larger than 200 μL are not necessary for urinanalysis, the other intended application for this AMBA system is wastewater samples where better concentration LOD's will be needed.

Mercury has a pronounced tendency to adsorb to surfaces and thus sample carryover in automated analysis systems is of particular concern. Carryover is reduced to less than 2.4% in the present system by alternating sample tubes with tubes containing water in the autosampler carousel and following the sample injection immediately with a water injection, as shown in Table I. Of course, this reduces the actual sample capacity of the autosampler by a factor of 2. However, with a capacity of 80 tubes, the instrument can still operate unattended for over 5 h and assay 40 samples in the process. It has been pointed out to us (C. J. Patton, U.S. Geological Survey, personal communication, 1989) that the autosampler described here with its pneumatically driven sample probe is essentially a reincarnation of a device described by Thiers et al. more than 2 decades ago (*5*). Indeed, the Thiers et al. device was more sophisticated in that it used two interconnected actuators mounted in an $X-Y$ plane to allow the probe to be lowered into a stationary wash solution between samples. Thus, the sample capacity of the carousel was not sacrificed. Such a design could be used profitably for analysis systems with greater analytical throughput rate. In any case, this type of an autosampler design is completely suitable for all cases where sample availability is not a problem. Because comparable commercial offerings typically cost 5 times as much, such designs should be worthy of consideration.

Registry No. Hg, 7439-97-6.

LITERATURE CITED

(1) Ping, L.; Dasgupta, P. K. *Anal. Chem.* **1989**, *61*, 1230–1235.
(2) Sweileh, J. A.; Lopez, J. L.; Dasgupta, P. K. *Rev. Sci. Instrum.* **1988**, *59*, 2609–2615.
(3) Sweileh, J. A.; Dasgupta, P. K. *Anal. Chim. Acta* **1988**, *214*, 107–120.
(4) American Chemical Society Committee on Environmental Improvement. *Anal. Chem.* **1980**, *52*, 2242–2249.
(5) Thiers, R. E.; Bryan, J.; Oglesby, K. *Clin. Chem.* **1966**, *12*, 120–136.

RECEIVED for review May 30, 1989. Accepted October 16, 1989. This work was supported in part by Arizona Instruments and the Dow Chemical Company.

MANUSCRIPT REQUIREMENTS

The following guide is published by the Editors of ANALYTICAL CHEMISTRY *to aid authors in writing, and editors and reviewers in expediting review and publication of manuscripts.*

SCOPE. The journal is devoted to the dissemination of knowledge concerning all branches of analytical chemistry. Articles either are entirely theoretical with regard to analysis or are reports of laboratory experiments that support, argue, refute, or extend established theory. Articles may contribute to any of the phases of analytical operations, such as sampling, chemical reactions, separations, instrumentation, measurements, and data processing. They need not refer to existing or even potential analytical methods in themselves, but may be confined to the principles and methodology underlying such methods. Articles dealing with minor modifications of known analytical methods should offer either a unique application of or a significant improvement over existing analytical methods.

In addition to regular research papers, *Correspondence* and *Technical Notes* are published. *Correspondence* may be brief disclosures of new analytical concepts of unusual significance. They may also represent important comments on the work of others, in which case the authors of the work being discussed will, ordinarily, be allowed to reply. *Technical Notes* should be brief descriptions of novel apparatus or techniques, requiring real ingenuity on the author's part, which offer definite advantages over similar ones already available.

Papers involving extensive use of computers will be judged by the usual criteria of originality, technical content, and value to the field. They should include a statement of the objectives and the procedural steps to the objective, and the results. However, *details* of procedural steps, including programs, should be omitted. Availability of the latter through commercial collections or by writing to the author should be clearly indicated in the text. Computational techniques for calculations of well-known analytical methods cannot be considered.

SUBMISSION OF MANUSCRIPTS. Papers submitted to ANALYTICAL CHEMISTRY are considered with the understanding that they have not been published and are not under consideration elsewhere.

Four complete copies of the manuscript are required. All copy must be typed double- or triple-spaced on 22 × 28 cm ($8^1/_2$ × 11 in.) or A4 paper on one side only (if a printer is used, it must be high quality), with text, tables, and illustrations of a size that can be mailed to reviewers under one cover.

In addition, include with your manuscript: (i) any paper of yours that is in press or under consideration elsewhere and includes information that would be helpful in evaluating the work submitted to *Analytical Chemistry*; (ii) written permission from any author whose work is cited as a personal communication, unpublished work, or work in press but who is not an author of your manuscript.

Reviewers suggested by authors may be used at the discretion of the editors.

Send all copies of the manuscript with cover letter to ANALYTICAL CHEMISTRY, 1155 Sixteenth St., N.W., Washington, DC 20036 (202-872-4570; FAX 202-872-6325).

TITLE. Use specific and informative titles with a high keyword content. Avoid trade names. Indicate, where applicable, compound or element determined, method, and special reagents (e.g., "Spectrophotometric Determination of Thallium in Zinc and Cadmium with Rhodamine B"). Do not use symbols, abbreviations, or series designations. Use one complete title rather than a title and subtitle. Careful attention should be paid to the choice of words (e.g., *determination* or *analysis*, etc.) to reflect correct usage.

AUTHORSHIP. Give authors' names in as complete a form as possible. First names, initials, and surnames should be included. Omit professional and official titles. Give the complete mailing address of the place where the work was done and include the telephone number of the corresponding author. Add the current address of each author, if different, on the title page of the manuscript using a numerical superscript and footnote to indicate the difference. The corresponding author is indicated by an asterisk.

ABSTRACT. Abstracts are required for all manuscripts, but will not be published with *Correspondence* and *Technical Notes*. The abstract (80–200 words) should describe briefly and clearly the purpose of the research, the principal results, and the major conclusions. State the objectives of the study, the limits of detection, the degree of accuracy and precision, and the major unique reagents, times, and temperatures, but avoid the lengthy stepwise recipe. The abstract should be essentially independent of the main text. Remember that the abstract will be the most widely read portion of the paper and will be used by the various abstracting services.

TEXT. Consult the publication for general style. Write for the specialist. Do not include information and details or techniques that should be common knowledge to the specialist.

General Organization. Indicate the breakdown among and within sections with center heads and side heads. Results and Discussion follow Experimental Section. Keep all information pertinent to a particular section within that section (e.g., do not present results in the Experimental Section). Avoid repetition. Do not use footnotes for descriptive or explanatory information; include the information at an appropriate place in the text.

INTRODUCTION

The introduction should state the purpose of the investigation and its relation to other work in the same field, but should not include an extensive review of the literature. If the manuscript describes a new method, reasons should be given why it is preferable to older methods.

EXPERIMENTAL SECTION

Use complete sentences (i.e., do not use outline form). Be consistent in voice and tense.

APPARATUS. List only devices of specialized nature. Do not include equipment that is standard in an analytical laboratory and used in the normal way.

REAGENTS. List and describe preparation of special reagents only. Do not list reagents normally found in the laboratory and preparations described in standard handbooks and texts.

PROCEDURE. Since all procedures are intended as instructions for other workers, give adequate details of critical steps to permit the work to be repeated by a qualified analyst. Published procedures should be cited but not described, except where the presentation involves substantially new modifications. Omit details of procedures that are common knowledge to those working in the field.

Safety Considerations: Describe all safety considerations, including any procedures that are hazardous, any reagents that are toxic, and any procedures requiring special precautions, in enough detail so that workers repeating the experiments can take appropriate safety measures. Appropriate procedures and references for the neutralization or deactivation, as well as ultimate disposal, of byproducts should be included.

RESULTS AND DISCUSSION

The results may be presented in tables or figures; however, many simple findings can be presented directly in the text with no need for tables or figures. The discussion should be concise and deal with the interpretation of the results. In most cases combining results and discussion in a single section will give a clearer, more compact presentation.

CONCLUSIONS

Use conclusions only when necessary for interpretation and not to summarize information already given in the text or abstract.

ACKNOWLEDGMENTS

Authors may acknowledge technical assistance, gifts, and the source of special materials.

LITERATURE CITED. References that are considered part of the permanent literature should be numbered in one consecutive series by order of mention in the text. However, the complete list of literature citations should be placed on a separate page, double-spaced, at the end of the manuscript. Reference numbers in the text should be placed in parentheses and on line. Repetition should be avoided by using the number corresponding to the original reference. Descriptive or explanatory (footnote) material should not routinely be given a reference number or included in the literature cited. This material should be included in the body of the text.

Use *Chemical Abstracts Service Source Index* abbreviations for journal names and include publication year, volume, and page number (inclusive pagination is recommended). Include *Chemical Abstracts* reference for foreign publications that are not readily available. List submitted articles as "in press" *only if* formally accepted for publication, and give the volume number and year if known. Otherwise use "submitted to" or "unpublished work" with place where work was done and date. Include name, affiliation, and date for "personal communications".

Please use the format given in the following examples.

(1) Koile, Ross C.; Johnson, Dennis C. *Anal. Chem.* **1979**, *51*, 741–744.

(2) Willard, Hobart H.; Merritt, Lynne L., Jr.; Dean, John A.; Settle, Frank A., Jr. *Instrumental Methods of Analysis*, 6th ed.; Van Nostrand: New York, 1981; Chapter 2.

CREDIT. On a separate page, give credit for financial support, meeting presentation information, and auspices under which work was done, including permission to publish. In the JOURNAL this information will immediately follow the received and accepted dates, and is not a part of the Acknowledgments.

FIGURES AND TABLES. Do not use figures or tables that duplicate each other or material already in the text. Straight line graphs will not normally be published; give the information in a table, or in a sentence or two in the text. Do not include tables or figures that have already been published.

Tables. Prepare tables in a consistent form, furnish each with an appropriate title, and number consecutively with Roman numerals in the order of reference in the text. Type each table on a separate page, and collate at the end of the manuscript.

Figures. Submit original drawings (or sharp glossy prints) of graphs and diagrams prepared on tracing cloth or plain white paper. If structures are given in the text, original drawings are to be provided. All lines, lettering, and numbering should be sharp and unbroken. If coordinate paper is used, use nonphotographic blue cross-hatch lines. Use black India ink and a lettering set for all letters, numbers, and symbols. Do *not* use a typewriter to letter illustrations.

Design illustrations to fit the width of one journal column (8.3 cm). The width of original drawings should be twice the publication size. Letters and symbols should be about 4 mm high on the original (2 mm in reduced journal version). Lines should be drawn with a light (#1 Leroy for graph grids), medium (#2 Leroy for graph borders or reference lines), or heavy (#5 Leroy for graph curves or emphasis) thickness on the original. Lettering on copy should be in proportion. Label ordinates and abscissas of graphs along the axes and outside the graph proper.

Supply good prints of photographs. Sharp contrasts are essential. Label each figure on the back with the name of the corresponding author and the figure number.

Number all figures consecutively with Arabic numerals in the order of reference in the text.

If drawings are mailed under separate cover, identify by name of author and title of manuscript.

Color reproduction is possible provided the author bears all incremental charges. An estimate of these charges will be given upon request. A letter acknowledging the author's willingness to defray the cost of color reproduction should accompany the revised manuscript.

Figure Captions. Include, on one page, a list of all captions and legends for illustrations. Make the legend a part of the caption rather than inserting it within the figure. Keep captions as brief as possible and include detailed information in the text.

BRIEF. On a separate page, state in 30 words or less the significant results obtained, emphasizing precision and accuracy data when possible. Do not repeat the title. No Briefs are necessary for *Correspondence* or *Technical Notes*.

NOMENCLATURE. Nomenclature should conform with current American usage. Insofar as possible, authors should use systematic names similar to those used by the International Union of Pure and Applied Chemistry and the Chemical Abstracts Service. For CA nomenclature advice consult the Manager of Nomenclature Services, P.O. Box 3012, Chemical Abstracts Service, Columbus, OH 43210. A name generation service is available through the Registry Services Department, Chemical Abstracts Service, P.O. Box 3343, Columbus, OH 43210.

Avoid trivial names. Well-known symbols and formulas may be used (write out in title and abstract) if no ambiguity is likely. Define trade names and abbreviations at point of first use. First letter of trade names is capitalized.

Use SI units of measurement (with acceptable exceptions) and give dimensions for all terms. If nomenclature is specialized, as in mathematical and engineering reports, include a Nomenclature section at end of paper, giving definitions and dimensions for all terms. Type all equations and formulas clearly and number all equations in consecutive order.

For specialized nomenclature used by this JOURNAL, see "Guide for Use of Terms in Reporting Data in ANALYTICAL CHEMISTRY", "Spectroscopy Nomenclature", and "SI Units", which appear annually, with the "Manuscript Requirements", at the end of the technical section in the first issue of the year. From time to time, ANALYTICAL CHEMISTRY publishes special nomenclature guides promulgated by various organizations.

General information about American Chemical Society publications, including preparation of manuscripts, is given in *The ACS Style Guide* (1986), available from Distribution Office, American Chemical Society, 1155 16th St., N.W., Washington, DC 20036 (800-227-5558 in the continental U.S.; in Washington, DC, or outside the U.S., call 202-872-4363).

Guide for Use of Terms in Reporting Data in ANALYTICAL CHEMISTRY

We have compiled the following list of frequently used terms and their definitions from ASTM Publication E456, 1989 Edition (Committee E-11 on Statistical Methods).

Precision refers to the closeness of agreement between randomly selected individual measurements or test results.

Accuracy refers to the closeness of agreement between an observed value and an accepted reference value.

Standard deviation is the most usual measure of the dispersion of observed values or results expressed as the positive square root of the variance.

Variance is a measure of the squared dispersion of observed values of measurements expressed as the sum of the squared deviations from the population mean or sample average.

Bias is a systematic error that contributes to the difference between a population mean of the measurements or test results and an accepted reference or true value.

Uncertainty is an indication of the variability associated with a measured value that takes into account two major components of error: bias and the random error attributed to the imprecision of the measurement process.

Repeatability is the closeness of agreement between mutually independent test results obtained with the same method in the same laboratory by the same operator with the same equipment within short intervals of time using test specimens taken at random from a single sample of material.

Reproducibility is the closeness of agreement between test results obtained in different laboratories with the same test method using test specimens taken at random from the same sample of material.

Spectroscopy Nomenclature

We have compiled the following list of frequently used terms, their definitions, and abbreviations. Sources used in this compilation were: ASTM Committee E 131 on Molecular Spectroscopy (1984 revision) and ASTM Committee E 135 on Analytical Atomic Spectroscopy (1986 revision).

Absorbance, *A*. The logarithm to the base 10 of the reciprocal of the transmittance, *T*.

$$A = \log_{10} (1/T) = -\log_{10} T$$

Absorptivity, *a*. The absorbance divided by the product of the concentration of the substance and the sample path length, $a = A/bc$. The units of b and c shall be specified.

NOTE 1. The recommended unit for b is the centimeter. The recommended unit for c is kilogram per cubic meter. Equivalent units are g/dm^3, g/L, or mg/cm^3.

NOTE 2. The equivalent IUPAC term is "specific absorption coefficient".

Absorptivity, Molar, ϵ. The product of the absorptivity, a, and the molecular weight of the substance.

NOTE. The equivalent IUPAC term is "molar absorption coefficient".

Analysis. The ascertainment of the identity or concentration, or both, of the constituents or components of a sample. See **determination**.

Concentration, *c*. The quantity of the substance contained in a unit quantity of sample.

NOTE. For solution work, the recommended unit of concentration is grams of solute per liter of solution.

Detectable Limit. Not recommended, see **detection limit**.

Detection Limit. A stated limiting value that designates the lowest concentration or mass that can be estimated or determined with confidence and that is specific to the analytical procedure used.

NOTE. Unless otherwise stated, the detection limit is assumed to have a confidence interval of about one standard deviation.

Determination. The ascertainment of the quantity or concentration of a specific substance in a sample. See **analysis**.

Electromagnetic Radiation. Energy propagated by an electromagnetic field. The electromagnetic spectrum includes the following approximate wavelength regions:

region	wavelength, Å	
γ ray	0.005 to 1.40	(0.5 to 140 pm)
X-ray	0.1 to 100	(0.01 to 10 nm)
far-ultraviolet	100 to 2000	(10 to 200 nm)
near-ultraviolet	2000 to 3800	(200 to 380 nm)
visible	3800 to 7800	(380 to 780 nm)
near-infrared	7800 to 30000	(0.78 to 3 μm)
middle-infrared	3×10^4 to 3×10^5	(3 to 30 μm)
far-infrared	3×10^5 to 3×10^6	(30 to 300 μm)
microwave	3×10^6 to 10^{10}	(0.3 mm to 1 m)

Frequency, ν. The number of cycles per unit time.

NOTE. The recommended unit is the hertz (Hz) (one cycle per second).

Spectrograph. An instrument with one slit that uses photography to obtain a record of a spectral range simultaneously. The radiant power passing through the optical system is integrated over time, and the quantity recorded is a function of radiant energy.

Spectrometer. An instrument with an entrance slit and one or more exit slits, with which measurements are made either by scanning the spectral range, point by point, or by simultaneous measurements at several spectral positions. The quantity measured is a function of radiant power.

Spectrophotometer. A spectrometer with associated equipment, so designed that it furnishes the ratio, or a function of the ratio, of the radiant power of two beams as a function of spectral position. The two beams may be separated in time, space, or both.

Spectroscopy. The branch of physical science treating the theory and interpretation of spectra.

Transmittance, *T*. The ratio of the radiant power transmitted by the sample to the radiant power incident on the sample.

Wavelength, λ. The distance, measured along the line of propagation, between two points that are in phase on adjacent waves.

SI Units

The move toward the usage of the International System of Units (SI) has been agreed to by ACS editors as general ACS policy. Although, in principle, the change to strict SI usage is desirable, necessary adjustments dictated by practical reality must be considered. This guide gives authors an idea of what exceptions are acceptable in articles published in ANALYTICAL CHEMISTRY. Also included are the SI base units, derived units, and prefixes. Units that are not compatible with SI or the acceptable exceptions, but which must be used in a manuscript, should be followed by the SI equivalent in parentheses, e.g., 1-in. (2.5-cm) tubing *or* 1-in. (2.54-cm) tubing. The number in the SI equivalent should include only as many digits as are significant for any particular use.

SI Base Units

Length	meter	m
Mass	kilogram	kg
Time	second	s
Electric current	ampere	A
Thermodynamic temperature	kelvin	K
Amount of substance	mole	mol
Luminous intensity	candela	cd
(supplementary units)		
Plane angle	radian	rad
Solid angle	steradian	sr

SI Derived Units

Area	square meter	m^2
Concentration	mole per cubic meter	mol/m^3
Density	kilogram per cubic meter	kg/m^3
Velocity	meter per second	m/s
Volume	cubic meter	m^3
Wavenumber	1 per meter	m^{-1}
(with special names)		
Capacitance	farad	F
Conductance	siemens	S
Electric charge, quantity of electricity	coulomb	C
Electric potential, potential difference, electromotive force	volt	V
Energy, work, quantity of heat	joule	J
Force	newton	N
Frequency	hertz	Hz
Illuminance	lux	lx
Inductance	henry	H
Luminous flow	lumen	lm
Magnetic flux	weber	Wb
Magnetic flux density	tesla	T
Power	watt	W
Pressure	pascal	Pa
Radioactive activity	becquerel	Bq
Resistance	ohm	Ω

SI Prefixes

10^{18}	exa	E
10^{15}	peta	P
10^{12}	tera	T
10^{9}	giga	G
10^{6}	mega	M
10^{3}	kilo	k
10^{2}	hecto	h
10^{1}	deka	da
10^{-1}	deci	d
10^{-2}	centi	c
10^{-3}	milli	m
10^{-6}	micro	μ
10^{-9}	nano	n
10^{-12}	pico	p
10^{-15}	femto	f
10^{-18}	atto	a

Acceptable Exceptions

Area	barn
Concentration	molal = mole per kilogram (m = mol kg^{-1}) molar = mole per liter (M = mol L^{-1}); *not* formal or normal
Conductance	mho (Ω^{-1})
Density	gram per cubic centimeter (g/cm^3)
Energy	electronvolt (eV); also keV, MeV
Length	angstrom (Å)
Plane angle	degree (°), minute (′), second (″)
Pressure	atmosphere (atm), bar, torr
Radioactivity of radionuclides	disintegrations per second (dps)
Second-order rate constants	1 per (mole per liter) per second (M^{-1} s^{-1})
Temperature	degree Celsius (°C)
Time	minute (min), hour (h), day (d), etc.
Volume	liter (L), milliliter (mL), microliter (μL)
Wavenumber	1 per centimeter (cm^{-1})

ANALYTICAL CHEMISTRY, VOL 62. NO. 1, JANUARY 1, 1990 • 93

Ethical Guidelines to Publication of Chemical Research

The guidelines embodied in this document were adopted by the editors of the Books and Journals Division (now the Publications Division) of the American Chemical Society in January 1985, endorsed by the Society Committee on Publications, and reaffirmed at the 1989 conference of Editors.

PREFACE

The American Chemical Society serves the chemistry profession and society at large in many ways, among them by publishing journals which present the results of scientific and engineering research. Every editor of a Society journal has the responsibility to establish and maintain guidelines for selecting and accepting papers submitted to that journal. In the main, these guidelines derive from the Society's definition of the scope of the journal and from the editor's perception of standards of quality for scientific work and its presentation.

An essential feature of a profession is the acceptance by its members of a code that outlines desirable behavior and specifies obligations of members to each other and to the public. Such a code derives from a desire to maximize perceived benefits to society and to the profession as a whole and to limit actions that might serve the narrow self-interests of individuals. The advancement of science requires the sharing of knowledge between individuals, even though doing so may sometimes entail foregoing some immediate personal advantage.

With these thoughts in mind, the editors of journals published by the American Chemical Society now present a set of ethical guidelines for persons engaged in the publication of chemical research, specifically, for editors, authors, and manuscript reviewers. These guidelines are offered not in the sense that there is any immediate crisis in ethical behavior, but rather from a conviction that the observance of high ethical standards is so vital to the whole scientific enterprise that a definition of those standards should be brought to the attention of all concerned.

We believe that most of the guidelines now offered are already understood and subscribed to by the majority of experienced research chemists. They may, however, be of substantial help to those who are relatively new to research. Even well-established scientists may appreciate an opportunity to review matters so significant to the practice of science.

Formulation of these guidelines has made us think deeply about these matters. We intend to abide by these guidelines, strictly, in our own work as editors, authors, and manuscript reviewers.

GUIDELINES

A. ETHICAL OBLIGATIONS OF EDITORS OF SCIENTIFIC JOURNALS

1. An editor should give unbiased consideration to all manuscripts offered for publication, judging each on its merits without regard to race, religion, nationality, sex, seniority, or institutional affiliation of the author(s). An editor may, however, take into account relationships of a manuscript immediately under consideration to others previously or concurrently offered by the same author(s).

2. An editor should consider manuscripts submitted for publication with all reasonable speed.

3. The sole responsibility for acceptance or rejection of a manuscript rests with the editor. Responsible and prudent exercise of this duty normally requires that the editor seek advice from reviewers, chosen for their expertise and good judgment, as to the quality and reliability of manuscripts submitted for publication. In reaching a final decision, the editor should also consider additional factors of editorial policy.

4. The editor and members of the editor's staff should not disclose any information about a manuscript under consideration to anyone other than those from whom professional advice is sought. (However, an editor who solicits, or otherwise arranges beforehand, the submission of manuscripts may need to disclose to a prospective author the fact that a relevant manuscript by another author has been received or is in preparation.) After manuscripts have been accepted for publication, the editor and members of the editor's staff may disclose or publish manuscript titles and authors' names, but no more than that unless the author's permission has been obtained.

5. An editor should respect the intellectual independence of authors.

6. Editorial responsibility and authority for any manuscript authored by an editor and submitted to the editor's journal should be delegated to some other qualified person, such as another editor of that journal or a member of its Editorial Advisory Board. Editorial consideration of the manuscript in any way or form by the author-editor would constitute a conflict of interest, and is therefore improper.

7. Unpublished information, arguments, or interpretations disclosed in a submitted manuscript should not be used in an editor's own research except with the consent of the author. However, if such information indicates that some of the editor's own research is unlikely to be profitable, the editor could ethically discontinue the work. When a manuscript is so closely related to the current or past research of an editor as to create a conflict of interest, the editor should arrange for some other qualified person to take editorial responsibility for that manuscript. In some cases, it may be appropriate to tell an author about the editor's research and plans in that area.

8. If an editor is presented with convincing evidence that the main substance or conclusions of a report published in an editor's journal are erroneous, the editor should facilitate publication of an appropriate report pointing out the error and, if possible, correcting it. The report may be written by the person who discovered the error or by an original author.

B. ETHICAL OBLIGATIONS OF AUTHORS

1. An author's central obligation is to present an accurate account of the research performed as well as an objective discussion of its significance.

2. An author should recognize that journal space is a precious resource created at considerable cost. An author therefore has an obligation to use it wisely and economically.

3. A primary research report should contain sufficient detail and reference to public sources of information to permit the author's peers to repeat the work.

4. An author should cite those publications that have been influential in determining the nature of the reported work and that will guide the reader quickly to the earlier work that is essential for understanding the present investigation. Except in a review, citation of work that will not be referred to in the reported research should be minimized.

5. Any unusual hazards inherent in the chemicals, equipment, or procedures used in an investigation should be clearly identified in a manuscript reporting the work.

6. Fragmentation of research reports should be avoided. A scientist who has done extensive work on a system or group of related systems should organize publication so that each report gives a well-rounded account of a particular aspect of the general study. Fragmentation consumes journal space excessively and unduly complicates literature searches. The convenience of readers is served if reports on related studies are published in the same journal, or in a small number of journals.

7. In submitting a manuscript for publication, an author should inform the editor of related manuscripts that the author has under editorial consideration or in press. The relationships of such manuscripts to the one submitted should be indicated.

8. It is in general inappropriate for an author to submit manuscripts describing essentially the same research to more than one journal of primary publication. However, there are exceptions as follows: (a) resubmission of a manuscript rejected by or withdrawn from publication in one journal; (b) submission of overlapping work to a second journal in another field, if workers in the other field are unlikely to see the article published in the first journal, providing that both editors are informed; and (c) submission of a manuscript for a full paper expanding on a previously published brief preliminary account (a "communication" or "letter") of the same work.

9. An author should identify the source of all information quoted or offered, except that which is common knowledge. Information obtained privately, as in conversation, correspondence, or discussion with third parties, should not be used or reported in the author's work without explicit permission from the investigator with whom the information originated. Information obtained in the course of confidential services, such as refereeing manuscripts or grant applications, should be treated similarly.

10. An experimental or theoretical study may sometimes justify criticism, even severe criticism, of the work of another scientist. When appropriate, such criticism may be offered in published papers. However, in no case is personal criticism considered to be appropriate.

11. The co-authors of a paper should be all those persons who have made significant scientific contributions to the work reported and who share responsibility and accountability for the results. Other contributions should be indicated in a footnote or an "Acknowledgments" section. An administrative relationship to the investigation does not of itself qualify a person for co-authorship (but occasionally it may be appropriate to acknowledge major administrative assistance). Deceased persons who meet the criterion for inclusion as co-authors should be so included, with a footnote reporting date of death. No fictitious name should be listed as an author or co-author. The author who submits a manuscript for publication accepts the responsibility of having included as co-authors all persons appropriate and none inappropriate. The submitting author should have sent each living co-author a draft copy of the manuscript and have obtained the co-author's assent to co-authorship of it.

C. ETHICAL OBLIGATIONS OF REVIEWERS OF MANUSCRIPTS

1. Inasmuch as the reviewing of manuscripts is an essential step in the publication process, and therefore in the operation of the scientific method, every scientist has an obligation to do a fair share of reviewing.

2. A chosen reviewer who feels inadequately qualified to judge the research reported in a manuscript should return it promptly to the editor.

3. A reviewer (or referee) of a manuscript should judge objectively the quality of the manuscript, of its experimental and theoretical work, of its interpretations and its exposition, with due regard to the maintenance of high scientific and literary standards. A reviewer should respect the intellectual independence of the authors.

4. A reviewer should be sensitive to the appearance of a conflict of interest when the manuscript under review is closely related to the reviewer's work in progress or published. If in doubt, the reviewer should return the manuscript promptly without review, advising the editor of the conflict of interest or bias. Alternatively, the reviewer may wish to furnish a signed review stating the reviewer's interest in the work, with the understanding that it may, at the editor's discretion, be transmitted to the author.

5. A reviewer should not evaluate a manuscript authored or co-authored by a person with whom the reviewer has a personal or professional connection if the relationship would bias judgment of the manuscript.

6. A reviewer should treat a manuscript sent for review as a confidential document. It should neither be shown to nor discussed with others except, in special cases, to persons from whom specific advice may be sought; in that event, the identities of those consulted should be disclosed to the editor.

7. Reviewers should explain and support their judgments adequately so that editors and authors may understand the basis of their comments. Any statement that an observation, derivation, or argument had been previously reported should be accompanied by the relevant citation. Unsupported assertions by reviewers (or by authors in rebuttal) are of little value and should be avoided.

8. A reviewer should be alert to failure of authors to cite relevant work by other scientists, bearing in mind that complaints that the reviewer's own research was insufficiently cited may seem self-serving. A reviewer should call to the editor's attention any substantial similarity between the manuscript under consideration and any published paper or any manuscript submitted concurrently to another journal.

9. A reviewer should act promptly, submitting a report in a timely manner. Should a reviewer receive a manuscript at a time when circumstances preclude prompt attention to it, the unreviewed manuscript should be returned immediately to the editor. Alternatively, the reviewer might notify the editor of probable delays and propose a revised review date.

10. Reviewers should not use or disclose unpublished information, arguments, or interpretations contained in a manuscript under consideration, except with the consent of the author. If this information indicates that some of the reviewer's work is unlikely to be profitable, the reviewer, however, could ethically discontinue the work. In some cases, it may be appropriate for the reviewer to write the author, with copy to the editor, about the reviewer's research and plans in that area.

D. ETHICAL OBLIGATIONS OF SCIENTISTS PUBLISHING OUTSIDE THE SCIENTIFIC LITERATURE

1. A scientist publishing in the popular literature has the same basic obligation to be accurate in reporting observations and unbiased in interpreting them as when publishing in a scientific journal.

2. Inasmuch as laymen may not understand scientific terminology, the scientist may find it necessary to use common words of lesser precision to increase public comprehension. In view of the importance of scientists' communicating with the general public, some loss of accuracy in that sense can be condoned. The scientist should, however, strive to keep public writing, remarks, and interviews as accurate as possible consistent with effective communication.

3. A scientist should not proclaim a discovery to the public unless the experimental, statistical, or theoretical support for it is of strength sufficient to warrant publication in the scientific literature. An account of the experimental work and results that support a public pronouncement should be submitted as quickly as possible for publication in a scientific journal. Scientists should, however, be aware that extensive disclosure of research in the public press might be considered by a journal editor as equivalent to a preliminary communication in the scientific literature.

COPYRIGHT STATUS FORM

Name of American Chemical Society Publication

Author(s)

Ms No.

Ms Title

Received

This manuscript will be considered with the understanding you have submitted it on an exclusive basis. You will be notified of a decision as soon as possible.

t or
e
e
or's
e and
ress

[THIS FORM MAY
BE REPRODUCED]

COPYRIGHT TRANSFER

The undersigned, with the consent of all authors, hereby transfers, to the extent that there is copyright to be transferred, the exclusive copyright interest in the above cited manuscript (subsequently referred to as the "work") to the **American Chemical Society** subject to the following (Note: if the manuscript is not accepted by ACS or if it is withdrawn prior to acceptance by ACS, this transfer will be null and void and the form will be returned.):

A. The undersigned author and all coauthors retain the right to revise, adapt, prepare derivative works, present orally, or distribute the work provided that all such use is for the personal noncommercial benefit of the author(s) and is consistent with any prior contractual agreement between the undersigned and/or coauthors and their employer(s).

B. In all instances where the work is prepared as a "work made for hire" for an employer, the employer(s) of the author(s) retain(s) the right to revise, adapt, prepare derivative works, publish, reprint, reproduce, and distribute the work provided that all such use is for the promotion of its business enterprise and does not imply the endorsement of the American Chemical Society.

C. Whenever the American Chemical Society is approached by third parties for individual permission to use, reprint, or republish specified articles (except for classroom use, library reserve, or to reprint in a collective work) the undersigned author's or employer's permission will also be required.

D. No proprietary right other than copyright is claimed by the American Chemical Society.

E. For works prepared under U.S. Government contract or by employees of a foreign government or its instrumentalities, the American Chemical Society recognizes that government's prior nonexclusive, royalty-free license to publish, translate, reproduce, use, or dispose of the published form of the work, or allow others to do so for noncommercial government purposes. State contract number: ____________________ .

SIGN HERE FOR COPYRIGHT TRANSFER [Individual Author or Employer's Authorized Agent (work made for hire)]

Print Author's Name

Print Agent's Name and Title

▶

Original Signature of Author on Behalf of All Authors (in Ink)

Date

Original Signature of Agent (in Ink)

CERTIFICATION AS A WORK OF THE U.S. GOVERNMENT

This is to certify that **ALL** authors are or were bona fide officers or employees of the U.S. Government at the time the paper was prepared, and that the work is a "work of the U.S. Government" (prepared by an officer or employee of the U.S. Government as a part of official duties), and, therefore, it is not subject to U.S. copyright. (This section should NOT be signed if the work was prepared under a government contract or coauthored by a non-U.S. Government employee.)

INDIVIDUAL AUTHOR **OR** AGENCY REPRESENTATIVE

Print Author's Name

Print Agency Representative's Name and Title

Original Signature of Author (in Ink)

Date

Original Signature of Agency Representative (in Ink)

FOREIGN COPYRIGHT RESERVED (NOTE: If your government permits copyright to be transferred, refer to section E and sign this form in the top section.)

☐ If **ALL** authors are employees of a foreign government that reserves its own copyright as mandated by national law, **DO NOT SIGN THIS FORM.** Please check this box as your request for the FOREIGN GOVERNMENT COPYRIGHT FORM (Blue Form) which you will be required to sign. **If you check this box**, mail this form to: Copyright Administrator, Books and Journals Division, American Chemical Society, 1155 Sixteenth Street, N.W., Washington, D.C. 20036, U.S.A.


Analytical Industrial and Engineering Chemistry Edition
MEETS A UNIVERSAL DEMAND NOW
INDUSTRIAL and ENGINEERING CHEMISTRY
The Explorer within four walls
J. T. BAKER CHEMICAL CO.
Baker's Analyzed
ANALYTICAL CHEMISTRY
JULY 1969
ANALYTICAL CHEMISTRY
ALYTICAL
HEMISTRY
FEBRUARY 1949
AUGUST 1979
analytical chemistry
Information Retrieval and Data Management
MARCH 1984
analytical chemistry
PRODUCT TAMPERING: TRACING THE SOURCE
Analytical CHEMISTRY
DECEMBER 1, 1987
ICP
Still the Panacea for Trace Metals Analysis? 1345 A